Single-Molecule Metal-Induced Energy Transfer: From Basics to Applications

Narain Karedla

Single-Molecule Metal-Induced Energy Transfer: From Basics to Applications

Dissertation

to acquire the doctoral degree in mathematics and natural science
“Doctor rerum naturalium”
at the Georg-August-Universität Göttingen

within the doctoral degree program

Physics of Biological and Complex Systems
of the Göttingen Graduate School of Neurosciences, Biophysics, and Molecular Biosciences (GGNB)
of the Georg-August University School of Sciences (GAUSS)

submitted by

Narain Karedla
from Hyderabad, India
Göttingen, 2016

THESIS COMMITTEE:

Prof. Dr. Jörg Enderlein (Referee)

Third Institute of Physics - Biophysics
Georg-August-University Göttingen

Prof. Dr. Andreas Janshoff (Co-Referee)

Institute for Physical Chemistry
Georg-August-University Göttingen

Prof. Dr. Sarah Köster

Institute for X-Ray Physics
Georg-August-University Göttingen

OTHER MEMBERS OF THE EXAMINATION BOARD:

Prof. Dr. Holger Stark

Department of Structural Dynamics
Max Planck Institute for Biophysical Chemistry

Dr. Gopalakrishnan Balasubramanian

Department of Nanoscale Spin Imaging
Max Planck Institute for Biophysical Chemistry

Dr. Andreas Neef

Bernstein Center for Computional Neuroscience Göttingen
Max Planck Institute for Dynamics and Self-Organization

Date of oral examination: 02.06.2016

Affidavit

Hereby, I declare that the presented thesis has been written independently and with no other sources and aids than quoted.

Parts of this thesis and few figures have been published in the following journal articles:

1. **Karedla, N.**; Chizhik, A.I.; Gregor, I.; Chizhik, A.M.; Schulz, O.; Enderlein, J. *"Single-Molecule Metal Induced Energy Transfer (smMIET): Resolving Nanometer Distances at Single Molecule Level"* ChemPhysChem **15** 705-11 (2014)

2. Ghosh,S.; Chizhik, A.M.; **Karedla, N.**; Debaliuk, M.O.; Gregor,I.; Schuhmann,H.; Seibt,M.; Bodensiek,K.; Schaap, I.A.T.; Schulz,O.; Demchenko,A.P.; Enderlein,J.; Chizhik,A.I. *"Photoluminescence of Carbon Nanodots: Dipole Emission Centers and Electron-Photon Coupling"* Nano Letters **14** 5656-5661 (2014)

3. **Karedla, N.**; Stein, S.; Hähnel, D.; Gregor, I.; Chizhik,A.I.; Enderlein, J. *"Simultaneous Measurement of the Three-Dimensional Orientation of Excitation and Emission Dipoles"* Physical Review Letters **115** 173002 (2015)

Göttingen, 12.04.2016

“*From a long view of the history of mankind - seen from, say, ten thousand years from now - there can be little doubt that the most significant event of the 19th century will be judged as Maxwell’s discovery of the laws of electrodynamics.*”

- Richard Feynman

Contents

Abstract

Single-molecule detection and spectroscopy have revolutionized the field of fluorescence microscopy. Due to their enormous potential in studying physics, chemistry and biology at molecular level, the number of single-molecule based techniques and methods has grown exponentially in the last two decades. A recent addition to the pool of existing single-molecule based techniques are superresolution imaging methods, which are used for resolving structures far below the diffraction limit of an optical microscope. However, a major limitation faced by most of the methods developed so far is the resolution along the axial direction, which is still an order of magnitude worse than the maximum lateral resolution achievable. In this thesis, we present a new concept for measuring distances of single molecules from a metal surface with nanometer accuracy using the energy transfer from the excited molecules to the surface plasmons of a metal film, which we term single-molecule Metal-Induced Energy Transfer (smMIET). We perform the first proof-of-principle experiments on single dye molecules and demonstrate an axial localization with nanometer accuracy. Here, we build the theoretical outline for the description of smMIET, and throw light on the potential for its application in structural biology.

Apart from this, in this thesis, we present the first experimental approach to determine *simultaneously* the *three-dimensional* excitation and emission dipole geometry of individual emitters. Here, we use defocused imaging in conjugation with radially polarized excitation scanning to characterize the emission and excitation transition probabilities. We demonstrate this approach on two commercially available dye molecules and obtain the distributions of the angle between their excitation and emission transition dipoles. This experimental tool can be used for elucidating more complex excitation/emission geometries, such as those found in fluorescent nano-crystals (quantum dots) and also for verifying the quantum chemical calculations that are used for predicting the structure and geometry of the molecular orbitals involved in an electronic transition.

1 Introduction

The first optical detection of a single molecule, based on the optical-absorption of dopant dye molecules in a host crystal at liquid-helium temperatures, was achieved by Moerner *et al.* in 1989 [1]. One year later, Orrit *et al.* corroborated this work with their experiments on the same system, instead detecting the fluorescence emission from single molecules [2]. These experiments marked the beginning of fluorescence based single-molecule experiments and single-molecule spectroscopy. With the advent of high repetition rate pulsed lasers, single photon sensitive detectors and fast electronics, many advanced single-molecule based experimental techniques have been realized [3–7]. Fluorescence Correlation Spectroscopy (FCS) [8, 9], Fluorescence Lifetime Correlation Spectroscopy (FLCS) [10, 11], single-pair Förster Resonance Energy Transfer (spFRET) [12, 13], Photon-Arrival-Time Interval Distribution (PAID) [14–16], Fluorescence Intensity and Lifetime Distribution Analysis (FILDA) [17] are few of the several methods that are widely used these days in polymer physics, biophysics, etc. for characterizing dynamics such as diffusion, aggregation-dissociation, conformational fluctuations of labeled biomolecules and proteins [18–20]. Photon counting and antibunching experiments are extensively used in quantum optics and quantum sensing applications [21–24].

Accurate single photon counting and timing with a pulsed laser excitation system is the heart of all these methods. Therefore, a unified instrumental approach suitable for all these methods was developed by modifying the classical Time-Correlated Single Photon Counting (TCSPC) system with a timing and recording scheme where each detected photon is assigned two time tags, one with respect to the delay from the last laser sync or signal from a high frequency oscillator, called the microtime τ, and second with respect to the start of the experiment, called the event-time t. The time resolution for the microtime goes down to a few picoseconds, whereas for the macrotime is usually counted over the number of syncs preceding the detection event [3]. In this way, the time of each detection event can be recorded with a picosecond resolution from the start of the experiment upto several hours. This mode of photon timing is called the Time-Tagged Time-Resolved (TTTR) counting. The basic instrumentation and the working details are published in the work of Wahl *et al.* [3] (see also [4, 5]).

One is not just limited to the picosecond timing resolution of the electronics mentioned above. The development of methods such as pump-probe spectroscopy, ultrafast fluorescence spectroscopy using up-conversion have made the study of ultrafast electronic and vibrational relaxations of single-molecule level at room temperature possible [25, 26]. With such techniques, one can study photophysical properties of single molecules with a temporal resolution on the order of femtoseconds.

Owing to it's high sensitivity, selectivity, and simplicity (compared to other microscopic techniques), fluorescence microscopy is an ubiquitous tool in biology. It is routinely used for studying complex cellular and sub-cellular processes using stable and high quantum yield fluorescent dye molecules that are labeled specifically to their target sites and acquiring high spatial and temporal information. However, the fundamental limitation of any optical system is its inability to provide spatial resolution below the wavelength of light, due to the wave nature of light, which typically lies in the range between 300 nm to 800 nm. Only recently, super-resolution methods, that circumvent the diffraction limit using various working principles have emerged. One class of such techniques are based on single-molecule localization on an acquired 2D intensity image on CCD cameras such as Photo-activated Localization Microscopy (PALM) [27], and Stochastic Optical Reconstruction Microscopy (STORM) [28], direct STORM (dSTORM) [29] and Points Accumulation In Nanoscale Topography (PAINT) microscopy [30]. The core idea of these methods is to label a sample with fluorescent molecules that are photo-switchable (or that bind transiently) and then to acquire many consecutive images with different sub-sets of molecules switched into a fluorescent *on* state in such a way that in each recorded image all fluorescing molecules are well separated from each other spatially. Then these isolated molecules from each image are localized with an accuracy that is much superior to the optical resolution limit of the used microscope using a Gaussian model. In the end, by pooling together all positions from all detected molecules, a pointillistic super-resolved image can be reconstructed.

The physical basis of these super-resolution methods is the ability to pinpoint the position of emitting molecules with much higher accuracy than the sizes of their image on the detector, that is, the Point Spread Function (PSF) of the microscope [31]. This lateral localization accuracy is directly related to the number of photons recorded from the single molecule, among various other factors, and is given by the equation:

$$\sigma_{xy}^2 = \frac{\sigma_{PSF}^2}{N}\left(\frac{16}{9} + \frac{8\pi\sigma_{PSF}^2 b^2}{Na^2}\right) \tag{1.1}$$

in which σ_{xy} is the localization precision, σ_{PSF} is the full-width-at-half maximum of the PSF, N is the number of photons collected from the molecule, b is the background noise level, and a is the pixel size of the detector. Under typical conditions, at room temperature, using conventional organic fluorophores, the achievable localization accuracy is around 10 nm laterally and thus is almost two orders of magnitude better than the diffraction limit of a typical microscope [32]. In this way, PALM, STORM, and dSTORM have found many applications in biological imaging with spectacular results; for example, see ref. [33]. By employing schemes such as astigmatism-based imaging, these techniques have been used for the study 3D ultrastructures in biological entities. However, the achievable axial resolution is still two orders of magnitude worse than typical distances and sizes of biomacromolecules, due to which their application in structural biology on macromolecular level is limited. The maximum achievable axial resolution in these techniques using the astigmatism approach is limited to 50 nm. Also, when the rotational freedom of the fluorescent molecule is restricted, one introduces a biased error while localizing using a 2D gaussian based PSF as in equation (1.2) [34, 35].

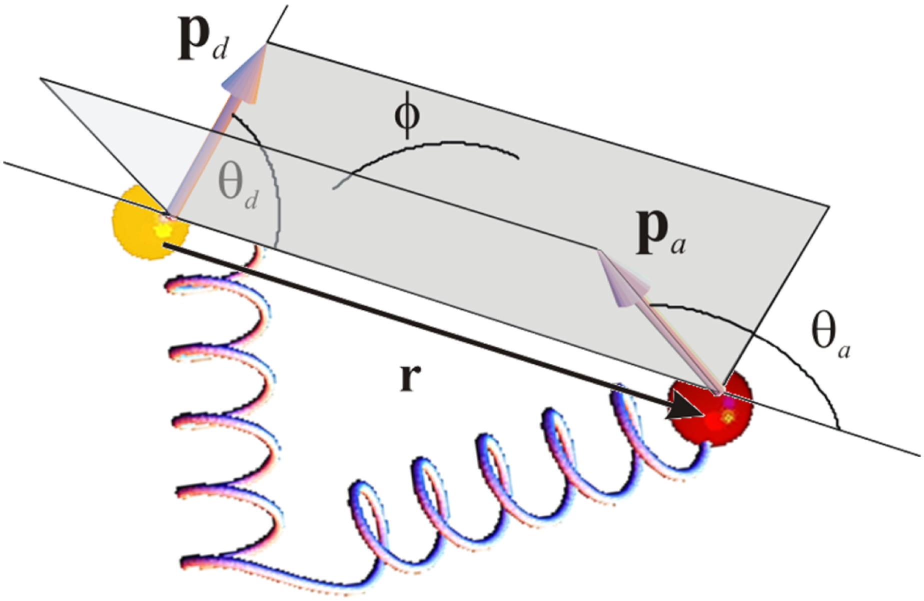

Figure 1.1: Geometry of the FRET system. $\mathbf{p}_d$ and $\mathbf{p}_a$ show the orientations of the donor's emission transition dipole and the acceptor's excitation transition dipole moment, respectively that are separated in space by $\mathbf{r}$. θ_a (θ_d) is the angle between $\mathbf{p}_a$ ($\mathbf{p}_d$) and $\mathbf{r}$. ϕ is the angle between the plane formed by $\mathbf{p}_a$ and $\mathbf{r}$ with $\mathbf{p}_d$ with the plane containing $\mathbf{p}_d$ and $\mathbf{r}$.

When it comes to sizes of few nanometers, the most used fluorescence-based optical method is Förster Resonance Energy Transfer (FRET) [36], named after its discoverer Theodor Förster [37]. FRET is based on the dipole–dipole interaction of two fluorophores, the so-called donor and acceptor. The near-field of the emitting donor falls off as r^{-3} , so the excitation efficiency of the acceptor follows a r^{-6} relationship. Due to this strong decline on a nanometer length scale, FRET is used as a molecular ruler [38]. Quantitatively, the rate of energy transfer from a donor to an acceptor molecule is given by the equation:

$$k_a = \frac{1}{\tau_d}\left(\frac{R_0}{r}\right)^6 \tag{1.2}$$

in which τ_d is the donor's unperturbed fluorescence lifetime, r is the distance between donor and acceptor, and R_0 is the so-called Förster radius that depends on the donor's emission spectrum, the absorption cross-section of the acceptor dipole at these wavelengths, and the relative orientation of both molecules with respect to each other. Usually it lies in the range of 2 to 6 nm. Single-pair FRET (spFRET) experiments were first realized by Ha *et al.* [39]. They used Near-field Scanning Optical Microscopy (NSOM) on immobilized short DNA fragments with attached FRET pairs. Subsequently, many studies have successfully used spFRET for studying biological problems at single-molecule level [40–48].

As powerful as FRET and spFRET are, they have two major shortcomings. First, the Förster radius R_0 critically depends on the relative orientation between donor and acceptor [44, 49]. A geometrical description of the situation is shown in figure 1.1. In the extreme case in which the donor's emission dipole is perpendicular to the acceptor's absorption dipole and both dipoles are orthogonal to the connecting line between them, the energy transfer efficiency is zero (at least in the dipole–dipole approximation). Usually, one assumes that both donor and acceptor are flexibly linked to the target molecule so that their orientation quickly changes during the excited state lifetime of the donor, which allows for quantitatively calculating the correct Förster radius. Unfortunately, if this assumption is not true, there is no experimental approach that could determine the full relative orientation between donor and acceptor, i.e. determine the three angles (θ_a, θ_a and ϕ) shown in figure 1.1. In that case, there is no way to quantitatively evaluate a FRET measurement and extract correct values for the distance $|\mathbf{r}|$ between them. The second limitation is the short-distance range over which FRET is applicable. Due to the rapid fall off in energy-transfer efficiency with distance, one cannot measure distances beyond 10 nm, usually.

In this thesis, we propose an alternative approach and present the first single-molecule study for measuring axial distances in the range of up to 100 nm with nanometer precision. It gives new perspectives for overcoming both the limitations of FRET and the current resolution limitations of image-based single-molecule localization. The method is based on the energy transfer from an excited fluorescent molecule to surface plasmons in a thin metallic film which will be described extensively in the theoretical section 2.4.3 and is thus called single-molecule Metal-Induced Energy Transfer (smMIET). Briefly, this energy transfer modifies excited-state lifetime of the emitting molecule. The change in lifetime depends on 1) the dipole's distance from the surface, 2) its orientation with respect to the surface, and 3) its intrinsic quantum yield. As a net result, the lifetime varies nonlinearly, but monotonically, with the dipole's distance from the metal surface within a range of 100 nm. Thus, one can use this monotonic lifetime–distance relation for converting the measured lifetime value into the distance of the emitter from the metal surface.

The first set of experiments demonstrating the possibility of exciting and detecting single fluorescent molecules through a thin metal film were performed by Stefani *et al.* [50], who used annular beams with high NA objectives to excite single molecules placed at known distances from the metal surface. In a previous publication, we successfully demonstrated the application of MIET for measuring the distances of densely labeled microtubules from a substrate with a thin gold film with nanometer accuracy [51]. Recently, MIET was also used for nanoprofiling the basal membrane of living cells over a metal surface. In chapter 3, we present the first experiments with MIET for axially localizing single molecules from a surface. The presented data show that smMIET indeed has the capacity of measuring distances of individual molecules from a surface with nanometer accuracy.

As we will see in our theoretical section, the emission properties of almost all organic fluorescent dyes are well described within the theoretical framework of an ideal electric dipole emitter, characterized by its oscillation frequency, dipole strength, and dipole orientation. Even if one takes into account that excitation and emission happens between an ensemble of energy levels in the ground and excited states, resulting in broad excitation and emission spectra, a molecule's excitation and emission properties are still well modeled by a superposition of dipole transitions having different oscillation frequencies but the same orientation. The orientation plays a crucial role in defining the photophysical properties of the molecule in an anisotropic environment such as close to a surface, in a nanocavity [52, 53], or in FRET [18, 54]. Therefore, in order to extend the smMIET approach to biological samples successfully, one must determine the orientation of fluorescent molecules. We will see in the forthcoming chapter that the orientation of the dipole significantly influences the total power it radiates in the vicinity of a metal surface, which makes it is absolutely necessary to determine the orientations of single molecules for performing smMIET on labeled biological samples.

While it is rather straightforward to determine the projection of an excitation/emission transition dipole into a plane perpendicular to the excitation/detection axis, by using polarized excitation and detection [39, 55], the determination of the complete three-dimensional orientation is much more difficult. Several methods have been developed for measuring the three-dimensional orientation of the emission transition dipole of single molecules. Among them are aberrated imaging [56], polarized evanescent field excitation and imaging [57, 58], defocused imaging [59, 60], or Bertrand lens imaging [61]. A few other methods are based on redistributing the collected emission in a way that allows the separate detection of emission into different solid angles [62–64], and therefore, determining the out-of-plane orientation by comparing the intensity ratios in these detected channels. More recently, methods based on wave-front engineering of emitted light using phase plates, quadrated pupils, or spatial light modulators have been used for determining the emission dipole orientation [65–67].

Most techniques measuring the three-dimensional orientation of the excitation dipole of a single emitter are based on scanning a molecule with a focused laser beam with temporally or spatially varying electric field polarization [68–73]. The simplest of these methods is to scan a molecule with a radially polarized excitation focus [74, 75]. Due to the inhomogeneous amplitudes of longitudinal and transversal polarization components in such a focus, each single-molecule scan shows a characteristic intensity pattern which depends on the three-dimensional orientation of its excitation transition dipole. Many of the above mentioned techniques have also been used to successfully determine the dimensionality and geometry of the excitation and emission transitions in fluorescent nanocrystals (quantum dots), and to characterize their behavior in complex electromagnetic environments [76–82]. In section 4.4, we will give a brief theoretical outline for determining the excitation dipole orientations of dye molecules using a radially polarized laser, and later describe the method of defocused imaging for estimating the 3D orientations of emission dipoles. Thereafter, we briefly explore and discuss the combination of smMIET with these two orientation determination methods in order to achieve a 3D localization accuracy with nanometer accuracy and future application in structural biology.

Apart from all the above, it is well known from fluorescence anisotropy measurements that for most fluorescent molecules, the excitation and emission transition dipoles are not the same but inclined to each other. The angle γ between these two dipole orientations enters the expression for the fundamental anisotropy of a fluorescing molecule [83]. A complete knowledge of the two orientations is also necessary when explaining properties such as excited state decay rates, quantum yield and enhancement effects in the vicinity of metallic nanostructures [84]. In this thesis, we present the first experimental setup which looks at the three-dimensional orientations and geometry of both excitation as well as emission dipoles of single emitters simultaneously, by combining these radially polarized laser scanning together with defocused imaging in one optical setup. We perform experiments on Atto 655 molecules spin-coated on a glass coverslip and Alexa 488 molecules embedded in a polymer and obtain the distributions of γ for both the molecules. This experimental tool can be used for elucidating more complex excitation/emission geometries such as those found in fluorescent nano-crystals (quantum dots) and also to verify the quantum chemical calculations used for predicting the structure and geometry of the molecular orbitals involved in an electronic transition.

2 Theory

In this chapter, we build the theoretical outline for the understanding of the fundamental electrodynamic and photophysical properties of a fluorescent emitter. We start with a quantum mechanical picture where we introduce a fluorescent molecule as a dipole emitter with a fixed transition dipole moment oriented in its molecular structure. Thereafter, we consider a dipole in an empty box with boundary conditions on the electromagnetic field's periodicity, in order to determine its absorption and emission coefficients and thereafter, connect these properties with its spontaneous emission rates. In order to account for its emission properties in the presence of a dielectric or a metal interface, we introduce a dipole in a semi-classical quantum optical framework. We start from a basic description of plane waves using Maxwell's equations, Fresnel's equations for reflection and transmission, etc. and ultimately calculate the total radiation power of a dipole as a function of its distance and orientation from such an interface. This completes our introduction to the concept of Metal Induced Energy Transfer (MIET).

2.1 Quantum Mechanical Picture of Fluorescence

From a quantum mechanical viewpoint fluorescence is a process which involves a repeated transition of a molecule between two quantized energy states (or the transition of electrons between two molecular orbitals) given by wave functions, say ψ_1 and ψ_2. The excitation from the ground state to the excited state takes place following an absorption of a photon of energy $h\nu$, followed by the decay of the molecule from the excited state back to the ground state. This is achieved either by the emission of a photon, or non-radiatively by transferring the energy to the surroundings or lost internally. The excitation and de-excitation processes are accompanied by perturbations in the delocalized electron cloud over the molecule's framework. These perturbations depend on the probability of a transition between two energy states and also on the selection rules based on the symmetry of the structure of molecular orbitals involved. Therefore, each transition takes place along a preferred direction in the molecule's framework which is known as the *transition dipole moment*, and the magnitude of this vector represents the probability of this transition. Below, we will briefly introduce this concept and touch upon some fundamental photophysical properties of a fluorescent molecule which are otherwise hard to explain from a purely classical framework.

2.1.1 Molecular Excitation and Emission

A complete explanation for the electronic spectra of molecules is extremely complex. An electronic transition is coupled with vibrational and rotational transitions which makes it even more complicated. However, in this section we will state some general rules and fundamental principles associated with the excitation and emission phenomena of fluorescent dyes. We refrain ourselves from dealing with the detailed quantum chemical treatment of the molecular states (those who wish to dive into the ocean might start by referring to excellent books such as [85]), but to begin with, the molecular states are treated as a linear combination of all the atomic orbitals involved, which acts as a good starting point for the molecular orbital theory. The wavefunction of a molecule in each state gives the overall probability of the electron's position in space.

Keeping the discussion between two nuclei and a single electron for the sake of simplicity, when two atomic orbitals ϕ_1 and ϕ_2 interact, two molecular orbitals $\psi_+ = \phi_1+\phi_2$ and $\psi_- = \phi_1-\phi_2$ are formed, where ψ_+ has lower energy, and is therefore called as *bonding orbital*, than ψ_-, which we call as an *antibonding orbital.* The potential energy curves, as a function of the internuclear distance, can be obtained by calculating the Hamiltonian over these wavefunctions. The potential energy depends on electron-nuclei interactions, the angular momentum of the electron's spin around its own axis and in the orbital, spin-orbital coupling, and other factors which play a major role in deciding the fate of the electron in each state. Figure 2.1 shows the general characteristics of potential energy observed for a bonding and antibonding orbital. Depending upon the symmetry and shape of the atomic orbitals involved, the molecular orbitals can be singly (σ) or doubly degenerate (π). In a many electron system, the electron-electron repulsion plays a dominant role too. Due to these interactions, the electrons occupy the energy states starting from the lowest energy state following Hund's rule of maximum multiplicity for the electron spin and Pauli's exclusion principle. The Highest Occupied Molecular Orbital is called the HOMO and the Lowest Unoccupied Molecular Orbital, above the HOMO in the energy ladder is termed the LUMO. We must emphasize here that for many electron systems, the potential energy between two nuclei is the effective curve taking all the electrons in the bonding and the antibonding orbitals into consideration. Thus, the two nuclei will be driven apart, or the bond is broken only when the net curve has antibonding nature. In other words, one can see the net potential energy curve as a summation of the curves calculated for each electron individually in its respective molecular orbital. We follow the general naming of the molecular orbitals such as σ and σ^*, π and π^* for bonding and anti-bonding orbitals of degeneracy one and two respectively; and n and n^* for non-bonding molecular orbitals which constitute a lone pair of electrons from an atom which does not take part in bond formation. The electrons can undergo electronic transitions to the higher antibonding states upon interaction with an incident electromagnetic radiation, but in some cases these orbitals are orthogonal to all the participating atomic orbitals and thus also the molecular orbitals, thereby prohibiting any such transitions.

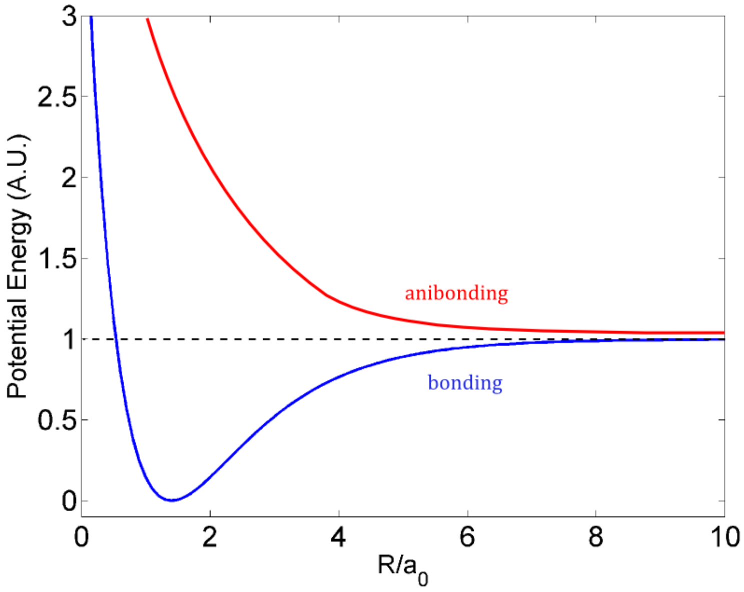

Figure 2.1: An exemplary plot showing energy as a function of distance for a bonding and an antibonding orbital.

This picture can be extrapolated to a many polyatomic organic molecule where each atom contributes to one or more atomic orbitals for bonding with its neighboring atoms. In such a molecule, several electronic transition are possible from its filled orbitals to higher vacant orbitals. Each transition requires a particular wavelength which is equal to the energy gap between the two molecular orbitals, and have different probabilities. The absorption and emission spectra for most strong electronic transitions in organic molecules are usually related to a transition involving a group of atoms in the molecule's structure, which is called the *chromophore*. Some of the most common chromophores involve carbonyl, nitro, nitroso groups, and carbon-carbon double bond systems. Chromophores with alternate double bonds are planar systems and have their π orbitals over the entire conjugation. The wavefunctions of the molecular orbitals can thus be approximated as waves with nodes at the edges of this box. The lowest orbital thus has no nodes in between the conjugation length and thus allows the maximum electron density between all the atoms. The number of nodes increase by one for each higher energy molecular orbital. These are called Hückel's molecular orbitals, named after Erich Hückel who calculated the molecular orbital picture for conjugated π organic molecules, including cyclic molecules. For a linear conjugated system with i number of π bonds, i molecular orbitals involved in the bonding. The energy of each state is given by $E_n = n^2h^2/8mL^2$, where L is the total length of the molecule (here one can approximate L as i times the length of a carbon-carbon bond with a bond order of 1.5) and m is the reduced mass of the electron. For such a molecular system, HOMO is the i^{th} molecular orbital and LUMO the $i+1^{\text{th}}$, and therefore the excitation wavelength ($\lambda = hc/(E_{i+1} - E_i)$), can be calculated using the simple equation:

$$\lambda = \frac{8mL^2c}{h(2i+1)} \tag{2.1}$$

For the dye molecules that absorb and fluoresce in the visible range, mainly the transitions between $\pi \leftrightarrow \pi^*$ and $n \leftrightarrow \pi^*$ are responsible. Thus the shape of the frontier orbitals (HOMO and LUMO) is chiefly determined by the conjugation structure of the chromophore. The wavelength range for the transitions $\sigma \leftrightarrow \sigma^*$ usually lies in the ultraviolet region.

The complete absorption spectra of polyatomic chromophores contains all the transitions that are possible. Each transition is associated with two molecular orbitals, and therefore represents a change of electron density over the structure of the molecule. For a transition between two states with wavefunctions ψ_f and ψ_i, the associated *transition dipole moment* is defined as:

$$\hat{\mathbf{M}}_{fi} = \left\langle \psi_f^* \left| q\hat{\mathbf{r}} \right| \psi_i \right\rangle = \int \psi_f^* \, q\hat{\mathbf{r}} \, \psi_i \, \mathrm{d}\tau \tag{2.2}$$

where $q\hat{\mathbf{r}}$ is the electric dipole moment operator and $\hat{\mathbf{M}}_{fi}$ is the matrix element of the transition dipole matrix $\hat{\mathbf{M}}$ corresponding to the transition $\psi_f \leftrightarrow \psi_i$. Clearly, the characteristics of ψ_i and ψ_f play an important role in determining the magnitude of the transition between the two states, which give us the selection rules that are fundamental for all spectroscopic studies. If the expectation value for the transition dipole moment operator between the two states is zero, the transition never takes place and it is said to be *forbidden*, and if it is a finite value, it is called an *allowed* transition. Since the dipole operator is a translation operator $\hat{\mathbf{r}}$ times charge, it depends only on the spatial part of the wave functions. One can interpret this is in the following way: if the molecular orbital ψ_i overlaps in space with the molecular orbital ψ_f then the molecule will absorb energy from an EM radiation with energy equal to the energy gap between these two orbitals. A simple example where this is not true, i.e. where the orbitals are spatially orthogonal, is a $\pi^* \leftarrow n$ transition in a carbonyl group. Since we already realized above that the non-bonding orbital n is orthogonal to all the molecular orbitals, the transition is forbidden. However, a weak absorbance is observed in most of the molecules containing the carbonyl group due to several reasons. One basic reason which we did not consider in all the arguments made above is the spin-orbital coupling. Even though it is strenuous to calculate the dipole moment of each transition for complicated structures such as for those shown in figure 2.2, simple rules from group theory in quantum mechanics can be of great help to predict at least which transition probabilities are necessarily zero or forbidden (see chapter 11 from the book [86] for example).

The spectra of the chromophore group shifts towards longer wavelengths due to the presence of other functional groups attached to it such as hydroxyl, amino, oxymethyl groups which are called *auxochromes*. These auxochromes do not absorb or emit light themselves but when present next to a chromophore, they increase the conjugation length due to their lone pair of electrons. One needs to take the auxochromes into account too while calculating the frontier orbitals for the dye molecules, which can majorly contribute to the shape of these orbitals by varying the number and position of the nodal planes in the chromophore's structure. For example, the chromophore responsible for the absorption and emission properties of Rhodamine 6G is the Xanthene core and if we look at the frontier orbitals of this chromophore alone, then the transition should take place with the shift of electron density majorly along the direction of O↔C7 [87]. However, experiments and theoretical calculations for this dye suggest the transition dipole moment along the direction of C12↔C6 [88]. This is due to the presence of the two amino auxochromes, whose lone pair of electrons also participate in the conjugation.

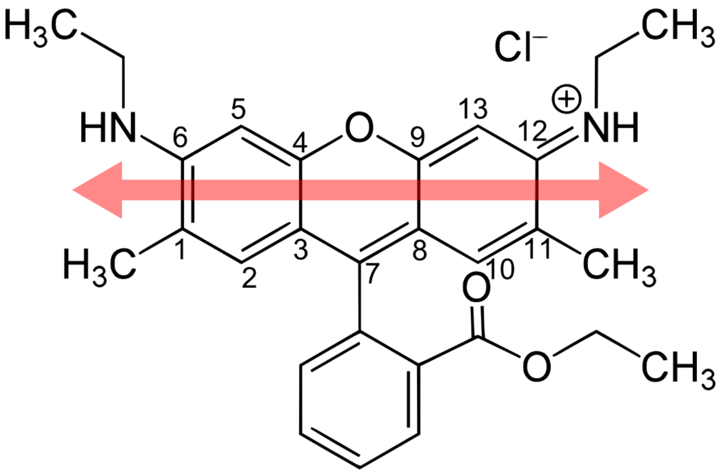

Figure 2.2: The structure of Rhodamine 6G showing the orientation of the transition dipole moment. The carbon atoms of the Xanthene core atoms are numbered C1 to C13. Two ethylamine auxochromes are attached one each on the carbons C6 and C12 which participate in the conjugation with the help of their lone pair of electrons. The group attached on C7 lies perpendicular to the plane of the chromophore due to steric hindrance and does not take part in the conjugation. The π molecular orbitals lie perpendicular to the frontier orbitals of the chromophore (see [89]).

2.1.2 Single-Singlet and Singlet-Triplet Transitions

Again, under the assumption that the coupling of the spin and orbital angular momentum is weak, we can separate the wavefunction of each molecular orbital into a spin and a spatial part.

$$\psi(\mathbf{r}_1\sigma_1, \mathbf{r}_2\sigma_2) = \uppsi(\mathbf{r}_1, \mathbf{r}_2)\mathcal{X}(\sigma_1, \sigma_2). \tag{2.3}$$

where $\mathcal{X}(\sigma)$ can be written as a combination of $\alpha(\sigma)$ or $\beta(\sigma)$ depending upon the sign of the electron spin (↑ or ↓) respectively. These functions are the eigenvalues of the Hermitian spin angular-momentum operator, and therefore are orthogonal. The ground state of the molecule is, in a majority of cases, a *singlet state*, where the spin of the electrons are paired, $\mathrm{S} = 0$. The spin multiplicity for such a paired state is $2\mathrm{S} + 1 = 1$. The spin part of the wave function is given by:

$$\mathcal{X}_i(\sigma_1, \sigma_2) = [\alpha(\sigma_1)\beta(\sigma_2) - \beta(\sigma_1)\alpha(\sigma 2)] \tag{2.4}$$

The antisymmetric function above on the right side is the *Pauli principle* which states that the total wave function of a system of electrons must be antisymmetric with respect to the interchange of any two electrons. If σ_1 and σ_2 are interchanged, the sign of the function becomes negative. This leads to the fact that the probability to find two electrons with same spin close to each other is zero. For the excited state however, when one electron is promoted to a higher molecular orbital, the total spin can be 0 or 1. The state when $S = 0$ is again a singlet, and the spin wavefunction is given by the same equation (2.4). But, for the total wave function to be antisymmetric, the spatial part has to be symmetric. Therefore,

$$\uppsi_f(\mathbf{r}_1, \mathbf{r}_2) = [\uppsi_1(\mathbf{r}_1)\uppsi_2(\mathbf{r}_2) + \uppsi_2(\mathbf{r}_1)\uppsi_1(\mathbf{r}_2)]\,. \tag{2.5}$$

where $\uppsi_1$ is the spatial wavefunction of obital in the ground state and When the total spin $S = 1$, the spin multiplicity is 3. This can be explained by the three possibilities for the spins of the two electrons, and therefore three wavefunctions associated:

$$\mathcal{X}_f(\sigma_1, \sigma_2)(\sigma_1, \sigma_2) = \begin{cases} [\alpha(\sigma_1)\alpha(\sigma_2)] & \uparrow\uparrow \\ [\alpha(\sigma_1)\beta(\sigma_2) + \beta(\sigma_1)\alpha(\sigma_2)] & \uparrow\downarrow \\ [\beta(\sigma_2)\beta(\sigma_1)] & \downarrow\downarrow \end{cases}$$

As the spin part is symmetric, now the spatial wavefunction takes up the antisymmetric nature in order to obey the Pauli's principle.

$$\therefore \uppsi_f(\mathbf{r}_1, \mathbf{r}_2) = [\uppsi_1(\mathbf{r}_1)\uppsi_2(\mathbf{r}_2) - \uppsi_2(\mathbf{r}_1)\uppsi_1(\mathbf{r}_2)]\,. \tag{2.6}$$

The Hamiltonian applied only on the spatial terms, which serves as a good approximation. With this approximation, we immediately conclude that the energies of three possibilities for the state $S = 1$ are equal. Thus, it is called a *triplet state*. Further, the energy of the triplet excited state is less than the energy of a singlet excited state. This holds true for any excited state. The following diagram shows the depiction of the states involved.

The wavefunction $\psi(\mathbf{r}_1\sigma_1, \mathbf{r}_2\sigma_2)$ is said to be *even parity* if it does not change its sign when the sign of the coordinates are inverted and it is *odd parity* otherwise. Since the dipole operator $\mathbf{p} = q\hat{\mathbf{r}}$ changes the sign $r \to -r$, the integral (2.2) vanishes if both the wavefunctions ψ_i and ψ_f have the same parity. Thus, either of them must have an odd and the other an even parity for the transition to take place. The even and odd nature of a wavefunction must not be confused with its symmetry with respect to the interchange of electrons. Separating the spin and spatial parts of the integral, we have:

$$\langle \psi_f^* \left|\mathbf{p}\right| \psi_i \rangle = \langle \mathcal{X}_f | \mathcal{X}_i \rangle \int \psi_f^* \, q \, \hat{\mathbf{r}} \, \psi_i \, \mathrm{d}^3 r \tag{2.7}$$

The spin term, $\langle \mathcal{X}_f | \mathcal{X}_i \rangle$ is non-zero only if the wavefunctions for both the states are identical. This is the first selection rule for electronic transitions, and it states that the spin state must not be altered in an electric dipole transition. This means that *singlet* state to *triplet* state transition is forbidden and vice versa. Thus, a molecule is excited from its singlet ground state S_0 to its singlet excited state S_1, which then returns to the ground state undergoing either spontaneous or stimulated emission. This cycle process must go on indefinitely, unless, as a rare event, the molecule undergoes what is known as *intersystem crossing*, and ends up in a metastable triplet state T_1. The probability of this transition depends primarily on the spin-orbital interaction where the triplet state 'mixes' with the pure singlet states so that a perturbed triplet state t_1 is formed [90].

$$\psi_{t_1} = \psi_{T_1} + \sum_k a_k \psi_{S_k} \tag{2.8}$$

where a_k give the coefficient of mixing with all possible singlet states S_k due to spin-orbital interactions. The square of these coefficients is proportional to the probability for a transition to the perturbed triplet state:

$$P = \frac{2\pi}{3\hbar^2} \sum_{k,j=1\to 3} (\mathrm{S}_k \left|q\hat{\mathbf{r}}\right| T_1^j)^2 \tag{2.9}$$

The mean lifetime of the triplet state is inversely proportional to the probability of singlet-triplet transition [91]. For a typical organic fluorophore, this is around $10^{-6} \sim 10^{-4}\, s$. During this time, the excitation-emission fluorescence cycle is broken, and the dye remains in the dark state. This temporal intermittency of intensity from a dye molecule is known as *blinking*.

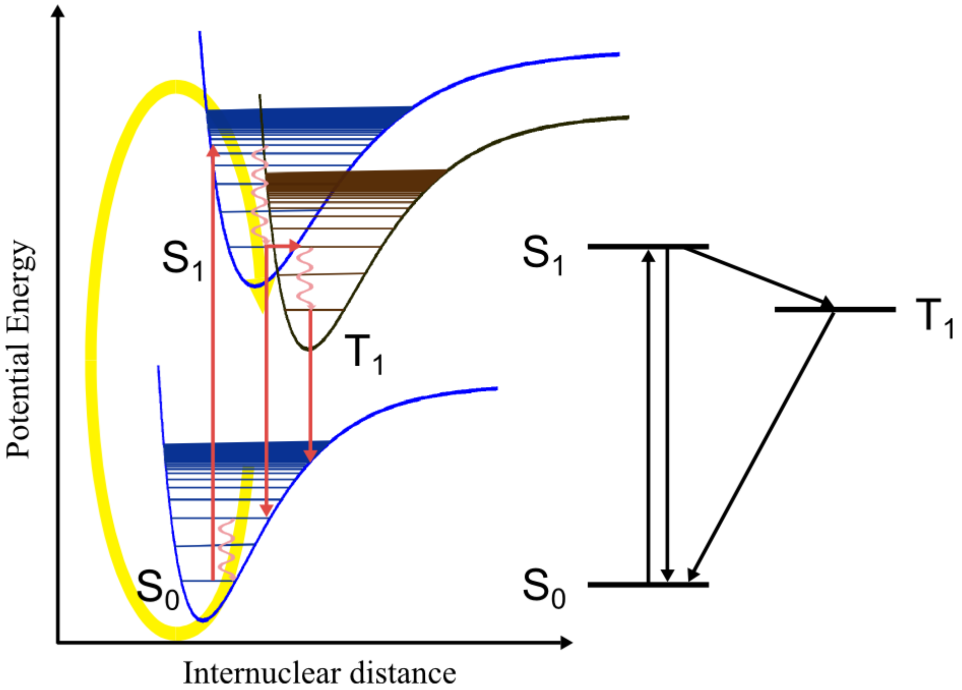

Figure 2.3: Franck Condon diagram showing the potential energy curves for a singlet ground state and excited state (S_0 and S_1) and a triplet state T_1. The red vertical arrows show the vertical transitions from the ground state to excited states and back.

2.1.3 Franck-Condon Principle

When an electronic transition takes place, the positions of all the nuclei are assumed to be stationary. This treatment is similar to the Born-Oppenheimer approximation which relies on the fact that the nuclear masses are much larger than the electron mass and thus the motions of both can be separated. This is the *Franck-Condon principle* and is the basis of all the vibronic transition analysis following an electronic transition. Figure 2.3 illustrates the energy diagram of the transitions showing the vibrational states in each electronic state. The equilibrium positions in the higher electronic states are shifted towards larger distances due to the fact that they have higher antibonding character. When a transition takes place between S_0 and S_1, the internuclear distance is equal to the bond length in the ground state and since the nuclei motion are fixed, the transition occurs to the vibronic state where the internuclear distance is on the edge of the potential energy curve as shown in the figure. Such transitions are called *vertical transitions*. Thereafter, the nuclei vibrate at this energy level around the shifted equilibrium distance and readjust to the changes in the electron density which in-turn alters the overall electron density over the molecule, and so on until a new equilibrium state is attained. The same is observed when the transition takes place from the excited states to the ground state. The probability of transition is given by the square of the overlap integral between the two vibrational states in the respective electronic states.

$$F(\nu', \nu) = \left| \int \psi_\nu(\mathbf{R}) \psi^*_{\nu'}(\mathbf{R}) \, \mathrm{d}\tau_N \right|^2 \tag{2.10}$$

where ψ_ν and $\psi_{\nu'}$ are the wavefunctions of the vibronic states in the ground and the excited states respectively and $\mathbf{R}$ denotes the nuclear coordinates during the transition. At room temperature, the electronic transition usually proceeds from its ground vibronic level. The factors $F(\nu', \nu)$ are the Franck-Condon factors and contribute to the shape of the intensity spectrum of electronic transitions.

2.1.4 Radiationless De-excitation

There are several relaxation processes in a molecule that proceed without the emission of photons. The *intersystem crossing*, where transitions occur between states of different multiplicity, introduced in the previous section, is an example. The relaxation of the molecule in higher excited states of the same multiplicity to the first excited state (for example $S_n \rightarrow S_1$) non-radiatively is known as *internal conversion*. Radiative decay occurs with an appreciable yield only from the lowest excited state of a given multiplicity. This is the well-known *Kasha's rule* in photochemistry.

The radiationless relaxation of a molecule when excited to a higher state can be completely internal due to some rearrangement reactions in the excited state. As described briefly also in the previous section, an electronic excitation alters the nuclear coordinates and the electron density of the molecule. This structural change costs the molecule some energy which is called the *reorganization energy* (λ), and is an example of an ultrafast process which lasts about a few femtoseconds to picoseconds ($10^{-15} \sim 10^{-11}$s). A well-known example to support this argument is a phenolphthalein molecule in basic aqueous solutions (pH $\sim$8.2 - 12). The phenolphthalein molecule, even though its structure is similar to the highly fluorescent fluorescein molecule, is non fluorescent. This is due to the fact that the total energy in its excited zero-order state (within the Born-Oppenheimer approximation) is converted into vibrational energy and torsional energy, which results in the rotation and vibration of the two phenyl rings attached to the central carbon. Whereas in the case of fluorescein, the two phenyl rings are fixed in a plane with the help of an oxygen atom forming a rigid structure. In such a case, the rate of the non-radiative process is low and most of the relaxation takes place either radiatively or through intersystem crossing [92]. The rate of the intramolecular relaxations is related to λ, such that, for high values of λ (where the electronic and vibrational coupling is strong), the non-radiative rates are high [93]. The linewidth and the exponential decay of the non-radiative processes also depend on the interaction between the excited zero-order state and the density of all the vibronic states located close to that state [94], which, as one would expect, directly depends on the number of atoms in the molecule. This is straightforward if one writes the transition probability similar to Fermi's golden rule (see equation (2.19)). Due to the presence of 'sparse' energy levels in small molecules, no intramolecular electronic relaxation processes are encountered and relatively longer excited state lifetimes τ_f are observed [95].

In order to complete our discussion concerning the pathways of molecular emission, one must introduce the well-known property that is used to characterize a fluorescent emitter, the quantum yield of radiation (Φ). As the name suggests, it represents the probability an excited molecule decays radiatively. Quantitatively, it represents the ratio of the number of photons *emitted* by the molecule to the number of photons that the molecule absorbed in a given time. Given the radiative rate κ_r and the sum of all the non-radiative rates possible κ_{nr}, the quantum yield is defined as:

$$\Phi = \frac{\kappa_r}{\kappa_r + \kappa_{nr}}. \tag{2.11}$$

2.1.5 Einstein's Coefficients and Spontaneous Emission Rate

In a seminal note from 1946 [96], Edward Mills Purcell first mentioned that it is possible to change the spontaneous emission rate of an emitter by placing it close to a resonant structure, for example a metallic cavity. This change of the spontaneous emission rate is due to the action of the emitted field onto the emitter itself when it is back-scattered by the cavity. However, there is a deep connection between the spontaneous emission rate of a quantum-mechanical emitter and its absorption and stimulated emission coefficients: In thermal equilibrium, the number of photons per time absorbed by an emitter from the vacuum electromagnetic field has to be balanced by an equal number of photons per time emitted by that emitter. This imposes a rigid relation between absorption and emission properties of an emitter. In this section, we will briefly recall the connection between spontaneous emission rate and induced absorption and emission coefficients for an electric dipole emitter in empty space. Although this can be considered classical textbook knowledge, it will help us to define all relevant quantities which will be important in the following sections which considers the spontaneous emission rates of a dipole next to a dielectric or a metallic interface.

We will start with considering an electric dipole emitter within an empty box of edge length L in thermal equilibrium at temperature T. It is assumed that the vacuum electromagnetic field within the box is in thermal equilibrium and obeys periodic boundary conditions with respect to the box. The vacuum electric field can be expanded into plane wave modes, $\mathbf{E} = \mathbf{E}_0 \exp(i\mathbf{k}\cdot\mathbf{r} - i\omega t)$, where $\mathbf{E}_0$ is the amplitude vector of a given mode and $\mathbf{k}$ its wave vector with length $k = \omega/\mathrm{c}$. Here, ω is the oscillation angular frequency of the mode, and c the vacuum speed of light, and is related to the

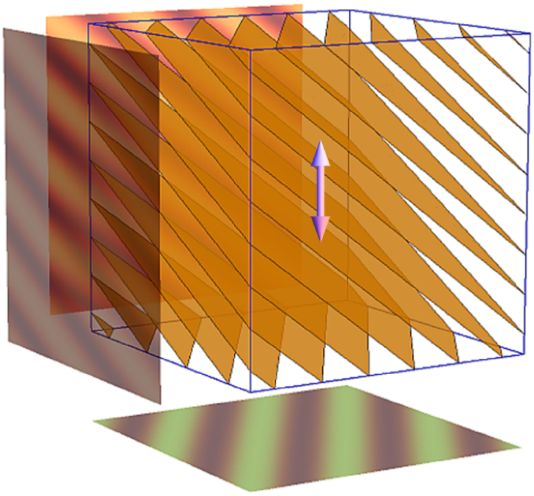

Figure 2.4: A dipole situated in an empty cubic box with edge length L. The wavefronts of one plane wave mode and its phase on the three sides of the cubes are shown here.

frequency $\nu = \omega/2\pi$. The imposed boundary conditions imply that we have for the x-component of the wave vector $k_x L = 2\pi n_x$, where n_x is an integer number. Similar conditions hold also for the y- and z-components. Thus, the mode density ρ_ν within frequency interval $d\nu$ and solid angle element $\sin\theta \mathrm{d}\theta \mathrm{d}\phi$ is given by

$$\rho_\nu L^3 \mathrm{d}\nu \sin\theta \mathrm{d}\theta \mathrm{d}\phi = 2\frac{k^2 \mathrm{d}k \sin\theta \mathrm{d}\theta \mathrm{d}\phi}{(2\pi/L)^3} \tag{2.12}$$

where the factor 2 on the right hand side takes into account that there are two different principal polarisations of the electric field. Using Planck's energy quantization and Bose-Einstein statistics, the average energy per mode is

$$\epsilon_\nu = \frac{h\nu}{\exp(h\nu/k_B T) - 1} \tag{2.13}$$

where h is Planck's constant, k_B is Boltzmann's constant, and T is the temperature. Thus, when taking into account that the mean energy density (energy per unit volume) is ϵ_ν/L^3, one finds the mean energy density per solid angle and frequency to be equal to

$$\epsilon_\nu \rho_\nu \mathrm{d}\nu = 2\frac{k^2 \mathrm{d}k \sin\theta \mathrm{d}\theta \mathrm{d}\phi}{(2\pi/L)^3}\frac{1}{L^3}\frac{h\nu}{\exp(h\nu/k_B T) - 1} = \frac{2h\nu^3}{c^3}\frac{\mathrm{d}\nu \sin\theta \mathrm{d}\theta \mathrm{d}\phi}{\exp(h\nu/k_B T) - 1} \tag{2.14}$$

which is Planck's famous formula for black-body radiation.

Now, the mean energy absorbed by an electric dipole is proportional to this energy density times an orientation factor, integrated over all possible propagation directions. The orientation factor takes into account that only electric field components along the orientation of the emitter's dipole contribute to energy absorption, and it is given by $\langle|\hat{\mathbf{E}}\cdot\hat{\mathbf{p}}|^2\rangle = (1/2)\sin^2\theta$, where $\mathbf{p}$ is the electric dipole amplitude vector of the emitter which is assumed to be oriented along $\theta = 0$. The angular brackets denote averaging over all possible orientations of $\hat{\mathbf{E}}$ with $\hat{\mathbf{E}} \perp \mathbf{k}$. Thus, one finds the following expression for the mean density per frequency of the electromagnetic field which takes part in energy absorption by the dipole emitter

$$\begin{aligned} S(\nu)\mathrm{d}\nu &= \frac{h\nu^3}{c^3}\frac{\mathrm{d}\nu}{\exp\left(h\nu/k_BT\right)-1}\int_0^{2\pi}\mathrm{d}\phi\int_0^{\pi}\sin\theta\cdot\sin^2\theta\mathrm{d}\theta \\ &= \frac{8\pi h\nu^3}{3\mathrm{c}^3}\frac{1}{\exp\left(h\nu/k_BT\right)-1} \end{aligned} \tag{2.15}$$

Considering all possible dipole orientations gives an additional factor of 3, and therefore, one has:

$$S(\nu)\mathrm{d}\nu = \frac{8\pi h\nu^3}{c^3}\frac{1}{\exp\left(h\nu/k_BT\right)-1} \tag{2.16}$$

The *effective* mode density or Density of States (DOS) $\tilde{\rho}_\nu$ of the electromagnetic field that is coupled to the energy absorption by the dipole emitter is given by:

$$\tilde{\rho}_\nu = \frac{8\pi\nu^2}{c^3} \tag{2.17}$$

From time dependent perturbation theory, the probability P for a transition of the molecular system between two quantum states with energies $\mathcal{E}_i$ and $\mathcal{E}_f$ when subjected to an electromagnetic radiation with an oscillation frequency ν for a time t_1, involving only the first order perturbation, averaged over all orientations of the dipole momemt $\mathbf{p}$ is given by [86]:

$$P_{if}(t_1) = \frac{1}{3\hbar^2}|\mathbf{p}|^2 t_1 \int S(\nu)\left(\frac{\sin\frac{1}{2}(\nu_{if}-\nu)}{\frac{1}{2}(\nu_{if}-\nu)}\right)^2\mathrm{d}\nu \tag{2.18}$$

where $\nu_{if} = |\mathcal{E}_f - \mathcal{E}_i|/h$. This shows that the transition probability has a sharp maximum when $\nu = \nu_{if}$ and other frequencies do not contribute much. Therefore, the transition probability per unit time, or *transition rate* between the two states is given by the expression:

$$W_{f\leftarrow i} = \frac{2\pi|\mathbf{p}|^2 S(\nu_{if})}{3\hbar^2} \tag{2.19}$$

This is the well-known *Fermi's Golden Rule* for the transition probability between two states, which was originally derived by Paul Dirac in the year 1927 in his beautiful manuscript titled "The Quantum Theory of the Emission and Absorption of Radiation" [97]. The interesting point to realize from the equation above is that while $(\mathcal{E}_f - \mathcal{E}_i) = h\nu_{if}$ represents the *absorption* of the radiation incident on the molecule, the case where $(\mathcal{E}_i - \mathcal{E}_f) = -h\nu_{if}$ represents the case where a molecule present in the excited state falls into the state with lower energy, emitting radiation at the same frequency ν_{if}. This phenomenon is called *stimulated emission.* The expression for the transition probability for the stimulated emission can be written similar to the expression given in equation (2.18) by replacing ν_{if} with $-\nu_{if}$ which gives the same transition rate as in expression (2.19). Ignoring all higher orders of perturbation, at thermal equilibrium, the transition rate shown in equation (2.19) directly gives the *Einstein coefficient of stimulated absorption* B_{if}

$$W_{f \leftarrow i} = \frac{2\pi |\mathbf{p}|^2}{3\hbar^2} S(\nu_{if}) = B_{fi} S(\nu_{if}) \tag{2.20}$$

Since the transition rate for the stimulated emission is identical to the rate of stimulated absorption, the *Einstein coefficient of stimulated emission* B_{fi} is exactly the same as B_{if}. Physically this translates to the statement that the same electromagnetic field which can excite the molecule from a state with lower energy to higher energy, can also act as an energy sink which brings the molecule from a higher energy state to a lower energy state. Therefore, one would conclude that the probability of finding a molecule in its ground state or excited state is equal. However, at a temperature T, if an ensemble of molecules is in thermal and radiation equilibrium the ratio of the population in the excited state to the ground state is given by Boltzmann statistics $\exp(-h\nu_{if}/k_B T)$. This supports the fact that a molecule in the excited state also emits radiation spontaneously, whether or not an external electromagnetic radiation field is present. Therefore, at equilibrium, one must have

$$N_f(A_{fi} + B_{fi} S(\nu_{if})) = N_i B_{if} S(\nu_{if}), \tag{2.21}$$

where N_i and N_f are the number of molecules in the initial and final state, respectively. A_{fi} in the equation above is the *Einstein coefficient of spontaneous emission.* From this equation the density of states $S(\nu_{if})$ can be written as:

$$S(\nu_{if}) = \frac{\left[\frac{A_{fi}}{B_{fi}}\right]}{\left[\frac{B_{if}}{B_{fi}}\right]\left[\frac{N_i}{N_f}\right] - 1} \tag{2.22}$$

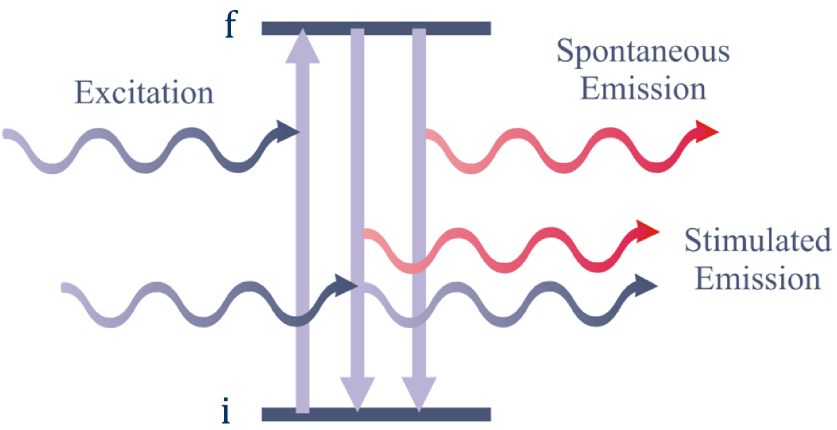

Figure 2.5: Diagram illustrating the elementary transitions of a molecule between the two states i and f in Einstein's model.

$$\because \frac{N_i}{N_f} = \exp\left(\frac{h\nu_{if}}{k_B T}\right) \text{ and } B_{if} = B_{fi}, \qquad S(\nu_{if}) = \frac{\left[\frac{A_{fi}}{B_{if}}\right]}{\exp\left(\frac{h\nu_{if}}{k_B T}\right) - 1} \tag{2.23}$$

Comparing with equation (2.16) one has:

$$A_{fi} = \frac{8\pi h\nu_{if}^3}{c^3} B_{fi} = \tilde{\rho}_\nu h\nu B_{fi} \tag{2.24}$$

This shows that the spontaneous emission is proportional to the cube of the transition frequency ν_{if}. Also important to note here is that the spontaneous emission is directly related to the probability of absorption which is itself proportional to the square of the transition dipole moment, thus the *strength* of the dipole transition. Note that three important fields of theories have been combined together here, namely Planck's theory for black body radiation, thermodynamics (Boltzmann distribution) and time dependent perturbation theory. The electromagnetic field here is also quantized and is seen as a collection of harmonic oscillators. The transfer of energy between the energy states of the radiation and the molecular system leads to the excitation and emission processes. The total rate of emission depends on both, the spontaneous emission and the stimulated emission. The mean lifetime of the molecule's exited state is inversely proportional to this total rate.

Absorption and Emission Cross Sections and Fluorescence Lifetimes

Let us for now model a molecule as a two state system, where there is no degeneracy associated with any of the states. The absorption cross section of a molecule, $\sigma_a(\nu)$, is the measure of the probability that it absorbs energy from the electromagnetic radiation field incident on it. It provides a relationship between the optical density of the sample and its concentration in spectroscopic analysis. It has the dimension of an area which can be interpreted as an effective cross-sectional area responsible for blocking an incident beam of electromagnetic waves of frequency ν. Let us define the stimulated absorption rate as

$$w_{i\to f}(\nu)\mathrm{d}\nu = b_{if}(\nu)S(\nu)\mathrm{d}\nu \tag{2.25}$$

where $S(\nu)$ is the energy density of the electromagnetic field per unit frequency and therefore $S(\nu)\mathrm{d}\nu$ is the energy density for the frequency range ν to $\nu+\mathrm{d}\nu$. $b_{if}(\nu)$ is the shape factor for the absorption spectrum of the molecule and represents the probability for the absorption at frequency ν to take place. The total rate of absorption is then the integral of the expression above.

$$W_{i\to f} = \int b_{if}(\nu)S(\nu)\mathrm{d}\nu \tag{2.26}$$

The absorption coefficient can be written in terms of direct measurable quantities, and it is simply the ratio of the total energy absorbed in unit time with the total incident irradiance I ($I = c\int S(\nu)\mathrm{d}\nu$).

$$\sigma_a(\nu) = \frac{h\nu W_{i\to f}}{I} = \frac{h\nu\int b_{if}(\nu)S(\nu)\mathrm{d}\nu}{c\int S(\nu)\mathrm{d}(\nu)} \tag{2.27}$$

If the absorption spectrum is approximated as a line spectrum, b_{if} is sharply peaked at ν_{fi} and is equal to B_{fi}, and hence, the absorption cross section can be written as:

$$\sigma_a = \frac{h\nu_{fi}}{c}B_{if} \tag{2.28}$$

In a similar way, the emission cross section of the molecule can be written in terms of the emission coefficients:

$$\sigma_e(\nu) = \frac{h\nu}{c}b_{fi}(\nu) = \frac{c^2}{8\pi\nu^2}a_{fi}(\nu) \tag{2.29}$$

The coefficient $a_{fi}(\nu)$ is the probability for the molecule in the excited state to decay spontaneously. Again, for the case of a sharp line spectrum, this is equal to A_{fi}. An important thing to mention here is that since the emission and absorption for such a two state system take place at the same frequency, the emission and absorption cross sections are completely identical $\sigma_e = \sigma_a \equiv \sigma$. The spontaneous decay lifetime τ_f, i.e. the statistical mean time the molecule stays in the excited state when there is no perturbation field then is inversely proportional to the spontaneous emission coefficient

A_{fi}, or:

$$\frac{1}{\tau_f} = \frac{8\pi}{c^2}\int \sigma(\nu)\nu^2 \mathrm{d}\nu = 8\pi c \int \frac{\sigma(\lambda)}{\lambda^4}\mathrm{d}\lambda \tag{2.30}$$

The above equation is called *Füchtbauer-Ladenburg relationship* [98] and it gives us the means to obtain the *radiative lifetime* of a two state system from the measured absorption/emission spectrum. This model works well as a good approximation for the estimation of radiative rates of atomic transitions where the absorption and the emission take place at the same frequency and can be well approximated as sharp lines. See references [99, 100] for example. However, this theory fails to predict the transition rates for molecular systems accurately. The main reason for this deviation is that the spectra of the molecules are much broader due to the presence of vibrational and rotational energy levels within each electronic state. We shall discuss this aspect further in the next session. But for now, this can be visualized as a collection of many individual oscillators oscillating at slightly different frequencies that can interact with the electromagnetic field and have different transition probabilities. Moreover, the emission spectrum of a molecule is spectrally red shifted compared to its excitation spectrum. This is the well known *Stokes shift* of a fluorescent molecule.

In order to include this effect, Strickler and Berg modified the theory by taking into account all the vibrational quantum states [101]. The net transition rate is taken as the sum of the transition rates from the lowest vibrational level of the higher electronic state to all the possible vibrational levels of the ground state.

$$A_{f0\to i} = K\frac{8\pi h}{c^3}\frac{\sum_l \nu^3_{k0\to nl} b_{k0\to nl}}{\sum_l b_{k0\to nl}} \tag{2.31}$$

where the summations are over all the vibrational states l of the ground electronic

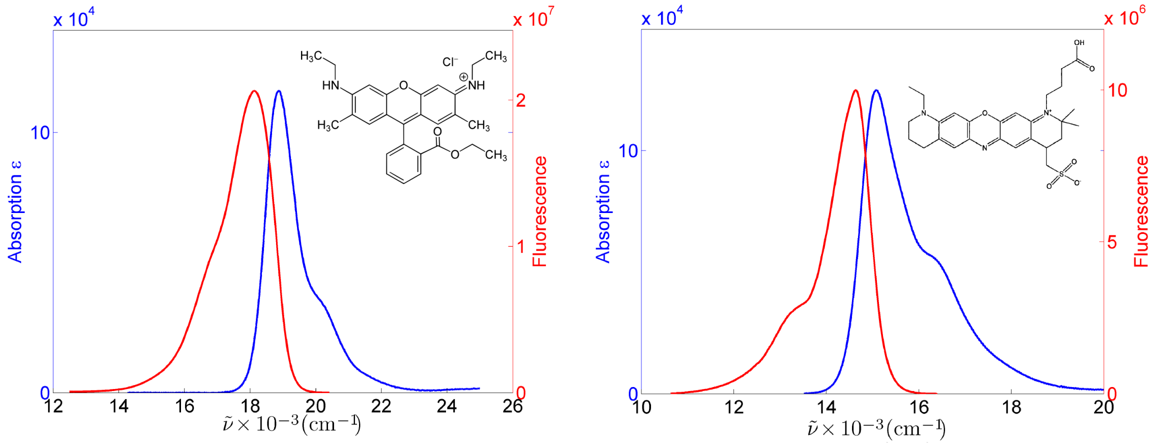

Figure 2.6: The left figure shows the excitation/emission spectra of Rhodamine 6G in ethanol and the right side for Atto 655 in water. The plots are against wavenumbers $\bar{\nu} = 1/\lambda$.

state, and K is a proportionality constant. Each term in the numerator is proportional to the intensity in the emission spectrum. Hence, the total rate of spontaneous decay is written, similar to equation (2.30) in the integral form

$$\frac{1}{\tau_f} = \frac{8\pi}{c^2} \frac{\int \mathrm{d}\nu \, F(\nu)}{\int \mathrm{d}\nu \, F(\nu)/\nu^3} \int \mathrm{d}\nu \, \sigma_a(\nu)/\nu \tag{2.32}$$

where $F(\nu)$ are the Franck-Condon factors introduced previously, which shape the emission spectrum and the integral on the right is over the absorption spectrum of the molecule. This is the well-known *Strickler-Berg equation* which connects both the absorption and emission spectra for determining the average lifetimes of the molecules in their excited states. One must observe that as a special case, if the absorption and emission spectra are sharp and take place at the same frequency, this equation gives the same result as the Füchtbauer-Ladenburg relationship (2.30) shown above. The integral on the right side can be written in terms of experimentally measured molar extinction coefficients $\epsilon(\nu)$. Given the quantum yield of the molecule and the refractive index of the medium, the equation can be written as:

$$\frac{1}{\tau_f} = 2.88 \times 10^{-9} n^2 \Phi \frac{\int \mathrm{d}\nu \, F(\nu)}{\int \mathrm{d}\nu \, F(\nu)/\nu^3} \int \mathrm{d}\nu \, \frac{\epsilon(\nu)}{\nu} \tag{2.33}$$

where ν is now the wavenumber in cm^{-1}. Figure 2.6 shows the spectra for the dye molecules Rhodamine 6G and Atto 655. The data for Rhodamine 6G has been taken from [102] and for Atto 655, from the website[1]. The quantum yields of these dyes are reported as 0.95 and 0.33 in the medium of the measurements. The spontaneous lifetimes calculated from equation (2.33) are 3.64 ns and 1.72 ns in water, whereas the true values reported in literature are 4.1 ns and 1.8 ns, respectively [103].

Spontaneous Emission Near Interfaces

In the preceding section we showed the connection between the spontaneous emission rate of a dipole emitter in empty space and the DOS $\tilde{\rho}_\nu$. When a molecule is present in a dielectric medium, the local DOS (LDOS) changes due to the scattering from the medium which leads to a modification of the spontaneous emission rates. Depending upon the solvent properties, thermal coupling between the dipole emitter and surrounding molecules can play a role in non-radiative energy transfer, due to collisions, known as *thermal decay* and hence shortening the lifetime of the molecule in the excited state [104].

The situation becomes complicated when placing such an emitter close to a dielectric or metallic interface. In that case, the spontaneous emission rate A_{fi} will change and becomes position- *and* orientation-dependent. Also, the effective DOS will now be

---

[1] http://www.atto-tec.com/

position- *and* orientation-dependent. One needs to calculate the LDOS in such a situation and use the relations developed in the previous section. The relation between the Einstein coefficients and LDOS remain the same as in equation (2.24). The properties of the metal determine the LDOS and depending on the distance from the metal, the electromagnetic coupling between the states of the dye molecule and the metal's surface plasmons varies, which together determine its radiative and non-radiative rates [105, 106]. However, the calculation of spontaneous emission rate of a dipole emitter is much more straightforward using the theory by Chance, Prock, and Silbey (CPS) where one calculates the total emission rates by using Fresnel's equations and energy *flux* density calculations using the Poynting vector [107]. This will the discussed thoroughly in the forthcoming sections.

2.2 Plane Waves and Maxwell's Equations

We begin our theoretical outline by highlighting the work of James Clerk Maxwell who set the groundwork for the electromagnetic theory of light in 1864. In classical electrodynamics, light is described as an electromagnetic wave (EM wave) with synchronized oscillations of electric (**E**) and magnetic (**B**) fields oriented orthogonal to each other, traveling with a speed c/n_{med} along a propagation direction **k**, where n_{med} is the refractive index of the medium, as shown in fig. 2.7. By synchronized oscillations, we mean that the fields **E** and **B** have the same oscillation frequency and phase. The vector **k** is orthogonal to both **E** and **B**. The classical theory of light is based on the well known Maxwell's equations, which are the fundamental equations for electricity and magnetism. In CGS units, these equations can be written as:

$$\nabla \cdot \epsilon \mathbf{E} = 4\pi\rho \tag{2.34}$$

$$\nabla \cdot \mathbf{B} = 0 \tag{2.35}$$

$$\nabla \times \mathbf{E} = -\frac{1}{c}\frac{\partial \mathbf{B}}{\partial t} \tag{2.36}$$

$$\nabla \times \left(\frac{\mathbf{B}}{\mu}\right) = \frac{\epsilon}{c}\frac{\partial \mathbf{E}}{\partial t} + \frac{4\pi}{c}\mathbf{j} \tag{2.37}$$

where ρ and $\mathbf{j}$ are the electric charge and current density respectively, and ϵ and μ are the dielectric susceptibility and magnetic permeability of the medium. These four equations were obtained from the well-known laws for electric and magnetic fields, the first two equations are Gauss' law for electric and magnetic fields; the third equation represents Faraday's law of magnetic induction and the fourth equation is Ampere's circuital law. These four coupled differential equations are satisfied simultaneously for all possible electromagnetic fields.

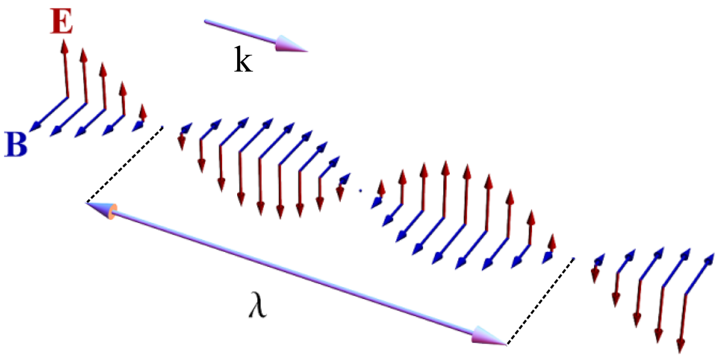

Figure 2.7: A Schematic showing an electromagnetic wave at a time t with $\mathbf{E}$ and $\mathbf{B}$ oscillating orthogonal to the direction of propagation $\mathbf{k}$. The wavelength λ of the EM wave is marked here as the distance over one complete cycle of oscillation.

Equations (2.34) and (2.35) stem from the fact that electric charges can exist in space whereas magnetic monopoles do not; and the electric field exiting a volume is proportional to the charge density present inside it whereas the total flux of the magnetic field through a closed surface is always zero. Gauss' law holds true even for moving charges which makes it more general than Coloumb's law. The force due to an electromagnetic field on a charge particle moving with an arbitrary velocity $\mathbf{v}$ is given by the Lorentz force,

$$\mathbf{F} = q[\mathbf{E} + (\mathbf{v} \times \mathbf{B})]. \tag{2.38}$$

An important point to note from equation (2.38) is that magnetic field due to any configuration of moving or static electric charges is always perpendicular to the direction of motion, and thus, does not perform any work.

In a source-free homogeneous medium with unity magnetic permeability $\mu = 1$(which is true for all of the work in this thesis), the simplest solution to Maxwell's equations is a plane wave, where the space-time behavior of the electric ($\mathbf{E}$) and magnetic ($\mathbf{B}$) fields can be written as $\propto \exp(i\mathbf{k}\cdot\mathbf{r} - i\omega t)$, where ω is the angular frequency of the oscillations. Inserting this space-time relation back into the equations (2.34), (2.35), (2.36) and (2.37) we get:

$$\mathbf{k} \cdot \mathbf{E} = 0 \tag{2.39}$$

$$\mathbf{k} \cdot \mathbf{B} = 0 \tag{2.40}$$

$$i\mathbf{k} \times \mathbf{E} = \frac{i\omega}{c}\mathbf{B} \tag{2.41}$$

$$i\mathbf{k} \times \mathbf{B} = -\frac{i\epsilon\omega}{c}\mathbf{E} \tag{2.42}$$

From equations (2.39) and (2.40), it is clear that **E**, **B** and **k** are mutually perpendicular. If we now apply the curl operator again on equation (2.36) and use the relations in equations (2.39) and (2.42), we obtain

$$\nabla \times \nabla \times \mathbf{E} = -\mathbf{k} \times (\mathbf{k} \times \mathbf{E}) = k^2\mathbf{E} = -\frac{\omega}{c}(\mathbf{k} \times \mathbf{B}) = \frac{\epsilon\omega^2}{c^2}\mathbf{E} \tag{2.43}$$

Therefore, from equation (2.43) we obtain the amplitude of the wave vector $|\mathbf{k}| = \sqrt{\epsilon}\omega/c$. The vector $|\mathbf{k}|$ characterizes the spatial periodicity of the electric field. If we define the refractive index of the medium by $n_{\text{med}} = \sqrt{\epsilon}$, we get the dispersion relation $|\mathbf{k}| = n_{\text{med}}\omega/c$ and the relation between the amplitudes of the electric and magnetic fields as $|\mathbf{B}| = n_{\text{med}}\,|\mathbf{E}|$.

For any electromagnetic field, the instantaneous energy flux is given by the Poynting vector:

$$\mathbf{S} = \frac{c}{4\pi}\mathbf{E} \times \mathbf{B} \tag{2.44}$$

For visible light **S** oscillates with a frequency $\sim 10^{15}$ Hz, which cannot be measured with any instrument. What is measurable is the time-averaged energy flux density $\langle \mathbf{S} \rangle$ (averaged over one period of oscillation) for an electromagnetic field, which is given by[2]

$$\langle \mathbf{S} \rangle = \frac{c}{8\pi}\text{Re}\{\mathbf{E} \times \mathbf{B}^*\} \tag{2.45}$$

These relations hold true for any plane wave solution of the electromagnetic field in a source-free homogeneous environment. Further, any field in such an environment can be described as a superposition of plane waves. We will use these relations extensively in our forthcoming sections where we investigate the field of an oscillating electric dipole in such environments.

The interaction of EM waves with conducting media can be understood well with the help of the Drude model for conductivity. The model is based on the fact that the valence and the conduction bands of metals overlap at room temperature, and as a result a large number of free electrons exist that are responsible for their high conductivity. Therefore, any electromagnetic oscillations incident on a metal perturb the electrons on the surface which are then set into an oscillation with the same frequency in order to counter these perturbations. The existence of conductivity can be taken into account by

---

[2] for derivation refer to "Principles of Optics", Born and Wolf [108]

simply introducing a complex dielectric constant into Maxwell's equations. The real of the dielectric constant (ϵ') is related to the bounded electrons and the lattice structure of the metal, whereas the imaginary part arises due to the free electrons. If we define σ as the specific conductivity of the material, then the *convection* current density $\mathbf{j}$ is given by:

$$\mathbf{j} = \sigma \mathbf{E} \tag{2.46}$$

Note here that σ is a function of frequency since we saw that bound electrons can be excited into the conduction band. Plugging equation (2.46) into Maxwell's equation (2.37), we have:

$$\boldsymbol{\nabla} \times \mathbf{B} = -\frac{i\omega}{c}\left[\epsilon'(\omega) + \frac{4\pi i}{\omega}\sigma(\omega)\right]\mathbf{E} \tag{2.47}$$

Using equation (2.43) we get the dispersion relation:

$$k^2 = k_0^2\left[\epsilon'(\omega) + \frac{4\pi i}{\omega}\sigma(\omega)\right] \tag{2.48}$$

where $k_0 = \omega/c$. The refractive index is thus a complex number which can be written as $\tilde{n} = n(\omega) + i\kappa(\omega)$.

$$\therefore \qquad \tilde{n}^2(\omega) = [n(\omega) + i\kappa(\omega)]^2 = \epsilon'(\omega) + \frac{4\pi i}{\omega}\sigma(\omega) = \epsilon(\omega) \tag{2.49}$$

This brings us to the relations:

$$\epsilon' = n^2 - \kappa^2 \tag{2.50}$$

and,

$$\frac{2\pi\sigma}{\omega} = n\kappa \tag{2.51}$$

2.3 Fresnel's Equations

After having familiarized ourselves with the basic properties of plane waves in a homogeneous environment, we now study their behavior when they encounter a locally flat interface separating two homogeneous media with different refractive indices n_1 and n_2. The wave vector $\mathbf{k}$ again represents a plane wave with a spatial periodicity of $|\mathbf{k}|$ and its propagation direction along the unit vector $\hat{\mathbf{k}}$. Furthermore, we will use a '±' subscript to indicate the global direction of propagation: "+" when the wave travels from medium 1 → 2; and "−" when it travels from medium 2 → 1 (see figure 2.8). To complete the picture, we must specify the direction of oscillation (polarization) of either

$\mathbf{E}$ or $\mathbf{B}$. We consider two explicit cases of polarization, one where $\mathbf{E}$ oscillates in the plane of incidence, $\mathbf{I}$, ($\mathbf{B}$ is then pointing out of the plane of incidence), denoted as the p-wave, or Transversal Electric (TE) wave; and the other where $\mathbf{E}$ oscillates out of the plane ($\mathbf{B}$ is then oscillating in the plane of incidence), which is denoted as the s-wave, or Transversal Magnetic (TM) wave. Any other polarization can be written as a linear combination of these two polarizations. Figure 2.8 represents the generalized situation of the problem where plane waves are incident from both sides of the interface onto it. The projection of $\mathbf{k}$ on the interface is denoted as $\mathbf{q}$, and the wave-vector component perpendicular to it is denoted by $\pm\mathbf{w_i}$, where the sign follows the same sense of direction as stated above. Before we get to the boundary conditions for the problem, we must note that the periodicity along the interface must be conserved, thus q is equal for all the four wave vectors. In order to simplify the notations in all the discussion that follows, we will work, without loss of generality, in a unit system where the length unit is chosen in such a way that the vacuum wavelength of light is 2π, and thus the length of the wave vector $|\mathbf{k}|$ in vacuum equal to one. Using elementary geometry, one has the

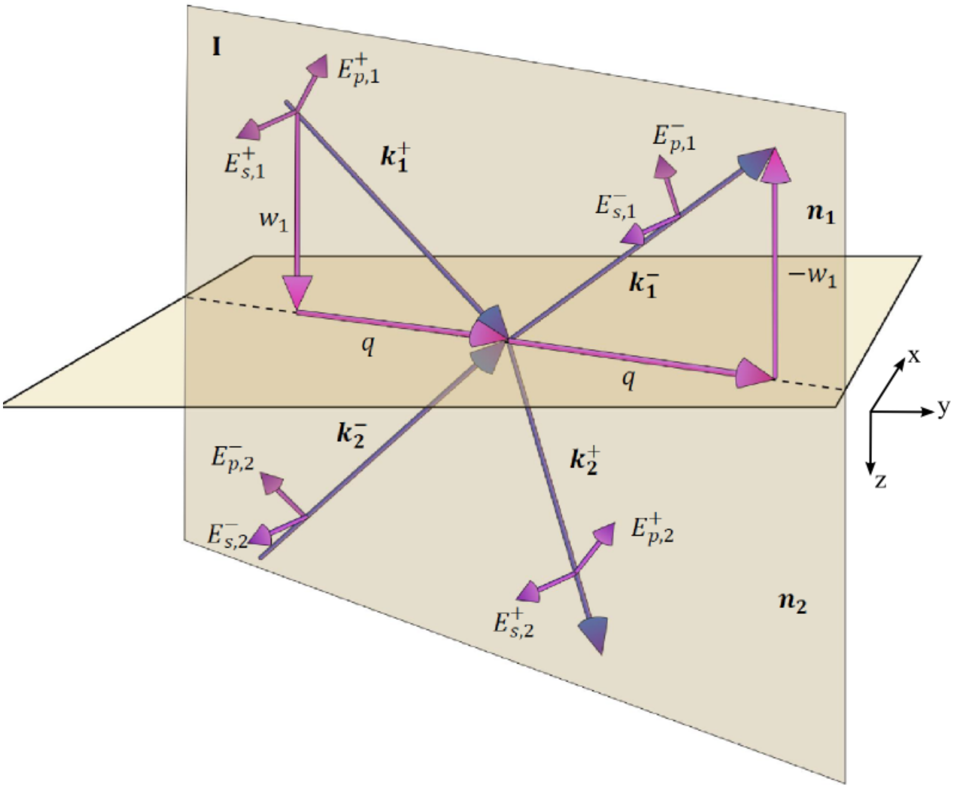

Figure 2.8: A schematic representation of plane waves at a dielectric interface between two media with refractive indices n_i (for $i = 1, 2$). The waves are denoted by their wave vectors $\mathbf{k}_i^{\pm}$ depending upon their direction with respect to the interface; and the electric field polarizations as E_p or E_s depending on their orientations with respect to the plane of incidence $\mathbf{I}$ as shown. The vector $\mathbf{k}_i^{\pm}$ is resolved into two components $\pm\mathbf{w}_i$ and $\mathbf{q}$ perpendicular and in the interface.

following:

$$\sin\theta_i = q/n_i \tag{2.52}$$

and

$$n_1{}^2 - w_1^2 = n_2{}^2 - w_2^2 \tag{2.53}$$

where θ_i are the angles of the wave vectors with respect to the normal of the interface. Equation (2.52) directly gives us *Snell's law of refraction* and *reflection* i.e. $n_1 \sin\theta_1 = n_2 \sin\theta_2$; and the wave vectors $\mathbf{k}_1^+$ and $\mathbf{k}_1^-$ have the same angle with the normal, θ_1.

Let us now establish the boundary conditions first by considering p-waves: In order to observe continuity in space, the tangential component of the electric field $\mathbf{E}$ and magnetic field $\mathbf{B}$ must be conserved across the interface. Thus we obtain

$$E_{p,1}^+ \cos\theta_1 - E_{p,1}^- \cos\theta_1 = E_{p,2}^+ \cos\theta_2 - E_{p,2}^- \cos\theta_2, \tag{2.54}$$

$$B_{p,1}^+ + B_{p,1}^- = B_{p,2}^+ + B_{p,2}^- \tag{2.55}$$

Using the relationship $|\mathbf{B}| = n_{\text{med}}\,|\mathbf{E}|$ and the fact that $\cos\theta_{1,2} = \frac{w_{1,2}}{n_{1,2}}$, we get

$$\frac{w_1}{n_1}E_{p,1}^+ - \frac{w_1}{n_1}E_{p,1}^- = \frac{w_2}{n_2}E_{p,2}^+ - \frac{w_2}{n_2}E_{p,2}^-, \tag{2.56}$$

$$n_1 E_{p,1}^+ + n_1 E_{p,1}^- = n_2 E_{p,2}^+ + n_2 E_{p,2}^- \tag{2.57}$$

These equations can be written in a compact matrix form as:

$$\begin{pmatrix} \frac{w_1}{n_1} & -\frac{w_1}{n_1} \\ n_1 & n_1 \end{pmatrix} \begin{pmatrix} E_{p,1}^+ \\ E_{p,1}^- \end{pmatrix} = \begin{pmatrix} \frac{w_2}{n_2} & -\frac{w_2}{n_2} \\ n_2 & n_2 \end{pmatrix} \begin{pmatrix} E_{p,2}^+ \\ E_{p,2}^- \end{pmatrix} \tag{2.58}$$

Performing necessary matrix operations, equation (2.58) can be rewritten as:

$$\begin{pmatrix} E_{p,1}^+ \\ E_{p,1}^- \end{pmatrix} = \frac{1}{2} \begin{pmatrix} \frac{w}{n} + n & -\frac{w}{n} + n \\ -\frac{w}{n} + n & \frac{w}{n} + n \end{pmatrix} \begin{pmatrix} E_{p,2}^+ \\ E_{p,2}^- \end{pmatrix} \tag{2.59}$$

where we use the notation $w = w_2/w_1$ and $n = n_2/n_1$. Let us denote the matrix in the equation (2.59) as $\hat{\mathbf{M}}_p$ for future reference. In the special case when an EM wave is incident from the side of the interface where the refractive index is n_1, we have

$$\begin{pmatrix} E_{p,1}^+ \\ E_{p,1}^- \end{pmatrix} = \hat{\mathbf{M}}_p \begin{pmatrix} E_{p,2}^+ \\ 0 \end{pmatrix} \tag{2.60}$$

Defining reflection and transmission coefficients as $R = E_1^-/E_1^+$ and $T = E_2^+/E_1^+$, we obtain:

$$R_p = \frac{n^2 - w}{n^2 + w}, \tag{2.61}$$

and

$$T_p = \frac{2n}{n^2 + w} \tag{2.62}$$

For the case of s-waves, the boundary conditions can be written similar to equations (2.54) and (2.55) as:

$$E_{s,1}^+ + E_{s,1}^- = E_{s,2}^+ + E_{s,2}^- \tag{2.63}$$

$$w_1 E_{s,1}^+ - w_1 E_{s,1}^- = w_2 E_{s,2}^+ - w_2 E_{s,2}^-, \tag{2.64}$$

Writing in the matrix form, we obtain,

$$\begin{pmatrix} E_{s,1}^+ \\ E_{s,1}^- \end{pmatrix} = \frac{1}{2} \begin{pmatrix} 1+w & 1-w \\ 1-w & 1+w \end{pmatrix} \begin{pmatrix} E_{s,2}^+ \\ E_{s,2}^- \end{pmatrix} \tag{2.65}$$

and the reflection and transmission coefficients are now given by:

$$R_s = \frac{1 - w}{1 + w}, \tag{2.66}$$

and

$$T_s = \frac{2}{1 + w} \tag{2.67}$$

Figure 2.9 shows the reflection coefficients as a function of incident angle θ_1, or $\cos^{-1}(w_1/k_1)$. From equation (2.61) we find that R_p is zero when $w = n^2$ or $\cos\theta_1/n_1 = \cos\theta_2/n_2$, which can be seen in both cases of incidence as shown in the figure. The angle of incidence where the reflection coefficient vanishes is called *Brewster's angle*. Since from Snell's law we have $n_1/n_2 = \sin\theta_2/\sin\theta_1$, the situation only occurs when $\theta_1 + \theta_2 = \pi/2$ or $n_2/n_1 = \tan\theta_1$.

2.3.1 Total Internal Reflection

From equation (2.59), we get the amplitude of the $\mathbf{E}_{p,2}^+$:

$$\mathbf{E}_{p,2}^+ = \hat{\mathbf{e}}_{p,2}^+ \frac{2E_{p,1}^+}{w/n + n} \tag{2.68}$$

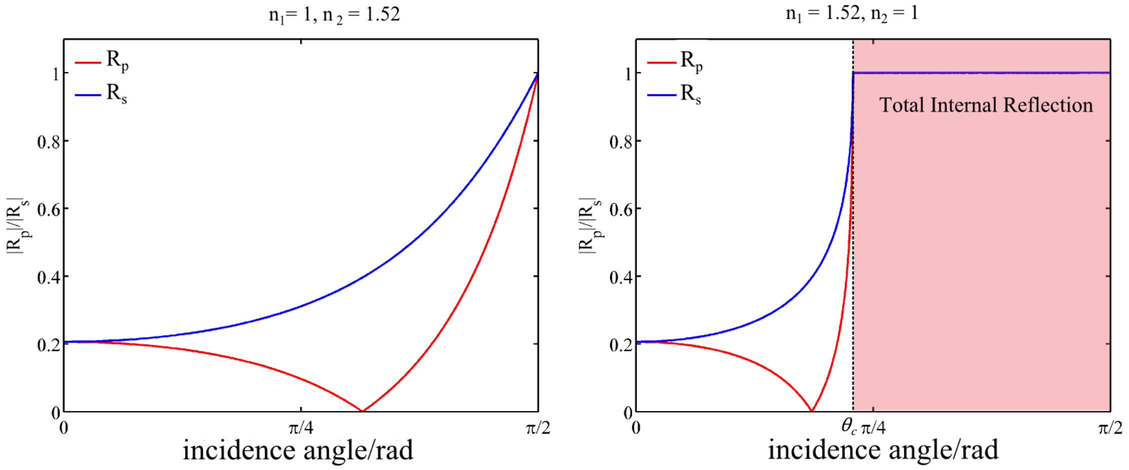

Figure 2.9: Calculated reflection coefficients R_p and R_s as a function of the incident angle θ_1 for an air/glass interface for incidence from the air medium (left) and from the glass medium (right). The angle where the reflection coefficient for the *p*-waves is zero is the *Brewster's angle*. The critical angle θ_c, above which total internal reflection occurs is shown as well.

where $\hat{\mathbf{e}}^+_{p,2} = \frac{w_2\hat{\mathbf{q}} - \mathrm{q}\hat{\mathbf{z}}}{n_2}$ is the unit vector along the polarization of the p-wave $\mathbf{E}^+_{p,2}$. Ignoring the time variation, the refracted plane wave can be written as $\propto \exp(-i\mathbf{k}^+_2 \cdot \mathbf{r})$. Observing that $\mathbf{k}^+_2 = \mathrm{q}\hat{\mathbf{q}} + w_2\hat{\mathbf{z}}$, we can rewrite the exponential term as $\exp(i\mathbf{q}\cdot\boldsymbol{\rho} + iw_2 z)$, where $\boldsymbol{\rho}$ is the two dimensional vector component of $\mathbf{r}$ within the interface. Using equation (2.53), w_2 can be written as:

$$w_2 = \sqrt{n_2^2 - n_1^2 + w_1^2} \tag{2.69}$$

This implies that w_2 becomes purely imaginary if $w_1 < \sqrt{n_1^2 - n_2^2}$. In this case, the spatial field dependence for the EM field represents a wave propagating along the interface in the plane of incidence (i.e. along the direction of $\hat{\mathbf{q}}$), but exponentially decaying perpendicular to the interface (along the z-axis). The amplitude decreases rapidly with the depth z, and the effective penetration depth is on the order of one wavelength. The wave is not transversal and is termed an evanescent wave. Remarkably, there is no transfer of energy across the interface and this phenomenon is called Total Internal Reflection (TIR). This can be shown by calculating the projection of the time averaged Poynting vector onto the normal of the interface, which is given by the expression:

$$\frac{\mathrm{c}}{8\pi}\mathrm{Re}\left\{(\mathbf{E}\times\mathbf{B}^*)\frac{w_2}{n_2}\right\} = \frac{\mathrm{c}}{8\pi}\mathrm{Re}\left\{n_2|\mathbf{E}|^2\frac{w_2}{n_2}\right\} = 0 \tag{2.70}$$

In the special situation when $w_1 = \sqrt{n_1^2 - n_2^2}$ or $\sin\theta_1 = n_2/n_1$ the wave propagates along the direction $\hat{\mathbf{q}}$, where total internal reflection starts, and the angle satisfying this condition is called "critical angle" (see figure 2.9).

It is important to note here that when TIR occurs, there is a phase shift between the incident and reflected waves. From the matrix equation (2.59) we get:

$$\frac{E_{p,1}^{+}}{E_{p,2}^{+}} = \frac{1}{2}\left(\frac{w}{n} + n\right) \tag{2.71}$$

$$\frac{E_{p,1}^{-}}{E_{p,2}^{+}} = \frac{1}{2}\left(-\frac{w}{n} + n\right) \tag{2.72}$$

Since, w is imaginary, each factor contributes to an additional phase term $\exp(\pm i\phi)$

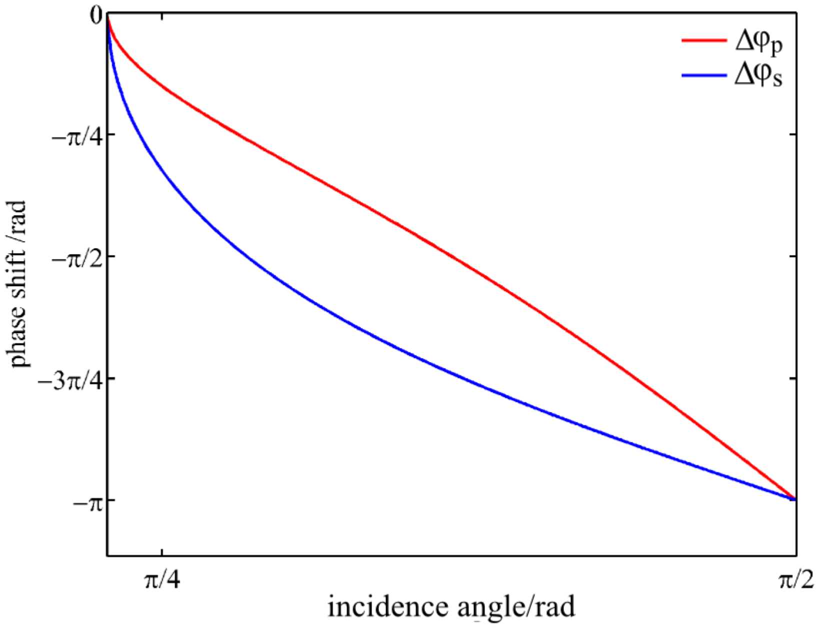

Figure 2.10: The phase shift between the incident and the reflected p- and s-waves at the interface separating air and glass ($n = 1.52$). The plot shows for $\theta > \theta_c$, below which the phase shift is zero for both waves.

and a total phase shift between the incident and reflected wave as:

$$\Delta\phi_p = -2\tan^{-1}\left(\frac{\operatorname{Im} w}{n^2}\right) \tag{2.73}$$

Similar is the case for s-waves and one can calculate the phase shift as:

$$\Delta\phi_s = -2\tan^{-1}\left(\operatorname{Im} w\right) \tag{2.74}$$

Figure 2.10 shows the calculated phase shifts for p-waves and s-waves at different incident angles. Since there is a phase shift between the incident and the total internally reflected rays, an interference is observed which leads to a shift in the reflected beam in the plane of the incidence towards the direction of propagation, which is known as *Goos-Hänchen Shift*.

2.3.2 Thin Layers and Frustrated Internal Reflection

We now consider the case where there are several thin layers stacked on top of each other. For the beginning, let us first consider the case where light traverses through two interfaces as shown in figure 2.11, separating three dielectric media ($n_i,\ i = 1, 2, 3$). To complete the picture, let us assign a thickness d for medium 2 sandwiched in between. Writing the transfer matrix for a p-wave at the second interface (between media 2 and 3), we have:

$$\begin{pmatrix} E_{p,2}^{+b} \\ E_{p,2}^{-b} \end{pmatrix} = \frac{1}{2} \begin{pmatrix} \frac{w_{23}}{n_{23}} + n_{23} & -\frac{w_{23}}{n_{23}} + n_{23} \\ -\frac{w_{23}}{n_{23}} + n_{23} & \frac{w_{23}}{n_{23}} + n_{23} \end{pmatrix} \begin{pmatrix} E_{p,3}^{+} \\ E_{p,3}^{-} \end{pmatrix} \tag{2.75}$$

where $E_{p,2}^{\pm b}$ are electric fields at the second interface traveling in the medium 2 towards (+) and away (−) from the interface, $w_{ij} = w_i/w_j$ and $n_{ij} = n_i/n_j$. Similarly, at the first interface, another transfer matrix can be constructed:

$$\begin{pmatrix} E_{p,1}^{+} \\ E_{p,1}^{-} \end{pmatrix} = \frac{1}{2} \begin{pmatrix} \frac{w_{12}}{n_{12}} + n_{12} & -\frac{w_{12}}{n_{12}} + n_{12} \\ -\frac{w_{12}}{n_{12}} + n_{12} & \frac{w_{12}}{n_{12}} + n_{12} \end{pmatrix} \begin{pmatrix} E_{p,2}^{+t} \\ E_{p,2}^{-t} \end{pmatrix} \tag{2.76}$$

where now $E_{p,2}^{\pm t}$ are electric fields at the first interface traveling in the medium 2 towards (+) and away (-) from the interface. The connection between the two sets of fields inside

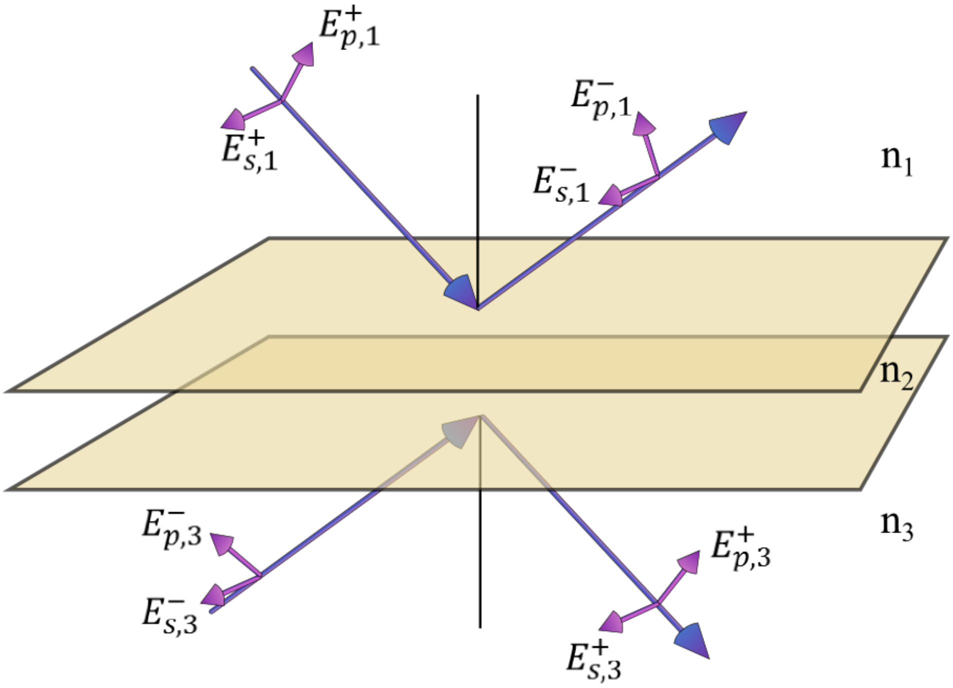

Figure 2.11: A thin dielectric layer with refractive index n_2 is situated between two materials with refractive indices n_1 and n_3. The electric field vectors for the light rays above and below the first and second interface are shown here together with their polarizations.

the medium 2 is given by the phase difference when a wave travels a distance d in the medium.

$$\begin{pmatrix} E_{p,2}^{+b} \\ E_{p,2}^{-b} \end{pmatrix} = \begin{pmatrix} e^{-iw_2 d} & 0 \\ 0 & e^{iw_2 d} \end{pmatrix} \begin{pmatrix} E_{p,2}^{+t} \\ E_{p,2}^{-t} \end{pmatrix} \tag{2.77}$$

where w_2 is the z-component of the wave-vector $\mathbf{k}_2$ in the medium. If w_2 is real then the matrix simply represents the phase accumulation for a plane wave propagating through the homogeneous medium of index n_2. Thus, the field in medium 3 can be written in terms of the field in medium 1 as:

$$\begin{pmatrix} E_{p,1}^{+} \\ E_{p,1}^{-} \end{pmatrix} = \frac{1}{4} \begin{pmatrix} \frac{w_{12}}{n_{12}} + n_{12} & -\frac{w_{12}}{n_{12}} + n_{12} \\ -\frac{w_{12}}{n_{12}} + n_{12} & \frac{w_{12}}{n_{12}} + n_{12} \end{pmatrix} \begin{pmatrix} e^{-iw_2 d} & 0 \\ 0 & e^{iw_2 d} \end{pmatrix} \begin{pmatrix} \frac{w_{23}}{n_{23}} + n_{23} & -\frac{w_{23}}{n_{23}} + n_{23} \\ -\frac{w_{23}}{n_{23}} + n_{23} & \frac{w_{23}}{n_{23}} + n_{23} \end{pmatrix} \begin{pmatrix} E_{p,3}^{+} \\ E_{p,3}^{-} \end{pmatrix} \tag{2.78}$$

Before proceeding further, let us examine two important phenomena here. For the first case, let us assume that $n_3 = n_1 > n_2$. The transfer matrix $\hat{\mathbf{M}}_p$ for p-waves, considering boundary conditions for both the interfaces can be written as:

$$\hat{\mathbf{M}}_p = \begin{pmatrix} \frac{w}{n} + n & -\frac{w}{n} + n \\ -\frac{w}{n} + n & \frac{w}{n} + n \end{pmatrix} \begin{pmatrix} \mathrm{e}^{-i\phi_2} & 0 \\ 0 & \mathrm{e}^{i\phi_2} \end{pmatrix} \begin{pmatrix} \frac{n}{w} + \frac{1}{n} & -\frac{n}{w} + \frac{1}{n} \\ -\frac{n}{w} + \frac{1}{n} & \frac{n}{w} + \frac{1}{n} \end{pmatrix} \tag{2.79}$$

where $w = w_2/w_1$ and $n = n_2/n_1$ and $\phi_2 = w_2 d$. Now, when there is TIR (i.e. w_2 is imaginary), the propagation matrix carries the loss of amplitude in the EM field when the plane wave propagates through the medium. $\hat{\mathbf{M}}_p$ can be simplified into the form of a 2×2 matrix as

$$\hat{\mathbf{M}}_p = \begin{pmatrix} A & B \\ B^* & A^* \end{pmatrix} \tag{2.80}$$

where $A = \cos\phi_2 - i/2\,(w/n^2 + n^2/w)\sin\phi_2$, $B = -i/2\,(w/n^2 - n^2/w)\sin\phi_2$. The matrix looks much similar for s-waves, $\hat{\mathbf{M}}_s$ can be obtained by putting $n = 1$ for the expressions of A and B. As we stated in the previous section, evanescent waves do not transmit any energy across the interface. However, if there is a third optically denser medium present, within one wavelength distance, from the first optically denser medium, these evanescent waves couple through and the energy is transmitted through the thin intermediate layer into the third medium. This phenomenon is similar to quantum tunneling and is called *frustrated internal reflection*, the term "Frustrated" appearing here due to the loss of energy in the reflected wave in the first optically rarer medium due to the effective evanescent-wave coupling. We will encounter this phenomenon later when discussing the interaction of en emitting electric dipole with a stack of layers.

In the case where $E_3^- = 0$, one has $E_1^+ = A \cdot E_3^+$. Therefore, the transmission coefficients are simply given by:

$$T_{p,s} = \frac{E^{+}_{3,(p,s)}}{E^{+}_{1,(p,s)}} = \frac{1}{A_{p,s}} \tag{2.81}$$

Let us next consider the case where $n_1 = n_3 < n_2$. In this case, the component of the wave vector parallel to the interface $\mathbf{q}$ inside the thin layer can exceed the maximum possible $q = k_1$ in the media with the lower refractive index. Thus, if one considers a wave such that $k_2 \geq q > k_1$, one has total internal reflection at the interfaces. The evanescent waves outside cannot transfer energy away from the stack, and therefore one has multiple reflections inside the thin layer which acts as a *waveguide*. However, only for a few values of q, the sandwiched medium acts as a waveguide. These values depend on the thickness of the layer, the refractive indices of all the media involved and the polarization of the electric field inside the thin layer. These values can be found by realizing the conditions that $E^{+}_{3} \neq 0$, $E^{+}_{1} = 0$, which can be done by finding the solutions of $A = 0$. For p-waves, we have:

$$A_p = \cos(w_2 d) - \frac{i}{2}\left(\frac{w}{n^2} + \frac{n^2}{w}\right)\sin(w_2 d) = 0 \tag{2.82}$$

where $w_2 = \sqrt{n_2^2 - q^2}$ and $k_2 \geq q > k_1$. The modes for the case of s-waves can be found similarly by solving for $A_s = 0$, where A_s is given by the expression:

$$A_s = \cos(w_2 d) - \frac{i}{2}\left(w + \frac{1}{w}\right)\sin(w_2 d) \tag{2.83}$$

2.3.3 Fresnel's Equations for a Metal Surface

Let us now study the reflection and transmission properties of plane waves upon incidence on a metal surface. We follow the same notation as in all our previous sections (for example section 2.3) and define n_1 as the dielectric medium above the interface and $\widetilde{n_2} = n_2 + i\kappa_2$ as the refractive index of the metal at a frequency ω. Let us first consider the case of p-waves. The electric field of a plane wave in medium 2 can be written as:

$$\mathbf{E}^{\pm}_{p,2}(\mathbf{r}, t) = E^{\pm}_{p,2} e^{i(\mathbf{k}_2^{\pm}\cdot\mathbf{r} - \omega t)} \hat{\mathbf{e}}^{\pm}_{\mathbf{2p}} \tag{2.84}$$

The wave vector $\mathbf{k_2}^{\pm}$ can be written as $\mathbf{k}_2^{\pm} = q\hat{\mathbf{q}} \pm w_2\hat{\mathbf{z}}$ where $\mathbf{q}$ is the projection of the wave vector onto the interface whose magnitude is given by $q = n_1 \sin\theta_1 = \widetilde{n}_2 \sin\widetilde{\theta}_2$ and $w_2 = \sqrt{k_2^2 - q^2}$. Therefore, $\mathbf{k_2}^{\pm}\cdot\mathbf{r} = q(\hat{\mathbf{q}}\cdot\boldsymbol{\rho}) \pm w_2 z$, where $\boldsymbol{\rho}$ is a two dimensional vector within the interface. Using this relation, the electric field in the metal can be written as:

$$\mathbf{E}^{\pm}_{p,2}(\mathbf{r},t) = E^{\pm}_{p,2} e^{i[q(\hat{\mathbf{q}}\cdot\boldsymbol{\rho})-\omega t]} e^{\pm i w_2 z} \hat{\mathbf{e}}^{\pm}_{\mathbf{2p}} = E^{\pm}_{p,2} e^{i[q(\hat{\mathbf{q}}\cdot\boldsymbol{\rho})\pm \mathrm{Re}(w_2)z-\omega t]} e^{\mp \mathrm{Im}(w_2)z} \hat{\mathbf{e}}^{\pm}_{\mathbf{2p}} \tag{2.85}$$

Before proceeding further, we must understand the behavior of the electric fields represented by equation (2.85). The first part of the expression on the right represents a plane wave propagating in the direction of $\hat{\boldsymbol{\rho}}$ with a wave vector $\mathbf{q}$; whereas the second part represents a phase shift (real part of w_2) and an exponential modification of the magnitude (imaginary part of w_2) of the electric field $E^{\pm}_{p,2}$ with its propagation along z-direction. The magnitude entirely depends on the sign of the quantity $\mathrm{Im}\{w_2\}$ where,

$$w_2 = \sqrt{(n_2^2 - \kappa_2^2 - q^2) + 2in_2\kappa_2}. \tag{2.86}$$

The sign of the imaginary part of w_2 depends on the sign of the term $n_2\kappa_2$ (principal square root). From equation (2.51), we see that this product is directly proportional to the specific conductivity which cannot be a negative number. This leads to the fact that the magnitude of $\mathbf{E}^{+}_{p,2}$ declines with increasing z and for the case of $\mathbf{E}^{-}_{p,2}$, the magnitude falls exponentially with the decrease of z. In other words, the magnitude of an electromagnetic wave penetrating the metal surface ($z > 0$), falls of exponentially with depth. The magnitude falls down by a factor of e^{-1} for $z = 1/\mathrm{Im}\{w_2\}$. For normal incidence, $\mathrm{Im}\{w_2\} = \kappa_2\omega/c$ and hence, $\kappa(\omega)$ is also called the *extinction coefficient.* It represents the attenuation of the electromagnetic waves propagating through the medium.

While deriving Fresnel's equations for the reflection and transmission of plane waves for a metal surface, one must observe the same boundary conditions for the electric and magnetic fields at the interface as given in section 2.3. The equations (2.54) to (2.64) can be written similarly for the case of a complex refractive index, and the transformation matrix approach we built in that section is valid here. Hence, the reflection coefficient for the case of p- and s-waves respectively is given by:

$$R_p = \frac{\widetilde{n}^2 - \widetilde{\mathrm{w}}}{\widetilde{n}^2 + \widetilde{\mathrm{w}}} \tag{2.87}$$

and,

$$R_s = \frac{1 - \widetilde{\mathrm{w}}}{1 + \widetilde{\mathrm{w}}} \tag{2.88}$$

Using $\widetilde{\mathrm{w}} = \mathrm{w}_2/\mathrm{w}_1$ and $\widetilde{n} = n_2/n_1$. Figure 2.12 shows the reflectivity $(R \cdot R^*)$ and phase shift $\Delta\phi$ for p- and s-waves on a gold/air interface as a function of wavelength and incident angle θ_1. For normal incidence ($\theta_1 = 0$), $\Delta = \Delta\phi_p - \Delta\phi_s = -\pi$, whereas for grazing incidence, $\Delta = 0$. Between these two extreme cases, there exists an angle θ_i

when $\Delta = -\pi/2$ and therefore a linearly polarized light is reflected as an elliptically polarized light. This angle is, in general, where the reflection coefficient for the p-waves is a non-zero minimum, and is called the *principle angle of incidence* [108].

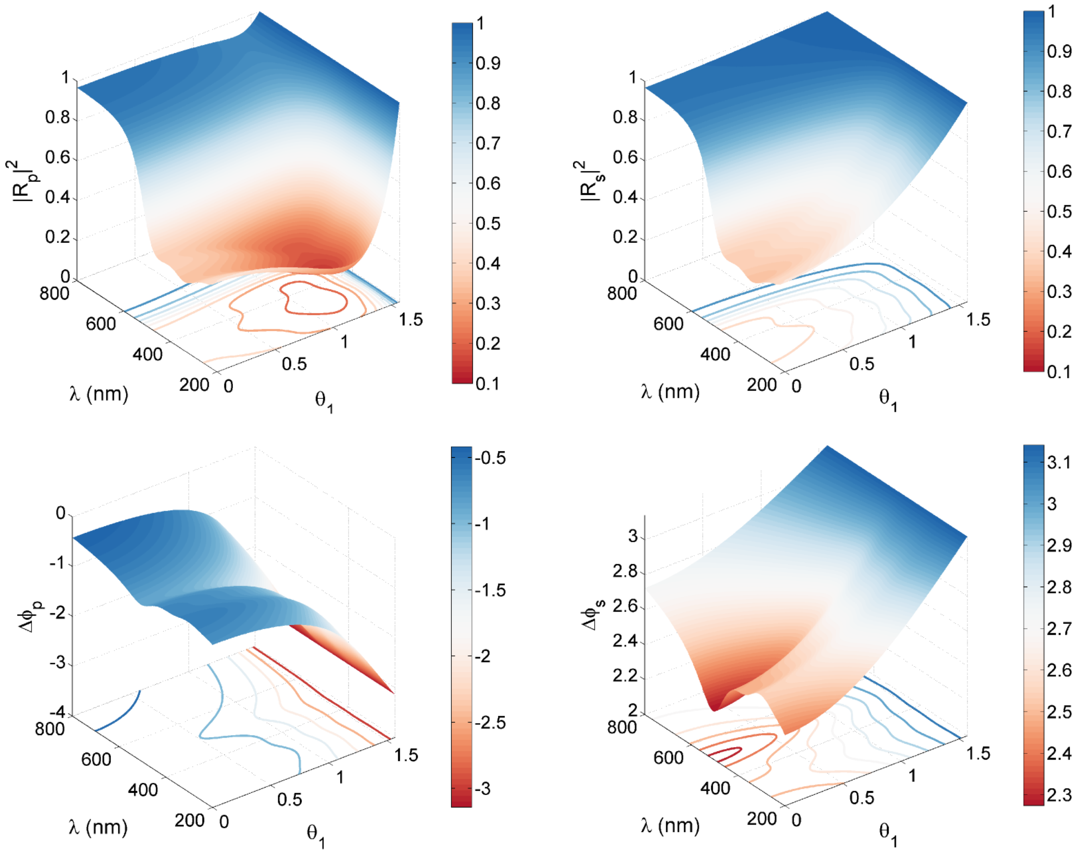

Figure 2.12: Surface plots and contours showing the reflectivity and phase shifts for p- and s- waves on a gold/air interface. For each wavelength, the reflectivity $|R_p|^2$ reaches a non-zero minimum at a certain incidence angle θ_i as can be seen from the top-left surface plot. The bottom two plots show the phase shift for p- and s-waves.

2.4 The Oscillating Dipole

Any change of charge or current distribution in space produces an EM radiation. The most fundamental source of an EM wave is an oscillating electric dipole. Almost all fluorescent organic dyes can be well described as ideal electric dipole oscillators. In this section we extensively study the behavior of an oscillating electric dipole in a homogeneous environment which will be vital for our further theoretical discussion and the work in this thesis.

2.4.1 Dipole in a Homogeneous Environment

Let us consider a dipole at position $\mathbf{r} = 0$ oriented along the z-axis with a distance d between its two equal but opposite charges ($+q$ and $-q$) that are oscillating around the center with a frequency ω. We first derive the field $\mathbf{E}(\mathbf{r})$ when the time is frozen, i.e. the positions of the two charges are fixed in space. The potential ψ at a position $\mathbf{r}$ away from the dipole can be written as:

$$\psi(r) = \frac{1}{\epsilon} q \left[\frac{1}{|\mathbf{r} - \mathbf{z}_+|} - \frac{1}{|\mathbf{r} - \mathbf{z}_-|} \right] = \frac{1}{\epsilon} q \left[\frac{|\mathbf{z}_- - \mathbf{z}_+| \cos\theta}{|\mathbf{r} - \mathbf{z}_+| \, |\mathbf{r} - \mathbf{z}_-|} \right] \tag{2.89}$$

where $\mathbf{z}_\pm$ are the positions of the point charges, and θ is the angle between the line joining position $\mathbf{r}$ to the position of the dipole and the axis of the dipole. When the point of interest is far away from the dipole ($r >> d$), the product $|\mathbf{r} - \mathbf{z}_+| \, |\mathbf{r} - \mathbf{z}_-|$ can be simply approximated as r^2. Therefore, the equation (2.89) can be written as:

$$\psi(r) = \frac{p \cos\theta}{\epsilon r^2} \tag{2.90}$$

$\mathbf{p}$ is the dipole moment defined as $\mathbf{p} = q\mathbf{d}$, where $\mathbf{d} = \mathbf{z}_- - \mathbf{z}_+$. The electric field $\mathbf{E}$ for the dipole can be calculated in the following way:

$$\mathbf{E}(\mathbf{r}) = -\boldsymbol{\nabla}\psi = -\left(\hat{\mathbf{r}} \frac{\partial}{\partial r} + \hat{\theta} \frac{1}{r} \frac{\partial}{\partial \theta} \right) \psi = \frac{2p\cos\theta}{\epsilon r^3} \hat{\mathbf{r}} + \frac{p \sin\theta}{\epsilon r^3} \hat{\theta} \tag{2.91}$$

Now $p\cos\theta$ can be written as $\hat{\mathbf{r}} \cdot \mathbf{p}$ and $p \sin\theta \hat{\theta}$ as $\hat{\mathbf{r}} \times (\hat{\mathbf{r}} \times \mathbf{p})$. Substituting these identities in the equation (2.91) gives us:

$$\mathbf{E}(\mathbf{r}) = \frac{2\hat{\mathbf{r}}(\hat{\mathbf{r}} \cdot \mathbf{p})}{\epsilon r^3} + \frac{\hat{\mathbf{r}} \times (\hat{\mathbf{r}} \times \mathbf{p})}{\epsilon r^3} = \frac{3\hat{\mathbf{r}}(\hat{\mathbf{r}} \cdot \mathbf{p}) - \mathbf{p}}{\epsilon r^3} \tag{2.92}$$

This represents the field of a static electric dipole and it is a stationary electric field where no propagating EM radiation is generated. The static field is present close to the dipole whose strength decays rapidly as a r^{-3} distance relationship form the center of the dipole. The time-averaged Poynting vector is proportional to r^{-6}. No energy is transported away from the dipole in this case because anything that falls of faster than r^{-2} cannot carry energy away.

EM waves are generated by non-stationary sources such as a non-uniformly moving point charge or an oscillating dipole. If we now want to calculate the EM radiation of an oscillating dipole, we need to take into account its temporal variation. Given non-zero $\rho(\mathbf{r}, t)$ and $\mathbf{j}(\mathbf{r}, t)$, which are now functions of time, it is not so straightforward to obtain unique solutions for the fields $\mathbf{E}(\mathbf{r}, t)$ and $\mathbf{B}(\mathbf{r}, t)$ from Maxwell's equations presented in section 2.2. Information travels with a finite speed and is delayed in time and in order to incorporate time-varying dipole moments, one needs to involve retarded potentials

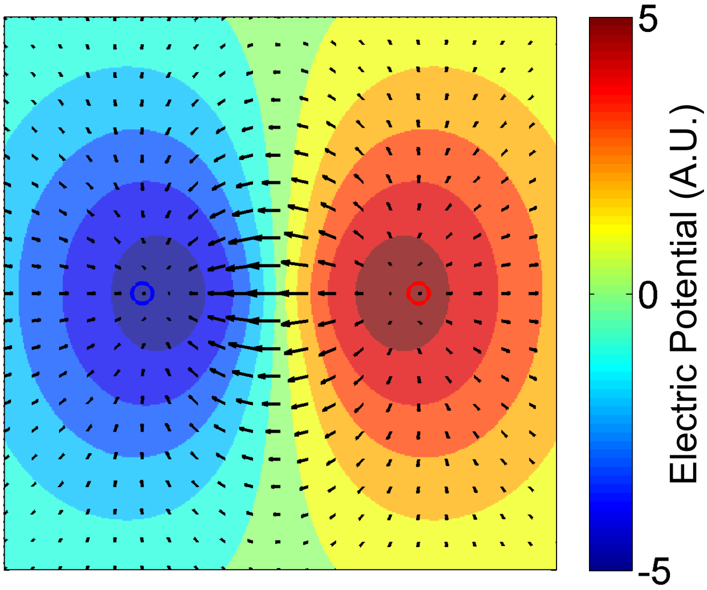

Figure 2.13: Contour plot of electrostatic potential of a static dipole oriented horizontally showing electric field lines. The red and blue circles represent the positions of positive and negative charges respectively. The arrows show the direction and magnitude of electric field lines.

with suitable gauge conditions. Here, we present an alternate way for obtaining the EM radiation which does not involve such a theoretical complexity.

Representing the time-variation of the oscillating dipole by the usual complex-valued notation $e^{-i\omega t}$ the positions of the two charges can be written as:

$$z_{\pm} = \pm\frac{d}{2}e^{-i\omega t} \tag{2.93}$$

and their respective velocities by:

$$v_{\pm} = \frac{dz_{\pm}}{dt} = \mp i\frac{d}{2}\omega e^{-i\omega t} \tag{2.94}$$

The current density, j is given by the sum of the product of charges with their respective velocities. Therefore,

$$j = -iqd\omega e^{-i\omega t} = -ip\omega e^{-i\omega t} \tag{2.95}$$

where $p = qd$ is the amplitude of the dipole moment. The dipole moment vector $\mathbf{p}$ is oriented along the direction from the negative to the positive charge. Therefore the vector $\mathbf{j}$ can be written as:

$$\mathbf{j} = -i\omega\mathbf{p}e^{-i\omega t}\delta(\mathbf{r}) \tag{2.96}$$

where,

$$\delta(\mathbf{r}) = \int \frac{\mathrm{d}^3k}{(2\pi)^3} e^{i\mathbf{k}\cdot\mathbf{r}} \tag{2.97}$$

is the Dirac delta function in three dimensions.

Let us now recall Maxwell's equations from section 2.2 and apply to our oscillating dipole system. $\mathbf{E}(\mathbf{r},t)$ can be written as $\mathbf{E}(\mathbf{r})e^{-i\omega t}$. Setting μ to unity (we consider non-magnetic materials in this thesis only), equation (2.37) and (2.36), using equation (2.96) can be written as:

$$\boldsymbol{\nabla}\times\mathbf{B} = \frac{4\pi}{c}\mathbf{j} + \frac{1}{c}\frac{\partial\mathbf{E}}{\partial t} = -4\pi i k_0\mathbf{p}\delta(\mathbf{r}) - ik_0\mathbf{E} \tag{2.98}$$

$$\boldsymbol{\nabla}\times\mathbf{E} = -\frac{1}{c}\frac{\partial\mathbf{B}}{\partial t} = ik_0\mathbf{B} \tag{2.99}$$

where we set $k_0 = \omega/c$. Using equations (2.98) and (2.99) we get:

$$\boldsymbol{\nabla}\times\boldsymbol{\nabla}\times\mathbf{E} = ik_0\boldsymbol{\nabla}\times\mathbf{B} = \epsilon k_0^2\mathbf{E} + 4\pi k_0^2\mathbf{p}\delta(\mathbf{r}) \tag{2.100}$$

Applying a spatial Fourier transform to the above equation, we get:

$$-\mathbf{k}\times\mathbf{k}\times\widetilde{\mathbf{E}} - \epsilon k_0^2\widetilde{\mathbf{E}} = (k^2-\epsilon k_0^2)\widetilde{\mathbf{E}} - \mathbf{k}(\mathbf{k}\cdot\widetilde{\mathbf{E}}) = 4\pi k_0^2\mathbf{p} \tag{2.101}$$

Multiplying both sides of equation (2.101) with $\mathbf{k}$, this simplifies to:

$$\mathbf{k}\cdot\widetilde{\mathbf{E}} = -\frac{4\pi}{\epsilon}\mathbf{k}\cdot\mathbf{p} \tag{2.102}$$

Substituting equation (2.102) back in (2.101) we obtain

$$\widetilde{\mathbf{E}} = \frac{4\pi}{\epsilon(k^2-\epsilon k_0^2)}\left[\epsilon k_0^2\mathbf{p} - \mathbf{k}(\mathbf{k}\cdot\mathbf{p})\right] \tag{2.103}$$

Passing back to real space from Fourier space, $\mathbf{E}(\mathbf{r})$ can be obtained using:

$$\mathbf{E}(\mathbf{r}) = \int \frac{\mathrm{d}^3k}{(2\pi)^3}\widetilde{\mathbf{E}}(\mathbf{k})e^{i\mathbf{k}\cdot\mathbf{r}}$$

Using equation (2.103) we get:

$$\mathbf{E}(\mathbf{r}) = \frac{4\pi}{\epsilon}\int \frac{\mathrm{d}^3k}{(2\pi)^3}\frac{\epsilon k_0^2\mathbf{p} - \mathbf{k}\,(\mathbf{k}\cdot\mathbf{p})}{(k^2-\epsilon k_0^2)}e^{i\mathbf{k}\cdot\mathbf{r}} \tag{2.104}$$

Now, one can observe that

$$\boldsymbol{\nabla}\cdot\left(\mathbf{p}e^{i\mathbf{k}\cdot\mathbf{r}}\right)=i(\mathbf{k}\cdot\mathbf{p})e^{i\mathbf{k}\cdot\mathbf{r}}$$

and therefore,

$$\boldsymbol{\nabla}\left(\boldsymbol{\nabla}\cdot(\mathbf{p}e^{i\mathbf{k}\cdot\mathbf{r}})\right)=-\mathbf{k}(\mathbf{k}\cdot\mathbf{p})e^{i\mathbf{k}\cdot\mathbf{r}} \tag{2.105}$$

Using the last relationship, one can write the electric field $\mathbf{E}(\mathbf{r})$ as:

$$\mathbf{E}(\mathbf{r})=\frac{1}{2\pi^2\epsilon}\left(\epsilon k_0^2+\boldsymbol{\nabla}\left(\boldsymbol{\nabla}\cdot\right)\right)\left[\mathbf{p}\int\frac{e^{i\mathbf{k}\cdot\mathbf{r}}}{k^2-\epsilon k_0^2}\mathrm{d}^3k\right] \tag{2.106}$$

The integral on the right hand side can be simplified by switching into spherical coordinate system such that the vector $\mathbf{r}$ is along the polar axis and the dipole oriented at an angle α to this direction. Thus, $\mathbf{k}$ can be written as:

$$\mathbf{k}=k\left(\sin\theta\cos\phi,\sin\theta\sin\phi,\cos\theta\right)$$

$$\therefore\mathbf{k}\cdot\mathbf{r}=kr\cos\theta$$

Using this, the integral can be treated as:

$$\begin{aligned}\int\frac{e^{i\mathbf{k}\cdot\mathbf{r}}}{k^2-\epsilon k_0^2}\mathrm{d}^3k&=\int_0^\infty\mathrm{d}k\,k^2\int_0^\pi\mathrm{d}\theta\,\sin\theta\int_0^{2\pi}\mathrm{d}\phi\,\frac{e^{ikr\cos\theta}}{k^2-\epsilon k_0^2}\\&=2\pi\int_0^\infty\mathrm{d}k\,k^2\int_0^\pi\mathrm{d}\theta\,\sin\theta\,\frac{e^{ikr\cos\theta}}{k^2-\epsilon k_0^2}\end{aligned}$$

by making the substitution $\zeta=\cos\theta$ in the second integral, we get

$$\begin{aligned}\int\frac{e^{i\mathbf{k}\cdot\mathbf{r}}}{k^2-\epsilon k_0^2}\mathrm{d}^3k&=2\pi\int_0^\infty\mathrm{d}k\,k^2\frac{1}{ikr}\frac{e^{ikr}-e^{-ikr}}{k^2-\epsilon k_0^2}\\&=\frac{2\pi}{ir}\int_0^\infty\mathrm{d}k\,k\frac{e^{ikr}-e^{-ikr}}{k^2-\epsilon k_0^2}\\&=\frac{2\pi}{ir}\left[\int_0^\infty\mathrm{d}k\,k\frac{e^{ikr}}{k^2-\epsilon k_0^2}-\int_0^\infty\mathrm{d}k\,k\frac{e^{-ikr}}{k^2-\epsilon k_0^2}\right]\end{aligned}$$

Substituting in the second integral $-k$ with k, we finally get

$$\int\frac{e^{i\mathbf{k}\cdot\mathbf{r}}}{k^2-\epsilon k_0^2}\mathrm{d}^3k=\frac{2\pi}{ir}\int_{-\infty}^\infty\mathrm{d}k\,k\frac{e^{ikr}}{k^2-\epsilon k_0^2} \tag{2.107}$$

The right hand side of equation (2.107) represents an integral over complex plane with two singularities $k = \pm\sqrt{\epsilon}k_0$. Using Cauchy's residue theorem[3], we select a contour which includes only the outgoing waves from the dipole, which are physically reasonable. i.e. the pole at $k = +\sqrt{\epsilon}k_0$, as shown in figure 2.14. Since r is always positive, we take the positive imaginary values for k so that $e^{ikr} \to 0$ when $|\mathrm{Im}(k)| \to \infty$.

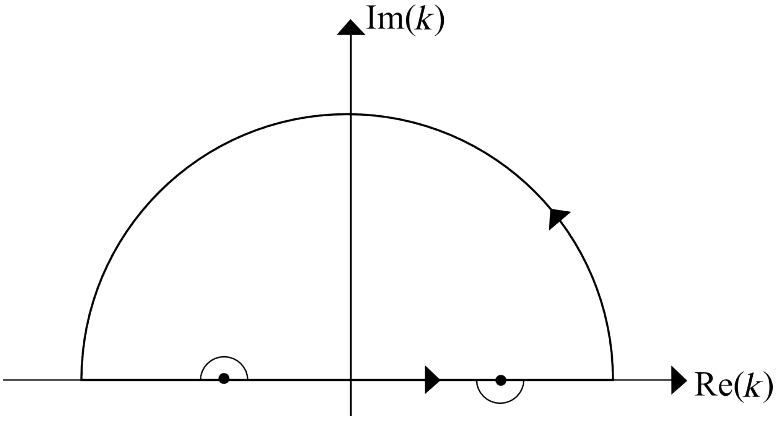

Figure 2.14: Closed contour showing the inclusion of the pole at $+\sqrt{\epsilon}k_0$ for our integration.

$$\frac{2\pi}{ir}\int_{-\infty}^{\infty}\mathrm{d}k\,k\frac{e^{ikr}}{k^2-\epsilon k_0^2} = \frac{2\pi}{ir}\oint_{\Gamma}\mathrm{d}k\,k\frac{e^{i\sqrt{\epsilon}k_0 r}}{k^2-\epsilon k_0^2} \tag{2.108}$$

$$= 2\pi^2\frac{e^{ikr}}{r} \tag{2.109}$$

Putting equation (2.109) in (2.106) we obtain the expression:

$$\mathbf{E}(\mathbf{r}) = \frac{1}{\epsilon}\left(k^2 + \boldsymbol{\nabla}\left(\boldsymbol{\nabla}\cdot\right)\right)\left[\mathbf{p}\frac{e^{ikr}}{r}\right] \tag{2.110}$$

where we used $k = \sqrt{\epsilon}k_0$. When explicitly performing the differential operations on the r.h.s., one obtains

$$\begin{aligned}\boldsymbol{\nabla}\left(\boldsymbol{\nabla}\cdot\right)\left[\mathbf{p}\frac{e^{ikr}}{r}\right] &= \boldsymbol{\nabla}\left[\left(\frac{ik}{r}-\frac{1}{r^2}\right)(p\cos\alpha)\,e^{ikr}\right]\\ = \Bigg[\left(-\frac{k^2}{r}-\frac{2ik}{r^2}+\frac{2}{r^3}\right)(p\cos\alpha)\,\hat{\mathbf{r}} &- \frac{1}{r}(p\sin\alpha)\,\hat{\boldsymbol{\theta}}\left(\frac{ik}{r}-\frac{1}{r^2}\right)\Bigg]e^{ikr}\\ = \Bigg[\left(-\frac{k^2}{r}-\frac{2ik}{r^2}+\frac{2}{r^3}\right)(\mathbf{p}\cdot\hat{\mathbf{r}})\,\hat{\mathbf{r}} &- \frac{1}{r}\hat{\mathbf{r}}\times(\hat{\mathbf{r}}\times\mathbf{p})\left(\frac{ik}{r}-\frac{1}{r^2}\right)\Bigg]e^{ikr}\end{aligned}$$

Finally, using the expansion $\hat{\mathbf{r}}\times(\hat{\mathbf{r}}\times\mathbf{p}) = \hat{\mathbf{r}}(\hat{\mathbf{r}}\cdot\mathbf{p}) - \mathbf{p}$ rearranging the terms, we find

---

[3] If $f(z)$ has singularities at N points in space, then

$$\frac{1}{2\pi i}\oint_C f(z)\mathrm{d}z = \sum_{n=1}^{N}\mathrm{Res}(f, z_n)$$

. Refer to "Complex Analysis" by Ahlfors [109].

the electric field $\mathbf{E}(\mathbf{r}, t)$ of the dipole:

$$\mathbf{E}(\mathbf{r}, t) = \left\{ \frac{k^2}{r} [\mathbf{p} - \hat{\mathbf{r}}(\hat{\mathbf{r}} \cdot \mathbf{p})] + \left(\frac{ik}{r^2} - \frac{1}{r^3} \right) [\mathbf{p} - 3\hat{\mathbf{r}}(\hat{\mathbf{r}} \cdot \mathbf{p})] \right\} e^{ikr - i\omega t} \tag{2.111}$$

The equation (2.111) represents the complete electric field of an oscillating electric dipole. As one can see, if we set $k = 0$, it reduces to the electric field of a static dipole (2.92). This is where the velocity of light $c = 1/\sqrt{\epsilon}$ comes into the picture. If one takes $c = \infty$, $k = 0$ and the solution to the potential is an instantaneously varying static field governed by the dipole moment $\mathbf{p}$ at any time t.

The terms scaling with r^{-2} and r^{-3} constitute the near-field of the dipole which plays a major role when considering its interactions with another oscillating dipole in its vicinity or in an inhomogeneous environment such as close to a surface or inside a nanocavity. The part of the field scaling with r^{-1} is the far-field component which contributes to the transport of radiation energy away from the dipole. The magnitude of the electric field depends on the length of the vector $[\mathbf{p} - \hat{\mathbf{r}}(\hat{\mathbf{r}} \cdot \mathbf{p})]$ which can be written as $p \sin \alpha$ where, α is the angle between $\mathbf{p}$ and the vector towards the point of interest $\mathbf{r}$ as shown in figure 2.15. It also scales as the inverse of the distance r. The direction of the field points towards the vector $\hat{\mathbf{r}} \times (\hat{\mathbf{p}} \times \hat{\mathbf{r}})$ which is perpendicular to $\mathbf{r}$ in the plane containing both the vectors $\mathbf{r}$ and $\mathbf{p}$. Thus, the amplitude of the electric field $|\mathbf{E}(\hat{\mathbf{p}})|$ along the direction of the dipole moment is zero at all times. Figure 2.16 shows the magnitude of the electric field in the plane of a dipole at a fixed time. The waves are propagating radially away from the center of the dipole with the electric field vector $\mathbf{E}(\mathbf{r})$ pointing in the direction perpendicular to the position vector $\mathbf{r}$ at each point. The magnetic field can be derived by taking the curl of the electric field in equation (2.110)

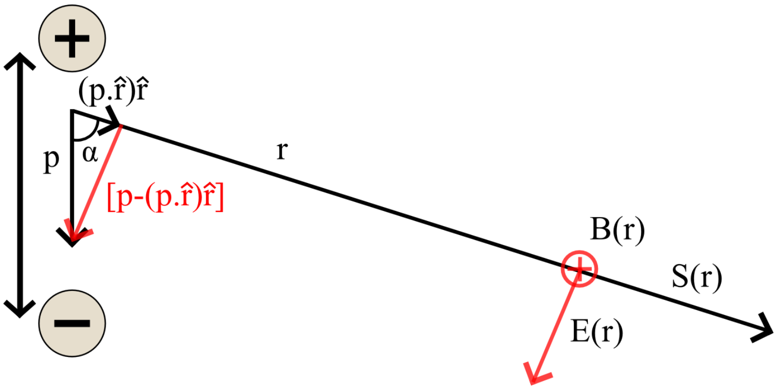

Figure 2.15: A schematic showing the orientations of the dipole moment vector $\mathbf{p}$, and its projection along the line of sight $\mathbf{r}$. The vector shown in red represents the direction and the magnitude of the electric field vector $\mathbf{E}(\mathbf{r})$. The magnetic field $\mathbf{B}(\mathbf{r})$ points into the plane of the paper as shown. The Poynting vector $\mathbf{S}(\mathbf{r})$ always points in the direction of $\hat{\mathbf{r}}$.

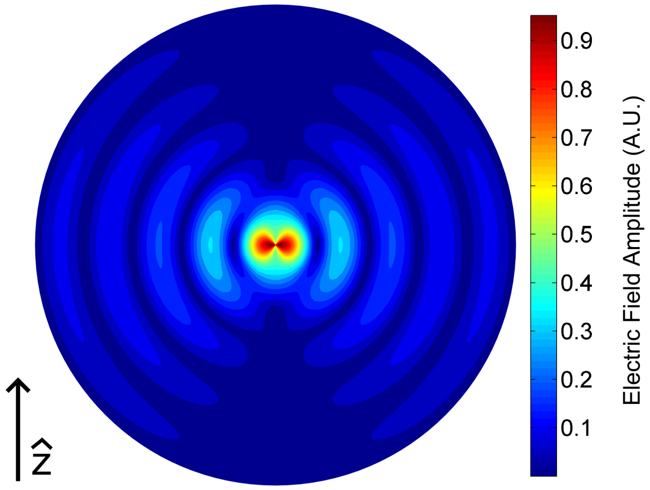

Figure 2.16: Contour plot showing the magnitude of the far-field component of an oscillating dipole's electric field which is oriented along $\hat{\mathbf{z}}$. The radius of the image is $\approx 2.5\lambda$

as follows:

$$\mathbf{B}(\mathbf{r}) = \frac{c}{i\omega}\boldsymbol{\nabla}\times\mathbf{E}(\mathbf{r}) = \frac{1}{ik_0}\boldsymbol{\nabla}\times\left[\frac{1}{\epsilon}\left(k^2+\boldsymbol{\nabla}\left(\boldsymbol{\nabla}\cdot\right)\right)\left[\mathbf{p}\frac{e^{ikr}}{r}\right]\right]$$

Since $\boldsymbol{\nabla}\times(\boldsymbol{\nabla}a)$, where a is a scalar field, is always zero, the above equation reduces to

$$\mathbf{B}(\mathbf{r}) = \frac{k^2}{ik_0\epsilon}\boldsymbol{\nabla}\times\left[\mathbf{p}\frac{e^{ikr}}{r}\right]. \tag{2.112}$$

Assuming again that the dipole is along the $\hat{\mathbf{z}}$, this brings us to the expression

$$\mathbf{B}(\mathbf{r},t) = \frac{\hat{\mathbf{r}}\times\mathbf{p}}{n_{\mathrm{med}}}\left(\frac{k^2}{r}+\frac{ik}{r^2}\right)e^{ikr-i\omega t} \tag{2.113}$$

Note that here we used the relations $k = k_0\sqrt{\epsilon}$ and $\sqrt{\epsilon} = n_{\mathrm{med}}$. The magnetic field lines can be drawn as concentric circles around the dipole vector $\mathbf{p}$ where the magnitude at point $\mathbf{r}$ is $\sim p\sin\alpha/r$ pointing normal to the plane containing $\mathbf{r}$ and $\mathbf{p}$. This result is also consistent to the fact that the field $\mathbf{B}$ is always perpendicular to the motion of charges or current direction. Thus the magnetic field does not perform any work on the oscillating dipole.

So far, we derived the complete radiation field of an oscillating dipole in a classical framework. Next we are interested in the angular distribution of the energy radiated away from the dipole, which we will consider in the following section.

Angular Radiation Distribution of an Oscillating Dipole

The magnitude of the Poynting vector $|\mathbf{S}|$ is proportional to $n_{\mathrm{med}}\,|\mathbf{E}|^2$ and it points along the propagation direction $\hat{\mathbf{k}}$. Before we calculate the average power radiated by an oscillating dipole, it is important to mention that the fast decaying near-field components which scale with the distance as r^{-2} and r^{-3} do not contribute in the transport of energy away from the dipole, since the surface integrals of these components over a sphere of say radius r yield a net flux proportional to r^{-2} and r^{-4} respectively which vanish for large values of r ($r \ll \lambda$). Thus these near-field components are also termed the non-propagating components which can be neglected in the current section where we consider dipole oscillating in a homogeneous space. However, these near-field terms play a key role when studying dipole-dipole interactions and resonance energy transfer (such as FRET), or when considering dipoles situated close to an interface separating a dielectric or conducting medium. We shall study the latter situations closely in the forthcoming sections which will complete our theoretical foundation for Metal-Induced Energy Transfer (MIET). For now, we can approximate the electric and magnetic fields around an oscillating dipole as

$$\mathbf{E}(\mathbf{r}) \sim k^2 \left[\mathbf{p} - \hat{\mathbf{r}}(\hat{\mathbf{r}} \cdot \mathbf{p})\right] \frac{e^{ikr}}{r} \quad \text{and} \tag{2.114}$$

$$\mathbf{B}(\mathbf{r}) \sim k^2 \left[\hat{\mathbf{r}} \times \mathbf{p}\right] \frac{e^{ikr}}{r n_{\text{med}}} \tag{2.115}$$

Therefore the far-field Poynting vector is given by:

$$\mathbf{S}(\mathbf{r}) \sim \frac{ck^4}{8\pi r^2 n_{\text{med}}} \hat{\mathbf{r}} \left[p^2 - (\hat{\mathbf{r}} \cdot \mathbf{p})^2\right] \tag{2.116}$$

$$= \frac{ck^4 p^2 \sin^2\theta}{8\pi r^2 n_{\text{med}}} \hat{\mathbf{r}} \tag{2.117}$$

Thus $\mathbf{S}(\mathbf{r})$ points away from the dipole's position and towards the point of interest. The magnitude of the flux density declines as the inverse of the square of the distance from the dipole. The total power radiated from an oscillating dipole is obtained by integrating the radial component of the Poynting vector over the sphere with radius r, and since the vector $\mathbf{S}$ is always normal to the surface, we have

$$S = \int_0^{\pi} \mathrm{d}\alpha \, \sin\alpha \int_0^{2\pi} \mathrm{d}\phi \, r^2 \frac{ck^4 p^2 \sin^2\alpha}{8\pi r^2 n_{\text{med}}} = \frac{1}{3n_{\text{med}}} ck^4 p^2. \tag{2.118}$$

Replacing k by $\sqrt{\epsilon} k_0$, we have

$$S = \frac{1}{3} c n_{\text{med}} k_0^4 p^2. \tag{2.119}$$

The angular distribution of the power per solid angle $\mathrm{d}\Omega$ is given by:

$$\frac{r^2 \mathrm{dS}}{\sin\alpha \mathrm{d}\alpha \mathrm{d}\phi} = \frac{c n_{\text{med}} k_0^4 p^2}{8\pi} \sin^2\alpha \tag{2.120}$$

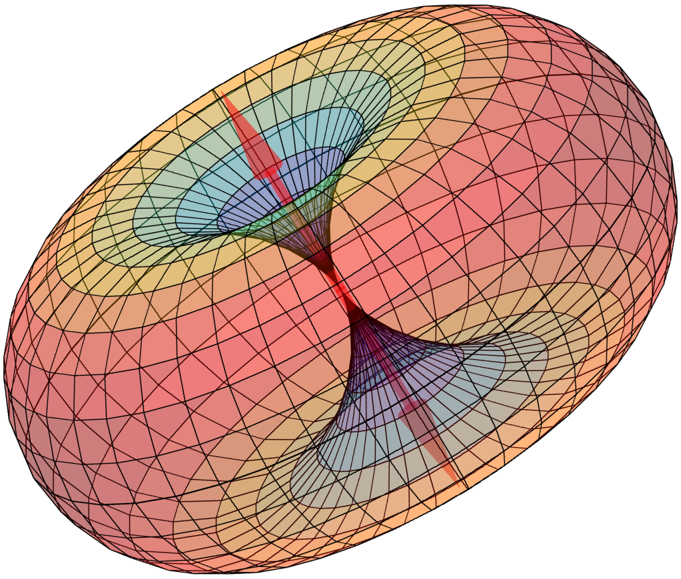

Figure 2.17: The angular distribution of radiation from a dipole which is oscillating along the double arrow in the center. The distance of the surface from the center represents the probability of obtaining an emitted photon when the dipole is repeatedly excited. It follows the $\sin^2\alpha$ law, where α is the angle measured from the dipole moment vector $\mathbf{p}$.

which directly gives the $\sin^2\alpha$ dependence of the radiation power from the dipole, where α is measured from the dipole's axis. Thus, the angular distribution looks like a torus with its axis along the dipole moment vector $\mathbf{p}$. This is shown in figure 2.17.

The total power radiated by the dipole can also be calculated using the integral over the normal component of the time-averaged Poynting vector through a surface enclosing the source

$$S = \oiint (\langle \mathbf{S} \rangle \cdot \hat{\mathbf{n}}) \mathrm{d}A \tag{2.121}$$

Using the Divergence theorem[4], this can be written as:

$$\begin{aligned} S &= \int_V \langle \boldsymbol{\nabla} \cdot \mathbf{S} \rangle \,\mathrm{d}V = \frac{c}{4\pi} \int_V \langle \boldsymbol{\nabla} \cdot (\mathbf{E} \times \mathbf{B}) \rangle \,\mathrm{d}V \\ &= \frac{c}{4\pi} \int_V \langle [(\boldsymbol{\nabla} \times \mathbf{E}) \cdot \mathbf{B} - \mathbf{E} \cdot (\boldsymbol{\nabla} \times \mathbf{B})] \rangle \,\mathrm{d}V \end{aligned}$$

Plugging in Maxwell's equations and taking the time average, this yields:

$$S = -\frac{1}{2} \mathrm{Re} \left(\int_V \mathbf{E} \cdot \mathbf{j}^* \mathrm{d}V \right) \tag{2.122}$$

where $\mathbf{j}$ is the current density in the source. Thus, the radiation power is equal to the negative work done per unit of time by the field acting on the source. Using the current

---

[4] If $\mathbf{F}$ is a continuously differentiable vector over a volume V and its neighborhood, then $\int_v (\boldsymbol{\nabla} \cdot \mathbf{F}) \mathrm{d}V = \oiint_A (\mathbf{F} \cdot \mathrm{d}\mathbf{A})$, where the vector element $\mathrm{d}\mathbf{A}$ points normal at each point to the surface of the volume V. For derivation, refer to [110]

density for the oscillating dipole given by the equation (2.96), the total power can be written as:

$$S = \frac{1}{2}\omega\mathbf{p}\cdot\mathrm{Im}\left(\mathbf{E}\right) \tag{2.123}$$

From a physics point of view, the above equation translates into the fact that the power radiated by an electric dipole is proportional to that component of the electric field which is along the direction of the dipole's axis and which is by $\pi/2$ out of phase with respect to the oscillation of the dipole moment.

The most important point to note from the equation (2.119) is the $k^4 \sim \lambda^{-4}$ dependence of the radiation power. The same law holds true for Rayleigh scattering theory of light, such as on density variations, which are smaller in size than the wavelength of the EM radiation scattered by them. Rayleigh scattering results from the electric polarization of the gas molecules due to their interaction with the radiation causing them to behave as oscillating dipoles. Thus, the above theory can be also applied to calculate the field around scattering particles. As shown in the above relation, the scattering cross section increases inversely proportional to the fourth power of the wavelength, and therefore the sky appears blue in color. Another interesting observation is the direct dependence of the radiation power on the refractive index of the medium. A dipole radiates more energy per unit of time if it is situated inside a medium of higher refractive index such as glass ($n = 1.5$) or water ($n = 1.33$). In a quantum mechanical picture, this translates to the fact that the excited molecules return faster from their excited state to the ground state when placed in such media. In other words, the average lifetime of the excited state τ_f is shorter in water or glass as compared to air. The purely radiative decay rate, or spontaneous emission rate of a classical dipole oscillator is given by the ratio of the average radiation power of the dipole and its total initial energy. Assuming no damping in the oscillations, which will be considered in a later section, the spring constant is given by $k = \omega^2 m$, where m is the effective mass of the dipole and ω is the angular frequency of the oscillating spring system. If x_0 is the initial oscillation amplitude, the initial energy of the oscillation system is given by

$$U_0 = \frac{1}{2}kx_0^2 = \frac{1}{2}m\omega^2\frac{p_0^2}{q^2}. \tag{2.124}$$

The radiation power is the rate of change of this initial energy which is given by equation (2.119).

$$\therefore \frac{\mathrm{d}U}{U_0} = -\frac{2}{3}\frac{q^2\omega^2 n_{\mathrm{med}}}{mc^3}\mathrm{d}t \tag{2.125}$$

which gives us the radiative rate κ_0 of the dipole.

$$\kappa_0 = \frac{2}{3}\frac{q^2\omega^2 n_{\text{med}}}{mc^3} \tag{2.126}$$

which is the inverse excited state lifetime (if there are no other de-excitation channels).

In the next section, we will study the behavior of a dipole emitter situated close to an interface separating two such dielectric media.

2.4.2 Dipole on a Planar Dielectric Interface

So far, we studied the properties of a dipole oscillating in a homogeneous environment. For our discussion in this section, let us consider a dipole situated on top of an interface separating the upper media (z < 0) with dielectric constant ϵ_1 and a lower medium (z > 0) with dielectric constant ϵ_2. Let the dipole moment vector be $\mathbf{p}$ at position $\mathbf{r}_0$. Let us further consider that $\mathbf{r_0}$ is a point in the medium 1, $z_0 < 0$. First, we write down the plane wave representation of the dipole's field in a homogeneous space with a dielectric constant ϵ_1 using (2.104).

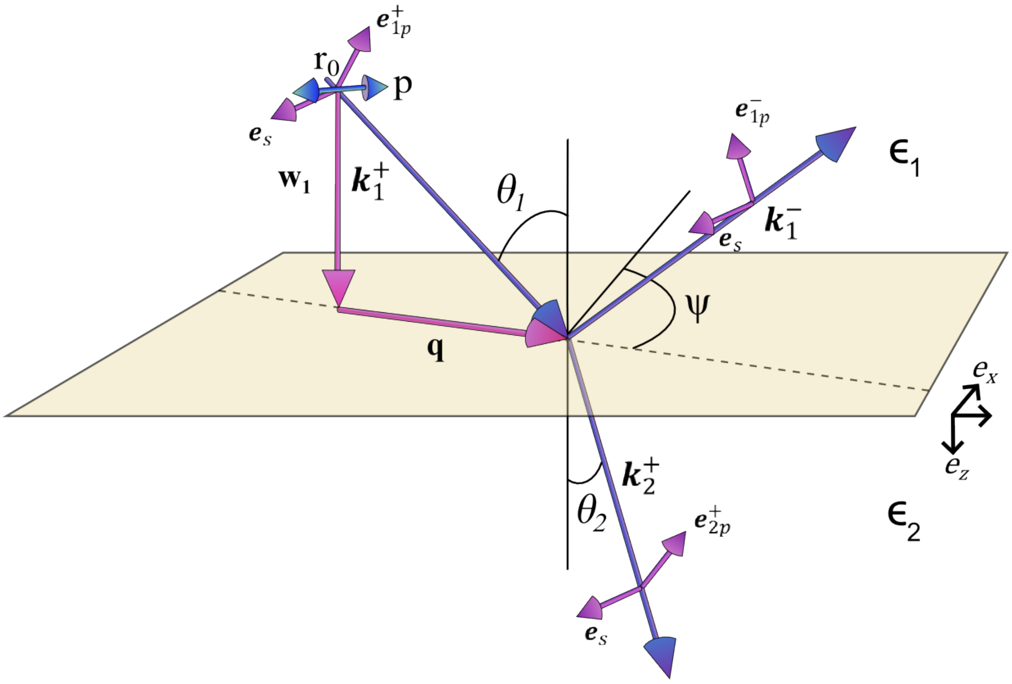

Figure 2.18: The general geometry of the vectors considered in this section. The interface separates two media ϵ_1 and ϵ_2 as shown. The unit vectors $\hat{\mathbf{e}}_{ip}^{\pm}$ represent the directions of electric field vectors in the plane of incidence, whereas the unit vectors $\hat{\mathbf{e}}_s$ point in the direction perpendicular to the plane of incidence. θ_1 and θ_2 are the angles of the vectors $\mathbf{k}_1^+$ and $\mathbf{k}_2^+$ with respect to the normal of the interface, and ψ is the angle the plane of incidence makes with respect to a fixed x-axis. $\mathbf{r}_0$ marks the position of the dipole $\mathbf{p}$. Note that $\mathbf{p}$ is doubly degenerate, and hence we show using a double arrow.

$$\mathbf{E}(\mathbf{r}) = \frac{4\pi}{\epsilon_1}\int \frac{\mathrm{d}^3k}{(2\pi)^3}\frac{\epsilon_1 k_0^2\mathbf{p} - \mathbf{k}(\mathbf{k}\cdot\mathbf{p})}{(k^2 - \epsilon_1 k_0^2)}e^{i\mathbf{k}\cdot\mathbf{R}} \tag{2.127}$$

where $\mathbf{R} = \mathbf{r} - \mathbf{r_0}$. Let us denote, as before, by $\mathbf{q}$ and w the horizontal (parallel to the interface) and vertical (orthogonal to interface) components of the wave vector $\mathbf{k}$. Performing in the above plane wave representation the integration over w and applying Cauchy's residue theorem leads to the so-called Weyl representation of the electric field of an oscillating dipole in homogeneous space,

$$\mathbf{E}(\mathbf{r}) = \frac{i}{2\pi\epsilon_1}\int \mathrm{d}^2\mathbf{q}\frac{\left[k_1^2\mathbf{p} - \mathbf{k}_1^{\pm}(\mathbf{k}_1^{\pm}\cdot\mathbf{p})\right]}{w_1}e^{i[\mathbf{q}\cdot(\boldsymbol{\rho}-\boldsymbol{\rho}_\mathbf{0})-w_1|z-z_0|]} \tag{2.128}$$

where $\mathbf{k}_j^{\pm} = \{\mathbf{q}, \pm w_j\}$ and $w_1(q) = \sqrt{k_1^2 - q^2}$ with $\mathbf{k_1} = \sqrt{\epsilon_1}\mathbf{k_0}$, and $\mathbf{k_1}^{+}$ applies for $z > z_0$ and $\mathbf{k_1}^{-}$ applies for $z < z_0$. When applying Cauchy's residue theorem, we have taken into account only the pole $w_1 = +\sqrt{k_1^2 - q^2}$ with positive real or positive imaginary value so that the Weyl representation integrates only over outgoing (or with distance exponentially decaying) plane waves, but not incoming or exponentially increasing plane waves.

The vector $k_1^2\mathbf{p} - \mathbf{k}_1^{\pm}(\mathbf{k}_1^{\pm}\cdot\mathbf{p})$ is a projection of $\mathbf{p}$ perpendicular to the direction of $\mathbf{k}_1^{\pm}$, and can thus be expanded into a system of two orthogonal unit vectors which are both orthogonal to $\mathbf{k}_1^{\pm}$, in particular

$$\hat{\mathbf{e}}_{1p}^{\pm} = \frac{1}{k_1}\left(\frac{\pm w_1 q_x}{q}, \frac{\pm w_1 q_y}{q}, -q\right)$$

and

$$\hat{\mathbf{e}}_s = \frac{1}{q}(-q_y, q_x, 0)$$

Both these vectors are indeed perpendicular to $\mathbf{k}_1^{\pm} = \{q_x, q_y, \pm w_1\}$, whereas $\hat{\mathbf{e}}_{1p}^{\pm}$ lies within the plane which is spanned by $\mathbf{k}_1^{\pm}$ and the normal to the interface (p-wave), and $\hat{\mathbf{e}}_s$ lies parallel to the interface (s-wave). Thus, the Weyl representation can be rewritten as

$$\mathbf{E}(\mathbf{r}) = \frac{ik_0^2}{2\pi}\iint\frac{\mathrm{d}\mathbf{q}}{w_1}\left[\hat{\mathbf{e}}_{1p}^{\pm}(\hat{\mathbf{e}}_{1p}^{\pm}\cdot\mathbf{p}) + \hat{\mathbf{e}}_s(\hat{\mathbf{e}}_s\cdot\mathbf{p})\right]e^{i[\mathbf{q}\cdot(\boldsymbol{\rho}-\boldsymbol{\rho}_\mathbf{0})+w_1|z-z_0|]} \tag{2.129}$$

Now it is obvious that the Weyl representation (2.129) is an expansion of the dipole's electric field over plane p- and s-waves. If w_1 is imaginary, they are which decay exponentially with distance away from the plane of the dipole ($z = z_0$). In order to calculate the complete field, one now needs to calculate the fields reflected by and transmitted through the interface, which can be done in a straightforward way by using Fresnel's relations that we had derived in section 2.3. These fields are given by

$$\mathbf{E}_R(\mathbf{r}) = \frac{ik_0^2}{2\pi} \iint \frac{\mathrm{d}\mathbf{q}}{w_1} \left[\hat{\mathbf{e}}_{1p}^{-} R_p (\hat{\mathbf{e}}_{1p}^{+} \cdot \mathbf{p}) + \hat{\mathbf{e}}_s R_s (\hat{\mathbf{e}}_s \cdot \mathbf{p})\right] e^{i[\mathbf{q}\cdot(\boldsymbol{\rho}-\boldsymbol{\rho}_0)+w_1|z_0|-w_1 z]}, \tag{2.130}$$

and

$$\mathbf{E}_T(\mathbf{r}) = \frac{ik_0^2}{2\pi} \iint \frac{\mathrm{d}\mathbf{q}}{w_1} \left[\hat{\mathbf{e}}_{2p}^{+} T_p (\hat{\mathbf{e}}_{1p}^{+} \cdot \mathbf{p}) + \hat{\mathbf{e}}_s T_s (\hat{\mathbf{e}}_s \cdot \mathbf{p})\right] e^{i[\mathbf{q}\cdot(\boldsymbol{\rho}-\boldsymbol{\rho}_0)+w_1|z_0|+w_2 z]}. \tag{2.131}$$

where we have introduced also the unit vector

$$\hat{\mathbf{e}}_{2p}^{+} = \frac{1}{k_2} \left(\frac{w_2 q_x}{q}, \frac{w_2 q_y}{q}, -q \right)$$

which is perpendicular to $\mathbf{k}_2^{+} = \{q_x, q_y, w_2\}$ with $w_2(q) = \sqrt{k_2^2 - q^2}$, and $R_{p,s}$ and $T_{p,s}$ are Fresnel's q-dependent reflection and transmission coefficients for plane p- and s-waves, respectively. Here, equation (2.130) is the reflected field ($z < 0$), and (2.131) is the transmitted field ($z > 0$). The term $e^{iw_1|z_0|}$ in both the reflected and transmitted fields takes into account the additional phase shift due to the plane wave propagation form the dipole's position to the interface. Two important points can be read off from equation 2.131:

1. The magnitude of the transmitted and reflected electric field depends on the orientation of the dipole vector $\mathbf{p}$ with respect to the plane of incidence. This is taken care of by the scalar products $\hat{\mathbf{e}}_{jp}^{\pm} \cdot \mathbf{p}$ and $\hat{\mathbf{e}}_s \cdot \mathbf{p}$.

2. The magnitudes of these electric fields clearly depend on the reflection and transmission coefficients $T_{p,s}$ and $R_{p,s}$, which are themselves functions of the angle of incidence and thus q of the plane waves with respect to the interface.

Let us now examine two important particular cases. In the first case, when $n_1 < n_2$ i.e., the dipole is in an optically rarer medium, such as water, on top of an optically denser medium, such as glass. In this case, all propagating waves in medium 1 are also propagating in medium 2 (since $w_2 = \sqrt{k_2^2 - k_1^2 + w_1^2}$ which is always real for $w_1 \leqslant k_1$ and $k_2 > k_1$). However, the amplitude of vector $\mathbf{q}$ can be larger than k_1 (it actually can go up to infinity). Thus, for the range of q-values with $k_1 < q \leq k_2$, one has non-propagating and exponentially decaying plane waves in medium 1 ($iw_1|z_0|$ is real and negative), which, however, become propagating in medium 2, contributing to the far field radiation in the lower half-space. This is similar to frustrated internal reflection which we studied before. We had seen that this process results in an energy reduction of the reflected plane (as compared to TIR) and a partial energy transfer to the denser medium beneath the thin layer. In the situation here, one can visualize this as a dipole losing more energy per time than one within a homogeneous medium 1 without any interface (energy tunneling into denser medium). This leads to an increase in total radiated power S and, as a resulting, to an decrease of the excited state lifetime τ_f. Finally, for values of q larger than k_2, all plane waves are exponentially decaying, and they do not contribute to any far-field energy propagation. The second case is the opposite, when the dipole is located in the optically denser medium ($n_1 > n_2$). In this case, there exist propagating plane waves in medium 1 which cannot propagate in medium 2 (for $k_2 < q \leq k_1$). For these values of q, the absolute values of the reflection coefficients R_p and R_s are equal to one, and depending upon the distance of the emitter from the surface, constructive or destructive interference with the directly emitted plane wave along $\mathbf{k}_1^-$ takes place in medium 1. In medium 2, these plane waves are evanescent and exponentially decay with distance z.

Angular Distribution of Radiation of a Dipole Near a Dielectric Interface

In the upper half-space (medium 1), the angular distribution of radiation can be calculated from the time-averaged Poynting vector ($\mathbf{S}(\mathbf{r}) \propto |\mathbf{E}|^2$) using the dipole's direct field together with the reflected field along direction $\mathbf{k}_1^-$. Using the electric fields from equations (2.129) and (2.130), we find that the energy flux radiated into a solid angle element $d\Omega^2 = (q/w_1k_1)\mathrm{d}q\mathrm{d}\psi$ into the upper half-space ($z < 0$) along direction $(\mathbf{q}, w_1)$ is proportional to

$$\frac{\mathrm{d}^2 S_u}{\mathrm{d}\Omega^2} \propto \frac{k_0^4 p^2}{4\pi^2} \left| \left[\hat{\mathbf{e}}_{1p}^-(\hat{\mathbf{e}}_{1p}^- \cdot \mathbf{p}) + \hat{\mathbf{e}}_s(\hat{\mathbf{e}}_s \cdot \mathbf{p})\right] + \left[\hat{\mathbf{e}}_{1p}^- R_p(\hat{\mathbf{e}}_{1p}^+ \cdot \mathbf{p}) + \hat{\mathbf{e}}_s R_s(\hat{\mathbf{e}}_s \cdot \mathbf{p})\right] e^{2iw_1|z_0|}\right|^2 \tag{2.132}$$

The exponential term at the end of the reflected term represents the additional phase shift due to the path difference between the plane directly emitted by the dipole towards $\mathbf{k}_1^-$, and the plane wave which first propagates towards the interface along $\mathbf{k}_1^+$, and which is then reflected by it towards $\mathbf{k}_1^-$. Since p and s-waves are orthogonal to each other, the modulus can be split into two terms each containing one of these components separately:

$$\frac{\mathrm{d}^2 S_u}{\mathrm{d}\Omega^2} \propto \frac{k_0^4 p^2}{4\pi^2} \left[\left|\left[\hat{\mathbf{e}}_{1p}^- + R_p \hat{\mathbf{e}}_{1p}^+ e^{2iw_1|z_0|}\right] \cdot \mathbf{p}\right|^2 + \left|\left[1 + R_s e^{2iw_1|z_0|}\right](\hat{\mathbf{e}}_s \cdot \mathbf{p})\right|^2\right] \tag{2.133}$$

Similarly, the energy flux density radiated into a solid angle element $d\Omega^2 = (q/w_2k_2)\mathrm{d}q\mathrm{d}\psi$ into the lower half-space ($z > 0$) along direction $(\mathbf{q}, w_2)$ is given by

$$\frac{\mathrm{d}^2 S_l}{\mathrm{d}\Omega^2} \propto \frac{k_0^4 p^2}{4\pi^2} \left|\frac{w_2}{w_1}\right|^2 \left[\left|T_p \hat{\mathbf{e}}_{1p}^+ \cdot \mathbf{p}\right|^2 + \left|T_s \hat{\mathbf{e}}_s \cdot \mathbf{p}\right|^2\right] e^{-2\mathrm{Im}(w_1)|z_0|} \tag{2.134}$$

The proportionality factors for each case can be obtained by considering the limiting case when the refractive indices of both media are identical, thus setting $R_p = R_s \equiv 0$

and $T_p = T_s \equiv 1$. By comparing the result with the angular distribution of radiation for a dipole in a homogenous medium with refractive index $n = n_1 = n_2$, i.e. with $(cnk_0^4/8\pi)\left[p^2 - (\hat{\mathbf{r}} \cdot \mathbf{p})^2\right]$, one finds the proportionality factors as $\pi cn/2$. This leads to the final expressions

$$\frac{\mathrm{d}^2 S_u}{\mathrm{d}\Omega^2} = \frac{cn_1 k_0^4 p^2}{8\pi} \left[\left| \left[\hat{\mathbf{e}}_{1p}^- + R_p \hat{\mathbf{e}}_{1p}^+ e^{2iw_1|z_0|} \right] \cdot \mathbf{p} \right|^2 + \left| \left[1 + R_s e^{2iw_1|z_0|} \right] (\hat{\mathbf{e}}_s \cdot \mathbf{p}) \right|^2 \right] \tag{2.135}$$

and

$$\frac{\mathrm{d}^2 S_l}{\mathrm{d}\Omega^2} = \frac{cn_2 k_0^4 p^2}{8\pi} \left| \frac{w_2}{w_1} \right|^2 \left[\left| T_p \hat{\mathbf{e}}_{1p}^+ \cdot \mathbf{p} \right|^2 + \left| T_s \hat{\mathbf{e}}_s \cdot \mathbf{p} \right|^2 \right] e^{-2\mathrm{Im}(w_1)|z_0|} \tag{2.136}$$

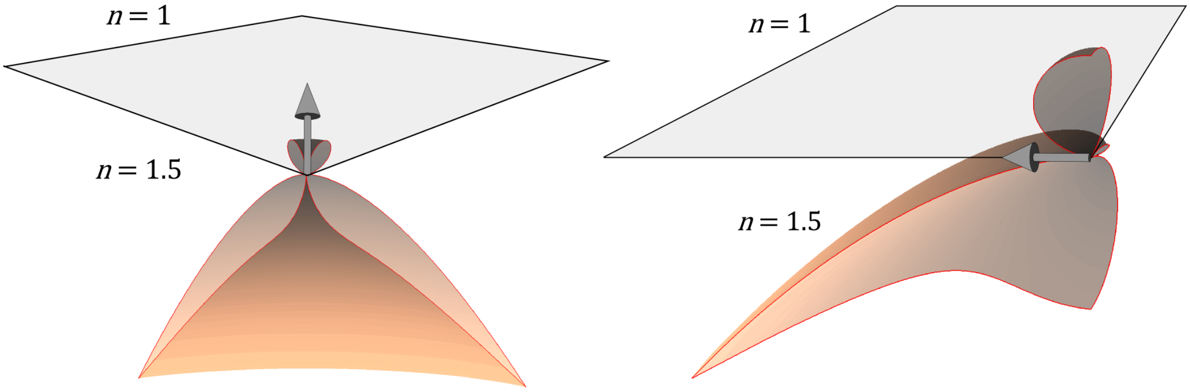

Figure 2.19: Angular distribution of radiation of a vertical (left) and a parallel (right) dipole on top of an air/glass interface.

Figure 2.19 shows the dramatic change of the angular distribution of radiation for an emitting dipole on an air/glass interface as compared to the toroidal distribution in a homogeneous medium. Note that the emission of a vertical dipole is symmetric around the vertical axis, but not for a horizontal dipole. The enhanced radiation into the glass medium is one of the key reasons why inverted microscopes that look from the glass side should be preferred for single-molecule detection and sensitive bioimaging. The angular radiation distribution of a dipole on the interface for various values of the refractive index of the lower half space is shown in figure 2.20. For comparison, we also show the emission when there is no interface, i.e. $n_1 = n_2$. A can be seen, the energy emitted into the optically denser medium is much higher for a vertical dipole than for a horizontal dipole. Moreover, most of the energy is emitted at high emission angles, which requires a high Numerical Aperture (N.A.) objective to collect this emission efficiently. The reason is that plane wave components which are evanescent in the dipole's medium can tunnel into the optically denser medium of the lower half space where they become propagating, carrying away energy. Figure 2.21 below shows the distribution for various values of dipole orientation angles towards the interface.

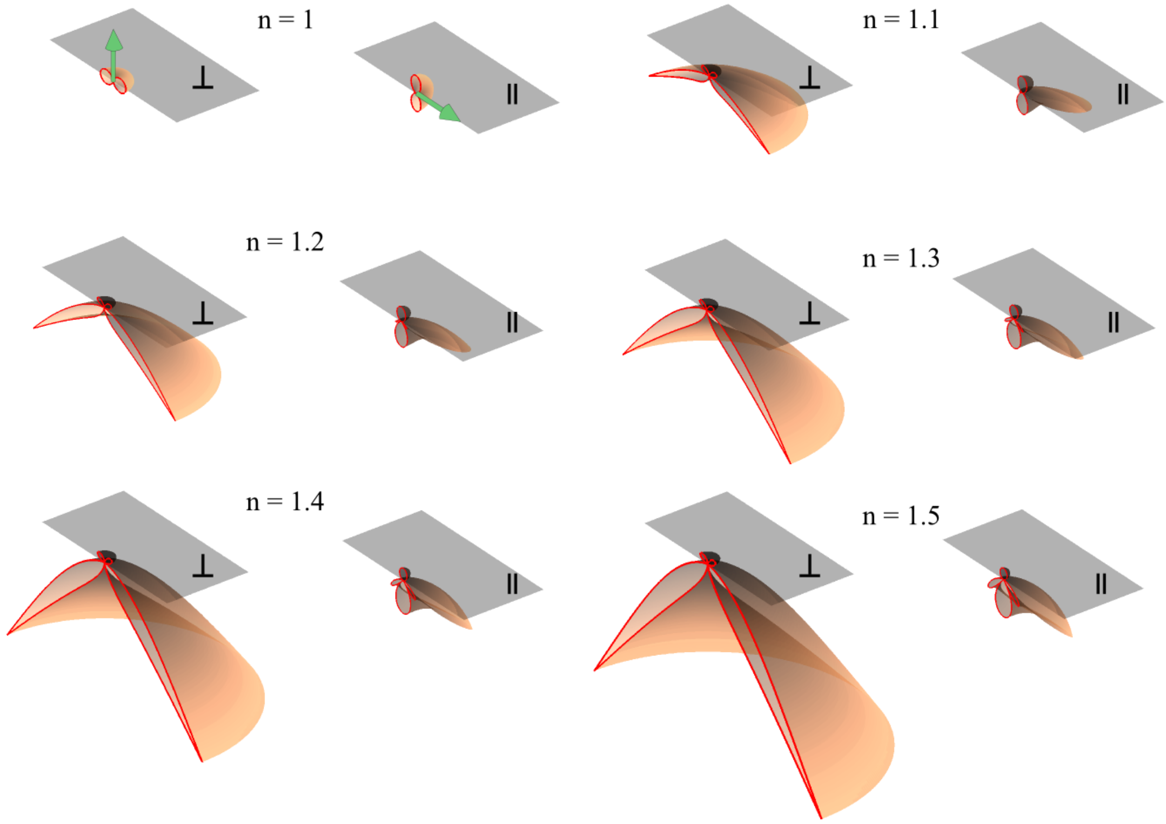

Figure 2.20: Angular distribution of radiation power from a vertical and a paralle dipole located at the interface separating two dielectric media of refractive indices as shown above and below the dipole's position.

Radiation Power of a Dipole on Top of a Dielectric Interface

The total power radiated by the dipole is given by the integral of angular distribution of radiation over all directions.

$$S = \int_0^{\pi/2} \mathrm{d}\theta_1 \sin\theta_1 \int_0^{2\pi} \mathrm{d}\psi \frac{\mathrm{d}^2 S_u}{\mathrm{d}\Omega^2} + \int_0^{\pi/2} \mathrm{d}\theta_2 \sin\theta_2 \int_0^{2\pi} \mathrm{d}\psi \frac{\mathrm{d}^2 S_l}{\mathrm{d}\Omega^2} \tag{2.137}$$

where θ_1 and θ_2 are the angles of wave vectors in media 1 and 2 ($\mathbf{k_1^-}$ and $\mathbf{k_2^+}$), respectively, and which are connected to the value of q via $\sin\theta_i = q/k_i$, for $i = 1, 2$. Thus, equation 2.137 takes the form

$$S = \int_0^{k_1} \mathrm{d}q \frac{q}{k_1 w_1} \int_0^{2\pi} \mathrm{d}\psi \frac{\mathrm{d}^2 S_u}{\mathrm{d}\Omega^2} + \int_0^{k_2} \mathrm{d}q \frac{q}{k_2 w_2} \int_0^{2\pi} \mathrm{d}\psi \frac{\mathrm{d}^2 S_l}{\mathrm{d}\Omega^2} \tag{2.138}$$

The upper limits for the integrations over q in the equation above are k_1 and k_2 for the upper and lower half-space, respectively. They represent the maximum possible projections of the wave vecotr into the plane of the interface for propagating waves in the respective half-space. The total power of emission S obtained is inversely proportional

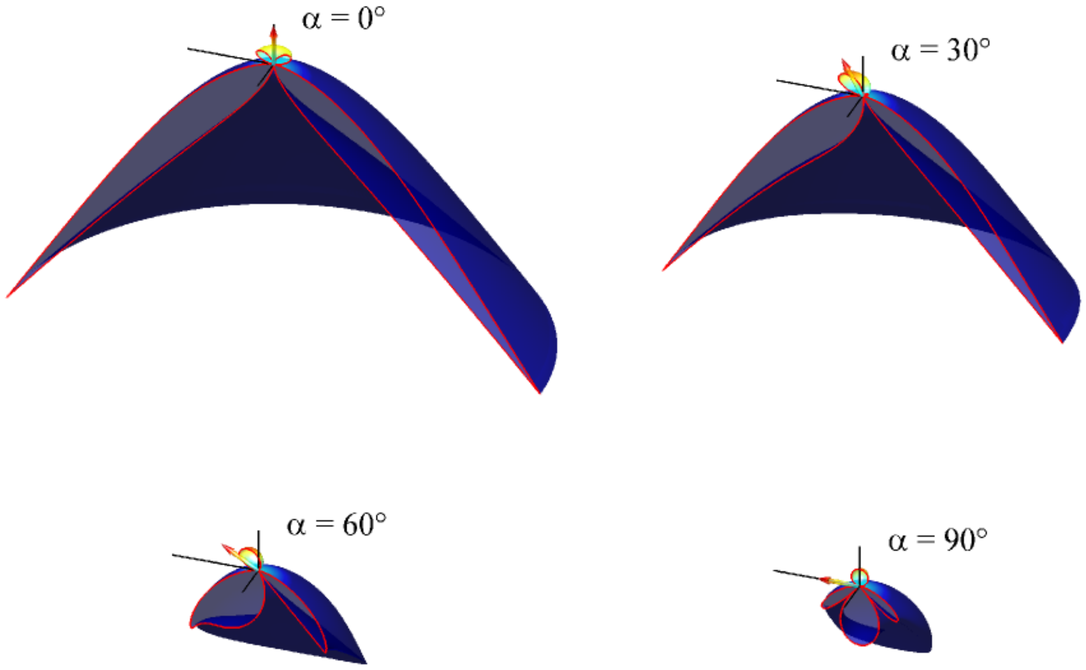

Figure 2.21: Angular distribution of radiation of dipoles with various orientations on top of an air/glass interface. α denotes the angle between the dipole and the vertical direction.

to the excited state lifetime of the dipole. In other words, the ratio of S with the total power of emission of a free dipole in a homogeneous medium of refractive index n_1 (S_0), where S_0 is the total power of a dipole in vacuum ($n_1 = 1$), gives us the inverse of the ratio of the excited state lifetimes in both cases.

It can be shown that the total emission power of a dipole with arbitrary orientation α towards the vertical axis is given by the sum of the emission of a parallel and a vertical dipole with dipole moments which are its projections on the horizontal and vertical axis, respectively:

$$S(\alpha, z_0) = S_{tot\,\perp}(z_0)\cos^2\alpha + S_{tot\,\|}(z_0)\sin^2\alpha \tag{2.139}$$

When the dipole is situated in the optically rarer medium close to the interface, $|z_0| < \lambda$, non-propagating near-field modes of the dipole can tunnel into the optically denser medium where they become propagating, which leads to an increase of the total radiation power. This can be observed as a faster decay of the excited state of a fluorescing molecule. An inverse effect takes place when the molecule is situated in the optically denser medium. Figure 2.22 shows the total power radiated by a dipole at different positions above a glass/water interface for both, horizontal and vertical

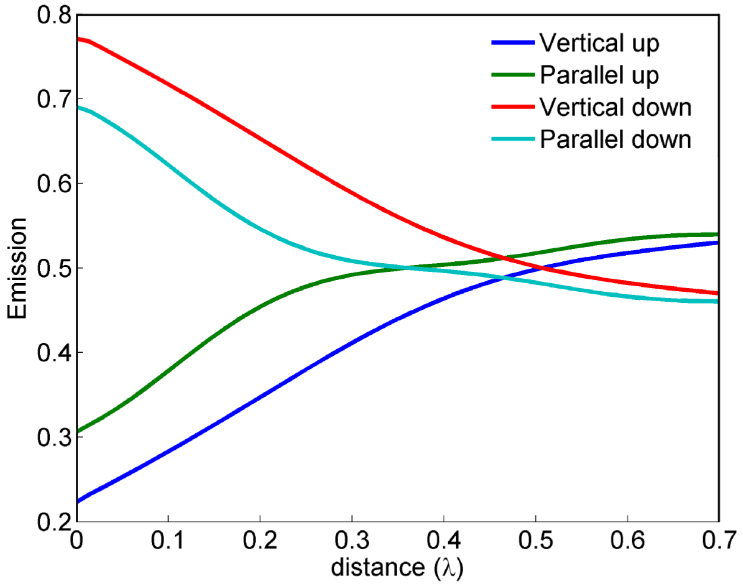

Figure 2.22: Figure showing the distribution of power as a function of distance from a water/glass interface for a vertical and parallel dipole present in water. For a dipole situated at the interface, about 70% of total radiation power is transmitted into the glass half-space which shows the prominence of the effective near-field field coupling with the interface.

orientations. Let us notice that the radiation power shows a periodic behavior with distance from the interface, with a period of $\lambda/\pi n_1$. This is also shown in figure 2.23.

2.4.3 Dipole on a Metal Surface

Let us now investigate the behavior of a dipole in the vicinity of a metal surface. The properties of a dipole change dramatically in the vicinity of a metal surface. Due to their complex dielectric properties, a part of the electromagnetic radiation that is incident of them is absorbed, and the rest is reflected back. The energy that is absorbed can be seen as a transfer of energy from the radiation to the oscillating plasmons on the surface. The situation is more complex due to the presence of an oscillating dipole close to a metal. Not only does a part of its radiated energy gets absorbed into the metal, but a near-field coupling between the dipole and the surface plasmons takes place. This changes the rate of energy emitted by the dipole dramatically. This is similar to what we saw earlier when a dipole is situated close to a dielectric interface in an optically rarer medium. We saw that a few non-propagating modes of a dipole tunnel through and become propagating in the optically denser medium. In case of metals, however, the energy that is transferred to the surface plasmons is attenuated along the z-direction. Therefore, the energy that is taken from the dipole's near-field is lost as heat in the metal internally and cannot be detected optically.

Several experimental studies have measured the effect of a metal surface on the fluorescence lifetime. During the early 70s, Drexhage and coworkers showed the influence

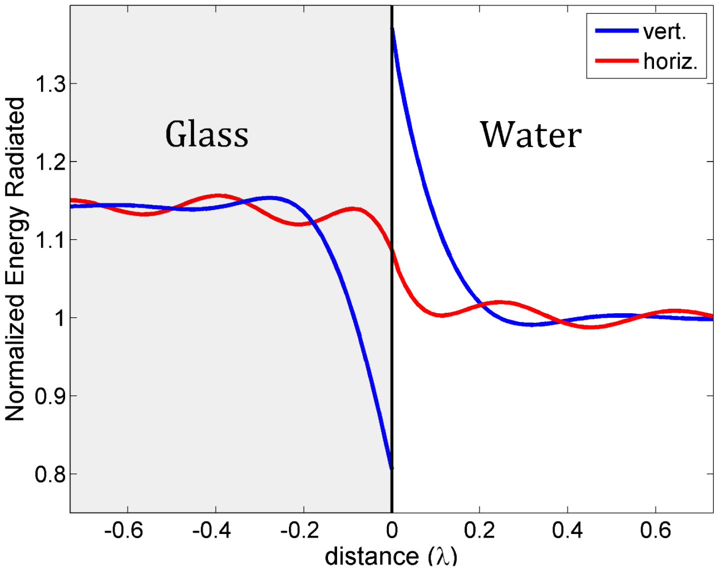

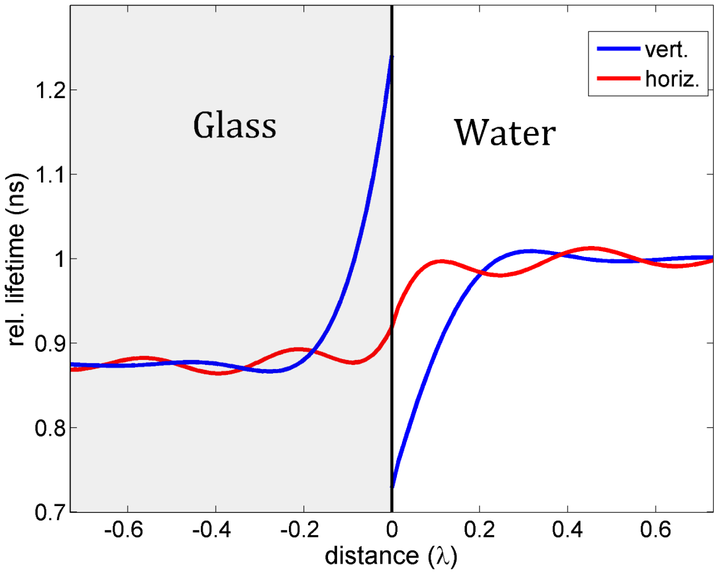

Figure 2.23: The top figure shows the total energy radiated as a function of dipole's distance from the interface for both, vertical and parallel dipoles. The energy is normalized against the total radiation power of a dipole in an unbounded water medium. The oscillation amplitude of the curves goes to zero and the power converges to 1 (or 1.5/1.33) when the distance is on the order of a few wavelengths. The bottom figure shows the relative excited state lifetime as a function of distance from the interface normalized to the values in water.

of a reflecting mirror on a monolayer of phosphorescent europium chelate complexes experimentally, and developed a model to explain the variations in fluorescence lifetimes based on the interference of a dipole's field with itself [111]. This model could explain well the oscillatory behavior of the radiation rates at large distances from the metal surface, however, it failed to answer the experimental results at short distances ($z_0 < \lambda$) where efficient nonradiative energy transfer from the excited molecule to the metal surface takes place. At short distances, the europium complexes were quenched since the transferred energy was lost to the metal completely. The situation becomes slightly different when there is a thin metal film instead of a metal slab. The reduction of the thickness to a few nanometers leads to two things: 1) The coupling of the dipole's field with the surface plasmons present on the bottom side of the metal leading to a further modification of the distance-dependent energy loss. 2) Some part of the energy transferred to the metal can now propagate into the lower dielectric medium. The propagating wave vectors are attenuated in amplitude by the thickness of the metal film, but optical detection of fluorophores is possible. This was demonstrated experimentally by Amos *et al.* by varying the thickness of a thin silver film on top of a glass coverslide [112].

Theoretical treatment for studying the behavior of a dipole in the vicinity of a metal surface was first performed by Kuhn in his model where the dipole is considered as a damped oscillator and involves the calculation of the reflected field at the dipole's position [113]. This way of calculating the total emission rates was already introduced in section 2.4.1 using Poynting's theorem. Later, Chance, Prock and Silbey worked out the energy-flux method, which we will introduce briefly as well, with which one can separate the total flux and radiation rates into the upper and lower half-spaces, useful for many practical purposes, such as calculating the amount of radiation from a dipole that can be detected through a thin film, etc [107]. The treatment is similar to that shown in the previous section where a dipole's reflected and transmitted fields are calculated when it is situated close to an interface and the total power radiated is calculated by integrating the Poynting vector for all the propagating waves in both half-spaces. However, here, to take the near-field coupling of a dipole to the metal surface into account, the integrals are over all possible wave vectors, where q goes from 0 to ∞. We start our discussion by taking the transmitted and reflected fields of an oscillating dipole placed on top of an interface from our previous section 2.4.2 using Fresnel's equations presented in the previous section.

$$\mathbf{E}_T(\mathbf{r}) = \frac{ik_0^2}{2\pi} \iint \frac{\mathrm{d}\mathbf{q}}{w_1} \left[\hat{\mathbf{e}}_{2p}^{+} T_p (\hat{\mathbf{e}}_{1p}^{+} \cdot \mathbf{p}) + \hat{\mathbf{e}}_s T_s (\hat{\mathbf{e}}_s \cdot \mathbf{p})\right] e^{i[\mathbf{q} \cdot (\boldsymbol{\rho} - \boldsymbol{\rho}_{\mathbf{0}}) + w_1 |z_0| + w_2 z]},$$

$$\mathbf{E}_R(\mathbf{r}) = \frac{ik_0^2}{2\pi} \iint \frac{\mathrm{d}\mathbf{q}}{w_1} \left[\hat{\mathbf{e}}_{1p}^{-} R_p (\hat{\mathbf{e}}_{1p}^{+} \cdot \mathbf{p}) + \hat{\mathbf{e}}_s R_s (\hat{\mathbf{e}}_s \cdot \mathbf{p})\right] e^{i[\mathbf{q} \cdot (\boldsymbol{\rho} - \boldsymbol{\rho}_{\mathbf{0}}) + w_1 |z_0| - w_1 z]}.$$

Here the reflection and transmission coefficients are complex numbers. The field in the upper half-space ($z < z_0$) can be written as a superposition of the dipole's field with its reflection from the interface

$$\begin{aligned}\mathbf{E}_{\uparrow} = \frac{ik_0^2}{2\pi} \iint \frac{\mathrm{d}\mathbf{q}}{w_1} \Big[& \hat{\mathbf{e}}_{1p}^{-}(\hat{\mathbf{e}}_{1p}^{+} \cdot \mathbf{p}) \left(e^{-iw_1(z-z_0)} + R_p e^{-iw_1(z_0+z)}\right) \\ & + \hat{\mathbf{e}}_s(\hat{\mathbf{e}}_s \cdot \mathbf{p}) \left(e^{-iw_1(z-z_0)} + R_s e^{-iw_1(z_0+z)}\right) \Big] e^{i\mathbf{q}\cdot(\boldsymbol{\rho}-\boldsymbol{\rho}_\mathbf{0})},\end{aligned} \tag{2.140}$$

and the field in the bottom half-space above the interface ($0 > z > z_0$) is given by

$$\begin{aligned}\mathbf{E}_{\downarrow} = \frac{ik_0^2}{2\pi} \iint \frac{\mathrm{d}\mathbf{q}}{w_1} \Big[& (\hat{\mathbf{e}}_{1p}^{+} \cdot \mathbf{p}) \left(\hat{\mathbf{e}}_{1p}^{+} e^{-iw_1(z_0-z)} + \hat{\mathbf{e}}_{1p}^{-} R_p e^{-iw_1(z_0+z)}\right) \\ & + \hat{\mathbf{e}}_s(\hat{\mathbf{e}}_s \cdot \mathbf{p}) \left(e^{-iw_1(z_0-z)} + R_s e^{-iw_1(z_0+z)}\right) \Big] e^{i\mathbf{q}\cdot(\boldsymbol{\rho}-\boldsymbol{\rho}_\mathbf{0})},\end{aligned} \tag{2.141}$$

The corresponding magnetic fields are obtained by performing the curl operation on the above equations followed by division by k_0:

$$\begin{aligned}\mathbf{B}_{\uparrow} = \frac{ik_0^2 n_1}{2\pi} \iint \frac{\mathrm{d}\mathbf{q}}{w_1} \Big[& \hat{\mathbf{e}}_s(\hat{\mathbf{e}}_{1p}^{+} \cdot \mathbf{p}) \left(e^{-iw_1(z-z_0)} + R_p e^{-iw_1(z_0+z)}\right) \\ & - \hat{\mathbf{e}}_{1p}^{-}(\hat{\mathbf{e}}_s \cdot \mathbf{p}) \left(e^{-iw_1(z-z_0)} + R_s e^{-iw_1(z_0+z)}\right) \Big] e^{i\mathbf{q}\cdot(\boldsymbol{\rho}-\boldsymbol{\rho}_\mathbf{0})},\end{aligned} \tag{2.142}$$

$$\begin{aligned}\mathbf{B}_{\downarrow} = \frac{ik_0^2 n_1}{2\pi} \iint \frac{\mathrm{d}\mathbf{q}}{w_1} \Big[& \hat{\mathbf{e}}_s(\hat{\mathbf{e}}_{1p}^{+} \cdot \mathbf{p}) \left(e^{-iw_1(z_0-z)} + R_p e^{-iw_1(z_0+z)}\right) \Big] e^{i\mathbf{q}\cdot(\boldsymbol{\rho}-\boldsymbol{\rho}_\mathbf{0})} \\ & - (\hat{\mathbf{e}}_s \cdot \mathbf{p}) \left(\hat{\mathbf{e}}_{1p}^{+} e^{-iw_1(z_0-z)} + \hat{\mathbf{e}}_{1p}^{-} R_s e^{-iw_1(z_0+z)}\right),\end{aligned} \tag{2.143}$$

Using these equations, one can calculate the power radiated along any direction $(\boldsymbol{\rho}, z - z_0)$. Further, energy flux through any plane can be calculated by taking the dot product of the Poynting vector with the normal to this plane and integrating over the whole plane. In this way, the total flux through a plane above the dipole's position $z < z_0$ and below $0 \geq z > z_0$ can be calculated using the above four equations. Let us find out the total energy emitted into the lower half-space at the interface ($z = 0$). Using equations (2.141) and (2.143), one can write the Poynting vector $\mathbf{S}_{\downarrow} = c/8\pi \mathrm{Re}\{\mathbf{E}_{\downarrow} \times \mathbf{B}_{\downarrow}^{*}\}$:

$$\begin{aligned}\mathbf{S}_{\downarrow}(\boldsymbol{\rho}, z=0) = \frac{ck_0^4}{32\pi^3} \mathrm{Re}\Bigg\{ & \iint \frac{\mathrm{d}\mathbf{q}}{w_1} \iint \frac{\mathrm{d}\mathbf{q}'}{w_1'^{*} k_1} e^{i(\mathbf{q}-\mathbf{q}')\cdot(\boldsymbol{\rho}-\boldsymbol{\rho}_\mathbf{0})} \\ & \Bigg[\left(\hat{\mathbf{k_1}}^{+} + R_p \hat{\mathbf{k_1}}^{-}\right) e^{-iw_1 z_0} (e^{-iw_1' z_0})^{*} (1 + R_p)^{*} (\hat{\mathbf{e}}_{1p}^{+} \cdot \mathbf{p}) (\hat{\mathbf{e}}_{1p}^{+'} \cdot \mathbf{p})^{*} \\ & + \left(\hat{\mathbf{k_1}}^{+} + R_s \hat{\mathbf{k_1}}^{-}\right)^{*} e^{-iw_1 z_0} (e^{-iw_1' z_0})^{*} (1 + R_s) (\hat{\mathbf{e}}_s \cdot \mathbf{p}) (\hat{\mathbf{e}'}_s \cdot \mathbf{p})^{*} \Bigg] \Bigg\}\end{aligned} \tag{2.144}$$

The above equation represents the energy flux at a point on the surface $(\boldsymbol{\rho}, z = 0)$. By taking the projection of this vector along $\hat{\mathbf{z}}$, using the relations $\hat{\mathbf{z}} \cdot \hat{\mathbf{k_1^{\pm}}} = \pm w_1/k_1$, and integrating over $\mathrm{d}^2\boldsymbol{\rho}$, we get the total radiation power through the interface $S_{\downarrow} =$

$\int \mathrm{d}^2\boldsymbol{\rho}\,(\mathbf{S}_{\downarrow}\cdot\hat{\mathbf{z}})$. This integration can be simplified by using the identity of Dirac's well-known delta-function,

$$\int \mathrm{d}^2\boldsymbol{\rho}\, e^{[i\boldsymbol{\rho}\,\cdot\,(\mathbf{q}-\mathbf{q}')]} = 4\pi^2\delta^2(\mathbf{q}-\mathbf{q}'),$$

since the terms inside the square bracket in equation (2.144) do not depend on $\boldsymbol{\rho}$. This reduces equation (2.144) to:

$$\begin{aligned} S_{\downarrow} = \frac{ck_0^4}{8\pi}\mathrm{Re}\Bigg\{ \iint \frac{\mathrm{d}\mathbf{q}}{|w_1|^2}\frac{qn_1^*}{k_1}\Big[& w_1(1-R_p)(1+R_p^*)\left|\hat{\mathbf{e}}_{1p}^{+}\cdot\mathbf{p}\right|^2 \\ & + w_1^*(1+R_s)(1-R_s^*)\left|\hat{\mathbf{e}}_s\cdot\mathbf{p}\right|^2\Big] e^{2\mathrm{Im}(w_1)z_0}\Bigg\} \end{aligned} \qquad (2.145)$$

Now, this equation represents the total energy flux at the interface and it contains the energy that is radiated from the dipole towards the interface together with the amount of energy reflected back. If a calculation was performed similarly at a plane above the dipole's position to give $S_{\uparrow}$, it would contain the dipole's radiation into the upper half space, together with the radiation reflected back as well. The total emission rate S can be calculated using equation (2.123) with the electric field at the position of the dipole calculated using either of the two equations (2.141) or (2.140) [114, 115].

Let us now consider closely the case of a vertical dipole, $\mathbf{p} = p\hat{\mathbf{z}}$. The integration over $\mathbf{q}$ can be carried out in spherical coordinates to give:

$$S_{\perp\downarrow} = \frac{ck_0^4p^2}{4}\mathrm{Re}\Bigg\{\int \frac{\mathrm{d}q}{|k_1w_1|^2}\frac{q^3n_1^*w_1}{k_1}(1-R_p)(1+R_p^*)e^{2\mathrm{Im}(w_1)z_0}\Bigg\} \qquad (2.146)$$

Using (2.140) and after some algebraic manipulations, the total radiation power $S_{\perp}$ is obtained as:

$$S_{\perp} = \frac{ck_0^4p^2}{2}\mathrm{Re}\Bigg\{\int \frac{\mathrm{d}q}{|k_1w_1|^2}\frac{q^3n_1^*w_1}{k_1}(1+R_pe^{-2iw_1z_0})\Bigg\} \qquad (2.147)$$

Similarly, for a parallel dipole, one has

$$\begin{aligned} S_{\parallel\downarrow} = \frac{ck_0^4p^2}{8}\mathrm{Re}\Bigg\{ & \int \frac{\mathrm{d}q}{|w_1|^2}\frac{qn_1^*}{k_1} \\ & \left[\frac{|w_1^2|}{k_1^2}w_1(1-R_p)(1+R_p^*) + w_1^*(1+R_s)(1-R_s^*)\right]e^{2\mathrm{Im}(w_1)z_0}\Bigg\} \end{aligned} \qquad (2.148)$$

and the total radiation power,

$$S_{\parallel} = \frac{ck_0^4p^2}{4}\mathrm{Re}\Bigg\{\int \frac{\mathrm{d}q}{|w_1|^2}\frac{qn_1^*w_1}{k_1}\left[\frac{|w_1^2|}{k_1^2}(1+R_pe^{-2iw_1z_0}) + (1+R_se^{-2iw_1z_0})\right]\Bigg\} \qquad (2.149)$$

All the integrals above are performed for all possible q (0 to ∞) values together with positive imaginary solutions of $w_1(q)$ only. This gives the total power emitted by the dipole into both the half-spaces $S_\uparrow$ and $S_\downarrow$. In order to calculate the rate of energy *detectable* in both the half-spaces, one limits the upper-limit of the integrals to propagating wave vectors only. An important point to note here is that for the integrals (2.146) and (2.148) when $q < k_1$, $\mathrm{Im}(w_1) = 0$, and therefore the integrals do not depend on the dipole's position. These then represent the "trivial transfer" of radiation power to the metal surface from the far-field of the dipole [107]. In other words, this shows the fraction of energy that is absorbed my the metal.

In order to complete the discussion here and to make use of what we just derived, we calculate the total power that is *detectable* in both half-spaces for the two cases of dipole orientations for a thin metal film on top of a glass coverslip. We do this by calculating the ratio of the net propagating part of the radiation power to the total power in both half-spaces. The above equations are true for such a stratified conducting/dielectric layer system, as long as one uses the effective reflection coefficients [108]. For a thin metal film sandwiched between glass and air, one has:

$$R_{p,s} = \frac{r_{p,s}^{12} + r_{p,s}^{23}\exp(2iw_2h)}{1 + r_{p,s}^{12}\, r_{p,s}^{23}\exp(2iw_2h)} \tag{2.150}$$

where the subscripts refer to p- and s-polarization, $r_{p,s}^{12}$ and $r_{p,s}^{23}$ are the Fresnel reflection coefficients for an air-to-metal and metal-to-glass interface, and $w_2 = \sqrt{(n_2^2 - 1)k_0^2 + w_1^2}$, where n_2 is the complex refractive index of metal.

Figure 2.24 shows the energy emitted that is detectable as a function of height. The quantum yield for the dipoles was assumed to be one. Note that at distances $z_0 > \lambda$, the total radiated energy into both half-spaces approach constant values that represent the net reflectance and transmittance of the metal film. Two important things must be noted from this figure. First, the thin gold film of thickness 10 nm is enough to quench the dipoles in its vicinity. Second, the plasmons excited due to the transfer of energy from the dipole radiate out in the bottom interface between gold and glass medium. Second, a part of the energy transferred to the plasmons from the oscillating dipole close to it is transferred further into the glass medium where it can propagate again. This energy now propagates in the form of plane waves and can be detected by our optical system with a high collection efficiency objective. The possibility to detect single molecules on top of a thin metal film, with some spacer in between, was first shown by Stefani *et al.* [50].

Dividing equation (2.147) by the total radiation power of a free dipole in the same medium ($n_1S_0 = cn_1k_0^4p^2/3$), the rate associated with the total photon flux from a

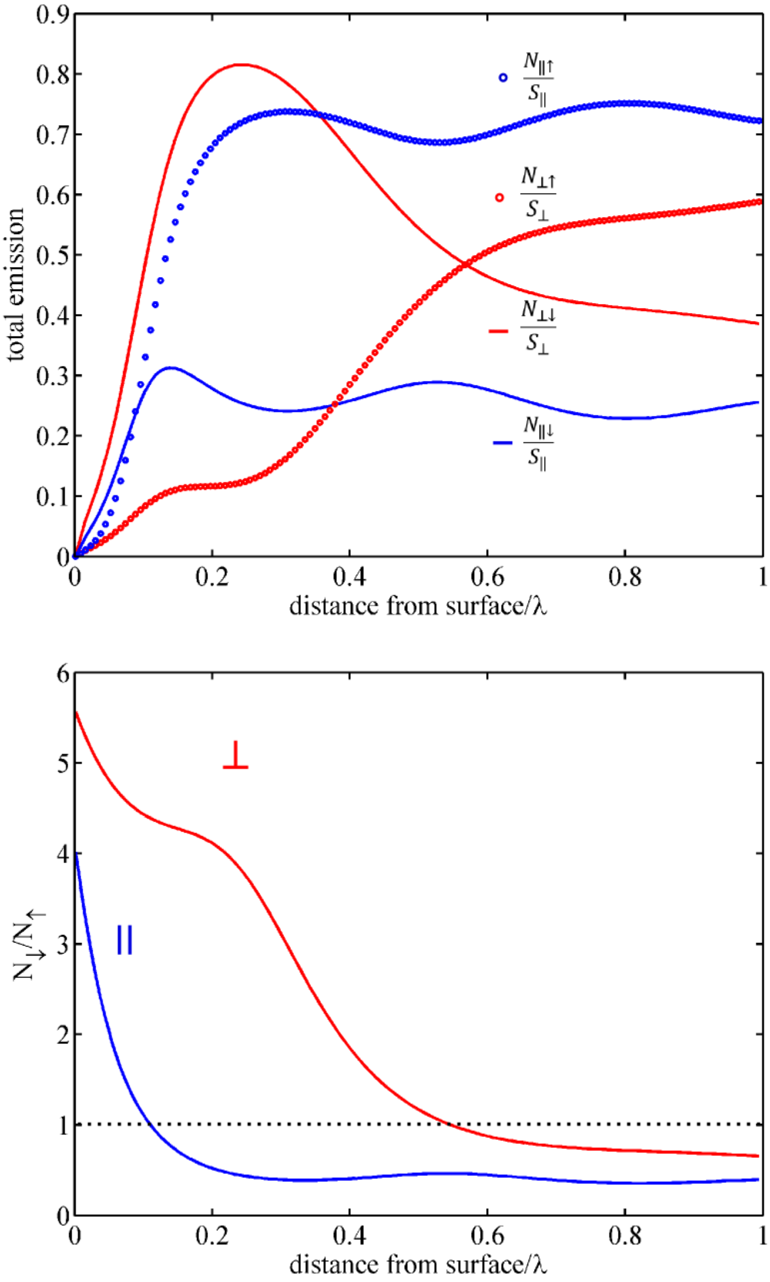

Figure 2.24: $N_\uparrow, N_\downarrow$ represent the detectable energy calculated for both the upper and lower half-spaces, respectively. The top figure shows the detectable radiation of a dipole ($\Phi = 1$) into the upper and lower half-spaces for both orientations as a function of distance d ($d = z_0/\lambda,\ \lambda = 690\,\mathrm{nm}$). The thin gold film of 10 nm is enough to quench the dipoles. This can be seen in the plot where the radiation in the upper and lower half-spaces approach zero when the dipole is placed at very small distances. A part of the energy that is transferred to the surface plasmons couples out at the gold/glass interface which propagates into the lower half-space. The bottom figure shows the ratio of the detectable emission power in the lower half-space vs the upper half-space for both the orientations as a function of distance from the metal surface. This shows that when a dipole is close to the surface of a thin film, the chance to detect it optically is higher through the glass beneath.

dipole close to a metal surface is

$$\kappa_{\perp} = \kappa_0 \left[1 - \frac{3}{2} \mathrm{Re} \left\{ \int_0^{\infty} \frac{\mathrm{d}u}{w_1} u^3 R_p e^{-2iw_1 z_0} \right\} \right], \tag{2.151}$$

where we used $u = q/k_1$ in the above equation, and κ_0 is the radiative rate of a free dipole (see equation (2.126)). On similar lines, the total photon flux of a parallel dipole can be obtained:

$$\kappa_{\parallel} = \kappa_0 \left[1 + \frac{3}{4} \mathrm{Re} \left\{ \int_0^{\infty} \frac{\mathrm{d}u}{w_1} u \left[R_s + (1 - u^2) R_p \right] e^{-2iw_1 z_0} \right\} \right]. \tag{2.152}$$

If the quantum yield ϕ of the free dipole is not unity, then the total rate of photons for a vertical dipole can be separated into the sum of a radiative ($\kappa_{r\,\perp}$) and a non-radiative decay rate ($\kappa_{nr\,\perp}$) as:

$$\kappa_{r\,\perp} = \kappa_0 \left[\Phi - \frac{3}{2} \Phi \,\mathrm{Re} \left\{ \int_0^{1} \frac{\mathrm{d}u}{w_1} u^3 \left(R_p \right) e^{-2iw_1 z_0} \right\} \right] \tag{2.153}$$

and

$$\kappa_{nr\,\perp} = \kappa_0 \left[(1 - \Phi) - \frac{3}{2} \Phi \,\mathrm{Re} \left\{ \int_1^{\infty} \frac{\mathrm{d}u}{w_1} u^3 \left(R_p \right) e^{-2iw_1 z_0} \right\} \right]. \tag{2.154}$$

The above equations are trivial to understand. w_1 is real only when u varies from $0 \rightarrow 1$, and since the radiative rate is associated with propagating plane waves originating from the dipole, the integral takes into account only these values of u. The factor $\kappa_0(1-\Phi)$ is the intrinsic non-radiative damping constant of the oscillation system and this represents the fraction of energy that is not available for any energy transfer or emission processes. The effect of the metal or the surroundings around the dipole is realized on the radiative fraction of the free dipole which is given by $\kappa_0\Phi$. Due to the presence of a metal surface here, a part of this radiative energy is rendered into non-radiative energy which is accounted for by the integral term in expression (2.154). Therefore, this integral represents the metal-induced energy transfer.

$$\kappa_{\mathrm{MIET}\,\perp} = \frac{3}{2} \kappa_0 \Phi \,\mathrm{Re} \left\{ \int_1^{\infty} R_p e^{-2iw_1 |z_0|} u^3 \frac{\mathrm{d}u}{w_1} \right\} \tag{2.155}$$

At distances in the order of a wavelength and closer to the metal surface, both the radiative as well as the non-radiative rates are modified as according to the equations (2.153) and (2.154), respectively. One more important thing to note here is that the extent of energy transfer to the metal is directly related to the quantum yield Φ of the dye molecules. Therefore one must know the exact quantum yield in order to estimate the total radiative rate and fluorescence lifetime as a function of distance. Figure 2.25 shows the variation of lifetimes with distance for the two orientations of a dipole with various

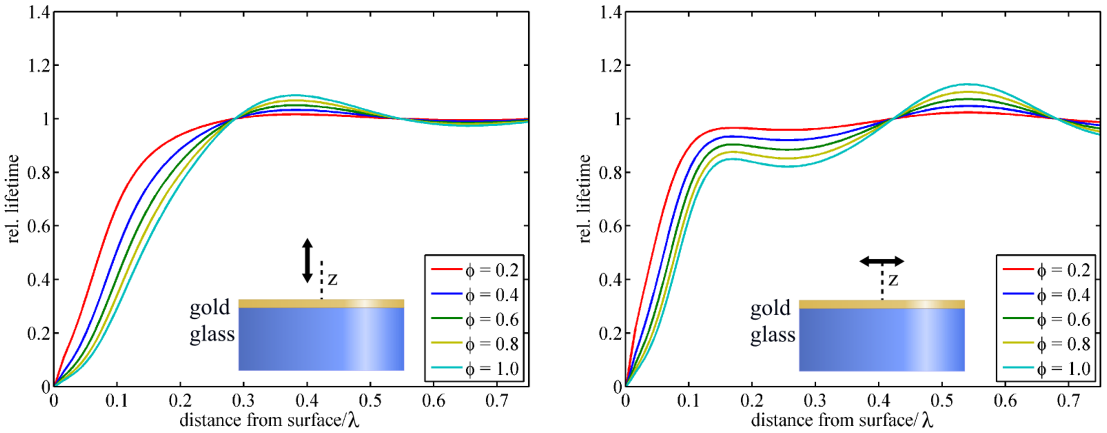

Figure 2.25: Left figure shows the relative lifetime variation with the distance from a 10 nm gold film for a vertical dipole with various quantum yield. The right figure shows the same for a parallel dipole

quantum yields. An important observation here is that at any height $|z_0|$ above the surface, the energy transfer scales proportionally with the quantum yield of the dye, as represented by equation (2.155). Therefore, if the free space lifetimes of two fluorescent molecules, with different quantum yields, are identical, then at a given distance from a metal surface, lifetime of the molecule with higher quantum yield is shorter than the lifetime of the other.

For a dipole oriented at an angle α with respect to the surface, one can derive the total emission power $S(\alpha, z_0)$, using the reflected electric field from equation (2.130), together with its own field, from equation (2.123) (Poynting's Theorem) that can be written in terms of the total emission power of a vertical and parallel dipole as in equation (2.123). If the quantum yield of the dipole is Φ, then the rate of photons or the rate of excited state decay, dividing the total emission power by $n_1 S_0$ (radiation power of a free dipole in the same medium), can be written as:

$$\kappa(\alpha, z_0) = \kappa_0 \left[(1 - \Phi) + \Phi \frac{S(\alpha, z_0)}{n_1 S_0} \right] = \frac{1}{\tau_f(\alpha, z_0)} \tag{2.156}$$

Figure 2.26 shows the MIET calibration curves of Rhodamine 6G ($\tau_0 = 1/\kappa_0 = 4.1$ ns and $\Phi = 0.95$, see reference [103]) for five different dipole orientations with water as a medium above a thin gold film (h=10 nm) at an emission wavelength $\lambda_{\mathrm{em}} = 525$ nm.

Regardless of its quantum yield and orientation α, the excited state lifetime of a single molecule shows a monotonic relationship with distance from the metal surface in the near-field limit, and therefore, it can be used to locate the emitter from the surface. This is much similar to FRET where the energy is transferred non-radiatively to another dipole. However, the distance to lifetime relationship in the case of FRET shows an inverse sixth power relationship ($\Delta\tau/\tau_0 \propto d^{-6}$), whereas in the case of an infinite plane of a metal surface, it is roughly proportional to d^{-3} to d^{-4} [107].

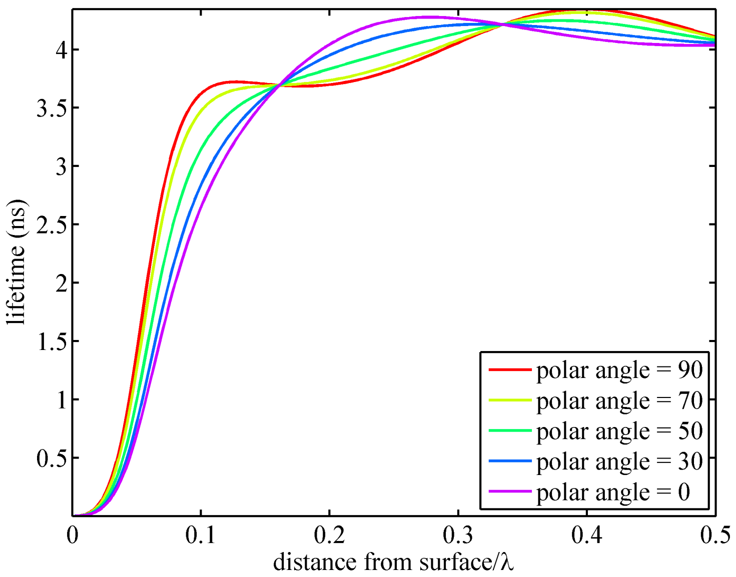

Figure 2.26: MIET calibration curves of Rhodamine 6G in water on top of a thin gold film at various polar angles. The calculations were done for a thin gold film of thickness $h = 10\,\mathrm{nm}$, with water as a medium above at a wavelength $\lambda_{\mathrm{em}} = 525\,\mathrm{nm}$. The free space parameters for the dye are taken from the reference [103].

This concludes the theory to explain the concept of metal-induced energy transfer completely. The emission properties of an electric dipole emitter in the presence of a dielectric or metallic interface are calculated by expressing its electric field as a superposition of plane waves and thereafter, calculating the reflected and transmitted fields by using Fresnel's equations. The modified spontaneous emission rate is then obtained directly by calculating the reflected field at its position and applying Poynting's theorem (2.122). Energy flux calculations by estimating the Poynting vector allows one to separate the total energy radiated into both half-spaces, and further, to picture the angular distribution of emission. This includes the involvement of various processes which have not been precisely named in this chapter such as Surface Plasmon Coupled Emission (SPCE), Surface Plasmon Resonance (SPR), Lossy Surface Waves (LSW), Radiating Plasmons (RP), etc [116–118]. Introducing these terms and terminology is confusing and is not required in order to explain all the necessary emission properties of a single molecule near a metal surface or a thin metal film. The theory above is in fact completely identical to the theoretical work of Purcell who derived the spontaneous emission probabilities of nuclear transitions in metallic resonators. The idea is based on the enhancement of the local density of final states in, for example, a cavity or near a conducting surface.

3 Single-Molecule Metal-Induced Energy Transfer (smMIET)

Abstract

We present a new concept for measuring distances of single molecules from a surface with nanometer accuracy using the energy transfer from the excited molecule to surface plasmons of a metal film. We measure the fluorescence lifetime of individual dye molecules deposited on a dielectric spacer. By using our theoretical model, we convert the lifetime values into the axial distance of individual molecules. Similar to Förster Resonance Energy Transfer (FRET), this allows emitters to be localized with nanometer accuracy, but in contrast to FRET the distance range at which efficient energy transfer takes place is an order of magnitude larger. Our technique can be potentially used as a tool for measuring intramolecular distances of biomolecules and complexes.

Parts of this chapter and some figures have been published in the journal article:

Karedla, N.; Chizhik, A.I.; Gregor, I.; Chizhik, A.M.; Schulz, O.; Enderlein, J. *"Single-Molecule Metal Induced Energy Transfer (smMIET): Resolving Nanometer Distances at Single Molecule Level"* ChemPhysChem **15** 705-11 (2014)

3.1 Experimental Setups

3.1.1 MicroTime 200 Setup

We used the commercial confocal system Microtime 200 (PicoQuant) for scanning our samples and lifetime imaging. Figure 3.1 depicts a schematic of the setup, which contains four basic parts:

1. **The microscope**: A modified Olympus IX-71 microscope (Olympus Deutschland) with an accessible standard side port on the right side was used for the experiments. The samples were scanned at a speed of 12 µm/s typically by using a three-axis piezo stage (P-562.3CD, Physik Instrumente) that was driven with a digital piezo controller (E-710.3CD Physik Instrumente).

2. **The excitation system**: A pulsed diode laser ($\lambda = 640\,\mathrm{nm}$, LDH-D-C-640, PicoQuant) with a pulse width of 100 ps full-width-at-half maximum was operated at a pulsing frequency of 40 MHz by using a multichannel picosecond laser driver (PDL 828 “Sepia II”, PicoQuant). A clean-up filter (Z640/10X, Chroma Technology) was used to block undesired wavelengths from the laser. The laser beam was then coupled to a polarization-maintaining single-mode optical fiber (PMC-400-4.2-NA010-3-APC- 250 V, Schäfter und Kirchhoff).

3. **The main optical unit**: The excitation light from the fiber output was collimated into a beam of 9 mm diameter by coupling it to an infinity-corrected 4X objective (UPLSAPO 4X, Olympus). The excitation beam was then reflected by using a dichroic mirror (FITC/CY5 (51008bs), Chroma Technology) to guide it into the side port of the microscope. The power used was in the range of 10–25 $\mathrm{kWcm^{-2}}$. A high numerical aperture objective was used to excite the samples (UAPON 100X OTIRF, 1.49 N.A., Olympus) and to collect the fluorescence emission. The emission light was then passed through the dichroic mirror and focused onto a 50 µm pinhole for confocal imaging. After the pinhole it was refocused by using a pair of achromatic lens doublets onto the active area ($\sim$ 200 µm) of a single-photon counting module (SPCM AQR-13, Perkin–Elmer, ($\sim$ 70% quantum yield of detection at $\lambda = 670\,\mathrm{nm}$). A band-pass filter (BrightLine HC 692/40, Semrock) was used in the detection pathway to block the back-scattered laser light and also a major part of gold photoluminescence. The dark count rate of the detector was less than 150 counts per second.

4. **Data acquisition and processing**: The Transistor-Transistor-Logic (TTL) pulses from the SPCM were recorded with a 2 ps time resolution by using a multichannel picosecond event timer and Time Correlated Single-Photon Counting (TCSPC) module (HydraHarp 400, PicoQuant) in the Time-Tagged Time-Resolved (TTTR)

acquisition mode [5]. The periodic sync signal for the time tags was obtained from the Sepia II driver and the markers from the piezo controller representing the start and end of a scan line were recorded as 'virtual photons'. The collected photon data was processed using the commercial software SymPhoTime v.5.2 (PicoQuant) giving the intensity and lifetime images. Pixels corresponding to single molecules were identified from this intensity image by using a custom Matlab routine that will be described below. A weighted average of pixel lifetime values with intensity values as weights was calculated separately for each individual molecule. Finally, a histogram of average lifetimes of all the identified single molecules in the image was plotted.

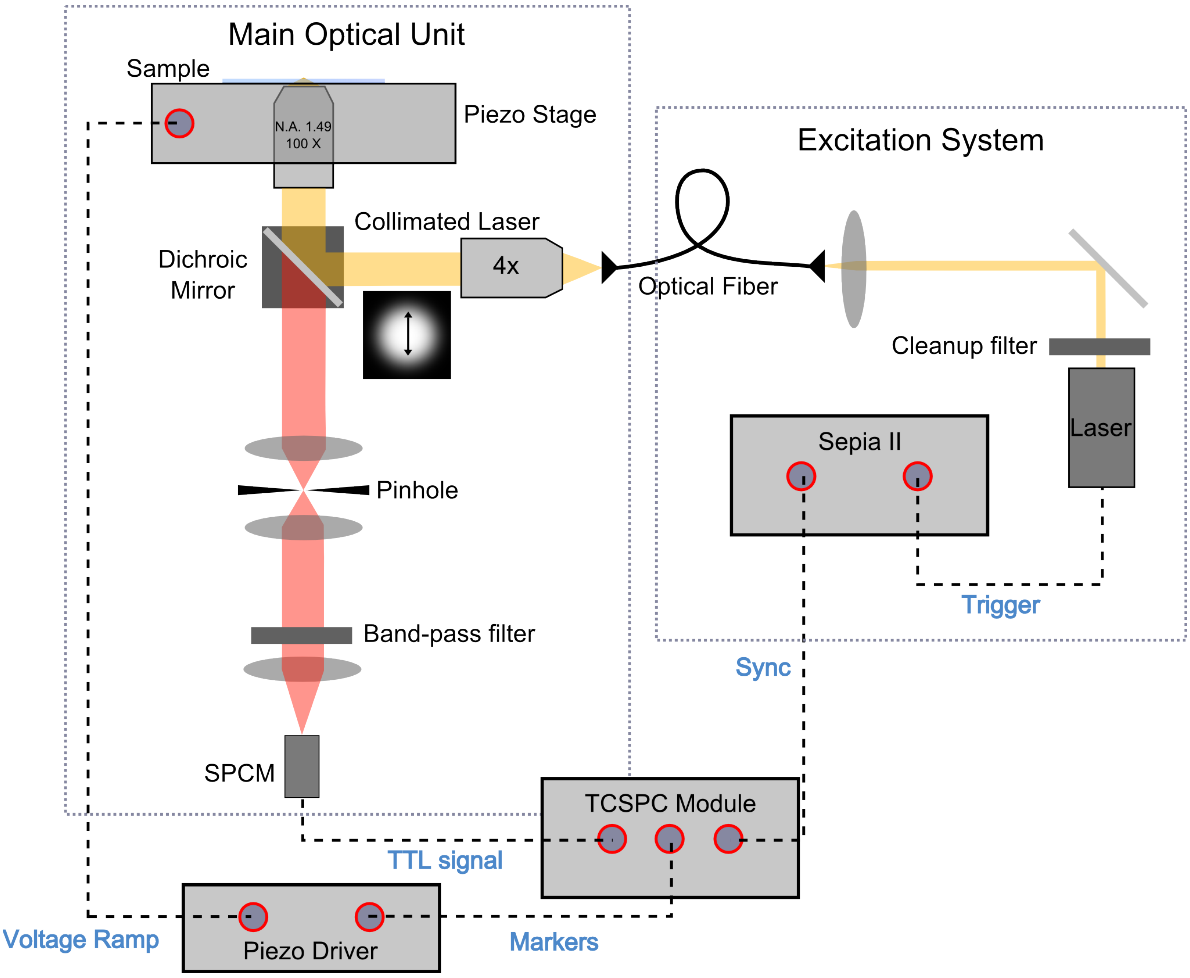

Figure 3.1: A schematic diagram showing the main parts of the Microtime 200 setup. The dashed lines show the synchronization of the various hardware components in the system.

3.1.2 Wide-field Setup for Defocused Imaging

An EMCCD (Electron Multiplying Charge Coupled Device) camera (iXon+ DU-885 K, Andor Technology, 1004 × 1002 pixels and 8 µm × 8 µm pixel size) was coupled to the trinocular observation port of an Olympus IX-71 microscope (Olympus Deutschland). For excitation, a $\lambda = 647\,\mathrm{nm}$ diode laser (PhoxX 647, 140 mW, Omicron Laserage, Germany) was modulated by using the “fire” output of the camera. The linearly polarized laser beam was focused on the back aperture of the objective (UAPON 100XOTIRF, 1.49 N.A., Olympus) that was shifted across the back aperture by using a movable mirror to illuminate the sample in Total Internal Reflection (TIR) mode with an average illumination power of $0.2\,\mathrm{kWcm^{-2}}$. The emission light was collected by using the same objective and passed through a dichroic mirror (Di01- R405/488/561/635-25 X 36, Semrock) and further filtered using a quad-band pass filter (FF01-446/523/600/677, Semrock) before it was focused onto the camera sensor.

3.2 Proof of Principle Experiments

3.2.1 Substrate Preparation

Glass coveslips (thickness 150 µm, refractive index 1.52) were cleaned piranha solution (3:1 v/v ratio of concentrated H_2SO_4 and 30% w/v H_2O_2) for about 15 minutes. These were later washed with water and used as substrates for vapor deposition of 2 nm titanium, 10 nm gold, and SiO_2 spacer of required thickness (20 nm, 30 nm, 40 nm, 50 nm in the order mentioned). The process was carried out under high-vacuum conditions ($\approx 10^{-6}\,\mathrm{mbar}$) by using an electron beam source (Univex 350, Leybold). The slowest rate of deposition was maintained ($1\,\text{Å}\,\mathrm{s^{-1}}$) to ensure maximum smoothness on the surface. The thickness of the layers was monitored by using an oscillating quartz unit during deposition and later verified by using atomic force microscopy. Atto 655 (Atto Tech GmbH) was diluted to 1 nM in Millipore water ($18.2\,\mathrm{M\Omega cm^{-1}}$ at 285 K). An aliquot of this solution (10 mL) was spin-coated onto the substrates prepared at 8000 rpm for 40 s. This dye was used mainly due its reported good photostability in air and long lifetime of around 3 ns [119]. For defocused imaging, substrates were prepared by evaporating 20 nm SiO_2 onto cleaned glass coverslips without any gold layer. Atto 655 (50 pM) was then spin-coated onto these substrates.

3.2.2 Results

The substrates were scanned on the Microtime 200 confocal microscope as described above in the experimental section. The area scans with focused linearly polarized gaussian laser show gaussian intensity patterns at the positions of the single molecules. These patterns were identified with a custom written Matlab algorithm for least square minimization pattern matching [120] using a 2D-gaussian mask. Figure 3.2 shows one such scan image which displays the single molecule intensity patterns identified by the program. The identified positions and pixels were then used on the average lifetime

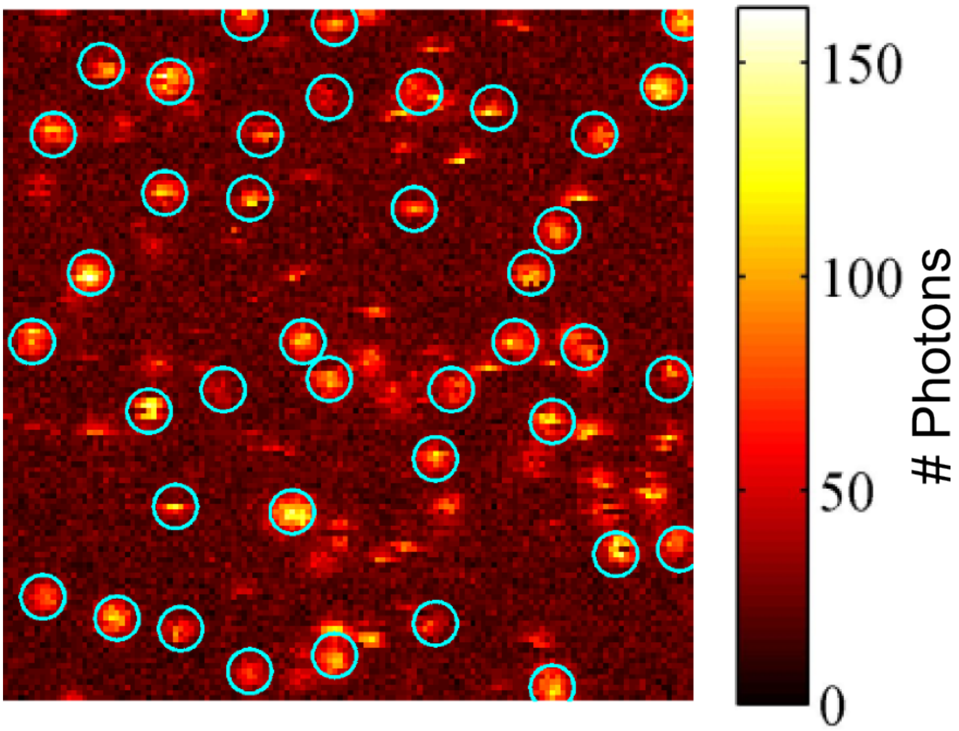

Figure 3.2: A scan image showing intensity patterns of single molecules spin coated on a glass substrate. The gaussian patterns identified by the pattern matching program are marked as cyan circles.

image obtained from the SymPhoTime software in order to calculate the fluorescence decay times for each individual molecule.

Measurements were performed on single molecules deposited on an SiO_2 spacer of various thickness above a thin metal film (2 nm titanium, 10 nm gold) on a glass cover slide. Scans of size 30 µm × 30 µm were acquired with a pixel size of 67 nm × 67 nm and a pixel pixel dwell time of 5 ms. Figure 3.3 shows one such intensity image on a SiO_2 spacer of thickness 30 nm. The background that can be seen on the image is due to the photoluminescence of gold. However, the average arrival time of the photoluminescence photons from a smooth gold surface is less than 2 ps, which does not affect the result of the measurement [122] when the fluorescence lifetime image is calculated by taking the arrival times of photons after a time gate at 0.5 ns after the Instrument Response Function (IRF) peak. The identified molecules without the background are displayed in figure 3.3 on the right panel. We repeated the measurements for four different SiO_2 spacer thicknesses, and the recorded average fluorescence lifetime images are shown in figure 3.4, in which we have already used the identified molecule positions to suppress any background that does not belong to individual molecule's fluorescence. Next, for each spacer thickness, we calculated the distribution of single-molecule fluorescence lifetimes which is shown in figure 3.5. The obtained lifetime values are (0.50 ± 0.06) ns, (0.81 ± 0.07) ns, (1.19 ± 0.08) ns, (1.50 ± 0.08) ns for 20 nm, 30 nm,

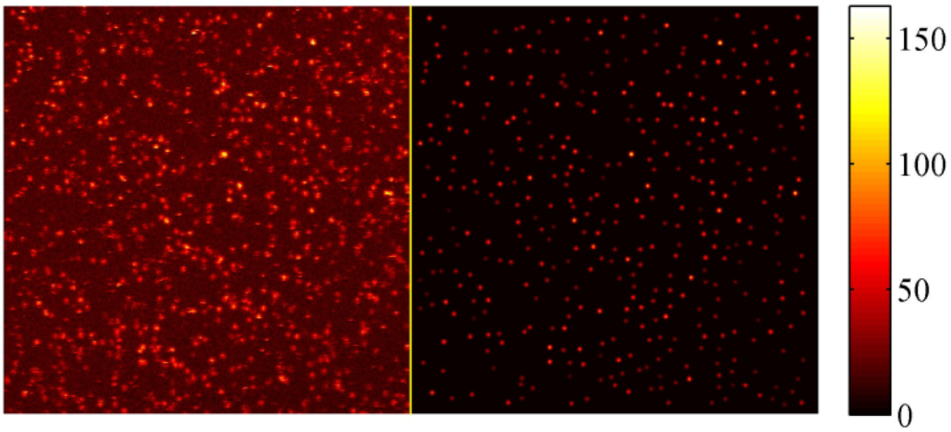

Figure 3.3: Left: Intensity image obtained from experiment. Right: Back-calculated image displaying all single molecules identified from the intensity image. The image size is 30 × 30 µm^2 [This image has been published in the article [121].]

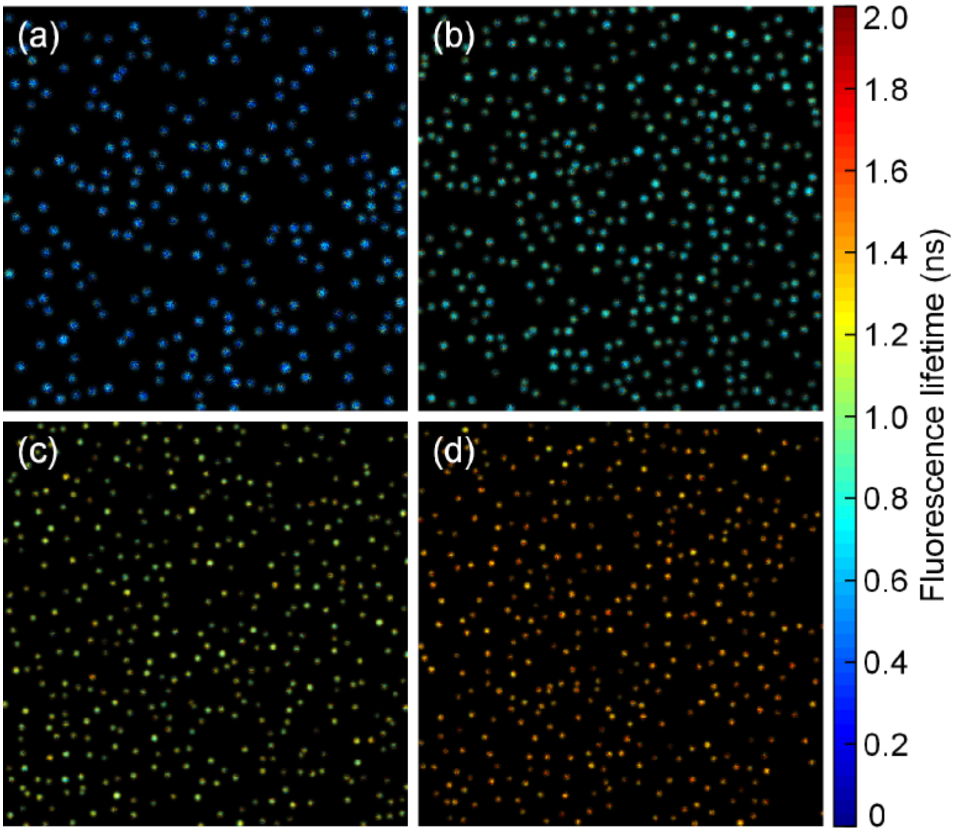

Figure 3.4: Lifetime images for a) 20, b) 30, c) 40, and d) 50 nm SiO$_2$ spacer thicknesses for the identified single-molecule pixels. The color bar shows the color index for lifetime values in nanoseconds. Each image is 30 × 30 µm^2. [This image has been published in the article [121].]

40 nm, and 50 nm spacer thicknesses, respectively.

Now, in order to evaluate the obtained lifetime values, we compare these with the theoretically estimated values using the CPS model (see section 2.4.3). Emission rates for a vertical and a parallel dipole $S_\perp(z)$ and $S_\parallel(z)$) were calculated for heights varying

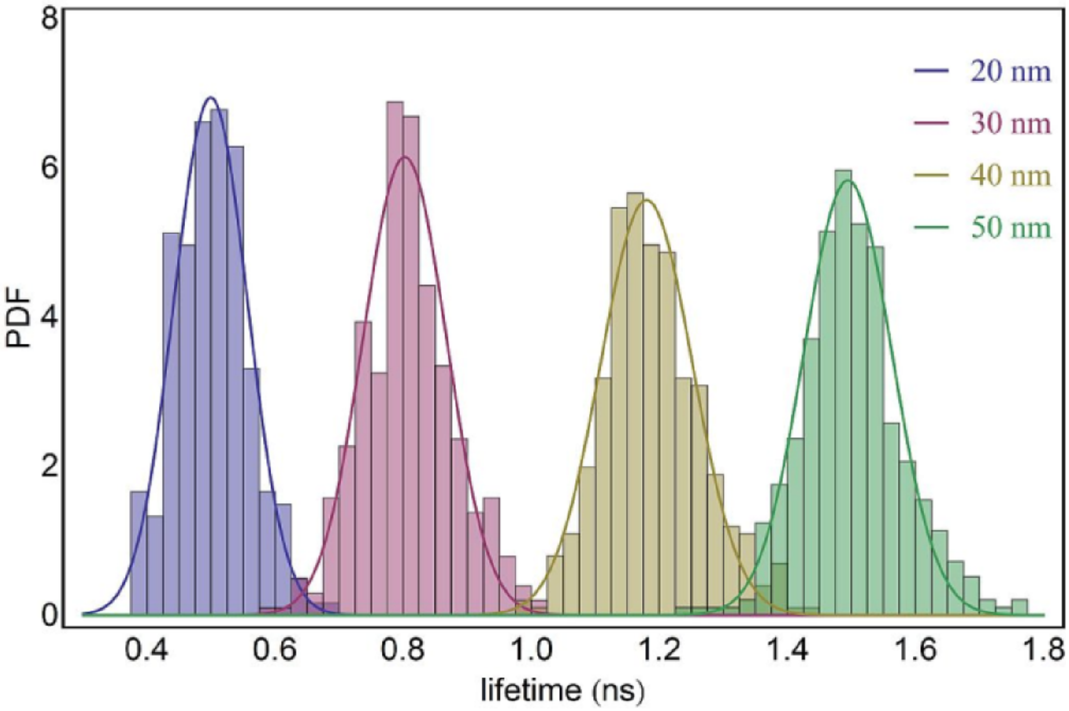

Figure 3.5: Lifetime distributions for the four samples with 20, 30, 40, and 50 nm SiO_2 spacers between the metal film and the deposited molecules. [This image has been published in the article [121].]

from 0 nm to 100 nm from the metal surface by using the bulk refractive indices of gold and titanium at $\lambda = 684\,\mathrm{nm}$ that are taken from the literature: $n_{Au} = 0.1706 + 3.7399i$ and $n_{Ti} = 2.1648 + 3.2552i$ [123]. The value for the quantum yield Φ of the used dye (Atto 655) was set to 0.3 as provided by the manufacturer[1]. using these calculated emission rates, the experimental lifetime values were fitted to equation (2.156) with free-space lifetime τ_0 and angle α (which indicates the ratio of horizontal to vertical dipoles) as free fit parameters. Figure 3.6 shows the fitted data along with curves of the MIET calibration curves for a horizontal and a vertical dipole. The shaded area in between these two curves indicates the possible lifetime values for a dipoles with polar orientation α in between these two extremes. From the fit we find that the observed lifetime–distance behavior is best described if almost all molecules are oriented horizontally, which is expected for dye molecules that are spin-coated from solution onto a flat surface [124].

In order to ascertain this, several defocused images of Atto 655 single molecules were taken on samples prepared by spin-coating Atto 655 on a thin SiO_2 layer (20 nm) evaporated directly on glass coverslips without any metal layer. All the images were acquired with a total exposure time of about 10 s with TIR illumination. The focus of the objective was shifted to $\sim 1\,\mu\mathrm{m}$ above the substrate/air interface. The camera was operated at a temperature of $-80°$ C, a preamp gain of 3.7, and an electron multiplying

---

[1] http://www.atto-tec.com/

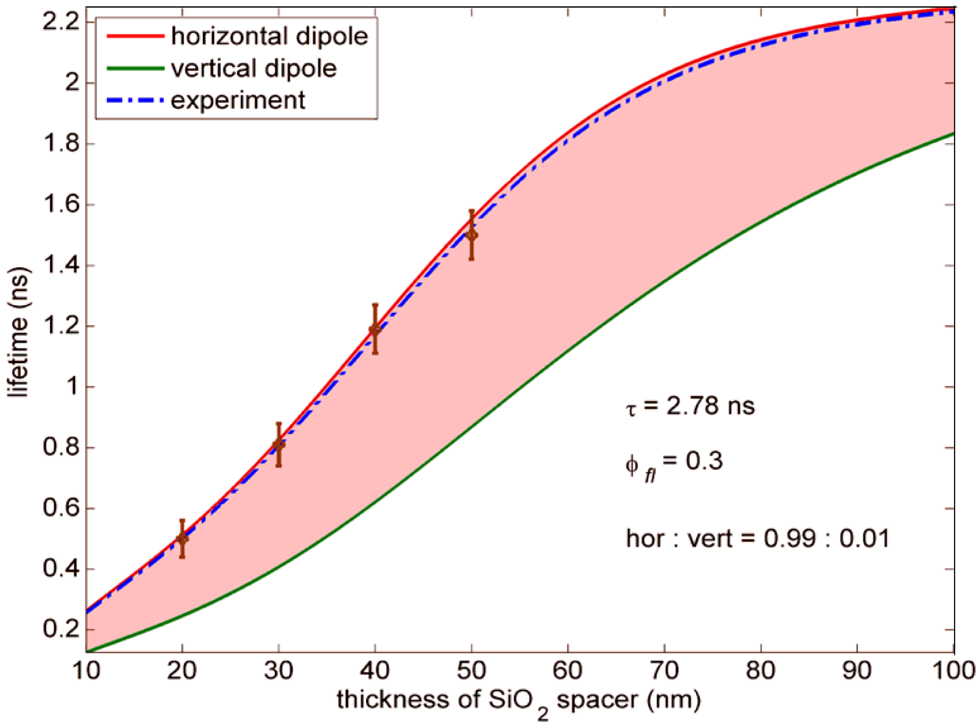

Figure 3.6: Fitting of experimental lifetime values by using equation 2.156. The unperturbed lifetime τ_0 obtained as a fit parameter is 2.78 ns, which is in good agreement with the lifetime of Atto 655 measured on glass/air interface [119]. [This image has been published in the article [121].]

gain of 5 to 10 depending on the brightness of the molecules. The left panel of figure 3.7 shows an exemplary image with defocused patterns of around 20 single molecules on a cropped CCD area of 512 × 512 pixels with an effective pixel size of 80 nm. Model patterns based on exact wave vector calculations were calculated for various orientations and defocusing values (See Patra *et al.* [120] or section 4.3.1 for theory). In order to estimate the correct value of the defocusing, we compared the patterns obtained in the images with computed patterns for horizontal dipoles at various values of defocusing. Because the horizontal dipole pattern at the SiO_2/air boundary is highly sensitive to the focus position, the correct value can be estimated to within 0.1 µm accuracy. For the image shown in figure 3.7 (left), the defocus value was estimated to be $\delta(z) = +0.9$ µm.

Next, we calculated the model patterns of defocused dipoles oriented at 826 different orientations in space (data not shown here, see figure 4.28 for example). These patterns were calculated by individually varying the azimuthal angle β (in-plane) and the polar angle α (out-of-plane) by 5°. The radius for computing the patterns was chosen as 20 pixels and therefore each model pattern is of size 41×41 pixels. For the sake of clarity we show the calculated patterns for various polar angles with a step of 5° in figure 3.8. These

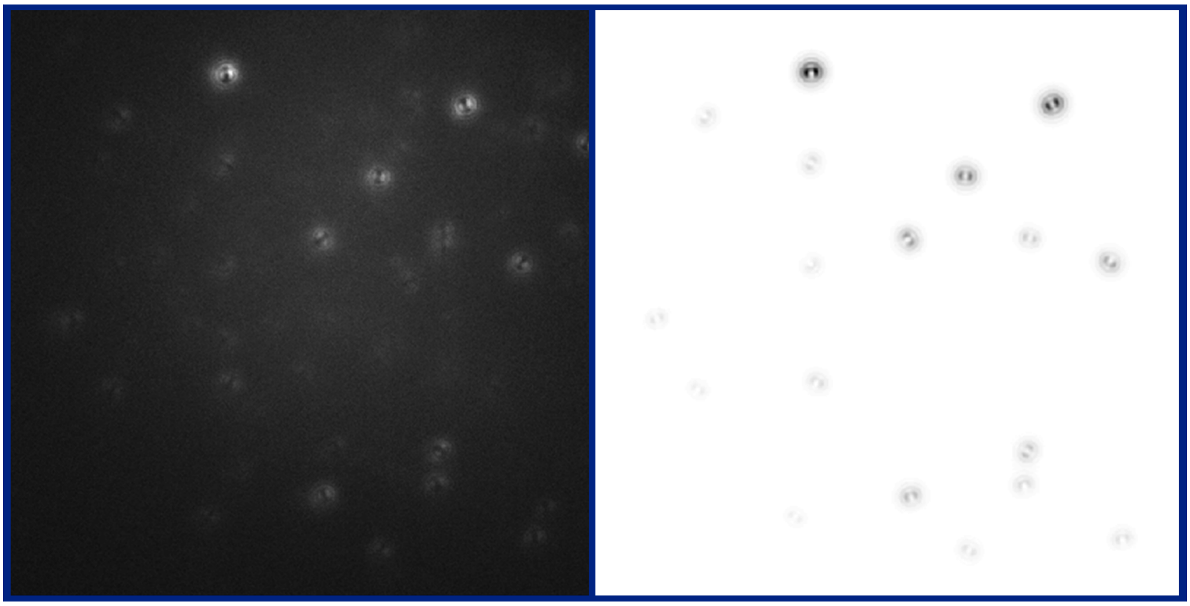

Figure 3.7: Left: Measured defocused image of Atto 655 single molecules on a SiO_2 layer (20 nm) evaporated on a glass coverslip. The image (512×512) was obtained by moving the focus of the objective 0.85 µm above the substrate/air interface. Right: The identified single-molecule patterns from the measured image obtained by pattern matching after background subtraction. The color has been inverted for better visibility.

model patterns were then used to match to the defocused images obtained by using a custom Matlab algorithm using a least squares minimization algorithm (see Patra *et al.* [120] or section 4.1.4 for details.). With such an analysis, the three-dimensional orientations of single molecules can be identified with a resolution of 5° for both the angles. the right panel of figure 3.7 shows the identified patterns of 18 single molecules. Similar pattern matching analysis was carried out on 25 such defocused images, for the same defocusing value, and lastly, a histogram of the inclinations for all the identified molecules was obtained, shown in figure 3.9. The histogram shows that about 268 out of 283 total identified patterns have inclinations $> 75°$. The fitting accuracy depends dramatically on the signal-to-noise (S/N) ratio of the defocused patterns and a poor S/N can deteriorate the resolution for determining the polar angles to as low as 20°, which is the case for most of the defocused patterns obtained in our images (see left panel in figure 3.7). Within these limitations, the result obtained from the distribution of single-molecule inclinations is in good agreement with the fitting result obtained above (figure 3.6) which estimates the percentage of horizontal dipoles.

The values of the fit parameters for equation (2.156), τ_0 and the ratio between horizontal and vertical dipoles, depend on the quantum yield Φ, which we take as 0.3. A slight reduction in the quantum yield, which can be the situation for single molecules at the air/SiO_2 interface, can shift the shaded area in figure 3.5 to higher lifetime values and thereby changes the ratio of horizontal to vertical dipoles. For example, if the quan-

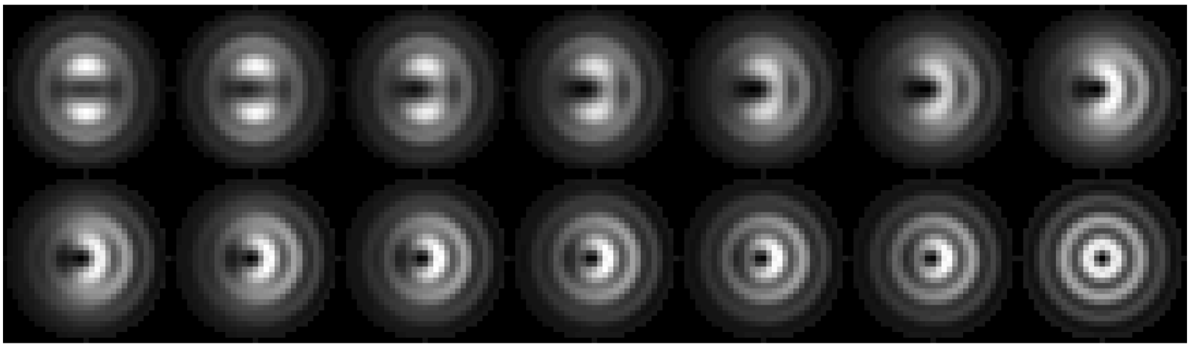

Figure 3.8: Calculated defocused patterns with effective pixel size 80 nm, defocus value 0.85 µm for polar angles $\alpha = 90°$, $85°$,..., $30°$ and $0°$ with respect to the vertical. These calculations were performed at the emission maximum of Atto 655, $\lambda = 680\,\text{nm}$.

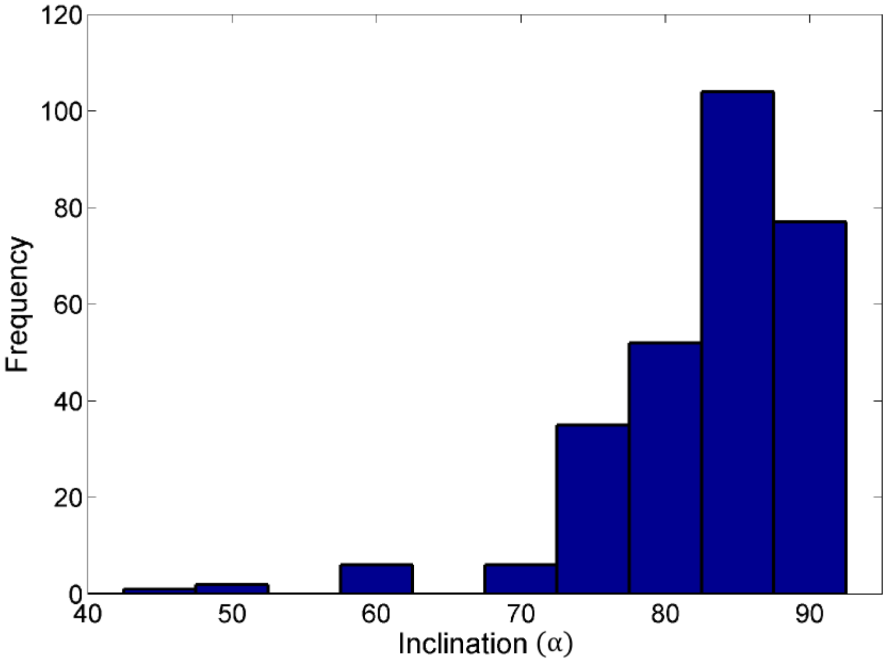

Figure 3.9: Histogram showing the single-molecule inclinations obtained by pattern matching analysis for 25 images taken from different areas in the sample.

tum yield was assumed to be 0.29, the ratio changes to 94:6, whereas the unperturbed lifetime value τ_0 rises to 2.85 ns.

3.2.3 Discussion and Outlook

The error of the observed single-molecule lifetime values is less than 0.1 ns, which corresponds to an axial localization accuracy of less than 2 nm for horizontal dipoles. Since the error of lifetime variation follows Poisson statistics, a reduction in the spread of the lifetime distribution can be achieved by increasing the number of collected photons per molecule, for example, by using suitable oxygen-scavenging protocols to reduce the rate

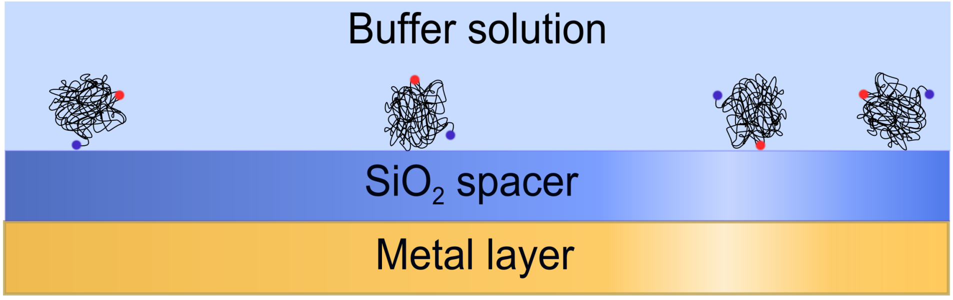

Figure 3.10: An illustration showing the application of smMIET for structural biology. The protein/macromolecule is labelled site-specifically with two labels much similar to FRET. Independent lifetime and orientation measurements are perfomed to obtain the heights of the two labels on each immobilized complex. Carrying out simple statistics, one can derive the distance between the two sites.

of photobleaching [125]. In our current experiments, we detected on average 369, 767, 1002, and 1031 photons per individual molecule for spacer thickness values of 20 nm, 30 nm, 40 nm, and 50 nm, respectively.

The physical basis behind smMIET is the energy transfer from the excited molecule to surface plasmons in the metal and it is thus quite similar to FRET. Unlike FRET where three relative orientation angles between donor emission and acceptor absorption dipoles are needed, which are inaccessible by using any independent measurement, here we need the out-of-plane orientation α of the emitting molecule with respect to the metal surface which can be obtained using the methods mentioned above. Moreover, the distance range over which smMIET works is much larger than FRET and as can be seen from figure 3.6, goes upto 100 nm. Therefore, in order to find its application in structural biology, one would need both the lifetime and orientation for nanometer-precise distance measurements. In our current measurement scheme, the fundamental limitation is that we have no means of measuring the orientation (polar angle) of the molecule simultaneously with the intensity and lifetime. As can be seen from figure 3.6, the relation between distance and lifetime is strongly orientation dependent. There are several options to achieve this, including defocused imaging [120, 126] scanning with radially polarized light [76], or detecting separately sub- and supercritical fluorescence emission [127]. However, all these methods require significant extensions and/or modifications of a conventional confocal laser scanning microscope, some of which we will investigate in the forthcoming chapter.

In combination with such orientation measurements, smMIET can determine distance values of single molecules from a surface with nanometer resolution. Already with our nonoptimized (in terms of photobleaching) measurements we could estimate the distance with accuracy higher than 2.5 nm. Although smMIET achieves this resolution only along one single axis, this method will open new fascinating possibilities for structural biology. For example, for determining the intramolecular distance between two fluorescent labels in a macromolecule, as shown in figure 3.10, one can envision using smMIET to measure the absolute height differences between both labels for a large number of macromolecules immobilized on a surface. Next, one could apply simple statistics to obtain the absolute distance between the labels.

In the forthcoming chapters we will enlist a few existing techniques for measuring the orientations of single molecules. The main focus will be to point out the most feasible method for obtaining the orientations together with the lifetime information in order to extend smMIET as a versatile tool for structural biology.

4 Single-Molecule Transition Dipole Imaging

Abstract

An electronic transition between two molecular energy levels is a redistribution of electron density over the molecule's structure following the interaction with the local electromagnetic field. Molecules that have a preferred direction for such a redistribution show a classical dipole behavior and this direction defines the excitation or emission transition dipole moment. Almost all organic dye molecules behave as electric dipole oscillators. In this chapter, we introduce two well-known methods, one for imaging the excitation transition probability, and the other for the emission transition probability of single emitters. Both of these methods are used for determining the complete three dimensional orientations of these two vectors in space. We apply them for the study of the excitation and emission properties of Carbon Nanodots (CNDs) that are novel fluorescent probes gaining popularity in bioimaging. We show that the CNDs are single dipole emitters similar to organic dyes. Thereafter, we present the first experimental method for determining the geometry of the two transition dipoles and their three-dimensional orientations *simultaneously* for each individual emitter. This directly gives us the angle γ in between both the vectors. We perform experiments on two dye molecule species, and the results show a non-negligible γ. We speculate that this arises due to a significant rearrangement in the backbone structure of the molecule following the excitation as a result of vibrational relaxations before the emission occurs. The feasibility of these two methods for smMIET experiments is also discussed.

Parts of this chapter and some figures have been published in the following journal articles:

1. Ghosh,S.; Chizhik, A.M.; **Karedla, N.**; Debaliuk, M.O.; Gregor,I.; Schuhmann,H.; Seibt,M.; Bodensiek,K.; Schaap, I.A.T.; Schulz,O.; Demchenko,A.P.; Enderlein,J.; Chizhik,A.I. *"Photoluminescence of Carbon Nanodots: Dipole Emission Centers and Electron-Photon Coupling"* Nano Letters **14** 5656-5661 (2014)
2. **Karedla, N.**; Stein, S.; Hähnel, D.; Gregor, I.; Chizhik,A.I.; Enderlein, J. *"Simultaneous Measurement of the Three-Dimensional Orientation of Excitation and Emission Dipoles"* Physical Review Letters **115** 173002 (2015)

4.1 Radially Polarized Laser Excitation

In contrast to a linearly, circularly or elliptically polarized light beam, a radially polarized laser beam has spacially varying polarization across any cross section perpendicular to the propagation direction at a moment of time. More specifically, a radially polarized laser represents an electric field oscillating along the radial direction at any point in its cross section. Figure 4.1 shows such a cross section. There are several ways to produce such a laser beam. Two of the widely used ways are by employing liquid crystal mode converters, or using four/eight half-wave plates oriented in each quadrant/octant in such a way that they rotate the incident linearly polarized laser beam into a radially polarized doughnut beam [128, 129].

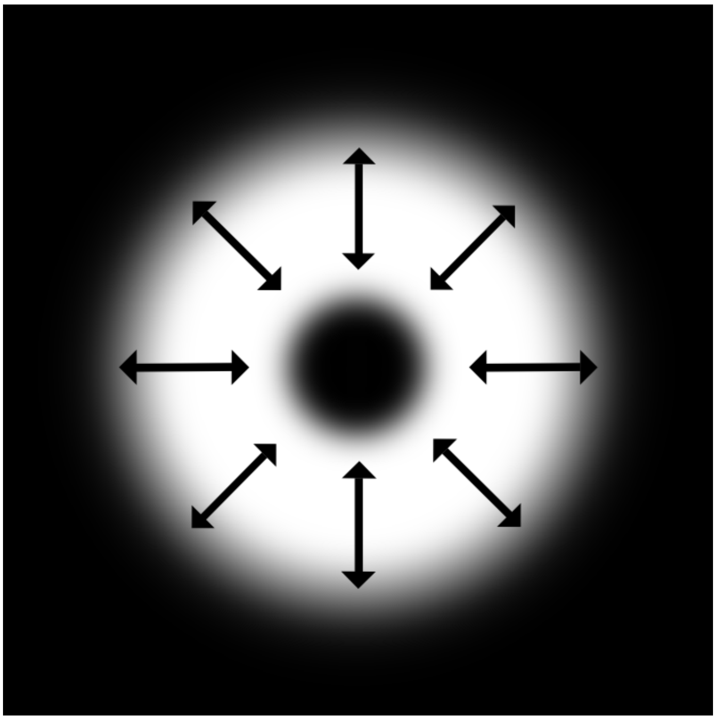

Figure 4.1: A radially polarized laser beam cross section. The double arrows show the plane of electric field oscillations. The polarization in the center is undefined. Note the axial symmetry and doughnut like intensity profile.

Let us define a coordinate system such that the z-axis is along the direction of the propagation of the beam. Then the electric field, before focusing into an objective, can be written as:

$$\mathbf{E_0} = f_r(r) \begin{pmatrix} E_0 \cos\phi \\ E_0 \sin\phi \\ 0 \end{pmatrix} \tag{4.1}$$

where ϕ is the angle measured from a defined direction, say the vertical with respect to

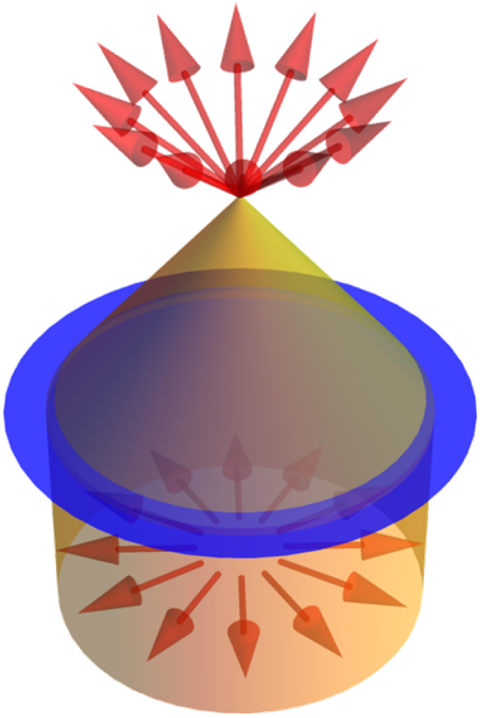

Figure 4.2: A radially polarized laser focused through a lens. The arrows point the electric field polarization before and after lens. At the optical axis in the focus, the electric fields add up to yield only a net z-polarized electric field.

the laboratory reference frame. The function $f_r(r)$ is the shape factor which accounts for the doughnut intensity profile, which can be assumed as a Gaussian function of radius r with maximum at a certain r_0 and width $r_0/2$ as a simple approximation; $f_r(r) = e^{-[(r-r_0)^2/r_0]}$. Now, if one places a linear polarizer in the beam path and rotates it, a dumbbell shaped intensity profile rotates according to the plane of the polarizer.

We would now like to study the structure of the electromagnetic field when such a radially polarized beam is focused to a point through an objective, which will be assumed as ideal lens system without any kind of aberrations. For the sake of simplicity, let us consider the situation where the medium on the other side of the lens is homogeneous, and has a refractive index n. The basic theory below can be extended to the more realistic case where there is a dielectric interface in between the lens and the focal plane. The beauty of the problem can be appreciated when one realizes the perfect radial symmetry of the beam around the optical axis. Figure 4.2 shows a simple geometrical picture of the situation in hand. At the focal point $\mathcal{O}$, the electric field vectors are arranged in a conical fashion as shown in the figure. Therefore, on the optical axis, they add up to yield a net z-polarized electric field, the longitudinal component of the field in the focal plane. On the other hand, moving approximately $\lambda/3$ away from the point $\mathcal{O}$ along any direction in the focal plane $\mathbf{r_p}$, the opposite vectors are now in-phase and add up to yield a net transverse electric field along the unit vector $\hat{\mathbf{r}}_p$.

A more precise treatment of the problem can be done by pursuing the work performed by Török and coworkers [130]. Writing the time-independent electric field at point $\mathbf{r}_p$ as a summation of plane waves, we have:

$$\mathbf{E}(\mathbf{r_p}) = -\frac{ik}{2\pi} \iint_{\Omega} \frac{\mathbf{a}(s_x, s_y)}{s_z} e^{ik(\hat{\mathbf{s}} \cdot \mathbf{r_p})} \, \mathrm{d}s_x \mathrm{d}s_y \tag{4.2}$$

where $\mathbf{s}$ is the vector along a light ray from the lens to the focus $\mathcal{O}$, $\mathbf{a}$ is the electric field vector after the lens and k is the wave number. The integral is defined over the solid angle Ω which is defined by the numerical aperture of the lens/objective. Now what remains is the calculation of the electric field $\mathbf{a}$ after the lens, as a function of the rays passing through the lens and propagating along the direction of vector $\mathbf{s}$ to the focal point $\mathcal{O}$. This can be done by taking the incident electric field $\mathbf{E_0}$ and rotating its angle by θ as it traverses through the lens.

$$\therefore \mathbf{a}(s_x, s_y) = \cos^{1/2}\theta f_r(\theta) \begin{pmatrix} E_0 \cos\phi \cos\theta \\ E_0 \sin\phi \cos\theta \\ E_0 \sin\theta \end{pmatrix} \tag{4.3}$$

where the factor $\cos^{1/2}\theta$ comes from the fact that the system follows Abbe's sine condition [131]. Note that now the shape function f_r is written in terms of θ instead of r. Transforming the integral variables s_x and s_y into spherical coordinates, we have

$$\mathbf{E}(\mathbf{r}_p) = -\frac{ik}{2\pi} \iint_{\Omega} \frac{\mathbf{a}(\phi, \theta)}{s\cos\theta} e^{ik(r_p \kappa)} \, \sin\theta \sin\theta \mathrm{d}\theta \mathrm{d}\phi \tag{4.4}$$

where $\kappa = n[\sin\theta \sin\theta_p \cos(\phi - \phi_p) + \cos\theta\cos\theta_p]$, $s_z = s\sin\theta$, and n is the refractive index of the medium. Splitting the total electric field as its x, y, z components, we have:

$$\mathbf{E}(\mathbf{r_p}) = \begin{pmatrix} e_x(\mathbf{r_p}) \\ e_y(\mathbf{r_p}) \\ e_z(\mathbf{r_p}) \end{pmatrix} = \begin{pmatrix} -E_0 \frac{ik}{2\pi} \int_0^{\theta_{\max}} \int_0^{2\pi} f_r(\theta) \cos\phi \cos^{3/2}\theta \sin\theta e^{ik_0[r_p\kappa]} \mathrm{d}\phi \mathrm{d}\theta \\ -E_0 \frac{ik}{2\pi} \int_0^{\theta_{\max}} \int_0^{2\pi} f_r(\theta) \sin\phi \cos^{3/2}\theta \sin\theta e^{ik_0[r_p\kappa]\mathrm{d}\phi} \mathrm{d}\theta \\ -E_0 \frac{ik}{2\pi} \int_0^{\theta_{\max}} \int_0^{2\pi} f_r(\theta) \cos^{1/2}\theta \sin^2\theta e^{ik_0[r_p\kappa]} \mathrm{d}\phi \mathrm{d}\theta \end{pmatrix} \tag{4.5}$$

where $\theta_{\max}$ is the maximum aperture of the objective or lens. It must be noted here that if in the expression of transverse component e_x, ϕ is replaced by $(\pi/2 - \phi)$, it yields the expression for the field component e_y because of the axial symmetry. Using the identity,

$$J_\nu(x) = \frac{1}{2\pi i^\nu} \int_0^{2\pi} \cos(\nu\theta) e^{ix\cos\theta} \, \mathrm{d}\theta \tag{4.6}$$

the integral for the fields over ϕ can be written in terms of Bessel functions, and the complete field in the focus can be written in terms of a transverse component e_t and a longitudinal component e_z as follows [132]:

$$\begin{pmatrix} e_t(\mathbf{r_p}) \\ e_z(\mathbf{r_p}) \end{pmatrix} = \begin{pmatrix} E_0 k \int_0^{\theta_{\max}} f_r(\theta) \cos^{3/2}\theta \sin\theta e^{ik[r_p \cos\theta \cos\theta_p]} J_1(k r_p \sin\theta \sin\theta_p) \mathrm{d}\theta \\ 2iE_0 k \int_0^{\theta_{\max}} f_r(\theta) \cos^{1/2}\theta \sin^2\theta e^{ik[r_p \cos\theta \cos\theta_p]} J_0(k r_p \sin\theta \sin\theta_p) \mathrm{d}\theta \end{pmatrix} \tag{4.7}$$

The complete treatment for the case when one focuses such a doughnut beam through a high numerical aperture objective (N.A. = 1.49) through a dielectric interface involves the calculation of the transmitted field using Fresnel equations and transmission coefficients [130]. Since the electric field has only p-waves in any plane containing the ray and the optical axis, the problem is much simpler and the field vector $\mathbf{a}$ after the dielectric interface can be written similar to equation 4.3:

$$\mathbf{a}(s_x, s_y) = \cos^{1/2}\theta_1 f_r(\theta_1) \begin{pmatrix} R_p E_0 \cos\phi \cos\theta_2 \\ R_p E_0 \sin\phi \cos\theta_2 \\ R_p E_0 \sin\theta_2 \end{pmatrix} \tag{4.8}$$

where R_p is the reflection coefficient for the p-waves as given in equation (2.61); θ_1 and θ_2 are the angles of the ray with respect to the optical axis before and after the dielectric interface related to each other by Snell's law of refraction, $n_1 \sin\theta_1 = n_2 \sin\theta_2$. Proceeding as above, one can write equations for the transverse and longitudinal and transverse field components similar to equations (4.7). Figure 4.3 shows the calculated intensities of both components above a glass/water interface.

The longitudinal component of the field arises due to the interference of the p-waves from all angles around the focus. In principle, since there is no electric field along the optical axis before and after the lens, the Poynting flux along this axis is zero. Thus, the longitudinal component has to be a non-propagating field. This field component can be probed only by monitoring the fluorescence intensity of a molecule that can couple with it [70]. This is similar to exciting a molecule with the non-propagating evanescent waves in TIR excitation. The amplitude of this field, as can be seen from figure 4.3, is much stronger as compared to the transverse component and it increases with the increase in N.A. of the lens. The structure in the focal plane can be obtained by putting $\theta_p = \pi/2$ in equation (4.7). Figure 4.4 shows the field components in the focal plane for a lens of numerical aperture (N.A.) 1.49 on a glass/air interface.

4.1.1 Excitation Patterns

Almost all of the fluorescent molecules can be approximated as electric dipole oscillators, and many of the absorption and emission properties can be described under this assumption. However, exceptions exist, such as NV$^-$ color centers in diamonds, rare-earth metal-chelates which behave as two dimensional degenerate dipoles, magnetic dipoles. Substituted metal-free phthalocyanine and porphyrazine structures exhibit fast

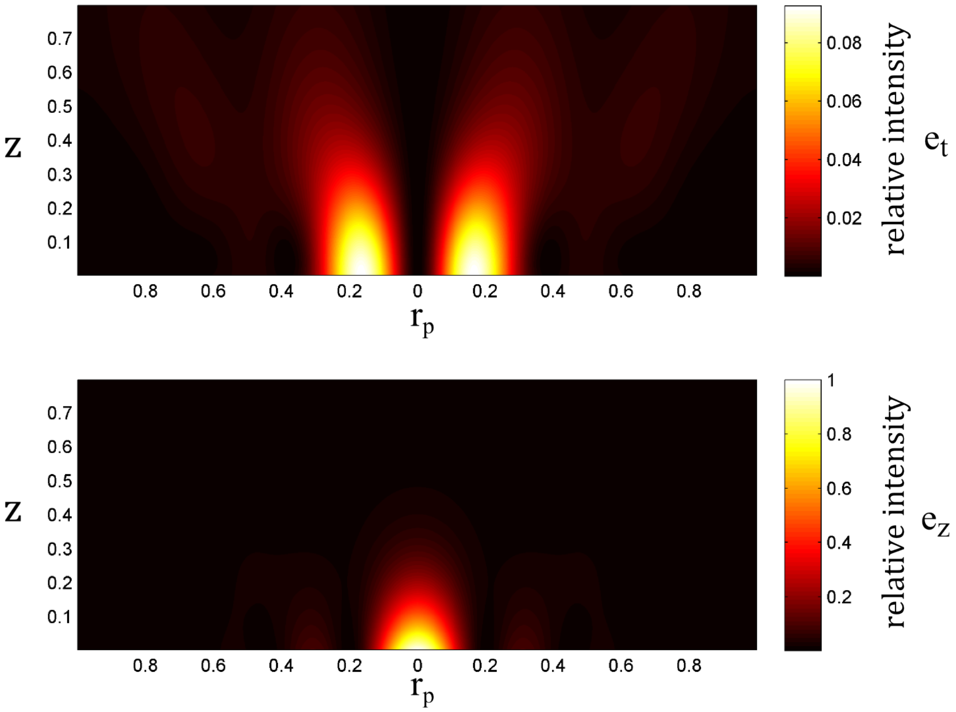

Figure 4.3: Top: The intensity of the transverse field components in a xz-plane on top of the glass surface in glass/water interface. The optical axis is along the zero $\rho = 0$. All dimensions are in μm. The intensity is normalized to the maximum of the longitudinal component. Bottom: The intensity of the longitudinal component in the focus.

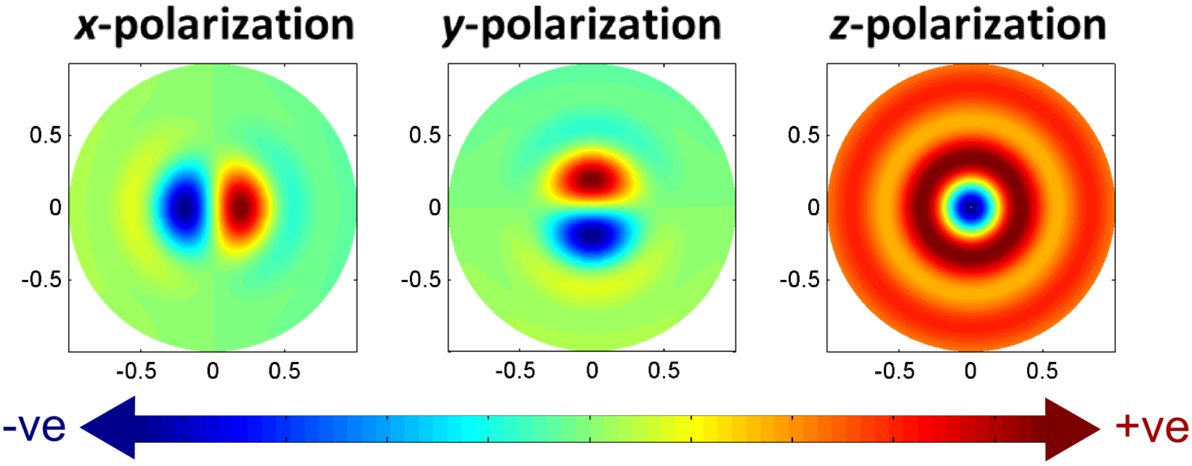

Figure 4.4: Electric field components and phase in the focal plane of a radially polarized focus can be seen as a summation of electric fields of polarizations around the x, y and z-axes. Calculations performed for N.A. = 1.49 at the glass/water interface. All axes in μm.

photo-induced tautomerization between their *cis-* and *trans-* molecular conformations such that they behave as double-dipole structures [75].

Scanning immobilized a single molecule with a focused radially polarized laser beam produces an intensity pattern as a function of position which relates to the probability of exciting it with the structured electric field inside the focal volume. The probability to

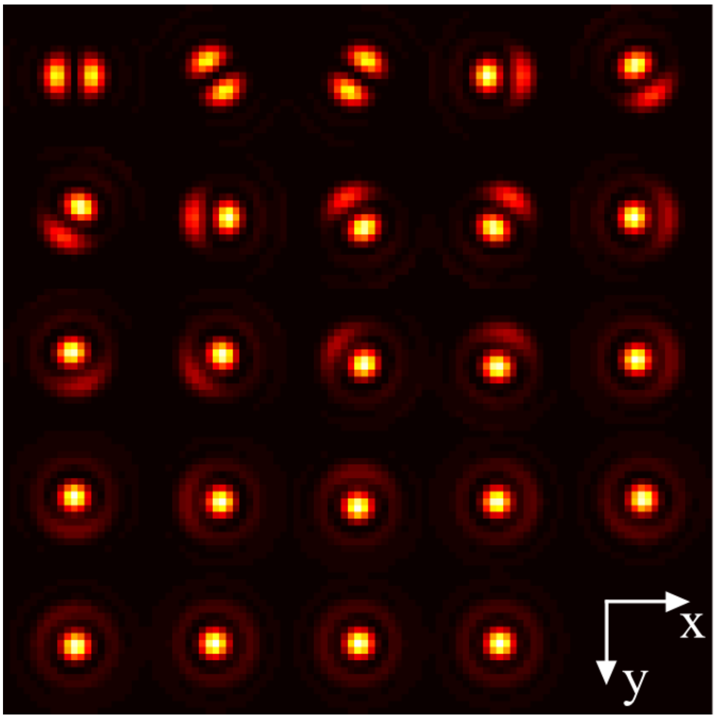

Figure 4.5: Calculated intensity scan patterns of single dipoles with a focused radially polarized laser excitation. The N.A. of the objective was 1.49, pixel size 50 nm at wavelength $\lambda = 514$ nm. The molecules are assumed to be on top of an air/glass interface, and the minimum angle for illumination $\theta_{\min}$ was set to be $\sim 20°$. Each pattern spreads over ~ 1 µm. Note that the images show normalized intensities. From top left to bottom right, α and β values are:

Column/Row	1 α, β	2 α, β	3 α, β	4 α, β	5 α, β
1	90°, 0°	90°, 60°	90°, 120°	75°, 0°	75°, 60°
2	75°, 120°	75°, 180°	75°, 240°	75°, 300°	60°, 0°
3	60°, 72°	60°, 144°	60°, 216°	60°, 288°	45°, 0°
4	45°, 90°	45°, 180°	45°, 270°	30°, 0°	30°, 120°
5	30°, 240°	15°, 0°	15°, 180°	0°, 0°	–, –

excite a molecule is proportional to the component of the electric field oriented parallel to its transition dipole, and therefore the intensity recorded as a function of position can be written was $I_f \propto |\mathbf{E}(\mathbf{r}) \cdot \mathbf{p}_{\text{exc}}|^2$, the proportionality constant being the collection efficiency of the system and the quantum yield of the dye. Unique intensity patterns for various orientations of the excitation dipole $\mathbf{p}_{\text{exc}}$ are obtained. Figure 4.5 shows calculated patterns for a few orientations of the excitation transition dipole.

Depending upon the orientation of the $\mathbf{p}_{\text{exc}}$, different proportions of the longitudinal and transverse components in the focus excite the molecule. Notice that for molecules lying flat on the surface ($\alpha = 90°$), the patterns have two C_{2v} symmetry planes, one along the dipole orientation, and the second perpendicular to it. Therefore, for the azimuthal angles β and $\beta + 180°$, identical scan patterns are observed. Due to the strong longitudinal component at the optical axis, orientations close to vertical, ($\alpha <$

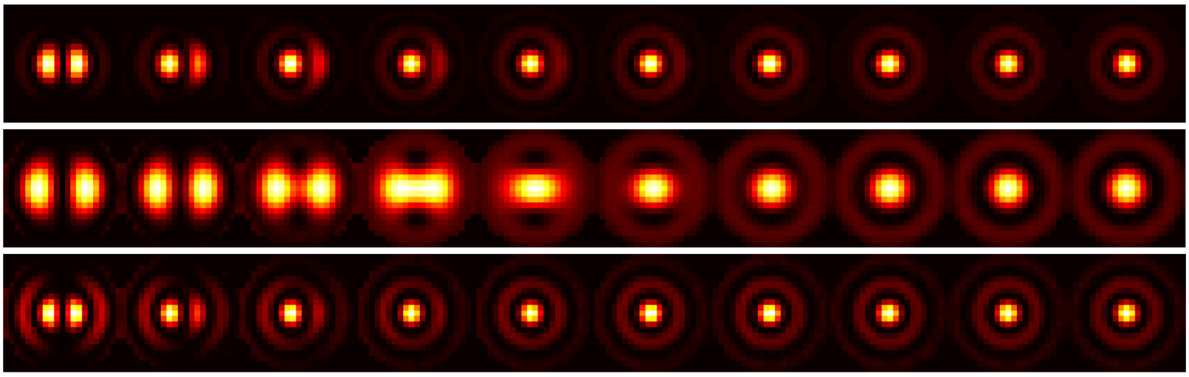

Figure 4.6: The top row shows excitation intensity patterns taken with a full beam, completely filling the back aperture of a 1.49 N.A. objective with a doughnut which leads to a $\theta_{\mathrm{min}} \approx 20°$. The middle row represents the patterns for a subcritical angle excitation, $\theta_{\mathrm{min}} \approx 20°$ and $\theta_{\mathrm{max}} \approx 36°$; and the bottom row for a TIRF excitation $\theta_{\mathrm{min}} \approx 52°$ and $\theta_{\mathrm{max}} \approx 78°$. The polar angles α of the dipole for the patterns left to right are $90°, 80°, ..., 10°, 0°$. Note that the images show normalized intensities.

60°), appear nearly indistinguishable. The ratio of the longitudinal and transverse components depends upon the N.A. of the objective and the size of the doughnut in the center. As described previously, an increase in N.A. increases the longitudinal component, which can be mainly attributed to the plane waves approaching the focus at high angles. On the other hand, reducing the size of the doughnut increases the in-plane radially-polarized transverse field. Figure 4.6 shows the scan images for a narrow excitation beam width such that the angles formed by the rays are below the critical angle at the air/glass interface ($\theta_c < 41.14°$, subcritical angle excitation) and images formed with a focus achieved from excitation rays above the critical angle (TIR excitation). Two important points must be stressed: 1) The excitation patterns formed by the subcritical excitation are spread over a larger area covering more pixels; 2) whereas in the case of TIR excitation, the patterns show pronounced side rings as compared to the full-beam excitation.

4.1.2 Experimental Setup

A custom-built confocal microscope with a pulsed white-light laser was used where the excitation beam path was modified with a liquid crystal mode converter (ARCoptix S.A.) in order to produce a radially polarized beam. The detailed setup description is as follows:

1. **Excitation system**: A circularly polarized pulsed white-light laser (Fianium SC400-4-80) with a pulsewidth of 50 ps and 20 MHz repetition rate was split into two linearly polarized beams using a polarizing beamsplitter. Each beam together with an acousto-optic tunable filter (AOTFnC-400.650-TN) served as independent excitation sources. The spectrally filtered polarized beams were coupled into separate polarization-maintaining single-mode optical fibers (PMC-400-4.2-NA010-3-

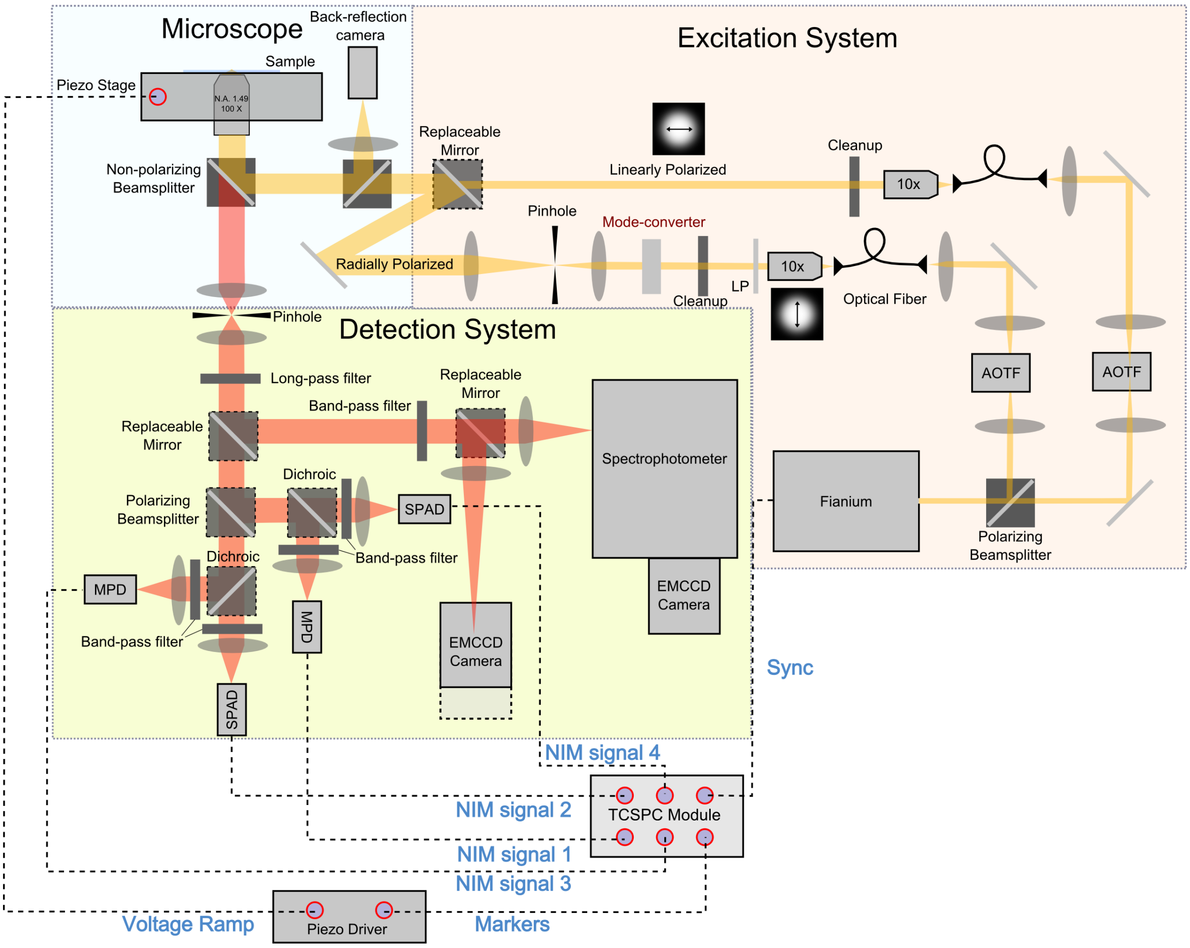

Figure 4.7: Sketch of the complete experimental setup. The excitation beam paths are shown in yellow whereas the emission is guided through the paths marked in red.

APC- 250 V, Schäfter and Kirchhoff, Germany), and thereafter collimated out to two individual beams of 4 mm diameter using infinity-corrected 10× objectives (UPLSAPO10X, Olympus). This step ensures a high quality TEM$_{00}$ (Transversal electromagnetic) mode excitation beam required for the experiments. A clean-up filter depending upon the wavelength required for the experiment (for eg., Z640/10X, Chroma Technology) was used to block unwanted wavelengths from the laser after the collimation. Whereas the horizontally polarized collimated light source was coupled directly into the microscope, the vertically polarized beam was led through a series of optical elements to generate a radially polarized laser. A mirror mounted on a magnetic flipping system (KB75/M, Thorlabs Inc.) was used to select between the two excitation sources. For the mode-conversion, an additional linear polarizer (LPVISE 100-A, Thorlabs Inc.) was added to further ensure the polarization of the beam, which is crucial for the beam quality after the mode-conversion. This beam was then passed through the liquid crystal cell (ARCoptix S.A.) which rotates the incident polarization into a radially or azimuthally polarized Laguerre-Gaussian beam depending if a voltage is supplied to the polarization rotator cell present in the mode converter or not. For a complete description of the mode converter, the reader is referred to the documentation of the device (http://www.arcoptix.com/index.htm). Thereafter, the beam was focused into a 25 µm pinhole and collimated up using a pair of achromatic doublet lenses (AC254-075-A,AC254-150-A, Thorlabs Inc.). This step is essential in order to reject any unnecessary higher order modes which might be present after the mode-conversion.

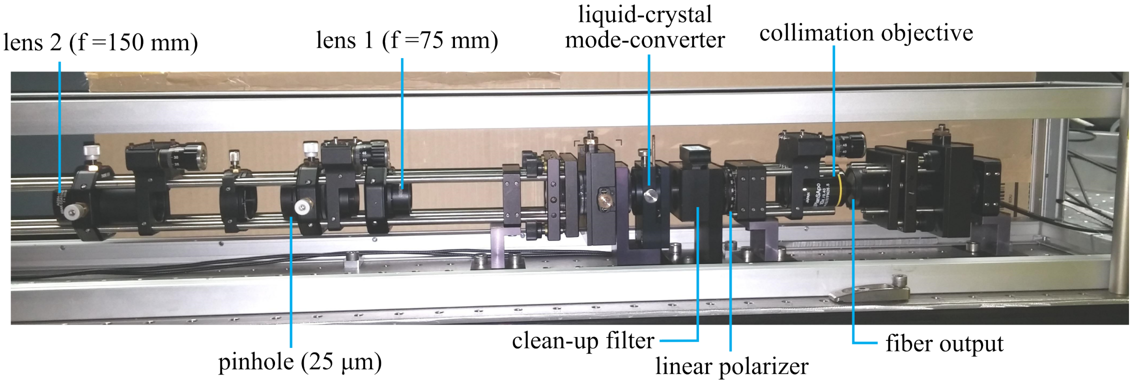

Figure 4.8: Generation of a radially of azimuthally polarized laser beam from a linearly polarized beam. Linearly polarized laser is collimated using an objective, mounted on a z-translation mount (SM1Z, Thorlabs Inc.) on the right end. The liquid crystal mode converter is mounted on a custom built mount which is coupled to an xy-translation (ST1XY-A/M, Thorlabs Inc.) and tilt stages (KC1-T, Thorlabs Inc.) for aligning the liquid crystal cell with respect to the incident beam. Thereafter, the output beam from the mode converter is focused through a pinhole for mode cleaning.

2. **Microscope**: The excitation sources were reflected onto a 30 R : 70 T non-polarizing beamsplitter cube inside the microscope into the back aperture of a high N.A. objective (UAPON 60XOTIRF, 1.49 N.A., Olympus). The non-polarizing beamsplitter is used here instead of a dichroic mirror in order to ensure that the beam is devoid of any unwanted polarization or astigmatic aberrations. This leads to the loss of fluorescent photons. A better solution to this drawback would be to use a 10 R : 90 T beamsplitter and higher excitation laser power. The sample was fixed on top of a piezo stage (P-562.3CD, Physical Instruments) that was driven using a digital piezo controller (E-710.3CD Physical Instruments). The collected fluorescence (through the same objective) is focussed onto a pinhole of 100 µm through a tube lens ($f = 180\,\mathrm{mm}$) for confocal imaging. A part of the laser is reflected back into the excitation pathway by the beamsplitter. For excitation beam diagnosis, a 10 R : 90 T beamsplitter was introduced into the excitation pathway. The 10% of the back-scattered laser was then focused onto a sensitive CCD camera (Pike F145B, 15 fps, Allied Vision Technologies), which we refer to as the back-reflection camera.

3. **Detection system**: After it was passed through the pinhole, the emission light

was recollimated using an achromatic doublet (AC254-150-A, Thorlabs Inc.). Since we use a non-polarizing beamsplitter in place of a conventional dichroic mirror, the backscattered laser was blocked using a long-pass filter, depending upon the excitation wavelength (for eg. EdgeBasic BLP01-647R, Semrock). Thereafter, the emission light can be guided into three subdetection systems using a custom designed flipping mirror assembly:

- single photon counting detection system
- high sensitivity spectrophotometer
- defocused imaging

For this section, the single photon counting subsystem mode was used and thus will be described here in detail. This subsystem has a two-color two-polarization detection scheme consisting of four single photon avalanche photodiodes (2 × τ-SPAD and 2×Micro Photon Devices (MPD), Picoquant). Their maximum detection efficiency of 70% and 50% is at wavelengths $\sim$ 700 nm and $\sim$ 500 nm respectively. The emission light was first split using a polarizing beamsplitter (PBS251, Thorlabs Inc.), and later spectrally divided by two dichroic mirrors (for eg. FF580-FDi01, Semrock) which were mounted in custom-built replaceable cube/plate holders. The photons were focused onto the active area of the detectors (diameter$\sim 100-150$ µm) using achromatic lenses (2×AC254-030-A, Thorlabs Inc.). The two-color two-detector scheme allows us a broad range of options for the detection of emission photon stream and choice of experiments such as anisotropy and rotational diffusion measurements, fluorescence correlation, antibunching experiments, and cross correlation experiments with up to four spectral channels. Band-pass filters can be used in front of the photodetectors in order to narrow down the spectral range of the detected photons around the maximum emission wavelengths of the fluorescent species and improve the signal-to-background ratio (for eg. FF01-692/40 Semrock, FF02-525/40 Semrock, for Atto 655, Green Fluorescent Protein, respectively).

For the work presented in this section, we use only one $\tau-$SPAD unless/otherwise mentioned. The details of the remaining subdetection systems will be explained in detail in the relevant sections in this thesis.

4. **Data acquisition and synchronization**: The scanning, data recording, synchronization of all the hardware and measurement visualization was done using a custom written LabView software. The NIM (Nuclear Instrumentation Module) output from the detectors were recorded and timed with a 2 ps time resolution using a multichannel event timer and Time Correlated Single-Photon Counting (TCSPC) module (HydraHarp 400, PicoQuant) in the Time-Tagged Time-Resolved (TTTR)

acquisition mode. We use a HydraHarp 400 (PicoQuant, Berlin) for most of the experiments. This event timing module has the capability to incorporate upto 64 input channels, while using one channel for an input from an external periodic signal such as a pulsed laser. The detection channels can be used for recording photons separated on the basis of their polarization or wavelength as was shown in the setup designs in figure 4.7. By plotting a histogram of the arrival times with respect to the preceding laser syncs (microtimes) of all the photons in their respective channels, one has the classical TCSPC for each detector; and by binning the photons using their macrotimes, into time bins of several microseconds to milliseconds, we get intensity time traces for each detection channel. In this way one can perform all correlation based experiments (FCS, FLCS, etc.), Fluorescence Lifetime Imaging Microscopy (FLIM), and several other types of data evaluation on the photon data stream depending upon the nature of the experiment and study processes from picoseconds to seconds range. The line-markers, representing the start and end of a scan line were obtained from the piezo controller and recorded as 'special' photons by the TCSPC module itself. The recorded data was later processed using custom written Matlab routines.

Alignment

One need not mention the necessity, and the arduous effort required, for a proper alignment in a custom-built microscope. In this section we describe the most pressing alignment details for a good quality radially or azimuthally polarized excitation. As described in the previous section, we use an apochromatic objective to collimate the laser out of a polarization-maintaining single-mode optical fiber to obtain a high quality TEM_{00} mode. The vertically polarized collimation beam was centered on the window of the mode converter in order to ensure a symmetric radially polarized beam. Any tilted or shifted incidence of the beam on the mode converter would show up as asymmetry in the beam cross section after passing through the pinhole. After this, the radially polarized beam is reflected into the microscope with a set of mirrors giving us the freedom to shift and tilt the beam for a centered and normal incidence in the back aperture of the objective. In order to achieve this, the image formed on the back-reflection camera is useful. When the glass/air interface of a usual coverslip is in the focal plane of the objective, the back reflected light is focused onto the camera. For a perfectly aligned excitation system, the spot defocuses symmetrically on the back reflection camera when the objective is moved up or down relative to the focus position. Any tilt, or shift would then show up as an asymmetric and shifting image on the camera. Further, aberrations such as astigmatism show up as an elliptical or distorted spot on the image when the objective is in the focus position.

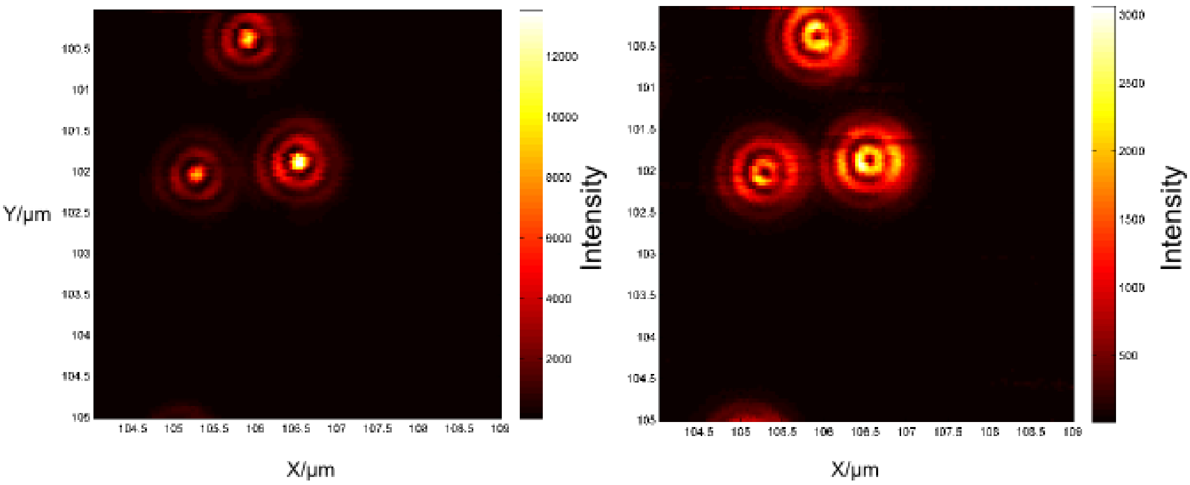

Figure 4.9: Excitation intensity patterns of fluorescent beads (Nile Red, 20 nm) scanned with a radially polarized laser (left) and an azimuthally polarized laser (right) with a wavelength $\lambda_{\mathrm{exc}} = 488$ nm with a 1.49 N.A. objective.

The conclusive check for the doughnut beams was done by scanning ∼ 20 nm fluorescent beads on a surface. These beads contain ∼ 200 single dye molecules oriented randomly inside and therefore act as isotropic absorbers/emitters with respect to electric field polarization. This method was used previously to check the mode of the beams [75]. A diluted solution of beads is spin-coated gently at a speed of 800 rpm on top of a clean glass coverslip distributing them in such a way that they can be probed by our excitation focus individually. Scanning them with the generated radially polarized laser and subsequently with an azimuthally polarized laser[1] focused at the glass/air interface probes the structure of the electric field present in the focus. Figure 4.9 shows a scan image of such beads with a well aligned beam.

4.1.3 Single-Molecule Excitation Images

Samples were prepared by spin-coating dye molecules over plasma cleaned glass coverslips (refractive index = 1.52, thickness ∼ 170 µm, Menzel). The dye molecules were dissolved either in water/organic solvent, or in a diluted polymer solution such as 0.1% w/v Poly(vinyl alcohol) (Mowiol 4-98, Sigma-Aldrich) in water or 0.1% w/v Poly(methyl methacrylate) (Sigma Aldrich) in toluene. The concentration of the dye in the solutions was kept between 0.1-1 nM in order to obtain a surface density of less than 1 μm^{-2} in the prepared thin films. With such a molecule density, one can excite molecules separately with the focused radially polarized laser and obtain scan patterns separately.

The pixel size was chosen between 40 nm - 70 nm, with a dwell time of 3 ms - 10 ms

---

[1] An azimuthally polarized laser has an electric field pointing in the tangential direction at each point across its cross section. When focused through an objective it has only a transverse component in the focal plane with no electric field along the optical axis.

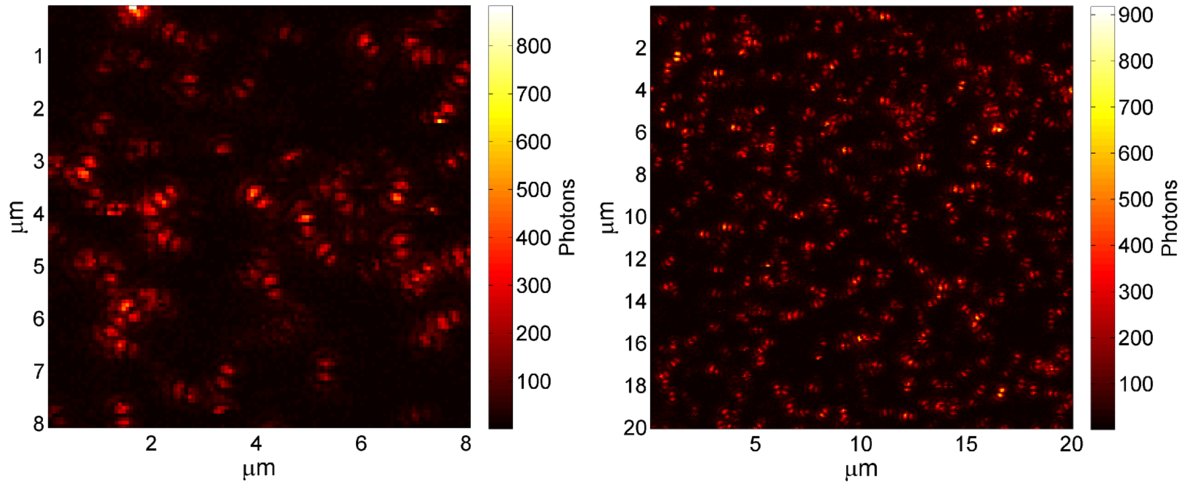

Figure 4.10: Scans of Rhodamine 6G spin-coated on a cleaned glass coverslip with a radially polarized excitation laser with a pixel size of 70 nm. Wavelength $\lambda_{\mathrm{exc}} = 488\,\mathrm{nm}$ was used for excitation with a power of $\sim 5\,\mathrm{kWcm^{-2}}$ with a pixel dwell time of 4 ms.

per pixel, and a laser power between 1-25 $\mathrm{kWcm^{-2}}$ depending upon the brightness and photostability of the molecule. Figure 4.10 shows two images of 8 µm × 8 µm and 20 µm×20 µm showing intensity patterns of Rhodamine 6G molecules spin-coated on top of a glass coverslip. The important point to notice in these images is that a majority of the intensity patterns correspond to dipoles which are oriented parallel to the surface, as can be observed from figure 4.5, which shows that these molecules lie flat on the surface, given their planar structure. One can also notice the random in-plane orientation of the molecules from these scan patterns. Each of these patterns spreads over 0.5 µm across. Ideally, one expects to see these molecules to behave identically and therefore show equal brightness in the scan image. However, as one can clearly see in the figures, this is not the case. This can be attributed to various parameters affecting the brightness of the molecule. Neglecting any orientation effects and electric field polarization, which do not play any significant role in the excitation of parallel dipoles using a radially polarized laser, the fluorescence intensity from a molecule, based on a simple and standard three state model, can be written as:

$$I_f \propto k_{\mathrm{exc}} k_{\mathrm{ph}} \tau \eta \tag{4.9}$$

where k_{exc} is the rate at which the molecule is excited from its singlet ground state to the single excited state. This rate is directly proportional to the absorption cross section of the molecule and for an organic fluorophore, the rate is typically on the order of $10^7\,\mathrm{s^{-1}}$. k_{ph} is the rate of triplet decay or the rate of phosphorescence, a phenomenon by which a molecule in its triplet state returns to its singlet ground state. Usually, one has $k_{\mathrm{ph}} \in [10^6\,\mathrm{s^{-1}}\ 10^4\,\mathrm{s^{-1}}]$. η is the collection efficiency of the optical setup. Taking into account the collection efficiency of the objective, the loses at each optical element, and the detector efficiency, one usually has a collection efficiency $\eta \approx 1 - 10\%$. τ is the lifetime of the excited state of the molecule, typically in the order of $\sim 10^{-9}$ s. It is related to Fermi's golden rule, which represents the probability of a transition to take place (refer to the theory section), by:

$$\frac{1}{\tau} = \frac{8\pi\omega}{3\hbar} |p|^2 \rho(\mathbf{r}, \omega) \tag{4.10}$$

where p is the transition dipole moment of the molecule, ρ is the local electromagnetic density of states, $\mathbf{r}$ is the position of the molecule on the surface and ω is the transition frequency.

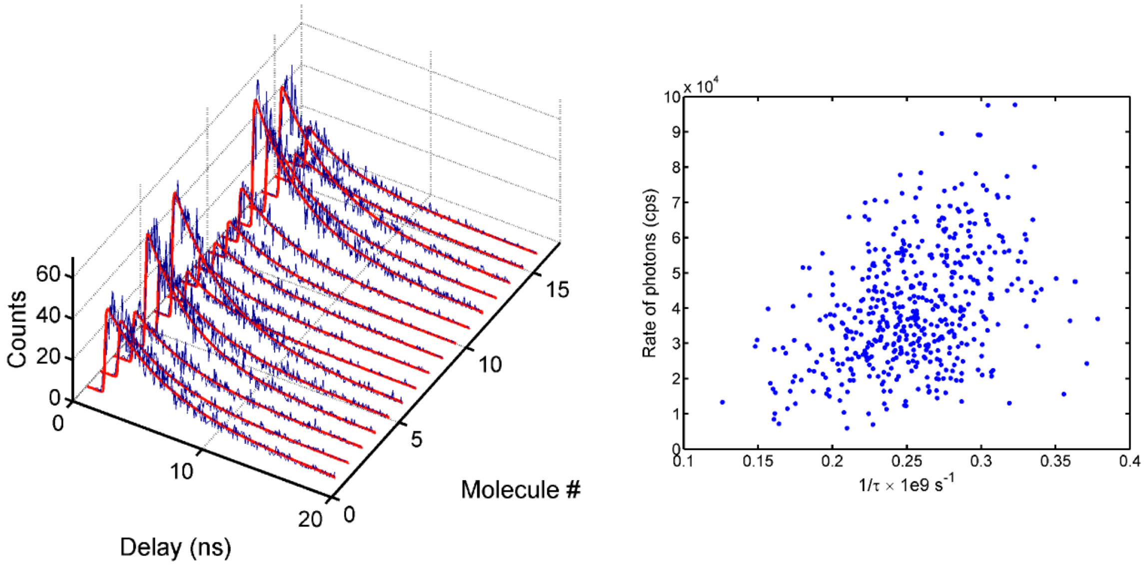

Figure 4.11: TCSPC curves and fits of photons collected from 16 molecules shown in the left panel of figure 4.10. The fitting was done using a parametric model for the instrument response function (IRF) as given in [133].

While η remains constant for all the molecules in a scan image, the rest of the parameters are effected by the interactions of the molecule with the substrate. Local charges present on the substrate lead to various electrostatic interactions with the charges on the molecule which in turn deform its backbone conformation. Such distortions would directly lead to spectral shifts, therefore altering the absorption cross sections, the transition dipoles $\mathbf{p}_{\mathrm{exc}}$ and $\mathbf{p}_{\mathrm{em}}$, and also the decay lifetimes $1/k_{\mathrm{ph}}$ and τ [134, 135], therefore affecting the overall brightness of the dye. The triplet state lifetime is typically in the order of few µs for dye molecules which is two orders of magnitude less than the scan rates. Therefore, one sees only the averaged photon rates. Depending on the structure, there can be multiple binding states and the molecule can switch to and fro between the states with a certain rate [136]. This is one of the several reasons that one occasionally observes blinking during the scanning process. Long living dark states due to photoinduced oxidation or reduction reactions also lead to observable blinking effects in a scan image.

Left side of figure 4.11 shows the TCSPC histograms of photons collected from the pixels corresponding to 16 individual molecules from the left image shown in figure 4.10. The figure also shows the fitted curves with a mono-exponential decay model. The right side of the figure shows a plot of average count rates observed from the scan images versus the rate of decay for about 480 Rhodamine 6G molecules. Any correlation between the points in such a plot would show the direct influence of the local environment on the brightness of the molecule. A slight trend can be seen here, which might indicate local effects of the substrate on Rhodamine 6G molecules. Since the molecules are excited with a fixed wavelength, the spectral shifts cannot be accounted for while estimating the detected photon count rates. For eg. a hypsochromic shift by only a couple of nanometers can alter the absorption cross section at the wavelength used for excitation severely which would be reflected in the observed count rates, and there is no way to disentangle such an effect from the changes observed in decay rates. For closely studying such effects, one would need to measure the emission spectra using measurement approaches such as Spectrally-Resolved Fluorescence Lifetime Imaging (SFLIM) [135, 136].

In some rare cases, the molecules on the glass surfaces showed rotational jumps that lead to a change in their dipole orientations. Figure 4.12 shows one such incidence where a molecule undergoes rotational jumps twice during the whole scan. Such instances have been observed before by Ha et. al. [55] using polarization modulation spectroscopy. An important observation from the calculated fluorescence lifetime image is that the rotational jumps do not change the decay rates of the molecule.

Single molecules in their excited singlet and triplet states are prone to two-step excitation where they are excited to higher electronic states. Molecules in these excited states are labile and undergo irreversible reactions with water or oxygen leading to the destruction of the chromophore or photobleaching [137]. Oxygen in the vicinity of a dye molecule plays a major role in the photophysics. A fluorophore present in its triplet state is annihilated by the oxygen molecule, effectively returning it to the singlet ground state. During this process, also singlet oxygen is formed which, on the other hand, can react with the fluorophore when present in higher singlet or triplet states thereby causing photobleaching. Therefore, depending on the photophysics of the dye alone, one can optimize the oxygen concentration in its surroundings in order to improve its stability. For this reason, dyes are embedded in rigid polymer matrices [138]. The diffusion of oxygen is reduced in these polymer films and varies from polymer to polymer. For eg. the permeability of oxygen in poly(methyl methacrylate) (PMMA) is much slower than in a polycarbonate membrane [139]. The oxygen concentrations in these membranes also depend on the thickness of the film which affect the molecule's overall brightness

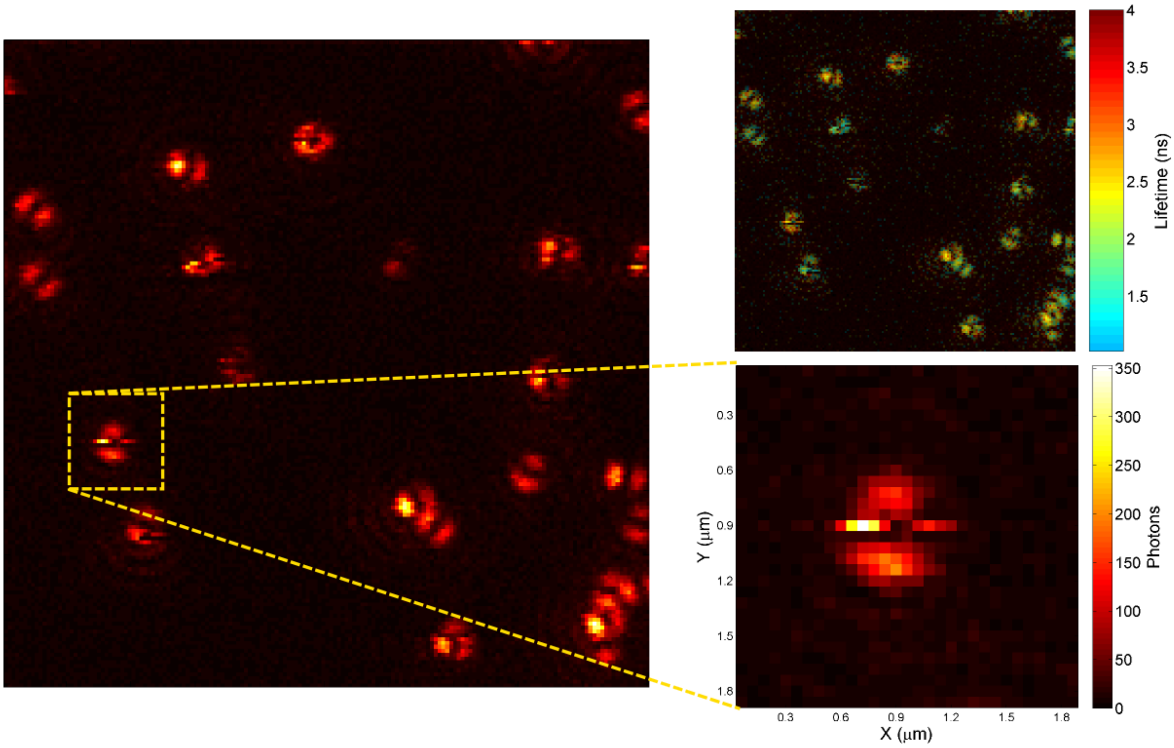

Figure 4.12: Scan image of Atto 655 molecules spin-coated on top of a glass surface. Image acquired with a pixel size of 60 nm and dwell time of 3 ms. An acousto-optic tunable filter (AOTF) was used to tune the wavelength of the white laser to a wavelength $\lambda_{\mathrm{exc}} = 640\,\mathrm{nm}$, with an excitation power of $\sim 5\,\mathrm{kWcm}^{-2}$ in the focus. The highlighted area shows a scan of a single molecule which undergoes rotational jumps twice. The top right image shows the average photon arrival time for each pixel. Observe that the fluorescence lifetime after each jump remains the same as before.

and stability.

Rhodamine 6G molecules were embedded in a polyvinyl alcohol (PVA) matrix and flushed with N_2 gas in a closed sample chamber. The scan images of single molecules in this thin film show randomly oriented excitation dipoles with respect to the vertical axis, in contrast to the previous measurements on a glass/air interface. Since the intensity of the scan patterns depends on the electric field components in the focal spot, $I_f \propto |\mathbf{E}(\mathbf{r}) \cdot \mathbf{p}_{\mathrm{exc}}|^2$, the molecules with orientations close to $\alpha = 0$ appear brighter than the horizontal molecules ($\alpha = 90°$). Figure 4.13 shows one such scan image. As can be seen, compared to the molecules that are oriented horizontally, the near-vertical ($\alpha > 60°$) are roughly two to three times brighter. Also, the horizontal molecules appear brighter than the average brightness of a molecule on glass substrate.

In order to estimate the orientations of the emitters shown in the scan image, we calculate model images of a single molecule emitter scanned with a radially polarized excitation focus as was shown in section 4.1.1 and thereby perform a least-square error minimization fitting using the model patterns as was done by Patra *et al.* [120], which will be described briefly in the section that follows.

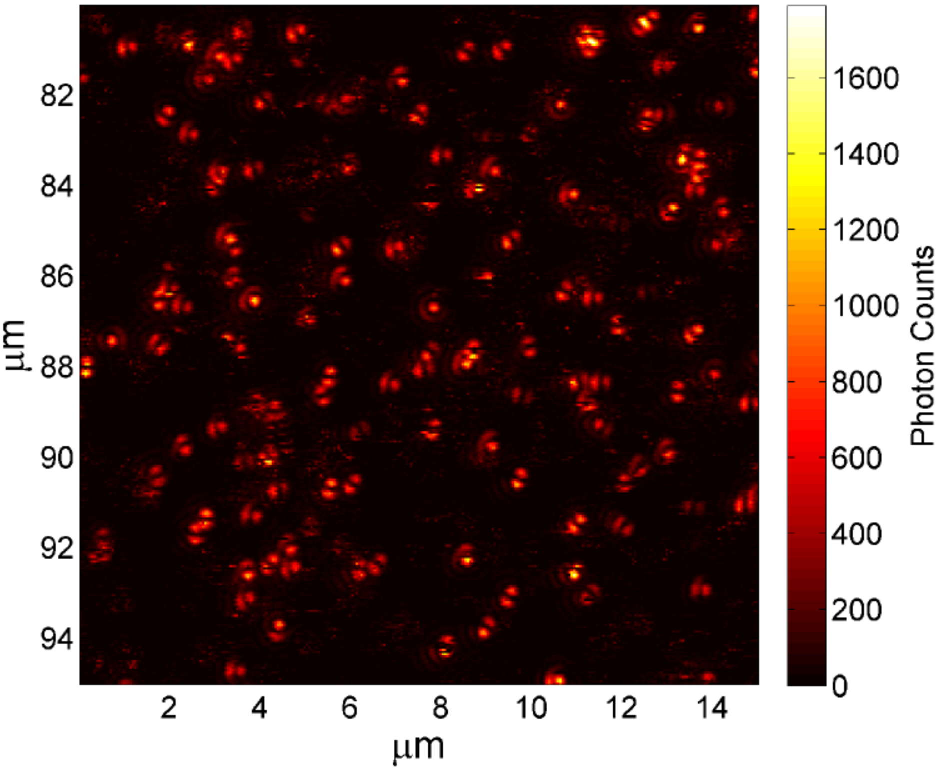

Figure 4.13: Scan image with a focused radially polarized laser of Rhodamine 6G embedded in a thin PVA layer with a pixel size of 60 nm and a dwell time of 4 ms/pixel. The excitation wavelength was set to $\lambda_{\text{exc}} = 488$ nm with an excitation power of 5 kWcm^{-2} in the focus.

4.1.4 Pattern Matching

The first step of pattern matching is the calculation of model patterns. This involves the exact wave-optical calculations of excitation patterns for molecules located in a medium of known refractive index, sandwiched between stratified layers of the substrate beneath and above, with their thicknesses, through a high numerical aperture objective. Patterns are calculated for a pre-determined in-plane β and out-of-plane angles α. The next and final step is to locate the modeled patterns within the measured scan image using a custom written Matlab routine based on the work shown in [120]. Briefly, for each calculated pattern, an error image is calculated according to the equation:

$$e_{mn}^{(r)} = (X^2)_{mn} - \frac{(Q_{mn}^{(r)})^2 + (X_{mn})^2 - 2P^{(r)}Q_{mn}^{(r)}X_{mn}}{1 - (P^{(r)})^2} \tag{4.11}$$

where $[m, n]$ is the index in the scan image and the error is calculated for each pattern $p^{(r)}$. $(X^2)_{mn}$ is the 2-dimensional convolution of the square of the raw image x_{mn} with a background matrix with a finite support s, which is usually the size of the pattern $[2L + 1, 2L + 1]$ or a circular disk of fixed number of pixels or radius L. The rest of the matrices are defined as:

$$X_{mn} = \frac{\sum_{j=-L}^{L} \sum_{k=-L}^{L} s_{jk} x_{m+j,n+k}}{\sqrt{(\sum_{j=-L}^{L} \sum_{k=-L}^{L} s_{jk}^2)}} \quad ,$$

$$Q_{mn}^{(r)} = \frac{\sum_{j=-L}^{L} \sum_{k=-L}^{L} s_{jk} x_{m+j,n+k} p_{jk}^{(r)}}{\sqrt{(\sum_{j=-L}^{L} \sum_{k=-L}^{L} s_{jk}^2)}} \quad ,$$

$$P^{(r)} = \frac{\sum_{j=-L}^{L} \sum_{k=-L}^{L} s_{jk} p_{jk}^{(r)}}{\sqrt{(\sum_{j=-L}^{L} \sum_{k=-L}^{L} s_{jk}^2)}}$$

For each pattern, a coefficient $C_{mn}^{(r)}$ is calculated by the equation:

$$C_{mn}^{(r)} = \frac{(Q_{mn}^{(r)}) - P^{(r)} X_{mn}}{1 - (P^{(r)})^2}$$

After calculating for all the patterns, the least error $\widetilde{e}_{mn}$ and the corresponding coefficient $\widetilde{C}_{mn}$ for each pixel are obtained and the pattern t responsible for the minimum error is identified. Only if the ratio $\widetilde{C}_{mn}/\sqrt{\widetilde{e}_{mn}} < \kappa$, the pattern t is identified as a good pattern centered at the pixel. If the value κ is predefined close to one, only those intensity patterns having a good signal-to-noise ratio and agreement with the modeled pattern t are given out. Figure 4.14 shows the recognized patterns for figure 4.13. The fitted image carrying the recognized patterns and the positions is calculated by $I_{mn}(x_i, y_i) = \widetilde{C}_{mn}(x_c, y_c) \times p^{(t)}$ where x_c, y_c is the position recognized by the molecule and x_i, y_i go from $x_c - L \to x_c + L$ and $y_c - L \to y_c + L$ respectively. Therefore, as a secondary result, one predicts the position of the molecules in the image at the pixel representing the minimum error.

Even though the pattern matching works nicely, there are several limitations. One of the major limitation which is intrinsic to the method is the limited number of the model patterns. One usually calculates the patterns with a step of 10° for α and β, which automatically translates into the resolution of the technique. Fitting with patterns calculated for smaller step sizes greatly slows down the pattern matching. The second disadvantage is that the molecules have to be separated in space in a way that their intensity patterns do not overlap, which leads to false results. Also, molecules which show blinking behavior may not be recognized or may lead to false results as well, which can be seen in figure 4.15 below.

Pattern matching, apart from of course obtaining the orientations of the dipoles, comes as an effective tool for single-molecule data analysis. Since one identifies the

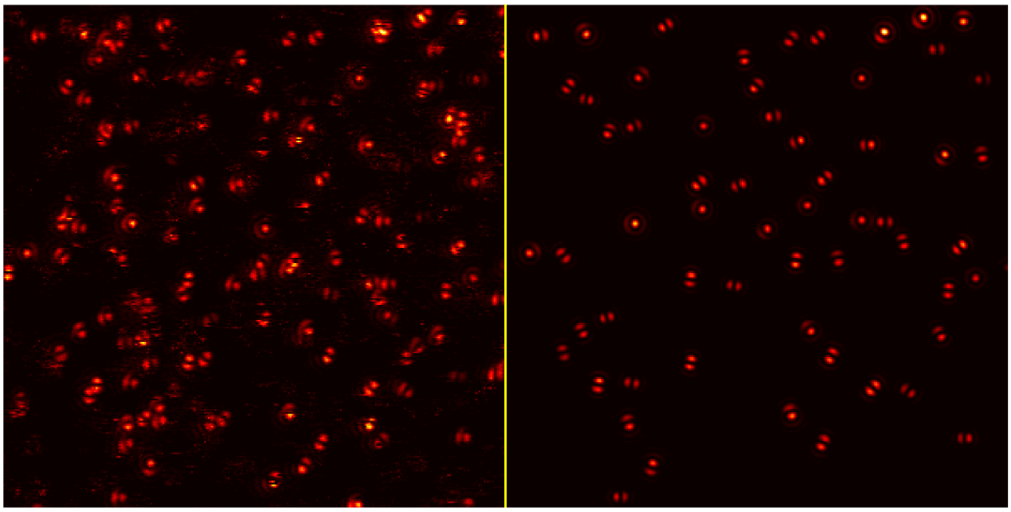

Figure 4.14: Figure showing the raw intensity image of Rhodamine 6G molecules in a thin PVA polymer scanned by a radially polarized laser together with the patterns matched by the least-squares minimization algorithm. In total, 86 molecules were identified. The pixel size of 60 nm, refractive index of the PVA was set to 1.49 and N.A. = 1.49 were used to calculate the model patterns.

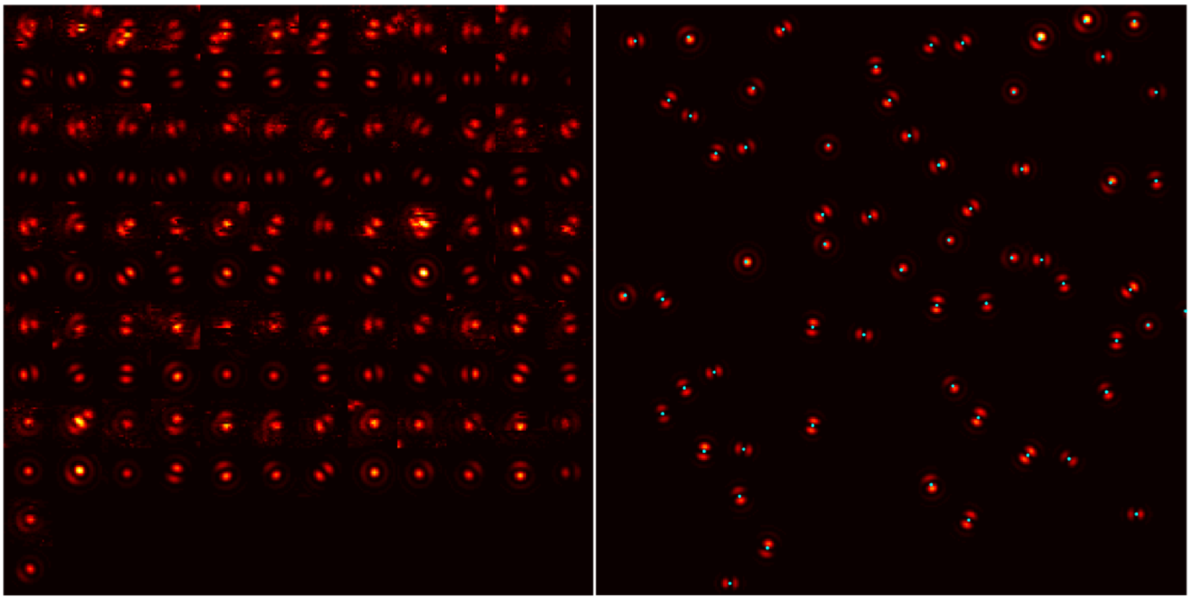

Figure 4.15: Left figure shows the recognized intensity patterns against the patterns matched. Every odd row shows the cropped raw image patterns and the row beneath shows the matched patterns. The right image shows the positions of the centers as cyan dots for the matched patterns.

pixels corresponding to each individual molecule, the collected photons from these pixels can be used for estimating decay rates and photophysical properties such as blinking behavior with much more statistics yielding a much higher accuracy than evaluating for each individual pixel. As stated and shown above, one has the position information of the dipoles which can be used for localization microscopy. Performing scans with a smaller pixel size can improve the lateral localization accuracy down to 30 nm. Further, combining the radial scanning with our smMIET method would allow one to localize

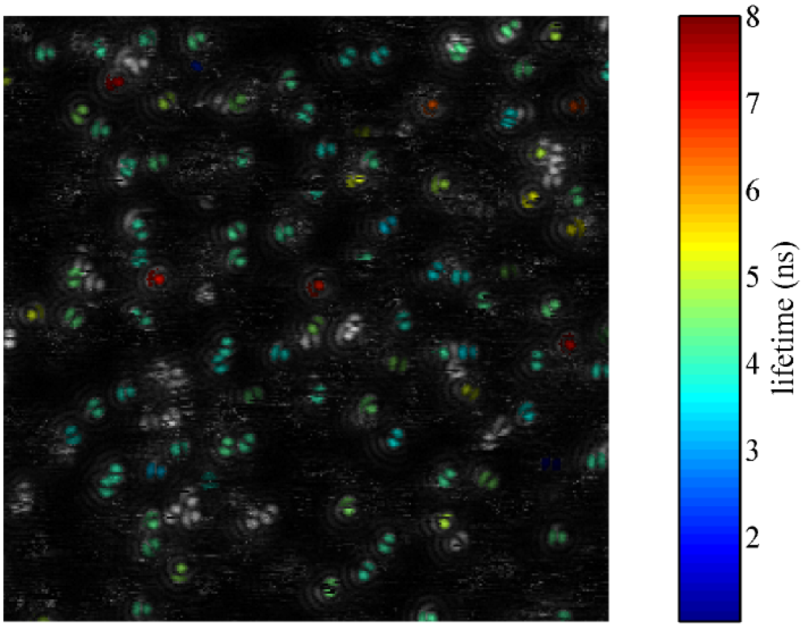

Figure 4.16: Image showing the fluorescence lifetimes of the identified Rhodamine 6G molecules. The lifetimes are calculated by collecting the photons from all the pixels belonging to each individual molecule. The fitting is done using a calculated IRF using a parametric model [133]. The intensity patterns which were not recognized by the pattern match algorithm, and therefore do not have a lifetime estimate, are shown in gray scale beneath the lifetime image.

these emitters with nanometer accuracy along the z-axis, which remains a challenge for several superresolution techniques (see chapter 1). Figure 4.16 below shows the lifetime image for the 86 identified molecules from image 4.13.

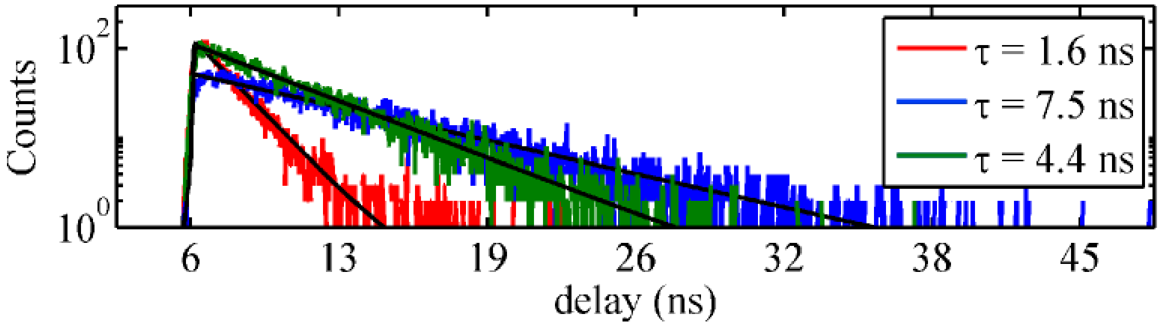

Figure 4.17: The TCSPC curves and fits of three individual molecules from image 4.16. The curves in the red and blue showing lifetimes of 1.6 and 7.5 ns are the two extreme cases observed.

The fitted lifetime values vary between 1.6 ns to 7.5 ns with an average of 4.5 ns and a standard deviation of 0.9 ns. The variation in the lifetime values can be attributed to two main reasons.

The first reason is the relative position and orientation of a dye molecule with respect to the polymer/air on the top. As was described in the theory chapter, the presence of a dielectric interface, such as in between the polymer (refractive index of 1.5) and air, can lead to a dramatic change in the emission properties of a dipole such as the

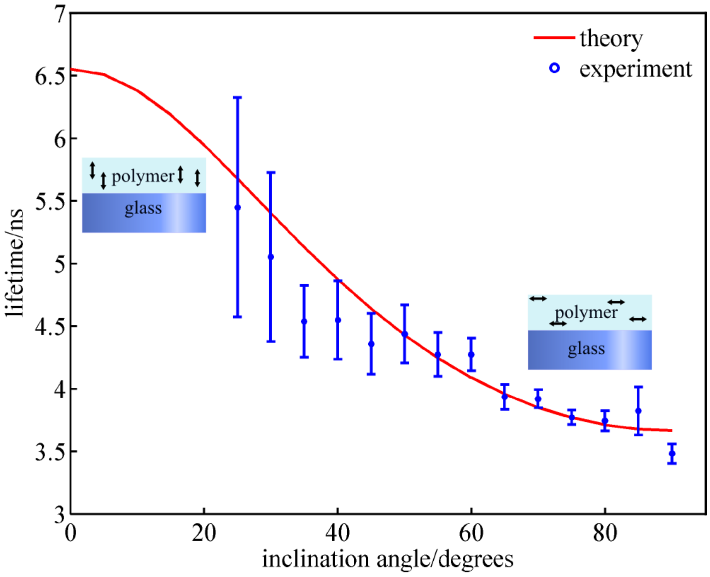

Figure 4.18: Average lifetime of a Rhodamine 6G molecule's excitation transition dipole oriented at an angle α with respect to the vertical in a thin polymer film ($n = 1.5$) of thickness ~70 nm with glass below and air above. The variation within the thin polymer layer is neglected and has been averaged for all heights.

angular distribution of the radiation and the total power radiated (see section 2.4.2). The lifetime values, especially of a vertical dipole, change significantly close to the interface separating the embedding medium and air (see figure 2.23 for example). As the distance from this interface increases, the lifetimes of the dipoles approach to the free space value inside the medium τ_0. We collected the lifetime values and the fitted orientations for about 630 Rhodamine 6G molecules from measurements such as shown in figure 4.13. Since the quantum yield of the dye is close to unity in aqueous solutions, we make a simple assumption that only the radiative rates change due to the presence of the molecule in the polymer. Using this assumption, the free space lifetime τ_0 of the dye and the quantum yield Φ are about 3.6 ns and 0.95, respectively. The blue data in figure 4.18 shows the distribution of the average lifetimes as a function of the inclination angle of the dipoles in the polymer. Assuming a uniform height distribution of the dye molecules throughout the thickness of the polymer film, the red curve shows the theoretical lifetimes averaged over a thickness of 70 nm as a function of the orientation. Although the data is in good agreement with the theoretical curve, which corroborates with the argument that strong variations in lifetime values in a thin polymer film are observed due to the interface effects, the correct estimates for free space parameters (τ_0 and Φ) and the thickness of the polymer can be obtained only through further experiments. One must measure dye molecules inside a thick polymer away from any dielectric interface in order to estimate the free space parameters.

Secondly, the presence of any chemical heterogeneity of the polymer matrix they are embedded in can adversely affect the excited state lifetime values. As was described in detail above, the dye molecules are highly sensitive to properties such as local viscosity and charges. The variations in the photophysical properties of single molecules can be attributed to the various possible interactions with the polymer matrix. Of course, changes in the structure of the backbone, the presence of oxygen, and liquid "pockets" in the vicinity of the molecules alter their properties dramatically. Before performing smMIET experiments, it is mandatory to select an appropriate matrix for immobilization and check for the uniformity of the lifetime values.

4.1.5 Multidimensional Emitters

An important application of radially polarized laser scanning, apart from the orientation information, is the determination of the dimensionality and geometry of the excitation transition. Almost all organic fluorophores show single dipole transition behavior. However, this is not true for all single emitters. The nitrogen-vacancy (NV^-) center in diamonds for example, shows a two dimensional degenerate transition dipole [140]. Quantum Dots, on the other hand, show an isotropic three dimensional excitation transition probability. Which means, scanning these samples with a radially polarized laser focus, gives patterns which are different from single dipole patterns and can be visualized as a sum of two or more dipole patterns. A two dimensional transition can be considered as two orthogonal dipoles lying in the plane perpendicular to the NV center axis. For calculating the scan patterns, we let one of these two dipoles to be oriented in the xy-plane and the other in the excitation plane perpendicular to it. Since the excitation is degenerate over the plane, we further simplify the situation by assuming that the two dipoles are of equal strength. Figure 4.19 shows a few modeled intensity patterns for various orientations of the normal vector tabulated below with a radially polarized excitation. Since the vertical component of a dipole is excited stronger than its horizontal component, the patterns for the excitation plane perpendicular to the xy-plane show resemblance with a single vertical dipole. One can distinguish such ambiguities only by scanning both, with a radially and azimuthally polarized laser excitation. For such an orientation of the excitation plane, the intensity pattern with an azimuthally polarized laser focus represents a single dipole oriented in the xy-plane. The calculated intensity patterns for the same orientations of the normal vector with an azimuthally polarized laser focus are also shown in figure 4.19. Only with the help of both the scans can one distinguish clearly between a single dipole excitation transition and a two dimensional transition. The intensity patterns for a three dimensional, isotropic excitation transition probability couple with the complete electric field polarization in the focus and resemble the scan patterns of fluorescent beads used for checking the alignment of the laser beam. Spherical quantum dots show such excitation probabilities and thus their scan patterns look similar to the results shown in figure 4.20.

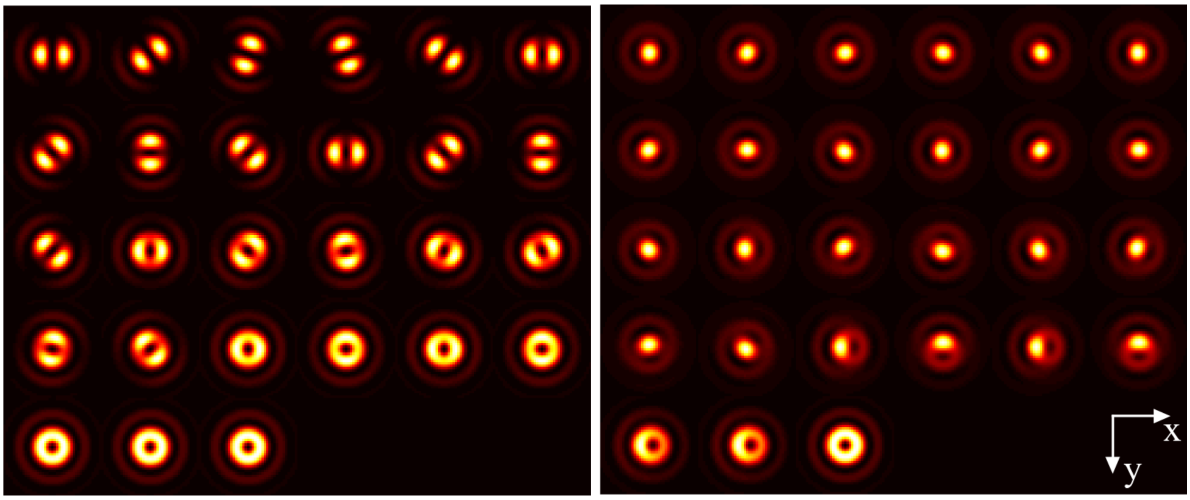

Figure 4.19: Calculated intensity scan patterns of a two dimensional degenerate excitation transition with a focused azimuthally polarized (left) and radially polarized laser excitation (right). The N.A. of the objective was 1.49, pixel size 30 nm at wavelength $\lambda = 564$ nm. The molecules are assumed to be on top of an air/glass interface, and the minimum angle for illumination θ_{min} was set to be $\sim 20°$. Each pattern spreads over $\sim 1\,\mu\mathrm{m} \times 1\,\mu\mathrm{m}$. Note that the images show normalized intensities and equal strength of both dipoles. From top left to bottom right, α and β values of the vector normal to the plane containing the two dipoles are:

Column/Row	1 α, β	2 α, β	3 α, β	4 α, β	5 α, β	6 α, β
1	90°, 0°	90°, 36°	90°, 72°	90°, 108°	90°, 144°	70°, 0°
2	70°, 45°	70°, 90°	70°, 135°	70°, 180°	70°, 225°	70°, 270°
3	70°, 315°	50°, 0°	50°, 51°	50°, 103°	50°, 154°	50°, 206°
4	50°, 257°	50°, 309°	30°, 0°	30°, 90°	30°, 180°	30°, 270°
5	10°, 0°	10°, 180°	0°, 0°	–, –	–, –	–, –

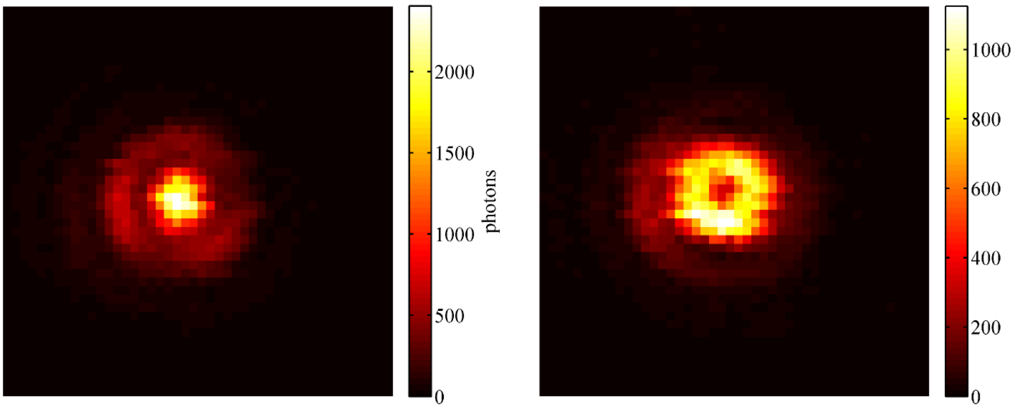

Figure 4.20: Intensity scans of a quantum dots with a radially (left) and azimuthally (right) polarized laser. The pixel size is 40 nm and the image represents an area of 1.8 µm × 1.8 µm.

4.2 smMIET with Radially Polarized Excitation

As we saw in the previous section's discussion, one receives both, the orientations as well as the excited state lifetime values for immobilized single molecules scanned with a radially polarized excitation. Together with quantum yield Φ and free space lifetime τ_0 (the unperturbed lifetime value in a homogeneous medium of refractive index n) values of the molecules, one can use the modified lifetime values and the orientations of the transition dipoles with respect to the metal substrate for obtaining their height above the surface. At a height z, the total energy radiated by a dipole at an arbitrary angle α with respect to the normal of the surface can be split into contributions of a parallel and a vertical dipole at the same height above the surface, as:

$$S(\alpha, z) = S_{\perp}(z) \cos^2 \alpha + S_{\parallel}(z) \sin^2 \alpha \tag{4.12}$$

This gives us the relationship for the lifetime values for an arbitrarily oriented dipole in terms of τ_0

$$\tau_f(\alpha, z) = \frac{\tau_0}{\Phi S(\alpha, z)/nS_0 + (1 - \Phi)} \tag{4.13}$$

where nS_0 is the power radiated by a dipole in free space ($nS_0 = cnp^2 k_0^4/3$). Before one can use the lifetime value and the orientation for determining the height of a single molecule, one must know the free space parameters τ_0 and Φ. For determining the free space lifetime in a polymer, one must be avoid any dielectric interface based effects, such as shown in figure 4.18. The easiest way is to sandwich a thin layer of polymer with the emitters dissolved in it between two thick layers (thickness $> \lambda_{\text{em}}$) on top of a clean glass surface. Such a measurement would provide us with the free space excited state lifetime (τ_0) of the emitter in the environment used for the smMIET experiments. Such measurements for Rhodamine 6G molecules in PVA polymer gave an average fluorescence lifetime of 2.9 ns. Given the free space lifetimes τ_0', τ_0 in two media of refractive indices n', n, the quantum yields of the emitter Φ', Φ are related as

$$\Phi = \Phi' \cdot \frac{\tau_0}{\tau_0'} \frac{n}{n'}. \tag{4.14}$$

Here we assume that the radiative rate κ_r of an emitter in bulk material is proportional to the total power radiated nS_0 (and therefore, proportional to the refractive index), whereas the non-radiative rate κ_{nr} can be estimated from the lifetime in that medium. Using the values of free space lifetime ($\tau_0' = 4.1$ ns) and quantum yield ($\Phi' = 0.95$) measured in aqueous medium from literature [103], we get a quantum yield of $\Phi = 0.77$ for the obtained lifetimes of Rhodamine 6G in the polymer.

Now that we have the free space parameters of the dye, we can exactly determine the lifetime of its excited state as a function height for a given orientation (α). One performs calculations for a parallel and vertical dipole according to the CPS model (see theory section 2.4.3) in order to obtain their total radiation power as a function of height $S_{\|}$ and $S_{\perp}$, respectively. With this, one proceeds by calculating the power emitted by the dipole oriented at the angle α as a function of height $S(\alpha, z)$, from equation (4.12). Lastly, one uses equation (4.13) to calculate the lifetimes $\tau_f(\alpha, z)$. Figure 4.24 show lifetimes plots for Rhodamine 6G molecules in a thin polymer film of refractive index 1.5 on top of a thin gold film (10 nm) with air above for various polar angles α. These plots act as calibration curves for the axial positions.

4.2.1 Methods

The substrates for MIET experiments were prepared similar to the procedure described in section 3.2.1. For the experiments in this section, we used an SiO_2 spacer of thickness 20 nm. 10 µL of (0.1% w/v) PVA/water solution, without any dye molecules, were spin-coated on top of the substrate at ∼8000 rpm for 60 seconds. Thereafter, 10 µL of 0.1 nM Rhodamine 6G solution was spin-coated on top of the polymer at the same speed. The microscope is described in detail in section 4.1.2 and a simplified setup design is shown in figure 4.21.Briefly, a pulsed white-light laser (Fianium SC400-4-80),

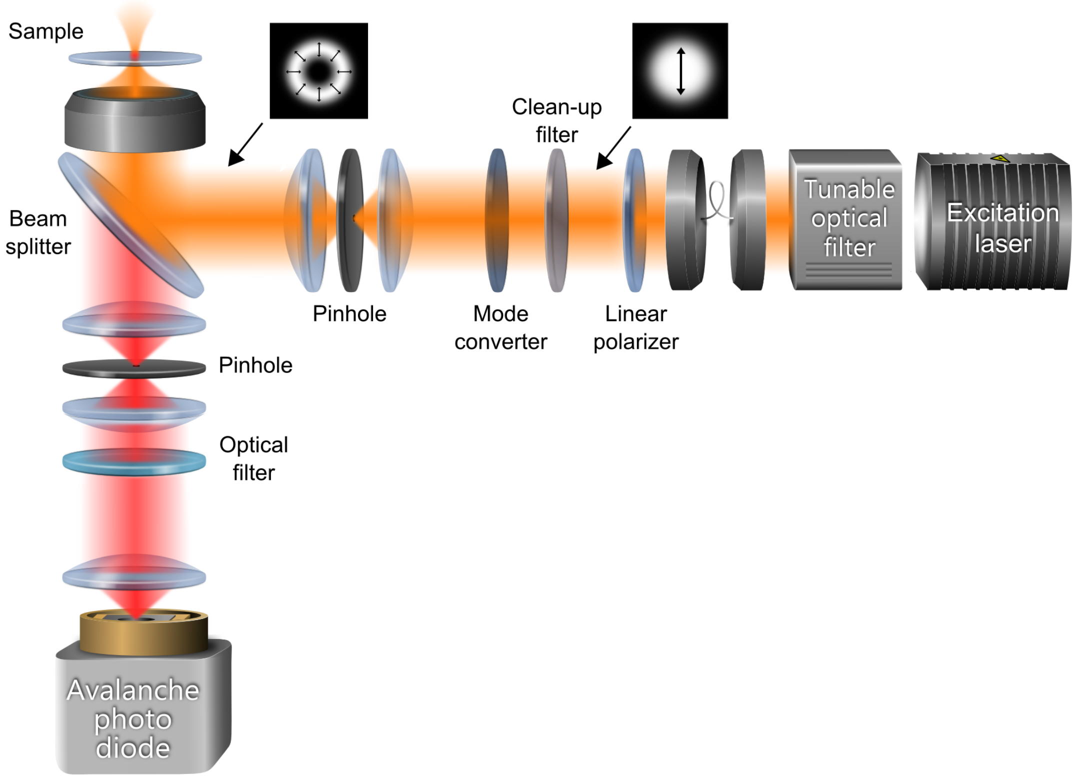

Figure 4.21: Setup design for a standard confocal microscope combined with radially polarized excitation.

together with a tunable acousto-optic tunable filter (AOTFnC-400.650-TN) was used for excitation. The excitation wavelength was tuned to 510 nm using the AOTF, and further filtered with a clean-up filter (FF02-510/10, Semrock). The voltage in the retarder cell of the mode-converter was set to 1.88 V in order to achieve a radially polarized Laguerre-Gaussian beam. We used excitation powers in the range of 1-5 kWcm^{-2} after the objective. Scans were performed with a pixel size of 50 nm and a dwell time of 5 ms per pixel. The emission was filtered using a band-pass filter with a maximum transmission around 542 nm (FF01-542/27, Semrock) and then focused onto a τ-SPAD (PicoQuant, Berlin) for detection. Intensity images were obtained using custom written Matlab routines using the photons arriving after a chosen time gate only in order to reject the photoluminescence of the metal film. The higher signal-to-noise ratio attained in this way contributes to an improvement in the quality of pattern matching results. The quality of pattern matching is significantly affected by the radius of the calculated model patterns, especially for the case where the intensity patterns are close to each other. For the excitation wavelength of ~510 nm using a 1.49 N.A. objective, we modeled the patterns using a radius of 400 nm in object space. This translates to a size of 17×17 pixels. Figure 4.22 shows an exemplary intensity image and the patterns recognized, with and without time gates. As can be seen in this figure, the chance of recognition for dim intensity patterns increases with the time-gated correction. The collected photons from the pixels identified for each molecule were fitted with a mono-exponential model in order to obtain the excited state lifetimes values.

4.2.2 Results and Discussion

The obtained raw data was processed as described above in the methods section. The step size for polar and azimuthal angles for calculating the model patterns was chosen as 5° and then pattern matching was performed in order to obtain the orientations of each single molecule. Thereafter, MIET calibration curves were calculated for a dipole oriented at various polar angles in a thin polymer assuming a polymer thickness of 20 nm, and the height based of each single molecule was obtained. Figure 4.24 shows the calibration curves as well as the height of the molecules for the fitted polar angles (0°, 5°, ..., 90°). The density of the molecules, as can be seen from this figure, is not uniform over the entire thickness of the polymer film. Also, the number of molecules for each orientation is not constant, as can be seen from the density of points on each curve in the figure. Therefore, we plotted the average orientation as a function of the axial position, shown in figure 4.24. The plot shows that close to the interfaces the dipoles are orientated almost parallel, whereas in the middle, the dipoles assemble in all possible orientations. The plot also shows an inhomogeneous distribution of molecules across the polymer.

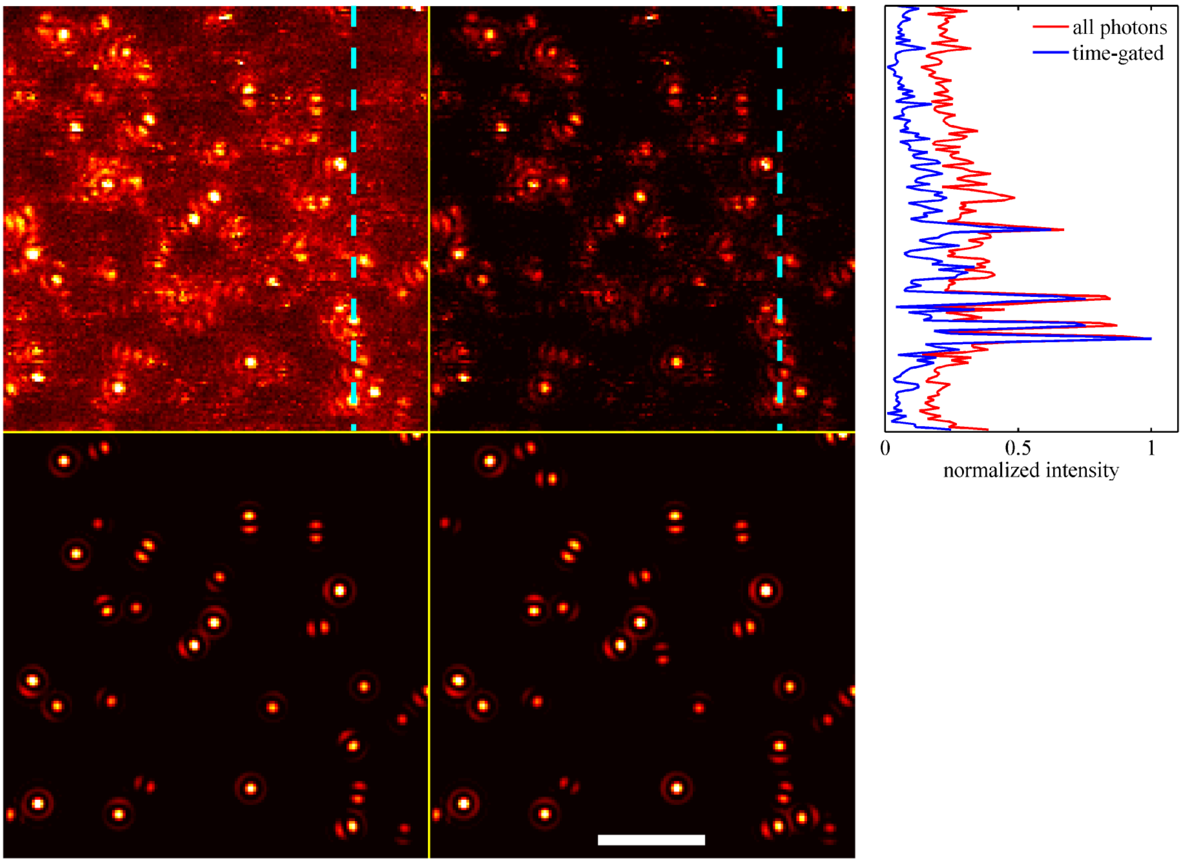

Figure 4.22: Left column shows the intensity image with all the photons recorded in the top and the patterns recognized in the bottom, whereas the right column shows the same for the case of time-gated photons. The reconstructed image with the patterns for the time-gated analysis has been enhanced by 1.5× to make the weak patterns more visible. Comparing the bottom figures, 4 more molecules were recognized and one artifact was removed in the right image after gating the photons. The scale bar marks a length of 2 µm. The plots in the right-top figure shows the intensities in the pixels corresponding to the same line in raw data with and without time-gating. The signal-to-noise enhancement was roughly 2 times after the gating.

There are several reasons for observing such a distribution of molecules. First, since the molecules were introduced following the casting of the polymer film by spin-coating, one would expect that the concentration of the molecules is low in the bottom layers of the polymer film. On the other hand, the top of a spin-coated polymer is not smooth and the height variations can be in the order of ±2 nm. This might explain the presence of only a few molecules higher than 12 nm. Also, the molecules close to the gold surface (in the bottom of the polymer) are quenched more than the molecules at larger distances, making them dimmer. Therefore, one has poor signal-to-noise ratios for the molecules close to the bottom interface, which makes it difficult for the pattern matching algorithm to detect, contributing to the overall distribution that we observe here. Moreover, the relative intensity of a parallel dipole is higher as compared to a vertical dipole in the bottom. This can be seen from figure 4.25 which shows the collection efficiency of parallel and vertical dipoles as a function of height which was calculated by the

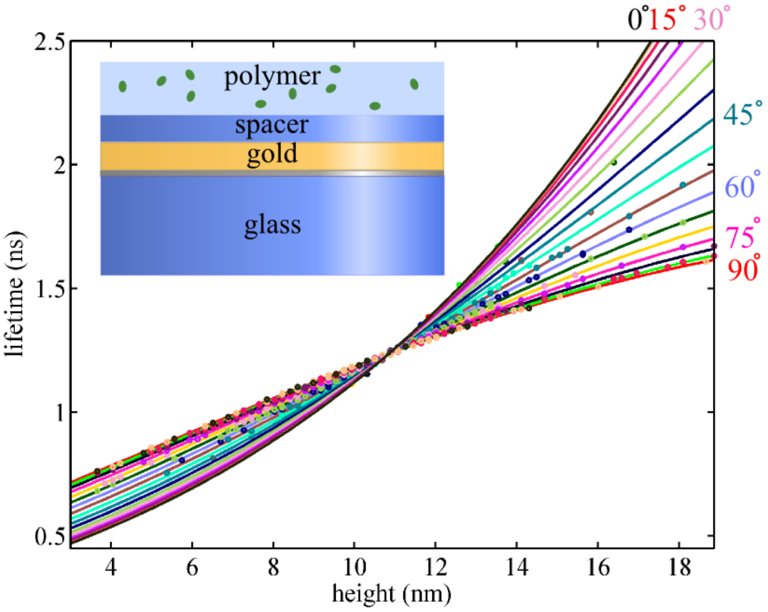

Figure 4.23: MIET calibration curves of a Rhodamine 6G molecule's lifetime at various heights in a 20 nm thick PVA polymer on top of a layered substrate for it's various orientations. The details of the substrate are described in the methods section above. Also the distribution of the axial positions of the molecules together with their orientations is shown along these curves.

fraction of the energy propagating into the collection cone of a 1.49 N.A. objective, using equation (2.145). Based on the trend seen in the curves, the chance of detecting a photon from a vertical dipole is low at the bottom of the polymer film which can be a contributing reason for the observed average orientation distribution. Although these might be a few reasons to explain the distributions seen in the figure, a complete understanding of the distribution and the orientations of the molecules requires modeling the diffusion and transport of the dye molecules into the pores of the thin film in the presence of centrifugal forces which is beyond the scope of this thesis.

There are several limitations for performing smMIET experiments using a radially polarized laser scanning. Orientation estimation using pattern matching algorithms provides reasonable results only when there are no artifacts such as blinking/bleaching or any overlap of intensity patterns. This limits the selection of dyes and the conditions of experiments in order to ensure photostability. Since each single molecule pattern spreads over an area of $\sim 1\,\mu\text{m} \times 1\,\mu\text{m}$, the concentration of fluorophores must be low enough in order to avoid any such overlap. Therefore, this technique is applicable only for a sparse distribution of labeled entities. The MIET calibration curves can be calculated, as shown above, for fixed dipole orientations or for the case where the dye has free rotational freedom and the rotational diffusion time is shorter than the average fluorescence lifetime so that it can be assumed to be isotropic emitter. Combining scanning with radially polarized excitation with superresolution techniques such as STORM or PALM means that one is limited to perform scans over a small area in order to achieve a fast frame

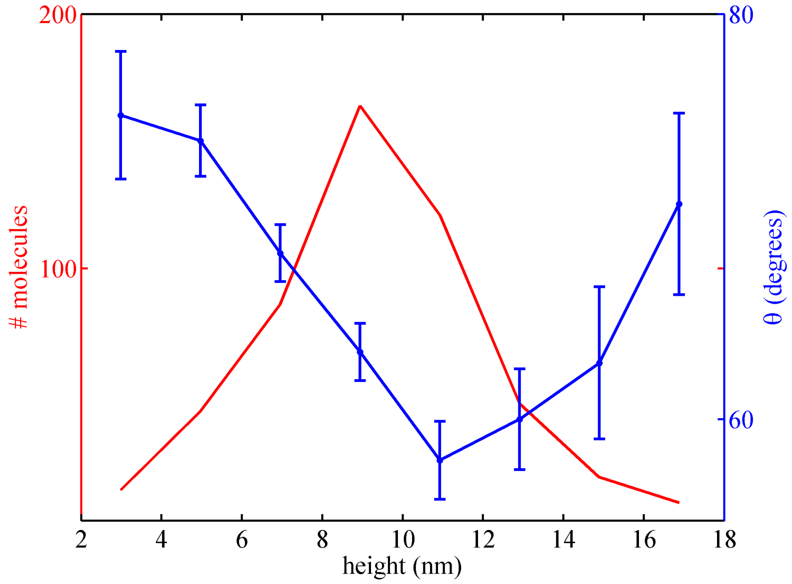

Figure 4.24: The distribution of Rhodamine 6G molecules and their average inclination as a function of height above the surface.

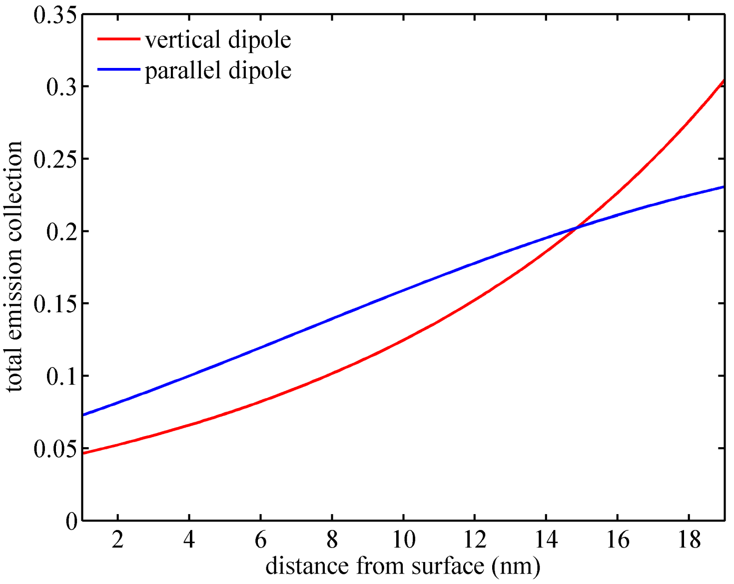

Figure 4.25: Total collection efficiency of a parallel and vertical dipole as a function of height above the SiO_2 spacer in a thin polymer film. The values represent the amount of power emitted into the collection cone of a 1.49 N.A. objective normalized to the total emission power of a dipole in free space.

rate and resolve multiple molecules fluorescing randomly. However, a major challenge for scanning an area repeatedly stems from the positioning inaccuracy and the drift one induces during scanning with a piezo stage. An probable solution to this problem is to use galvo scanning mirrors before the objective or two fast electro-optic deflectors before the linearly polarized laser is converted into a radially polarized beam. However, this requires stringent optical alignment which might be a limitation for robust and simple microscopic designs. Therefore, we proceed with our quest for an optimal solution of combining smMIET with orientation measurements. In the next section we will discuss the option of defocused imaging which is widely used for determining the three dimensional orientations of single molecules and comparatively robust and simpler in instrumentation and alignment than achieving a good quality radially polarized beam profile using a liquid crystal mode converter as we saw in this section.

4.3 Defocused Imaging

As we saw in the theory chapter, the emission characteristics of a dipole emitter are dramatically influenced by the presence of a dielectric interface in its vicinity (see section 2.4.2). In particular, significant changes in the angular distribution of the radiation are observed. The core idea behind defocused imaging is to acquire this information by imaging the emission at a defined defocused plane [59]. A blurred, but characteristic, intensity pattern is recorded which contains all the information to determine the three dimensional orientation of the fluorescent molecule's emission transition dipole moment ($\mathbf{p}_{\mathrm{em}}$). In this section, we provide a brief outline of the theory involved behind these defocused patterns.

4.3.1 Theory

We start our theoretical considerations from the derivation of the transmitted electric field of a dipole on a dielectric interface from section 2.4.2. In particular, we refer to the Weyl representation of the transmitted field (2.131)

$$\mathbf{E}_T(\mathbf{r}) = \frac{ik_0^2}{2\pi} \iint \frac{\mathrm{d}\mathbf{q}}{w_1} \left[\hat{\mathbf{e}}_{2p}^{+} T_p (\hat{\mathbf{e}}_{1p}^{+} \cdot \mathbf{p}) + \hat{\mathbf{e}}_s T_s (\hat{\mathbf{e}}_s \cdot \mathbf{p}) \right] e^{i[\mathbf{q} \cdot (\tilde{\mathbf{n}} - \tilde{\mathbf{n}}_{\mathbf{0}}) + w_1 |z_0| + w_2 z]}. \tag{4.15}$$

Here we use the same sense of orientation and conventions as previously used: The positive direction of z is downwards into the medium n_2, $z > 0$ below the interface. The dipole is present in medium n_1 at a position $(\tilde{\mathbf{n}}_{\mathbf{0}}, z_0)$, $z_0 < 0$. Since only the far-field emission plays a role here, we consider the components with $|\mathbf{q}| \leq n_1 k_1$ only, neglecting all imaginary solutions. The electric field for a vertically oriented dipole ($\mathbf{p} = p\hat{\mathbf{z}}$) contains only p-waves. The area element $\mathrm{d}\mathbf{q}$ can be treated as $\mathrm{d}\mathbf{q} = q\mathrm{d}q\mathrm{d}\psi = k_2 w_2 \sin\theta_2 \mathrm{d}\theta_2 \mathrm{d}\psi$. Therefore, the magnitude of the electric field at an emission angle θ_2 per solid angle $\mathrm{d}\Omega = \sin\theta_2 \mathrm{d}\theta_2 \mathrm{d}\psi$ is given by

$$\mathbf{E}_p^{\perp}(\theta_2) = \hat{\mathbf{e}}_{2p}^{+} E_p^{\perp}(\theta_2) = -\hat{\mathbf{e}}_{2p}^{+} \frac{q w_2 n_2}{w_1 n_1} T_p e^{i w_1 |z_0|}. \tag{4.16}$$

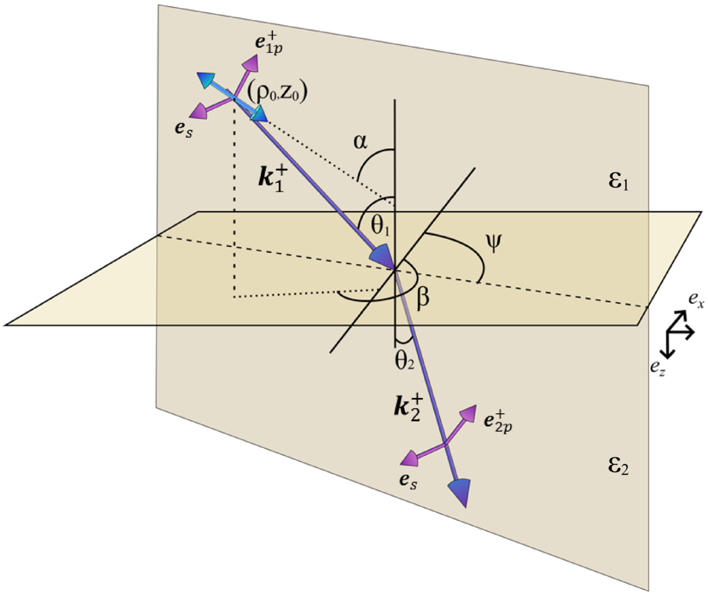

Figure 4.26: A schematic showing the geometry of vectors considered in this section. The dipole is located at a position $(\rho_{\mathbf{0}}, z_0)$ with an orientation (β, α). The interface separates the two media $n_1 = \sqrt{\epsilon_1}$ and $n_2 = \sqrt{\epsilon_2}$ as shown. The unit vectors $\hat{\mathbf{e}}_{ip}^+$ represent the directions of p-waves, and $\hat{\mathbf{e}}_s$ for s-waves. θ_1 and θ_2 are the angles the vectors $\mathbf{k}_1^+$ and $\mathbf{k}_2^+$ make with respect to the normal of the interface, and ψ is the angle between the plane of incidence and the x-axis on the interface as shown.

For the case of a parallel dipole, one has both p- and s-waves in the transmitted electric field. The field not only depends on the angle with respect to the optical axis θ_2, but also changes with the azimuthal angle ψ. We therefore, split up the field into two components

$$\hat{\mathbf{e}}_{2p}^+ E_p^{\|}(\theta_2)\cos\psi = \hat{\mathbf{e}}_{2p}^+ \frac{w_2 n_2}{w_1} T_p e^{iw_1|z_0|}\cos\psi, \tag{4.17}$$

and

$$\hat{\mathbf{e}}_s E_s^{\|}(\theta_2)\sin\psi = -\hat{\mathbf{e}}_s \frac{w_2 n_2}{w_1} T_s e^{iw_1|z_0|}\sin\psi. \tag{4.18}$$

Thus, for every dipole oriented at an angle (β, α) where β is the angle from the positive x-axis and α, the inclination with respect to the optical axis, the magnitude of the electric field at direction (θ_2, ψ) per solid angle can be written in terms of the components of a vertical and parallel dipoles.

$$\mathbf{E}(\theta_2, \psi) = \left[\hat{\mathbf{e}}_{2p}^+ E_p^{\|}(\theta_2)\cos(\psi - \beta) + \hat{\mathbf{e}}_s E_s^{\|}(\theta_2)\sin(\psi - \beta)\right]\sin\alpha + \hat{\mathbf{e}}_{2p}^+ E_p^{\perp}(\theta_2)\cos\alpha \tag{4.19}$$

Let us now consider the imaging optics of the setup. A geometrical depiction is provided in figure 4.26. A defocusing can be achieved in two ways: i) By shifting the

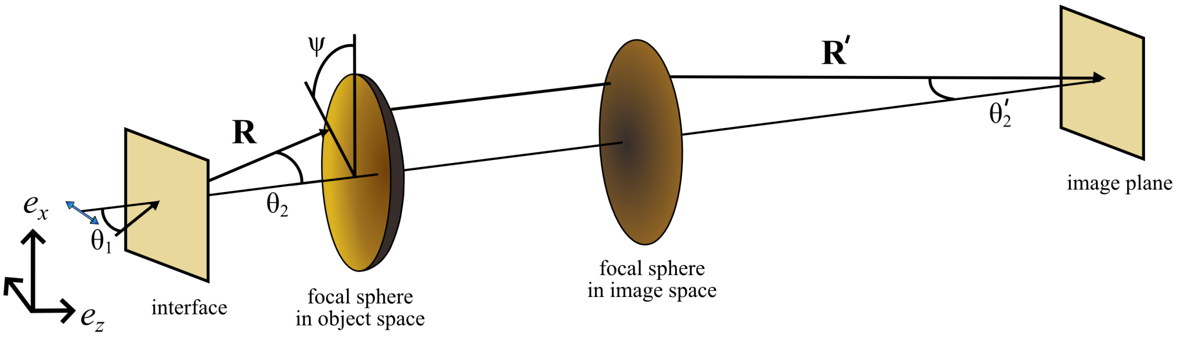

Figure 4.27: The geometry of the imaging setup. The dipole is placed on the optical axis in a medium of refractive index n_1 at a distance z_0 from the interface at $z = 0$. The medium between the interface and the focal sphere in the object space has a refractive index n_2. The focal sphere in image space and the image plane are present in a medium of refractive index n'. $\mathbf{R}$ is the vector from the focal point of the objective to a point on the focal sphere in object space, $|\mathbf{R}|$ is the focal length of the objective. It is marked here as the radius of the focal sphere in the object space with center at the point of the intersection of the interface with the optical axis. Similarly, $|\mathbf{R}'|$ represents the focal length in image space.

objective, and therefore its focal plane, relative to the interface. Remember here that the molecule under consideration is present at a distance $|z_0|$ from this interface. ii) By placing the detector away from the focal plane. In a wide-field fluorescence microscope such as that considered in chapter 3, these two ways produce the same result and are completely identical. Here, in this section, we will specifically consider the case where the detector is shifted from its imaging plane. The mathematics of the image formation remains, once again, completely identical to the work of Böhmer *et al.* [59]. As we saw in section 4.1, the electric field around the optical axis in the image plane, considering aberration free optics, is described by the integral formula from Richards and Wolf [131]

$$\mathbf{E}(\mathbf{r}') = -\frac{i|\mathbf{k_2}|}{2\pi} \iint_{\Omega} \mathbf{a}(s'_x, s'_y) e^{ik'(\hat{\mathbf{s}}' \cdot \mathbf{r}')} \, \mathrm{d}\boldsymbol{\Omega}' \tag{4.20}$$

where the solid angle element is $\mathrm{d}\boldsymbol{\Omega}' = \frac{\mathrm{d}s'_x \mathrm{d}s'_y}{s'_z}$, and the integration extends over the complete angular space $\boldsymbol{\Omega} = (\theta'_2, \psi)$; ψ varies from 0 to 2π and θ'_2 from 0 to θ'_{max}. The relationship between θ_2 and θ'_2 is given by Abbe's sine condition, $n_2 \sin\theta_2 = Mn' \sin\theta'_2$; and therefore, $\theta'_{\mathrm{max}} = \arcsin(\mathrm{N.A.}/Mn')$, where N.A. denotes the numerical aperture of the objective and n' is the refractive index of the imaging medium, usually air, and M is the magnification of the system. $\mathbf{k_2}$ and $\mathbf{k}'$ are the wave vectors of light in the object (in glass) and image space, respectively. Vector $\mathbf{a}$ represents the strength vector right at the 'focal sphere', i.e. the sphere with center on the imaging plane at the optical axis (see figure). $\mathbf{r}'$ is the coordinate of the target point in the image plane from the focal sphere, where the electric field is being calculated. Thus, for a vertical dipole, it is given by equation (4.16) and for a parallel dipole by the sum of both p- and s-fields presented in equations (4.17) and (4.18). The main idea behind equation (4.20) is to present the electric field magnitude in the image space as a superposition of plane waves. The field magnitude for a vertical dipole at a plane before or after the focal plane can be expressed, by slightly modifying this equation as

$$\mathbf{E}^{\perp}(\mathbf{r}') = M\int_0^{\theta'_{\max}} \mathrm{d}\theta'_2 \sin\theta'_2 \int_0^{2\pi} \mathrm{d}\psi \sqrt{\frac{n'\cos\theta'_2}{n_2\cos\theta_2}}\, \hat{\mathbf{e}}'_p E_p^{\perp} \exp(ik'\hat{\mathbf{s}}'\cdot\mathbf{r}') \tag{4.21}$$

and for a parallel dipole

$$\mathbf{E}^{\parallel}(\mathbf{r}') = \\ M\int_0^{\theta'_{\max}} \mathrm{d}\theta'_2 \sin\theta'_2 \int_0^{2\pi} \mathrm{d}\psi \sqrt{\frac{n'\cos\theta'_2}{n_2\cos\theta_2}}\, (\hat{\mathbf{e}}'_p E_p^{\parallel}\cos\psi + \hat{\mathbf{e}}_s E_s^{\parallel}\sin\psi) \exp(ik'\hat{\mathbf{s}}'\cdot\mathbf{r}') \tag{4.22}$$

where

$$\begin{aligned} \hat{\mathbf{e}}'_p &= (\cos\psi\cos\theta'_2, \sin\psi\cos\theta'_2, -\sin\theta'_2) \\ \hat{\mathbf{e}}_s &= (-\sin\psi, \cos\psi, 0) \\ s' &= (-\cos\psi\sin\theta'_2, -\sin\psi\sin\theta'_2, \cos\theta'_2) \end{aligned}$$

and $\hat{\mathbf{s}}'\cdot\mathbf{r}'$ can be expanded as

$$\hat{\mathbf{s}}'\cdot\mathbf{r}' = \hat{\mathbf{s}}'\cdot(\mathbf{R}' + \boldsymbol{\rho}' + \mathbf{z}') = R' - \rho'\sin\theta'_2\cos(\psi - \phi') + z'\cos\theta'_2 \tag{4.23}$$

where R' is the focal distance in the image space and (ρ', ϕ', z') are the coordinates of the target point on the plane in cylindrical coordinates centered at the point of intersection of the optical axis with the focal plane in image space. Therefore, $\boldsymbol{\rho}'$ is a vector pointing to the target point from the optical axis, z' is the distance of the target point from the focus along the optical axis and ϕ' is the angle between $\boldsymbol{\rho}'$ and $\hat{\mathbf{e}}_x$. The square root factor in equation (4.22) together with magnification M ensure energy conservation [131]. The connection between the coordinates of the position of the dipole in object space and image space are found using the relations $\boldsymbol{\rho}' = M\boldsymbol{\rho}$, for the distance away from the optical axis and, $z' = M^2 z$ along the optical axis. These relations also state that in order to achieve a defocusing of δz in object space, one must displace the detector by a distance $M^2\delta z$ in the image space and vice-versa.

Similar relations for the amplitude of the magnetic field in the image space can be found:

$$\mathbf{B}^{\perp}(\mathbf{r}') = Mn'\int_0^{\theta'_{\max}} \mathrm{d}\theta'_2 \sin\theta'_2 \int_0^{2\pi} \mathrm{d}\psi \sqrt{\frac{n'\cos\theta'_2}{n_2\cos\theta_2}}\, \hat{\mathbf{e}}_s E_p^{\perp} \exp(ik'\hat{\mathbf{s}}'\cdot\mathbf{r}') \tag{4.24}$$

and

$$\begin{aligned}\mathbf{B}^{\|}(\mathbf{r}') = \; & Mn' \int_0^{\theta'_{\max}} \mathrm{d}\theta'_2 \sin\theta'_2 \int_0^{2\pi} \mathrm{d}\psi \sqrt{\frac{n'\cos\theta'_2}{n_2\cos\theta_2}} \left(\hat{\mathbf{e}}_s E_p^{\|}\cos\psi - \hat{\mathbf{e}}'_p E_s^{\|}\sin\psi\right) \\ & \times \exp(ik'\hat{\mathbf{s}}'\cdot\mathbf{r}'). \end{aligned} \tag{4.25}$$

The integration over ψ can be performed analytically. The electric field magnitude for a dipole oriented at (β, α), writing the electric and magnetic fields as a combination of parallel and vertical dipoles (see equation (4.19)), is given by

$$\begin{Bmatrix} E_j \\ B_j \end{Bmatrix} = \int_0^{\theta'_{\max}} \mathrm{d}\theta'_2 \sin\theta'_2 \sqrt{\frac{n'\cos\theta'_2}{n_2\cos\theta_2}} \begin{Bmatrix} e_j \\ b_j \end{Bmatrix} \times \exp(ik'\hat{\mathbf{s}}'\cdot\mathbf{r}') \tag{4.26}$$

where we used the abbreviations:

$$\begin{aligned}\begin{Bmatrix} e_x \\ e_y \end{Bmatrix} = \; & \frac{\sin\alpha}{2} \begin{Bmatrix} J_0\cos\beta\left(\cos\theta'_2 E_p^{\|} - E_s^{\|}\right) - J_2\cos\left(2\phi' - \beta\right)\left(\cos\theta'_2 E_p^{\|} + E_s^{\|}\right) \\ J_0\sin\beta\left(\cos\theta'_2 E_p^{\|} - E_s^{\|}\right) - J_2\sin\left(2\phi' - \beta\right)\left(\cos\theta'_2 E_p^{\|} + E_s^{\|}\right) \end{Bmatrix} \\ & - i\cos\alpha\cos\theta'_2 J_1 \begin{Bmatrix} \cos\phi' \\ -\sin\phi' \end{Bmatrix} E_p^{\perp} \end{aligned} \tag{4.27}$$

and

$$\begin{aligned}\begin{Bmatrix} b_x \\ b_y \end{Bmatrix} = \; & n'\frac{\sin\alpha}{2} \begin{Bmatrix} -J_0\sin\beta\left(E_p^{\|} - \cos\theta'_2 E_s^{\|}\right) + J_2\sin\left(2\phi' - \beta\right)\left(E_p^{\|} + \cos\theta'_2 E_s^{\|}\right) \\ J_0\cos\beta\left(E_p^{\|} - \cos\theta'_2 E_s^{\|}\right) - J_2\cos\left(2\phi' - \beta\right)\left(E_p^{\|} + \cos\theta'_2 E_s^{\|}\right) \end{Bmatrix} \\ & - in'\cos\alpha J_1 \begin{Bmatrix} \cos\phi' \\ -\sin\phi' \end{Bmatrix} E_p^{\perp}. \end{aligned} \tag{4.28}$$

J_n are Bessel functions of the first kind of n-th order, with functional argument $k'\rho'\sin\theta'_2$ ($\rho' = |\boldsymbol{\rho}'|$). The final position dependent intensity in the image plane is given by the z component of the Poynting vector

$$S = \frac{c}{8\pi}\hat{\mathbf{e}}_z \cdot \mathrm{Re}\{\mathbf{E}\times\mathbf{B}^*\}. \tag{4.29}$$

Note that these equations are written considering a two lens system with magnification M. The derivation for a four lens system remains the same except for the fact that the images will be inverted in the xy-plane. Therefore, one must then replace ϕ' with $-\phi'$ in the final equations for e_j and b_j. Intensity patterns for a few orientations of the $\mathbf{p}_{\mathrm{em}}$ for a four lens system are calculated and shown in figure 4.28.

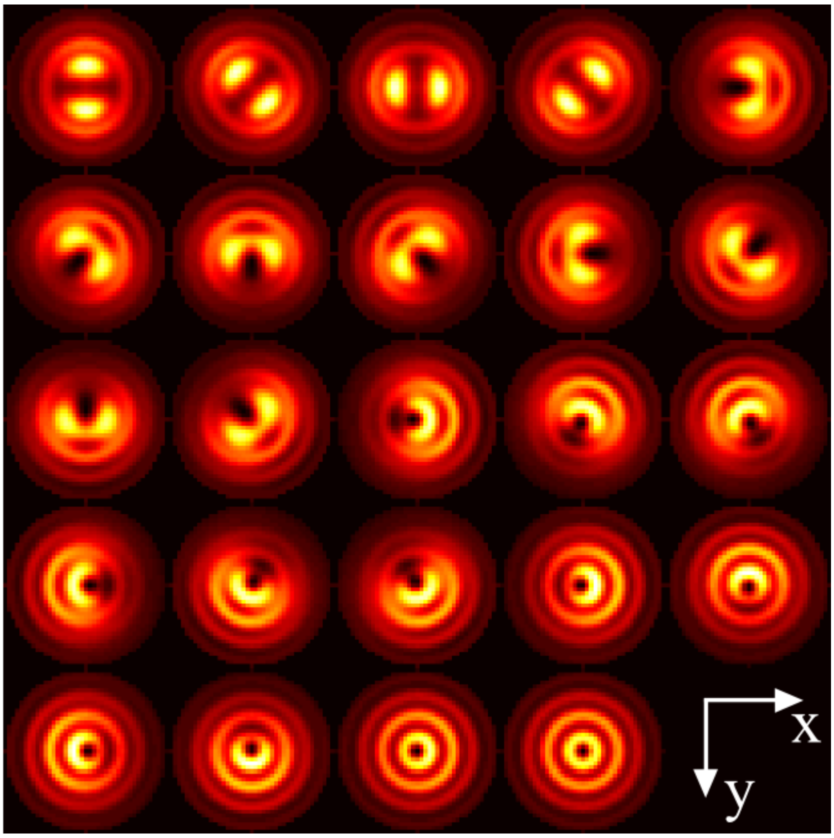

Figure 4.28: Calculated intensity images of a dipole on a camera plane with a defocusing value of $\delta z = 0.9\,\mu\text{m}$ in the object space. The emission wavelength was set to $\lambda_{em} = 690\,\text{nm}$ The N.A. of the objective for the calculations was set to 1.49, with a net magnification of $M = 200$. The refractive index in image space was set to $n' = 1$. The camera pixel size was $13\,\mu\text{m} \times 13\,\mu\text{m}$. The dipoles were assumed to be on top of an air/glass interface ($z_0 = 0$) and on the optical axis ($n_1 = 1; n_2 = 1.52$). Each pattern spreads over 20×20 pixels on the detector. Note that the images show normalized intensities. From top left to bottom right, α and β values for the calculated dipole patterns are:

Column/Row	1 α, β	2 α, β	3 α, β	4 α, β	5 α, β
1	90°, 0°	90°, 45°	90°, 90°	90°, 135°	70°, 0°
2	70°, 45°	70°, 90°	70°, 135°	70°, 180°	70°, 225°
3	70°, 270°	70°, 315°	50°, 0°	50°, 60°	50°, 120°
4	50°, 180°	50°, 240°	50°, 300°	30°, 0°	30°, 90°
5	30°, 180°	30°, 270°	10°, 0°	0°, 0°	–, –

4.3.2 Experimental Setup

A wide-field based imaging setup has been described in detail in section 3.1.2 earlier. A total illumination area of $80\,\mu\text{m} \times 80\,\mu\text{m}$ in the object space, an exposure time of $\sim 3\,\text{s}$ and an average illumination power of $0.2\,\text{kWcm}^{-2}$ gave excellent signal-to-noise ratio in the defocused intensity patterns for single molecules (see figure 3.8). In this section, we will describe mainly the setup for measuring the defocused patterns using a focused illumination and a camera that has been displaced from the focal plane in the image space.

The excitation system and sample preparations were described in section 4.1.2. The fluorescence collected by the objective was recollimated using an achromatic doublet (AC254-150-A, Thorlabs Inc.) and any backscattered laser was blocked using a long-pass filter (EdgeBasic BLP01-647R, Semrock). The pinhole, between the tube lens and the achromatic doublet, was omitted for the sake of alignment simplicity. In principle, a pinhole with a diameter of 100 µm to 150 µm diameter should not alter the imaging properties of the setup at all, except in contributing to the blocking of unwanted background arising due to the presence of molecules above and below the excitation focus if any. In the limit that the emitters are well scattered in space and separated from each other, the pinhole does not make any significant difference and just adds to the alignment efforts. After recollimation and filtering, the emission light was reflected by a custom designed flipping mirror assembly into the defocused imaging detection system (see figure 4.7 for a complete design of the setup). An additional band-pass filter was inserted in the beam path in order to narrow down the spectral range of the detected photons (FF01-692/40 Semrock, for Atto 655 molecules). Thereafter, the light was focused on an EMCCD camera (iXon DU860-D, Andor) using a large focal length lens (AC508-1000-A, Thorlabs Inc.) mounted on an xy-translation mount (LM2XY, Thorlabs Inc.). The net magnification of the setup was $M = 400$ which, taking into account the pixel size of the camera (24 µm × 24 µm), results in an area of 60 nm × 60 nm per pixel in the object space. In order to achieve a defocused image plane, the camera was mounted on a stage which was placed in between two rails, facilitating the change of position by sliding (see figure 4.29). For a defocusing of -0.9 µm in object space ($\delta z = 0.9$ µm), the camera was shifted by a distance of 14.5 cm ($M^2\delta z$) towards the lens from the imaging focal plane. The focal plane in image space was located by focusing the laser on the air/glass interface of an empty coverslip, imaging the back-reflected light onto the camera chip without any filters (or with a neutral-density filter if the back-reflected intensity was too high), and sliding the camera along the rails such that the image shows a Gaussian spot with the narrowest width (Note that due to the high magnification and the M^2 relationship between the axial distances in the image space and object space, an error of 1 mm translates to ±6.25 nm in object space, which is negligible compared to the size of the excitation volume). Depending on the brightness and stability of the molecules, the laser power and exposure time were adjusted. For example an excitation power of 0.5 kWcm^{-2} was used together with an exposure of 5 s for Atto 655 molecules at glass/air interface.

4.3.3 Pattern Matching and Lateral Localization

A brief introduction to superresolution techniques based on point spread function (PSF) fitting was given earlier (see introduction chapter). One can achieve arbitrarily high

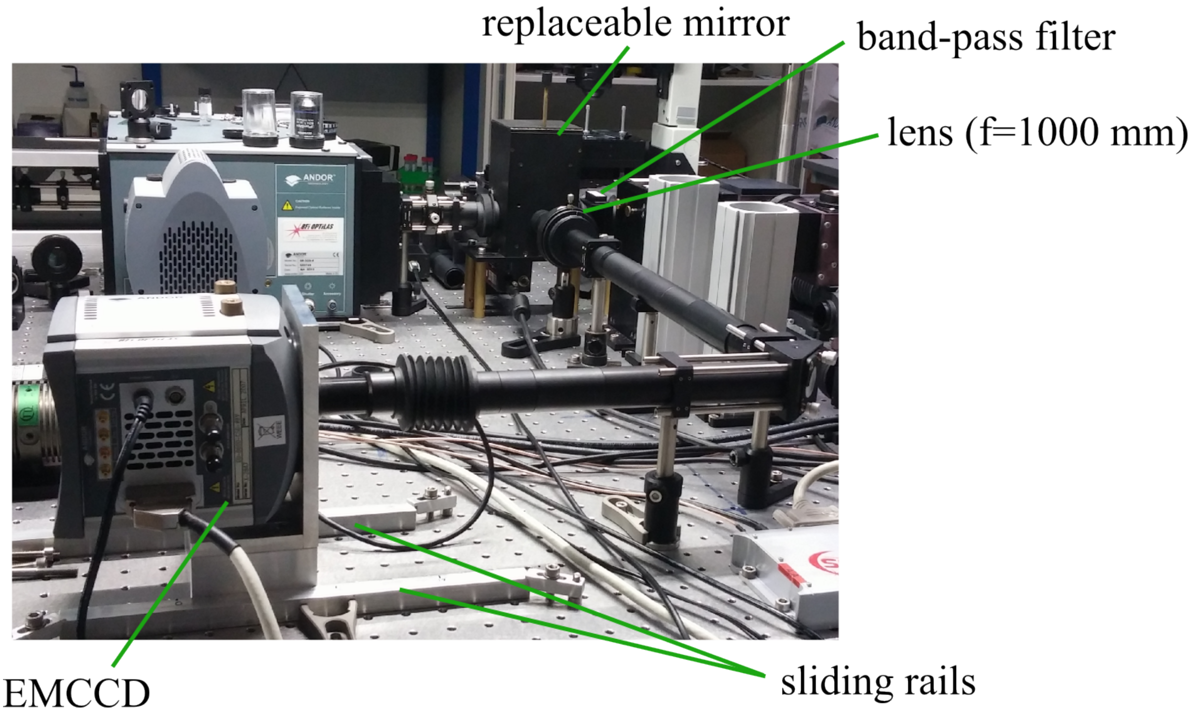

Figure 4.29: The setup used for defocused imaging.

lateral localization precision by increasing the number of photons from the emitter, assuming that the single molecules are perfect isotropic emitters (see the references in the introduction of the article [34] for further details). A 2D Gaussian PSF model is used for localizing spatially well-separated single-molecule intensity patterns [141]. However, this assumption is violated, especially when it comes to samples where the rotation freedom of the dye molecules is restricted. Anisotropic intensity distributions arise on the imaging plane due to the anisotropic emission patterns of these dipoles (see also section 2.4.2). An error, as high as 10 nm is introduced in the estimation of position while detecting immobilized molecules in the focus of high N.A. objectives [34].

The problem gets much more severe when the dipole emitters are situated above or below the objective's focal plane, and when they are close to a dielectric interface. This leads to severe localization errors [142]. The Poynting vector for the field on the image plane can be written as [143]

$$\begin{aligned} S(x,y)|_{\beta,\alpha} \propto\ & I_{\parallel}\{p_{\parallel}(\rho') + \Delta p_{\parallel}(\rho')\cos(2\phi' - 2\beta)\}\sin^2\alpha \\ & + I_{\times}p_{\times}(\rho')\sin\alpha\cos\alpha\cos(\phi'-\beta) + I_{\perp}p_{\perp}(\rho')\cos^2\alpha \end{aligned} \tag{4.30}$$

where ρ' has the same meaning as in the theory section and now $x' = \rho'\cos\phi'$ and $y' = \rho'\sin\phi'$. The integral in equation (4.26) goes from 0 to $\theta'_{\max}$, where $\theta'_{\max} = \arcsin(\text{N.A.}/Mn') \approx \frac{\text{N.A.}}{Mn'}$ is a very small number. This allows one to simplify these integrals greatly by using cumulant approximations for Bessel functions J_n for $n = 1, 2, 3$ (see supplementary of [143] for example). The functions $p_{\parallel}$ and $p_{\perp}$ here represent

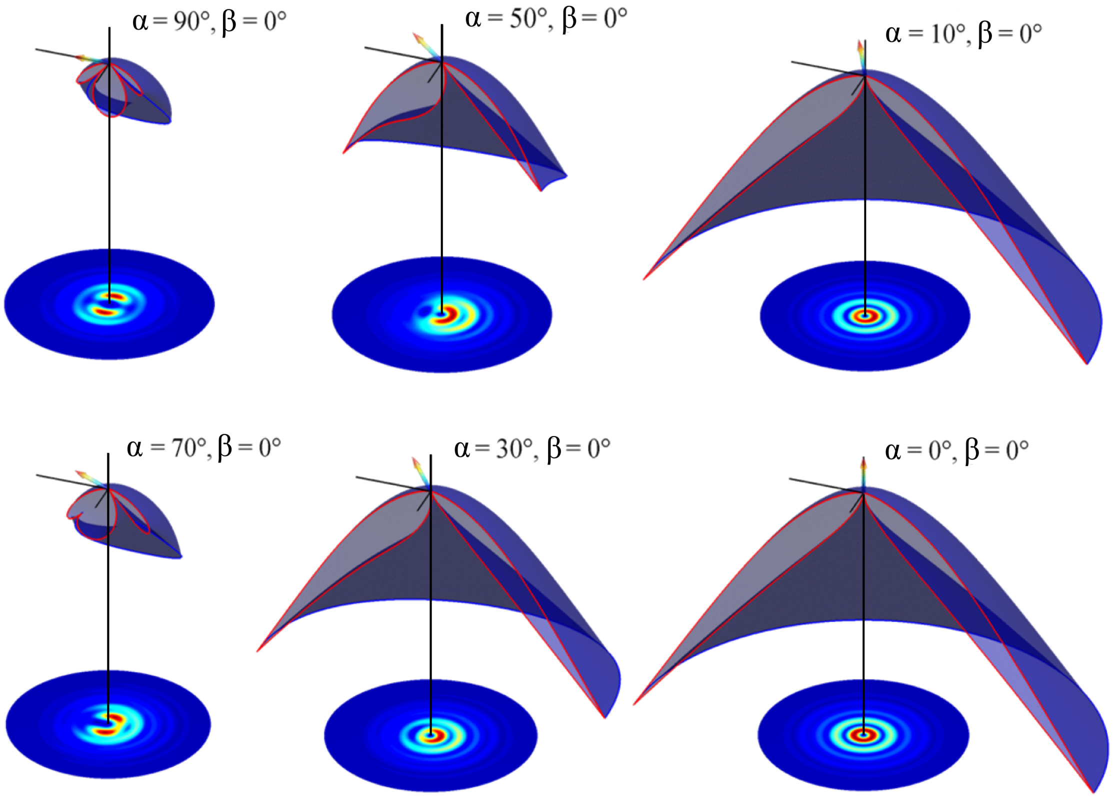

Figure 4.30: Sectioned radial distribution of dipoles situated on the optical axis into the lower half-space oriented at various polar angles. The patterns below show the intensity distribution on a defocused imaging plane. Notice the shifted center-of-intensity in these patterns with respect to the optical axis. Also notice the inversion of the intensity distribution with respect to the radial distribution. This is only true for a wide-field based defocused imaging.

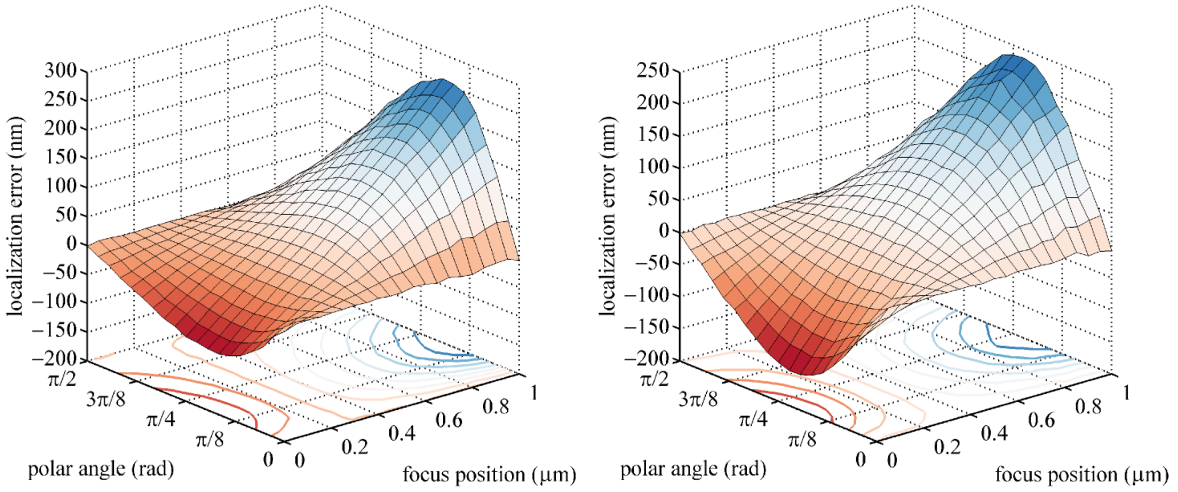

Figure 4.31: Left figure shows the localization error for various polar angles α and defocusing values for a 1.2 N.A. objective, and the right for N.A. = 1.49. The position of the dipole is fixed at 0.3 µm above the interface.

the intensity of an isotropic distribution of parallel and a fixed perpendicular dipole, respectively, whereas $\Delta p_{\|}$ marks the anisotropy connected with the radial part of the intensity distribution of a fixed parallel dipole and the cosine function involving β, its angular anisotropy. The presence of $\cos 2(\phi' - \beta)$ in the equation indicates the presence of two 2-fold symmetries in the patterns, connected with the contribution from a parallel dipole. The cross term $p_\times$ and its pre-factor dictate the anisotropy connected with the radial and angular component of the intensity distribution for a dipole with orientation in between these two extreme cases. The remaining functions $I_\|, I_\perp$ and $I_\times$ are normalization terms for the p terms in the equation. Figure 4.30 shows the projection of the angular distribution of fixed dipoles at various orientations directly below their locations. The intensity distribution of a parallel dipole shows two 2-fold symmetry planes, one along the dipole's direction, and another perpendicular to it. The symmetry along this axis ($\beta = 0$) is present for all orientations, as can be seen from the figure. This is in agreement with the cosine function in the cross term which is even for angles centered around $\phi' = \beta$. The intensity pattern for a vertical dipole is completely symmetric around the optical axis ($C_{\infty v}$), since now, both the cross term, as well as the term for a parallel dipole, are zero.

In the projections shown in the figure, one can clearly observe the dramatic shift of the centroid (center-of-intensity) for orientations that are in-between a parallel and a vertical dipole. We simulated the intensity patterns by fixing $\beta = 0$ (along the x-axis), and systematically varying the out-of-plane angle α by 5° for a dipole fixed in a medium with refractive index of water ($n_1 = 1.33$) placed $0.3\,\mu$m away from a glass coverslip $n_2 = 1.52$ ($z_0 = -0.3\,\mu$m). We chose a pixel size of 80 nm in object space, a wavelength of 680 nm, an N.A. of 1.49, and varied the focus position of the objective from the glass/water interface up to $1\,\mu$m deep with a step of 50 nm. For each focus position, we calculated raw images with a total of 10^4 photons for the pattern with Poisson statistics. We then fitted the patterns with the standard weighted least-square-error minimization routine for a 2D Gaussian model and compared the localized centroid of the pattern with its true position as was describe in section 4.1.4. Several raw images were simulated for each angle and defocusing value in order to achieve reliable statistics. The same was repeated for detection with a 1.2 N.A. objective. The results are summarized in figure 4.31. As expected, severe localization errors were observed for high defocusing values. At a focus position of $0.7\,\mu$m, these errors were as high as 200 nm. The change of sign with the increase in defocusing value indicates the shift of the centroid along the direction of the projection of the dipole in the xy- plane (in this case, along the x-axis). This can be visualized from the patterns shown in figure 4.32.

Another important observation from figure 4.31 is that even in the plane of the dipole ($z = 0.3\,\mu$m), one has a non-zero localization error for an orientation in between a parallel and perpendicular direction. This is in total agreement with the work of Enderlein *et al.* [34]. Figure 4.33 below shows the error as a function of orientation.

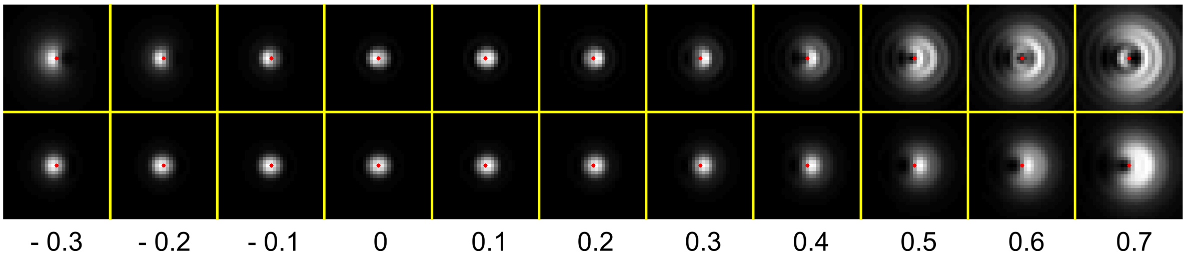

Figure 4.32: From left to right, calculated intensity patterns for a dipole with orientation $(40°, 0°)$ at different focus positions with respect to the dipole itself. The position of the focus with respect to the dipole's plane is indicated below in µm. Positive values indicate that the focal plane is above the dipole's position. The red dots in each frame mark the position of the dipole. One can clearly see the shift of the centroid along the x-axis when the focal plane moves. The pixel size is 80 nm in object space. The top row shows the patterns for N.A. = 1.49, whereas the bottom row, N.A. = 1.2

The 1.49 N.A. objective collects more efficiently the fluorescence photons emitted at super-critical angles from a dipole close to the glass interface. This leads to highly anisotropic patterns from dipoles oriented even at angles as small as 10° from the xy-plane or the optical axis.

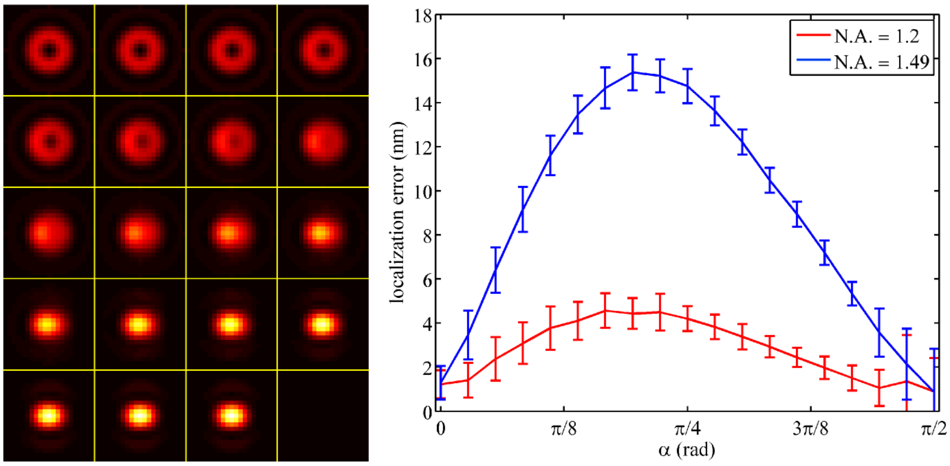

Figure 4.33: Left panel shows the calculated intensity patterns of dipoles oriented at angles $\alpha = 0°, 5°, 10°, ..., 90°$ (from left top to right bottom) as would be seen if present in the focus of a 1.49 N.A. objective. One can clearly see the shifted centroid in the images with orientations between 40° to 60° where the asymmetry is prominent. The right graph shows the localization error as a function of orientation for the two objectives chosen for study here.

If one knows the defocusing value and the 3D orientation of the emission dipole, the shift in the intensity centroid can be taken into account and corrected for. However, when the defocusing values are large (> 0.4 µm) one observes intensity patterns (with a high N.A. objective), such as shown in figure 4.32, which can be recognized with a pattern matching algorithm. Figure 4.34 shows an exemplary wide-field image showing defocused patterns of Atto 655 molecules at glass/air interface. Each pattern spreads over 40 × 40 pixels on the camera. Patterns were calculated according to the model developed in the theory section for various angles. This was done by individually varying the azimuthal and the polar angles (β, α) in equation 4.26 and thereafter, calculating the position dependent Poynting vector to get the spatial intensity patterns. By performing a pattern matching using a least-square-error minimization algorithm as described in section 4.1.4, one estimates not only the 3D orientation of the $\mathbf{p}_{\text{em}}$, but also the lateral position of the emitter. The right image in figure 4.34 shows the reconstructed image based on the identified pattern and the corresponding coordinates of the center. The precision of the lateral position one obtains using such a pattern matching algorithm is equal to one pixel in object space, since the errors are calculated by shifting the patterns pixel by pixel. Also, since the model patterns were calculated by varying the in-plane and out-of-plane angles (β, α) by a finite value (10° in the figure shown below), the precision of the orientations is limited by this value.

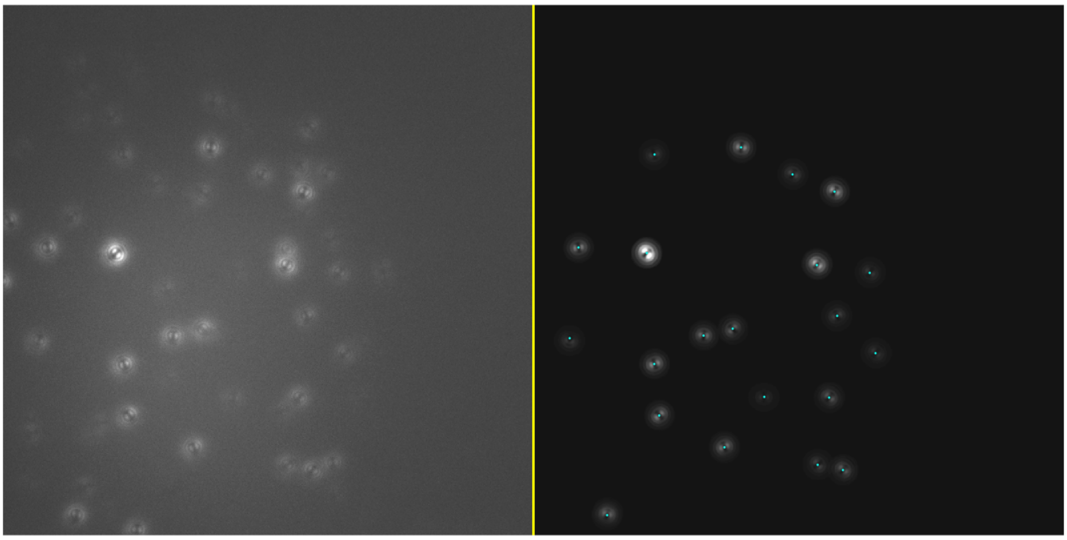

Figure 4.34: Left figure shows an image showing widefield defocused intensity patterns of Atto 655 molecules spin-coated on a glass surface. The camera pixel size was 8 µm × 8 µm. The images were taken with a high N.A. objective (N.A. = 1.49, 100x TIRF, Olympus). The net magnification of the imaging setup was 160, thus giving an effective pixel size of 50 nm in object space. The exposure time was set to 3 s. The right image shows the matched patterns using the least-square-error minimization algorithm. The cyan dots in the center show the localized position of the dipoles obtained from the pattern matching algorithm.

In order to overcome these limitations, one can either upsample the image to a finer pixel grid and choose a smaller step variation of the two angles for pattern calculations, which makes it computationally expensive; or use the preliminary results as initial guesses for further refining the parameters, for each individual pattern, using a simplex or conjugate gradient based optimization algorithm. The optimization can be accomplished using a least-square-error function or a maximum likelihood estimator [143] with position, orientation angles, brightness and background as fit parameters. With such an analysis, one can achieve sub-pixel lateral localization precision and higher precision for determining the 3D orientations. We describe this method in detail in the forthcoming sections.

4.3.4 Multidimensional Emitters

Earlier we mentioned a few exceptions for emitters which show a single dipole based excitation transition such as defect centers in diamonds and quantum dots. Similarly, not all emitters exhibit single dipole transition geometries in their emission. Symmetric quantum dots, for example, show a degenerate transition dipole isotropic in a plane ("bright plane"), perpendicular to a "dark axis", along which they do not emit. However, any elongation or asymmetry in the shape of the crystal results in an emission along this "dark axis" [144, 145]. Thus, the intensity in the image space can be expressed as a superposition of three linear dipoles mutually orthogonal to each other with differing contributions [146]. For an orientation (β, α) of the "dark axis", two dipoles I_1 and I_2 perpendicular to each other on the plane perpendicular to this vector can be visualized. The total intensity can then be written as:

$$I_{\text{total}} = \kappa I_{\beta,\alpha} + (1-\kappa)\left[\frac{1+\eta}{2} I_1 + \frac{1-\eta}{2} I_2\right] \tag{4.31}$$

where κ and η define the intensity ratios for the three dipoles. For perfectly symmetric semiconductor crystals, $\kappa \approx 0$ and $\eta \approx 0$. Figure 4.35 shows calculated patterns for a few orientations of the "dark axis" for such a nanocrystal. In the case when $\kappa = 1$, one has a linear dipole transition moment, which leads to patterns identical to organic dye molecules such as those shown in figure 4.28.

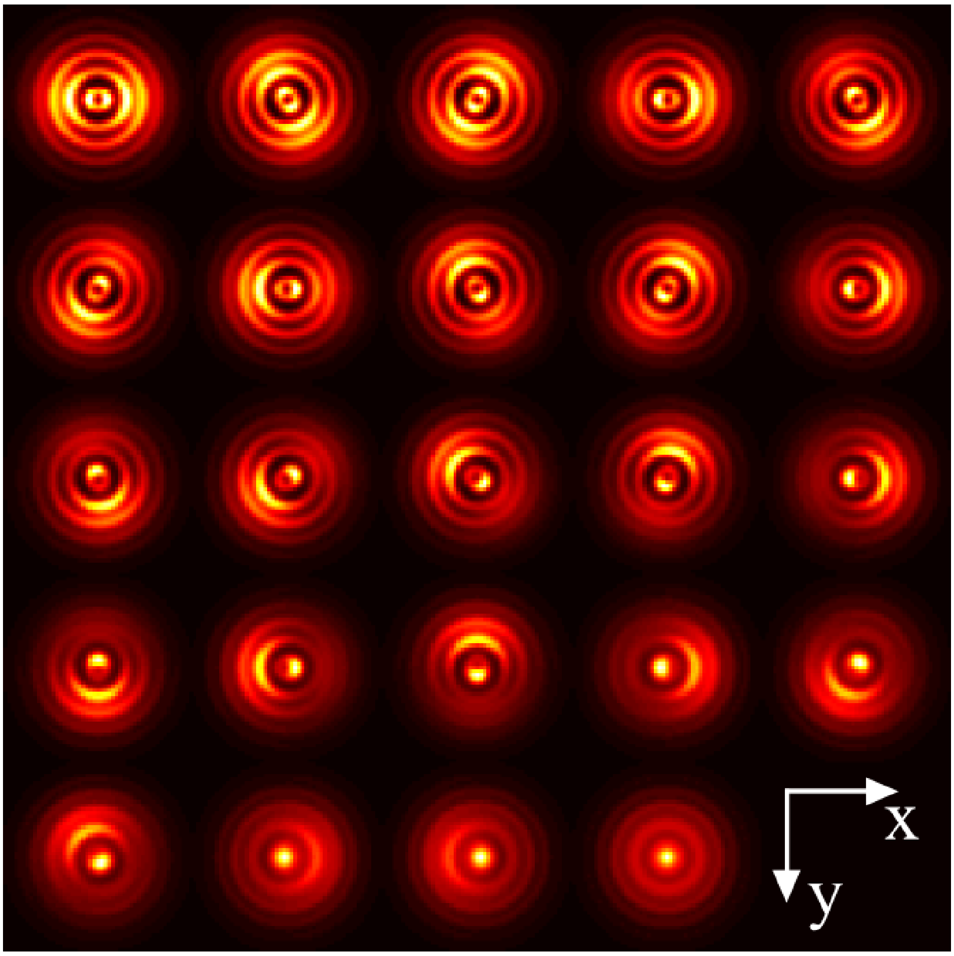

Figure 4.35: Calculated emission intensity patterns of a defocused symmetric quantum dot ($\kappa = 0$, $\eta = 0$) with the "bright plane" oriented at various angles. The calculations were done for a defocus value $\delta z = 1.2\,\mu\text{m}$, air as a medium above the quantum dots, imaged with a high N.A. (N.A. = 1.49) objective, at wavelength $\lambda_{\text{em}} = 590\,\text{nm}$. A pixel size of $65\,\text{nm} \times 65\,\text{nm}$ was assumed in object space. The out-of-plane (α) and in-plane β orientations of the "dark axis" are:

Column/Row	1 α, β	2 α, β	3 α, β	4 α, β	5 α, β
1	90°, 0°	90°, 60°	90°, 120°	75°, 0°	75°, 60°
2	75°, 120°	75°, 180°	75°, 240°	75°, 300°	60°, 0°
3	60°, 72°	60°, 144°	60°, 216°	60°, 288°	45°, 0°
4	45°, 90°	45°, 180°	45°, 270°	30°, 0°	30°, 120°
5	30°, 240°	15°, 0°	15°, 180°	0°, 0°	–, –

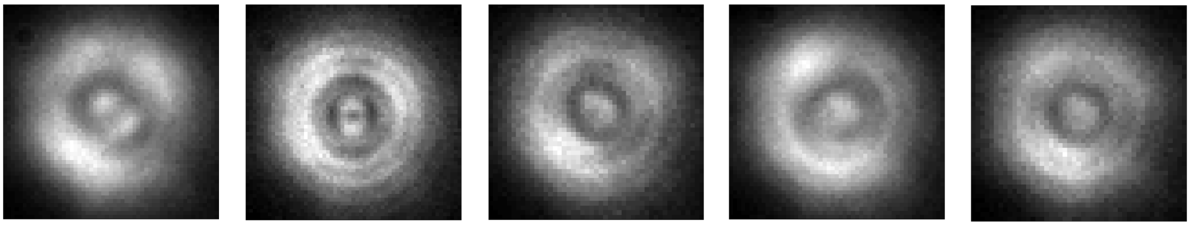

Figure 4.36: Captured emission patterns of a few quantum dots (CdSe/ZnS, PlasmaChem) with a 1.49 N.A. objective, at a defocusing value of $\delta z \approx 1.2\,\mu\text{m}$ and emission wavelength $\lambda_{em} = 590\,\text{nm}$. The effective pixel size was $65\,\text{nm} \times 65\,\text{nm}$.

4.4 Excitation-Emission Transition Dipole Imaging

So far we saw that intensity patterns produced by scanning with a radially polarized laser beam reveal the excitation transition probability of the emitter, whereas the intensity patterns recorded on a defocused image plane yield information regarding the emission transition probability, specifically, their dimensionality and orientation. We discussed briefly the origin of the dipole behavior in transition processes in our theory chapter 2.1.1. We saw that the complete absorption spectrum of a polyatomic chromophore contains all possible transitions, each associated with two of its molecular orbitals. The change of electron density over the structure of the molecule, associated with an individual transition dictates the orientation of the transition dipole moment with respect to the molecule's structure. In our theoretical outline, we also introduced briefly the Franck-Condon principle for transitions between two electronic states. According to this principle, the positions of the nuclei remain fixed during the process of excitation and emission, which leads to the so-called *vertical transitions* from the vibrational ground state of the electronic ground state to one of the overlapping vibrational excited state in the electronic excited state (see figure 4.37). Each vibrational state, which corresponds to a different set of expectation values for the mean position of all the atoms in the molecule, has a unique electron density distribution. However, what remains a constant in every electronic state, is the number of nodes (or planes across which the wavefunction changes sign) in the overall electron density. The number of nodes is higher for higher electronic states due to which the equilibrium position of the effected nuclei, and therefore the corresponding potential energy curve, shifts towards higher inter-atomic distances. The transition probabilities between a vibrational state of the electronic ground state and any vibrational state of the electronic excited state, are given by the overlap integral of the wave functions of the vibrational states involved, which are known as the Franck-Condon factors (see equation (2.10)). These factors are the heart of *electron-phonon* coupling. Following the electronic transition, which usually takes the molecule to a higher vibrational state, a non-radiative vibrational relaxation, and a resultant structural readjustment of the molecule takes place. The total reorganization energy for the full excitation-emission cycle, the measure of the so-called *Stokes shift*, is thus directly related to this structural readjustment.

The important point in the whole discussion above, which must be highlighted in the context of the experiments and results that follow, is that during each vibrational relaxation process accompanying an electronic transition, the electron density over the complete molecule's framework is modified, before the next electronic transition occurs. In simpler words, the net transition dipole of excitation ($\mathbf{p}_{\mathrm{exc}}$) is usually not the same as the transition dipole of emission process ($\mathbf{p}_{\mathrm{em}}$). For examples corroborating this argument, see references [147–150]. Ultrafast spectroscopy which yields time resolved fluo-

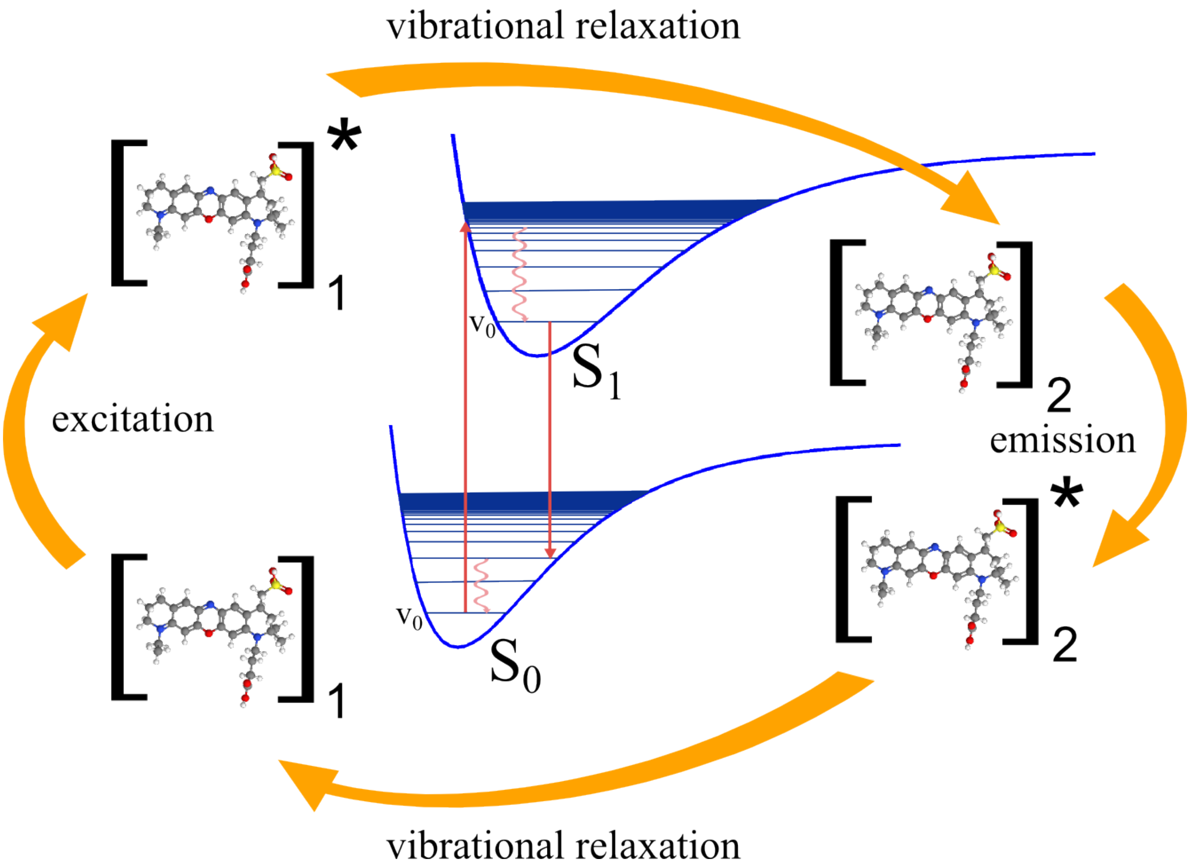

Figure 4.37: A molecule in its ground state (S_0, v_0) with structure 1 undergoes an excitation, when a vertical transition to a higher vibrational state $v_p, p \neq 0$ in the excited state S_1 takes place. The molecule in this state (S_1, v_p) has the same structure 1, which is unstable (therefore marked as an asterisk (*) sign in the figure). Immediate vibrational relaxation of the molecule takes place leading it to a structure 2. The molecule now populates the state (S_1, v_0) which can be seen as a metastable state, where it stays for a time τ_f (average lifetime) before proceeding with a radiative or a non-radiative de-excitation process. A radiative emission is another vertical transition from the zero vibrational state of the excited state S_1, v_0 to a higher vibrational state in the ground state $(S_0, v_q), q \neq 0$. Again, the structure of the molecule in this state is the same, and it undergoes rapid vibrational relaxation to the initial ground state structure 1.

rescence absorption and fluorescence spectra with a resolution of few femtoseconds, such as in the work shown in [150], is used to monitor and study such structural relaxation processes accompanying an electronic transition. Our aim in this section is to show the first experimental results for the *simultaneous* determination of the three-dimensional orientations of both, the $\mathbf{p}_{\mathrm{exc}}$ as well as the $\mathbf{p}_{\mathrm{em}}$, of each individual fluorescent emitters immobilized on a substrate in a polymer.

4.4.1 Experimental Setup and Methods

Figure 4.38 shows a schematic representation of the optical setup used here. A pulsed white light laser (Fianium SC400-4-80) together with an acousto-optic tunable filter (AOTFnC-400.650-TN) was used for excitation ($\lambda_{\mathrm{exc}} = 640\,\mathrm{nm}$). The linearly polarized TEM_{00} beam was then passed through a pixelated liquid crystal mode converter

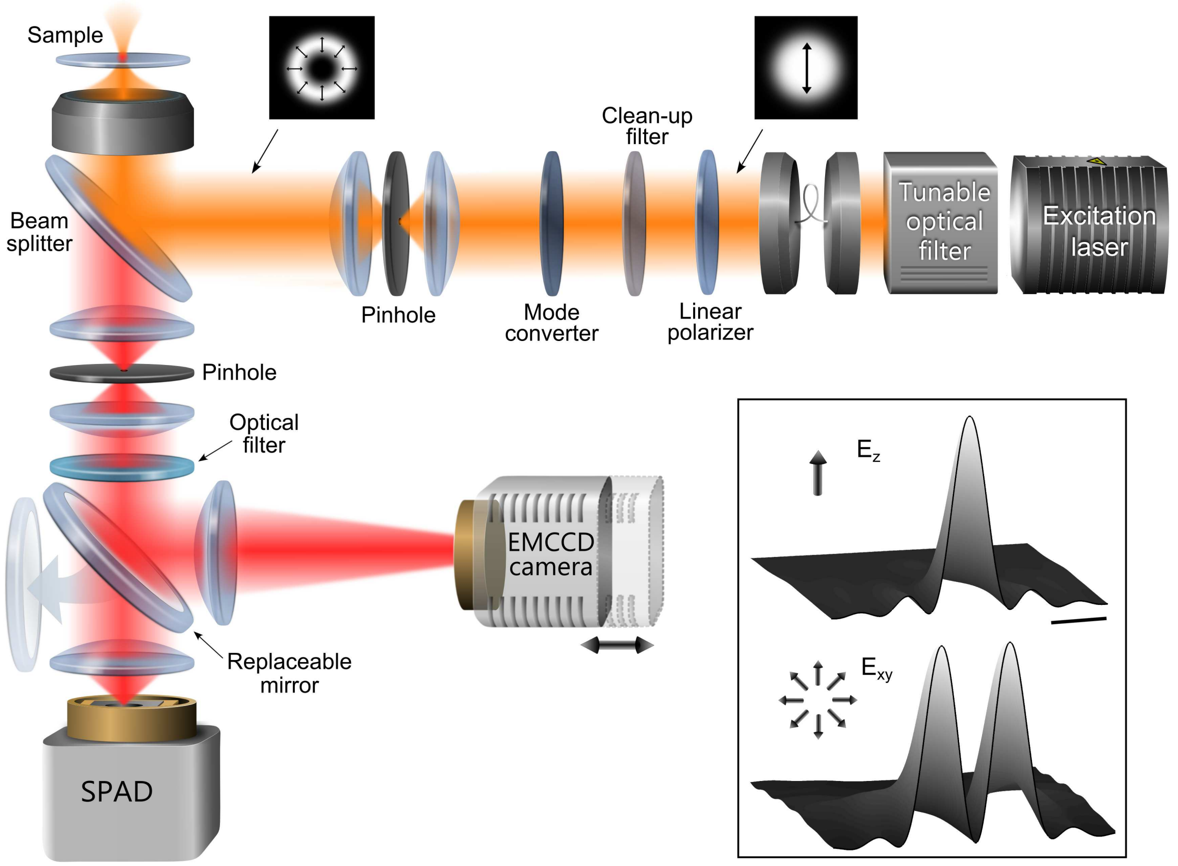

Figure 4.38: Experimental setup showing the path of the excitation beam in yellow and the fluorescence emission pathways as red. The collimated (TEM_{00}) pulsed laser is passed through a linear polarizer (LP). Any unwanted wavelengths present were blocked using a clean up filter (CL) before the beam was passed through the mode converter. Thereafter, the beam was mode cleaned by focusing through a pinhole (PH) leading to a doughnut profile radially polarized laser. The beamsplitter (BS) reflects the laser into the objective which focuses the light onto the sample. The inset shows the calculated longitudinal and the transverse electric field components on the surface of the substrate 0.5 µm around the optical axis (scalebar = 200 nm) The sample is scanned first by focusing the photons onto a single photon avalanche photodetector (SPAD), to obtain the excitation image and the positions of the emitters. Later, a replaceable mirror is placed to reflect the emission photons onto an EMCCD camera shifted from the imaging plane, and a defocused image at each position is captured. [This figure has been published in the article [151].]

(Arcoptix S.A.) which rotates the light polarization spatially to generate a radially polarized TM_{01} beam. This beam was then focused on the surface of a sample through a high N.A. objective lens (APON 60X OTIRF, N.A. = 1.49, Olympus) after reflecting on a 30 R : 70 T non-polarizing beam splitter (ThorLabs BS019). The sample was prepared by spin-coating 10 µL of 1 nM Atto 655 (AttoTech, GmbH) dye solution on top of a cleaned glass ($n_{ref} = 1.52$) coverslip and then scanned using a piezoelectric stage with a pixel size of 50 nm. Collected photons were focused onto the active area of a single-photon avalanche photodiode (τ-SPAD, PicoQuant) and counted with a multichannel picosecond event timer (HydraHarp 400, PicoQuant). The backscattered excitation light was blocked using a long pass filter (BLP01-635R, Semrock BrightLine) and additional band pass filters (Semrock BrightLine FF01-692/40). The laser power, $\sim 4\,\mathrm{kW/cm^2}$, and the sample scanning rate, 3 ms per pixel were chosen optimally so as to minimize photobleaching of the dye molecules and achieve a reasonable signal-to-noise ratio in the excitation images. Thereafter, the piezo stage was parked on each molecule's position, identified from the scan image, and the fluorescence collected was guided with the help of a replaceable mirror onto an EMCCD camera (iXon DU860-D, Andor Technology). For the chosen magnification, the pixel size of the camera corresponds to $60\,\mathrm{nm} \times 60\,\mathrm{nm}$ area in the object space. The camera was shifted from the image plane by about $\delta z = 0.9\,\mu\mathrm{m}$ above the focal plane in the object space. Each image was acquired with an exposure of 9 s, an electron multiplying gain of 100, and with the excitation power of $\sim 10\,\mathrm{kW/cm^2}$. All the data collection and hardware synchronization was performed on a custom written LabVIEW platform.

As a second system, we investigated molecules of the dye Alexa 488 (Invitrogen) embedded into a thin layer of polymer by spin-coating a 0.1% w/v PVA/water (refractive index 1.55) solution containing 1 nM of the dye on top of a cleaned coverslip at 6000 rpm for 60 seconds, yielding a distribution of immobilized single molecules within a thin polymer film. The sample was excited with an excitation power of $1.6\,\mathrm{kW/cm^2}$ at 485 nm and a dwell time per pixel same as the previous measurements. As before, backscattered excitation light was blocked using suitable long (BLP01-488R, Semrock) and band pass (FF02-525/40, Semrock) filters. The defocused images were obtained at the same excitation power but with the camera set to a position such that the effective defocusing at the object space δz was around $0.6\,\mu\mathrm{m}$, and the acquisition time was now 15 s.

4.4.2 Results

Measurements on Single Molecules

The first row in figure 4.39 shows 5 out of 131 excitation patterns of the Atto 655 molecules acquired during the scans. The peak count rates observed for these molecules range between 17 to 30 kHz in the focus of excitation and the total number of photons collected between 1×10^3 to 4.5×10^3. We estimated the excited-state decay lifetime (τ_f) for each molecule individually after pattern matching. The τ_f values show a distribution peaked around 2.84 ns. The third row in figure 4.39 shows the defocused images corresponding to the excitation patterns shown in the first row. We estimated the number of photons in each pixel by converting the counts into photon numbers, taking into account the electron-multiplying gain used and the sensitivity of the camera. This was done by first subtracting the camera bias from the recorded camera counts, multiplying the resultant with the sensitivity (average number of photons required to produce one

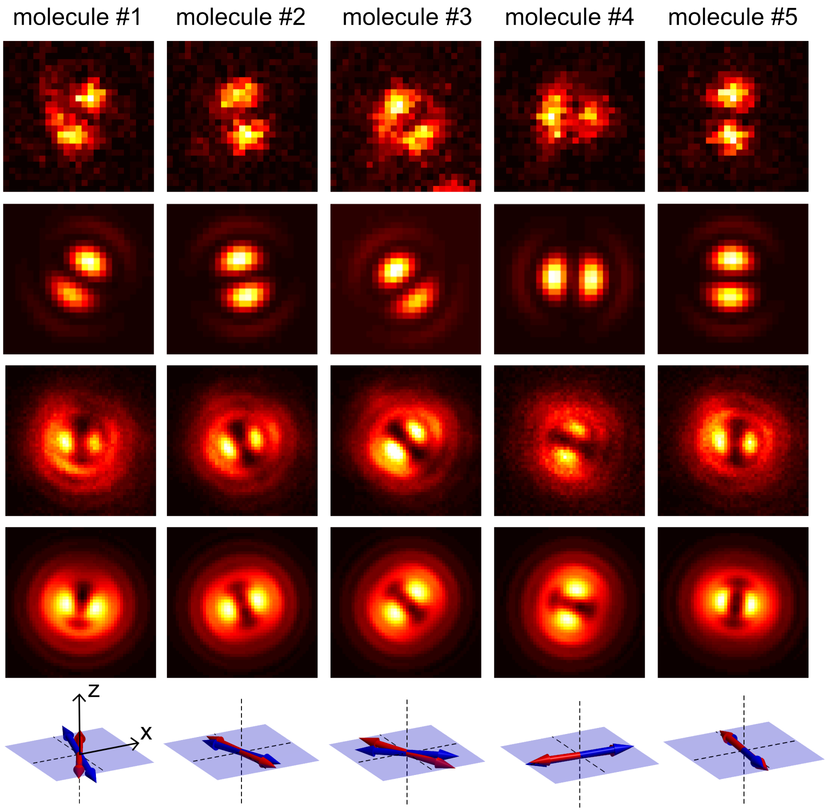

Figure 4.39: Emission and excitation patterns of five Atto 655 molecules. The top row shows the excitation images, the second row the corresponding fitted patterns, the third row shows the defocused images, and the fourth row the fitted emission patterns. The scan pixel size is 50 nm and each excitation image is 25 × 25 pixels; whereas the camera pixel size is ∼60 nm with each defocused image spanning over 40 × 40 pixels. The last row is a depiction of both the excitation (light) and emission (dark) dipole orientations, as fitted from the measurements. The α and the β values indicate the orientation with respect to the z- and x-axes, shown for the first molecule. [This figure has been published in the article [151].] The fitted orientation angles for both dipoles are:

Molecule #	β_{exc}	α_{exc}	β_{em}	α_{em}
1	61.2°	83.2°	86.6°	76.4°
2	101.6°	89.2°	288.8°	87.9°
3	124.5°	83.1°	315.9°	87°
4	356.9°	88.6°	162.7°	83.8°
5	87.5°	7.92°	82.2°	88.1°

count, which depends on the pre-amp setting and the read-out rate), and finally dividing it by the electron gain used. The total number of photons detected per molecule determined in this way range between 1.6×10^5 to 1.2×10^6.

For data evaluation, we first performed the least-squares minimization pattern matching that we described in section 4.1.4 for both excitation and emission intensity patterns. The obtained fit parameters served as the initial guess values for the optimization of a log-likelihood function assuming Poissonian statistics [143]

$$L = -\sum_{\mathbf{r}} \left[I(\mathbf{r}) \cdot \log(A \cdot P(\mathbf{r}|\mathbf{r}_P, \beta, \alpha) + B) - (A \cdot P(\mathbf{r}|\mathbf{r}_P, \beta, \alpha) + B) \right] \tag{4.32}$$

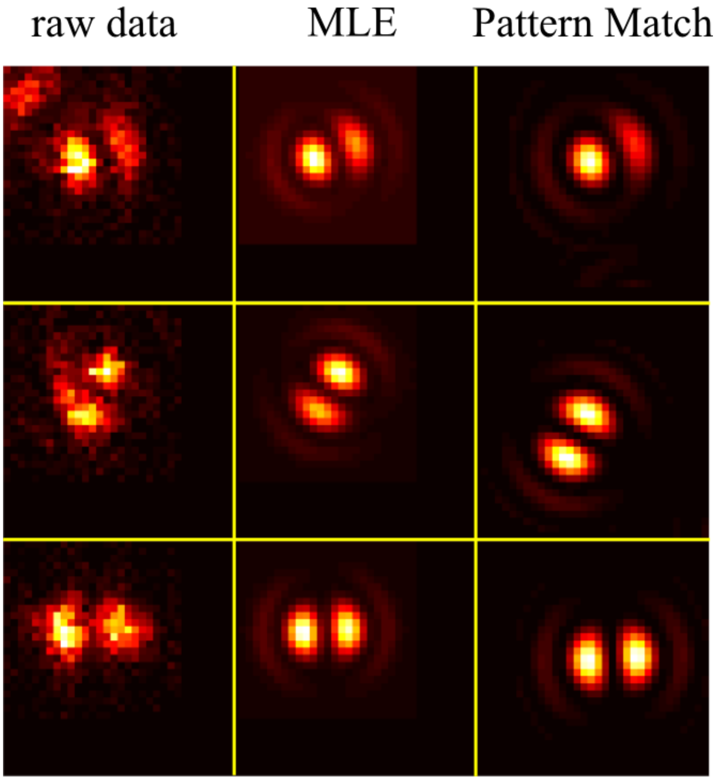

Figure 4.40: The left column shows the raw data cropped from scan images acquired using a radially polarized laser for three molecules. The right column shows the patterns identified using the least-squares minimization pattern match algorithm; whereas the middle column shows the refinement of the parameters using the described maximum likelihood estimation (MLE).

Molecule #	MLE (β, α)	Pattern Match (β, α)
1	$(340.0°, 80.3°)$	$(339°, 75°)$
2	$(118.8°, 83.2°)$	$(115°, 90°)$
3	$(176.3°, 88.3°)$	$(175°, 90°)$

which yields refined parameters beyond the discrete set of values recovered by the pattern matching. Here, $I(\mathbf{r})$ denotes the measured image and $P(\mathbf{r}|\mathbf{r}_P, \beta, \alpha)$ is the pattern calculated using the wave-optical model described in section 4.3.1. The optimization was done for the parameters $\mathbf{r}_P, \beta, \alpha, A, B$, where $\mathbf{r}_P$ is the pattern's central location, A is the integrated intensity, and B the background intensity value. The optimization algorithm was based on a conjugate gradient method. Refinement of the fit using the log-likelihood function increases the fit accuracy by five to ten-fold. Theoretically, one could use, for the pattern matching, a set of patterns with a ten-fold finer angular spacing of α- and β-values, which would make the log likelihood-based refinement obsolete. However, such an approach would be computationally prohibitive.

The second and fourth rows of figure 4.39 show the fitted excitation and emission patterns for five Atto 655 molecules. In order to estimate the fitting errors, we applied a bootstrap algorithm where new noisy samples were generated based on the estimated parameters, and then fitted again. In this way, a distribution for each parameter was obtained using the above maximum likelihood estimator by fitting one thousand re-sampled images. The α-values for almost all molecules were close to 90°, which indicates that the spin-coated molecules were lying mostly flat on the substrate consistent with what we saw in our previous work in section 3.2.2. The standard errors of α and β for the orientation of $\mathbf{p}_{\text{exc}}$ were both smaller than 2°, whereas for the orientation of $\mathbf{p}_{\text{em}}$, they were both smaller than 0.4°. These small values of the standard deviations for the obtained angles are due to the high number of total detected photons per molecule. Figure 4.41 shows the result of bootstrapping for the estimation of the orientations of both the TDMs of a molecule. Further, the small values of the standard deviations for the angles obtained using the bootstrap method described above establishes the accuracy of the fitting method for the model intensity patterns calculated with the number of photons and the background values estimated from the fitting itself. The quality of the defocused images is sensitive to small obstructions or any undesired tilt present in the emission pathways, which are hard to rectify in a custom built setup that lead to slightly asymmetric defocused images. This does not, however, affect the estimation of the in-plane angles β, but introduces small systematic errors in the estimation of the out-of-plane angles α of the $\mathbf{p}_{\text{em}}$, affecting slightly the accuracy of the fitted results.

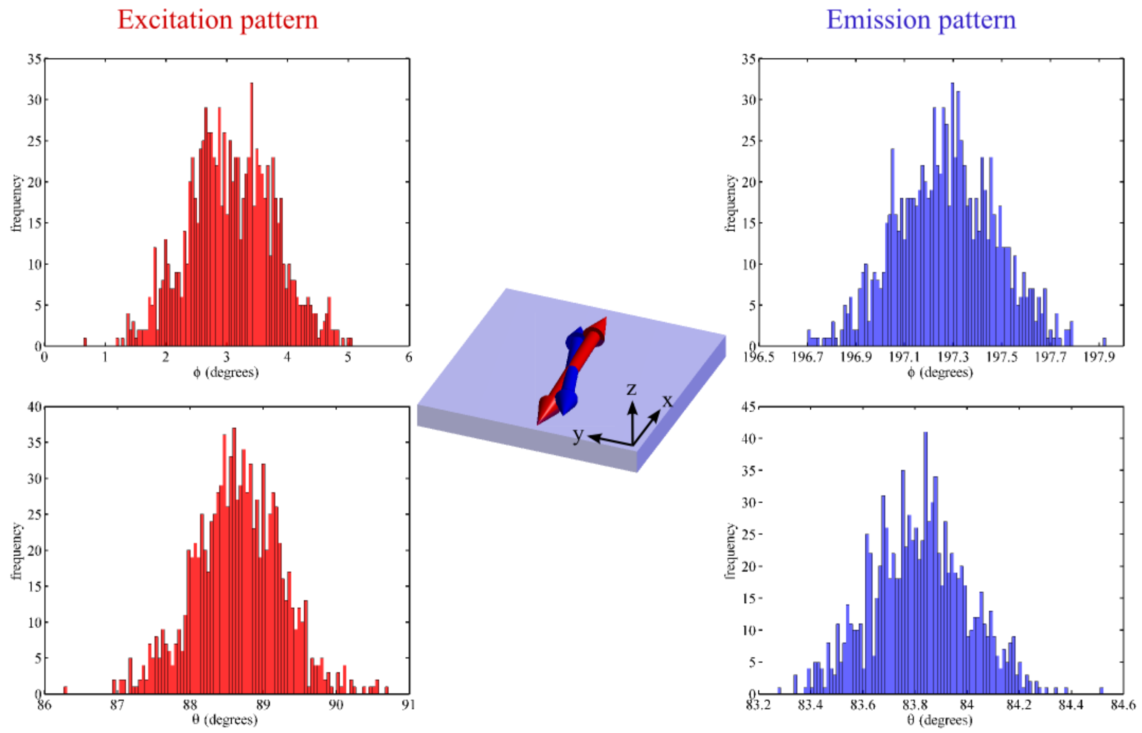

Figure 4.41: Bootstrap results showing the distribution of the orientations for an Atto 655 molecule. The number of photons collected during the scanning was ∼ 3.2×10^3 whereas ∼ 2.4×10^5 on the defocused camera for the emission pattern. The standard deviations of β and α from the bootstrap data of the excitation pattern are 1.6° and 1.5°; whereas for the emission pattern they are 0.5° and 0.4°.

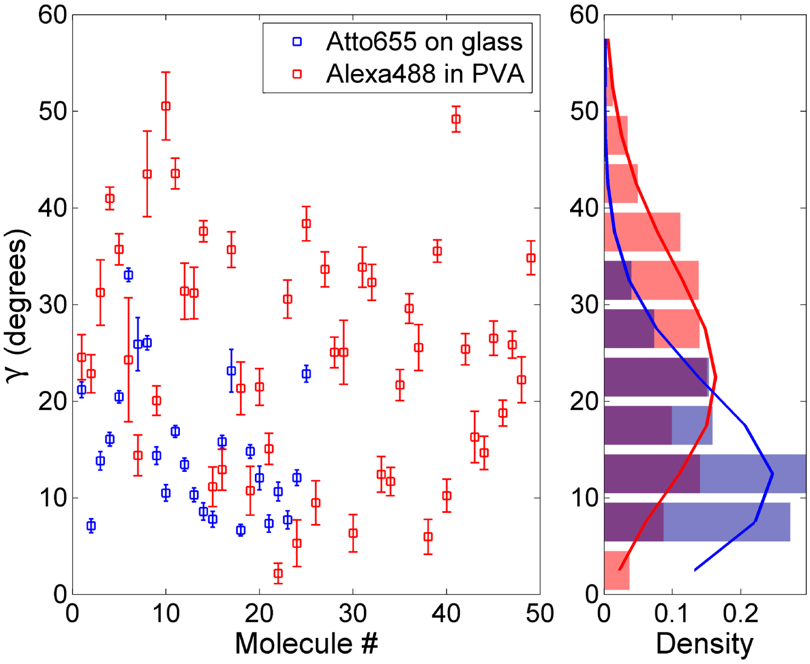

Figure 4.42: Distributions of determined γ values (left) and their corresponding distribution (right) for 25 molecules Atto 655 molecules on a glass surface (blue), and for 49 Alexa 488 molecules embedded into a polymer film (red). The error bars shown in the left figure were estimating using a bootstrapping algorithm. The right side shows the probability distributions with a bin width of 5°. The distributions were fitted with a Poisson distribution (solid lines) yielding a mean value of γ equal to 14.6° for Atto 655 and equal to 22.5° for Alexa 488. The results for the first five molecules of Atto 655 correspond to the the five measurements shown in figure 4.39 and listed in table beneath. [This figure has been published in the article [151].]

The total number of photons collected from the Alexa 488 molecules ranged between 2×10^4 and 1.5×10^5 on the defocused camera, and between 0.7×10^3 and 3.4×10^3 in the excitation images. Now, the determined α-values showed a broad distribution between 0° and 90° indicating that the molecules immobilized within the polymer layer did not have a preferred orientation parallel to the surface, in contrast to the Atto 655 sample. The standard errors of α and β for $\mathbf{p}_{\text{exc}}$ were around 5°, whereas for $\mathbf{p}_{\text{em}}$ they were around 1°. The difference in precision between the Atto 655 and the Alexa 488 measurements can be explained by (i) the fewer number of total photons that were collected from the Alexa 488 dye molecules; and (ii) the smaller defocusing value chosen in order to achieve a good signal-to-noise ratio, which affects the accuracy of estimating the α and β values, in particular, for dipoles oriented almost vertically.

After obtaining the orientations of both $\mathbf{p}_{\text{exc}}$ and $\mathbf{p}_{\text{em}}$, it is now straightforward to estimate the inclination angle γ between excitation and emission dipoles for each molecule. Figure 4.42 shows the distribution of γ for 25 measured Atto 655 molecules and for 49 Alexa 488 molecules. The values for γ vary between 7° and 33° with a mean of $\sim$ 15° for Atto 655 molecules, whereas a larger mean value of $\sim$ 23° and broader distribution for the Alexa 488 molecules. This shows that there is a significant variation of the transition dipoles during the excitation and emission processes for both the species.

Ensemble Anisotropy Measurements

In order to compare the obtained values with an ensemble estimate for the γ values, we performed time-resolved anisotropy measurements on $\sim 1\,\mu$M in 90% glycerol solutions of the two dyes. The anisotropy measurements were performed by focusing two orthogonally polarized lasers of the same excitation wavelength through a low numerical aperture (UPlanSApo 20x, N.A. = 0.75, Olympus) air objective. A low N.A. objective is essential for such measurements in order to reduce the depolarization of the excitation laser in the focus. For the excitation of Atto 655 molecules, we used two 640 nm diode lasers (LDH-D-C-640, PicoQuant) with a pulse width of 100 ps, pulsed alternatively with a repetition rate of 40 MHz each with the help of a multichannel picosecond diode laser driver (PDL 828 'Sepia II', PicoQuant). This gives a time delay of 12.5 ns between the two alternate polarization pulses in the focus. Clean-up filters (Z640/10X, Chroma Technology) were used to block any unwanted wavelength from the lasers. The power of each laser was set to $0.1\,\mathrm{kW/cm^2}$. The high concentration ensured the presence of all possible orientations of the excitation and emission transition dipoles. The emission collected through the same objective was focused onto a 50 µm pinhole and thereafter split and refocused onto the active area (180 µm) of two Single Photon Counting Modules (SPCM CD, Excelitas Technologies Inc., timing resolution 350 ps) by a polarizing beamsplitter cube. The emission light was filtered from any background or scattering by passing through band-pass filters (BrightLine HC 692/40, Semrock) in front of the detectors. The detected photons were recorded with 8 ps time resolution by a multichannel picosecond event timer and TCSPC module (HydraHarp 400, PicoQuant). In such an experimental setup, each detector measures two consecutive fluorescence decay curves within one complete excitation cycle, one corresponding to the laser which is parallel in polarization to the detector (higher amplitude) and the other which is orthogonal to it (lower amplitude). The four TCSPC curves thus recorded can be named as $I_{\parallel,\parallel}$,$I_{\parallel,\perp}$, $I_{\perp,\parallel}$, $I_{\perp,\perp}$ where the first symbol represents the polarization of the laser with respect to a fixed $\parallel$ and $\perp$ orientation in the laboratory reference frame and the second symbol marks the orientation for the detection. The time resolved anisotropy $r(\tau)$ is calculated from the following equation:

$$r(\tau) = \frac{\sqrt{I_{\parallel,\parallel}(\tau) \times I_{\perp,\perp}(\tau)} - \sqrt{I_{\parallel,\perp}(\tau) \times I_{\perp,\parallel}(\tau)}}{\sqrt{I_{\parallel,\parallel}(\tau) \times I_{\perp,\perp}(\tau)} + 2\sqrt{I_{\parallel,\perp}(\tau) \times I_{\perp,\parallel}(\tau)}} \tag{4.33}$$

where τ is the time delay between the laser pulse and tcspc channel. Here, τ is determined separately for each TCSPC curve. The time channel corresponding to roughly half the maximum counts on the rising edge of the TCSPC curve was identified as $\langle\tau_0\rangle$. An exponential tail fitting is performed on $r(\tau)$ and the rotational diffusion D of the dye molecules is obtained. Thereafter, the r_0 for Atto 655 was obtained by extrapolating the fitted curve to time τ_0. This corresponds to the ensemble average of the angle between the excitation and the emission dipoles $\langle\gamma\rangle$ values, which is given by (see also reference [83]):

$$\langle\gamma\rangle = \cos^{-1}\sqrt{\frac{5r_0+1}{3}}, \quad 0 \leqslant \gamma \leqslant \frac{\pi}{2} \tag{4.34}$$

Similarly, the measurements for Alexa 488 were performed using two orthogonally polarized 485 nm (LDH-P-C-485B) lasers, appropriate clean-up filters (F49-488, AHF) before them, and band-pass filters (FF01-525/30) in the detection.

We obtained $r_0 = 0.361$ and 0.33 for the Atto 655 and Alexa 488 measurements, which that correspond to $\langle\gamma\rangle$ values of 14.9° and 19.9° respectively using equation 4.34. These are values are in good agreement to the mean values from the single-molecule data presented above.

4.4.3 Discussion and Outlook

The important message that is conveyed from these measurements is that significant reorganization in the structure of the molecules after the excitation takes place which leads to an overall change in the electron density over the structures before the emission takes place. This shows up as non-negligible $\langle\gamma\rangle$. One can model the electron density maps of the molecule's structure in the excited and ground vibrational states in the HOMO and LUMO electronic states, similar to the calculations shown in [147], in order to compare the obtained values with the theoretical calculations (beyond the scope of this thesis). It is beyond the scope of our work to account for the wide variations in γ that we observe for individual molecules. We, however, speculate that the bending of the molecule's backbone structure, depending on the extent of local electrostatic and van der Waals interactions with the substrate can be a key reason. Correlating the values of γ together with the force of binding with the interface, measured using single-molecule force sensitive techniques might be useful to investigate the local surface effects [152].

The method we present here can be extended to the imaging of magnetic dipoles, electric multipoles, and quantum dots, and probe their behavior in different electromagnetic environments. Quantum dots, as we saw in the previous section, have a 2D degenerate emission transition dipole located in a plane perpendicular to their crystalline c-axis [27]. Theoretical calculations and a few experimental results show that when placed close to metallic nanostructures or optical antennas, the degeneracy is lifted off and they show polarized emission properties similar to a dipole [13, 28]. A complete behavior of the transitions properties can only be studied by monitoring both, the excitation and emission transition dipole imaging simultaneously.

One can try various combinations of methods that determine the excitation and emission transition dipoles of molecules, such as, the combination of radially polarized excitation scanning together with a detection scheme as was employed in work of Hohlbein *et al.* by splitting the emitted photons onto three single photon counting detectors is much suited for rapidly measuring the orientations of both transitions dipoles of single molecules [62]. By comparing the intensity ratios on the detectors, one can determine, using simple relations, the in-plane and out-of-plane orientations for the emission transition dipole of a single chromophore. In this way, one has all the information, including the fluorescence lifetime of each molecule, just while acquiring a scan image. In comparison to the method we adopted for the study above, this method is faster (up to an order of magnitude) and can achieve a higher throughput, since one need not collect a high number of photons for the emission as we require. However, the significant advantage of using defocused imaging for the determination of the emission transition probabilities, over most existing techniques, is its ability to distinguish between a single dipole emitter and a multidimensional or isotropic emitter. The structural details of the emission from exotic emitters, such as quantum dots for example, can be resolved and investigated easily by using this method. By introducing a beamsplitter in place of a mirror, such that only 70% of the light is used for defocused imaging, the remaining fraction of the detected photons can be used used for fluorescence lifetime estimation, for studying the photophysics of the emitter, and even photon antibunching studies if the emission center is stable enough. This information can be highly useful when studying the photoluminescence properties of such exotic emitters.

Together with the orientation information, one obtains the lateral position of an emitter in the object space. Due to the high number of photons collected on the camera, the precision of position determination, or localization precision, can go down to a few nanometers. From the bootstrapping results of the data presented above, we achieve 2 to 3 nm lateral localization precision indeed. This means, if combined with smMIET technique, one has all the information, i.e. fluorescence lifetimes, emission transition dipole orientations for obtaining the axial distances, and defocused intensity patterns to localize the molecules laterally. Thereby, one can localize individual emitters in all three dimensions, with nanometer precision. It must again be pointed out here that the lateral position obtained from such an analysis already takes into account the asymmetric angular emission distribution from a fixed dipole, and therefore, is free of any orientation artifacts.

4.5 Transition Dipole Imaging of Carbon Nanodots

Carbon Nanodots (CNDs) are fluorescent carbon nanoparticles which have recently attracted enormous attention due to their bright photoluminescence (PL), solubility in water, low toxicity, easy functionalization, chemical inertness and one-step preparation [153–155]. In order to fully understand the origin of their PL, we investigated the dimensionality of their transition dipole moments ($\mathbf{p}_{\mathrm{exc}}$ and $\mathbf{p}_{\mathrm{em}}$). Depending on the origin of the PL, the dimensionality of the TDM changes [156, 157] from one dimensional dipole for single chromophores for example, to an isotropic distribution of emission probability in a highly symmetric emitter such as silicon nanocrystals [158]. Molecules such as benzene and crystal violet show two-dimensional degenerate TDMs due to their symmetrical planar structures [159].

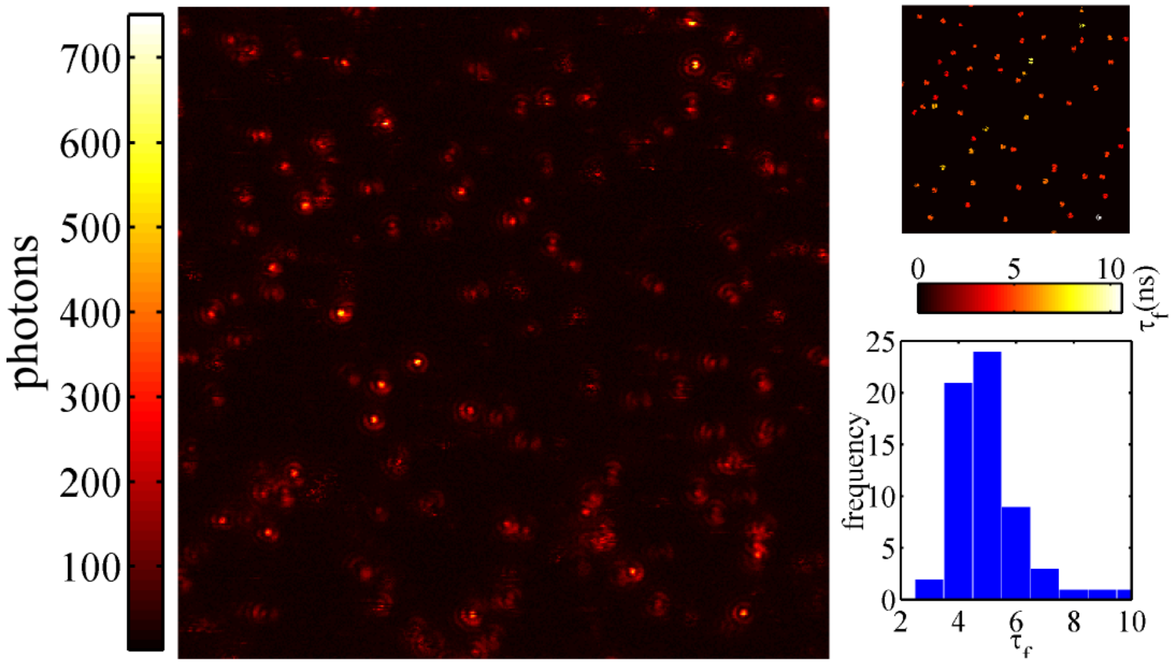

Figure 4.43: The left image shows intensity patterns of CNDs scanned by a radially polarized laser. The image size is 12.5 × 12.5μm^2 with a pixel size of 50 nm and a pixel dwell time of 5 ms. The excitation was done using a 488 nm laser at a power of ∼ 5 kWcm^2. The top right image shows the lifetime image with the calculated lifetime values for each single emitter. The right bottom graph shows the histogram of all the lifetimes of all the emitters identified. 62 intensity patterns were identified using the pattern matching algorithm.

The synthesis of carbon dots is given in detail in the supplementary information of Ghosh *et al.* [160]. Samples were prepared by spin-coating a droplet of an aqueous solution of these particles on a glass coverslide. Thereafter, we scanned the sample with a focused radially polarized laser beam with wavelength of 488 nm. Figure 4.43 shows one such a scan performed with a 488 nm radially polarized laser. The image clearly shows fixed single dipole $\mathbf{p}_{\mathrm{exc}}$ behavior. More than that, one sees that no CND has

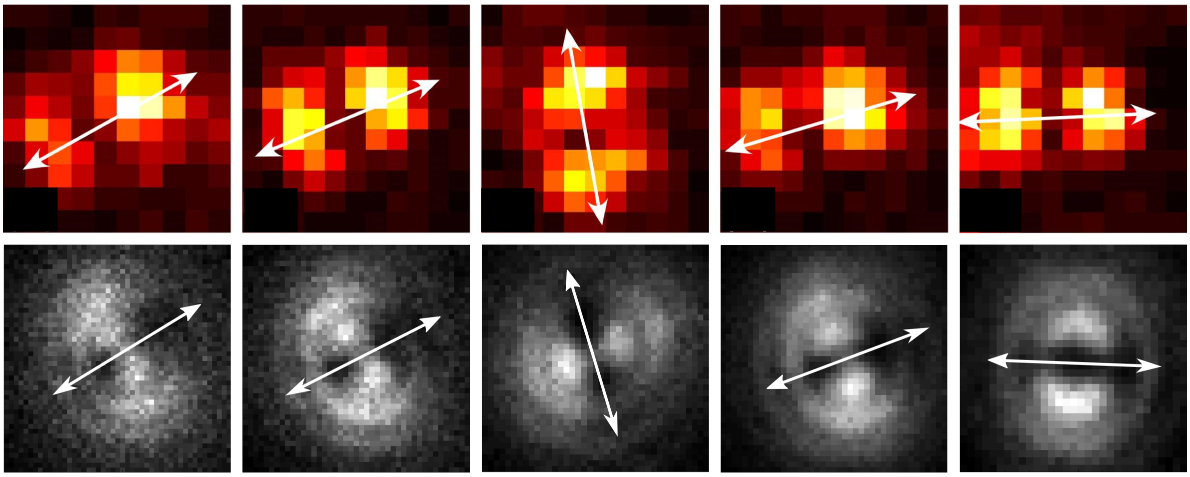

Figure 4.44: Top row shows scans of 5 carbon dot particles with radially polarized laser with a wavelength of 488 nm. The orientations of the $\mathbf{p}_{\mathrm{exc}}$ for these patterns are shown with the double arrows. The bottom row shows the defocused images of the corresponding molecules together with the orientations of the $\mathbf{p}_{\mathrm{em}}$ shown by the double arrows. [This figure has been published in the article [160].]

more than one emission center. Of course, one can argue that there might be multiple emitters oriented in same direction, for which one needs to perform careful antibunching measurements or step-wise bleaching experiments. Some intensity time traces are shown in the supplementary figure S5 in [160] which prove that the CNDs have single emission centers. The presence of single dipole $\mathbf{p}_{\mathrm{exc}}$ indicates that the PL originates from charge recombination of defect centers in the CND. Further, we performed experiments to determine the $\mathbf{p}_{\mathrm{exc}}$ and $\mathbf{p}_{\mathrm{em}}$ simultaneously on individual particles. Figure 4.44 shows scans of 5 particles with radially polarized laser excitation and their corresponding defocused images which also show single dipole behavior. The defocusing value was approximately 0.9 µm above the focal plane. The figure shows that the excitation and emission takes along a particular orientation in each particle. The angle between these both TDMs does not exceed 5° for these particles.

5 Discussion and Outlook

5.1 MIET on Metal Thin Films

The quenching of fluorescence and the modification of emission rates of a dye molecule depend on several factors such as the refractive index and thickness of the metal film, the layers and thicknesses the media above and below, the emission wavelength and quantum yield of the dye. Depending on the requirement of the experiment (the axial resolution desired, the maximum height range, refractive index of the medium) and dye characteristics one must to calculate the MIET calibration curves in order to find the most suitable metal film and its thickness. Even though it is difficult to predict a suitable metal, a few general trends can be speculated based on their properties. In order to simplify the situation, let us fix the emission wavelength and thickness of the metal film to 690 nm and 10 nm respectively. We assume that the thin metal film is deposited on top of glass ($n = 1.52$) and the medium above is water ($n = 1.33$). We further take the quantum yield of the emitter as unity. The refractive index of these metals at this wavelength are listed in the form of a table below[12].

Metal	Refractive index (690 nm)
Aluminum	1.58 + 7.93i
Beryllium	3.43 + 3.24i
Chromium	3.63 + 4.26i
Copper	0.22 + 4.00i
Gold	0.17 + 3.79i
Nickel[2]	2.15 + 3.93i
Palladium	1.94 + 4.47i
Platinum	2.50 + 3.93i
Silver	0.17 + 4.22i
Titanium	2.18 + 3.27i
Tungsten	3.66 + 2.79i

---

[1] The refractive indices were calculated using the Brendel-Bormann model using the values given in [123].

[2] We assume the relative magnetic permeability as unity for the case of Nickel.

Figure 5.1 shows the variation of lifetimes for an isotropic emitter, or a dipole that is rotating faster than its excited state lifetime so that it can be considered as an isotropic emitter. From Hagen-Rubens relationship, the conductivity of a metal is related to the reflection coefficient (at normal incidences).

$$|R| \approx 1 - 2\sqrt{\frac{\omega}{2\pi\sigma}} \tag{5.1}$$

where ω is the angular frequency of light. Therefore, at a particular wavelength, the conductivity is roughly proportional to the inverse of the transparency of the metal. Since, $|T| \propto 1 - |1 - |n|/1 + |n||^2$, it gives us that silver is the best conductor, closely followed by gold and then copper, at the chosen wavelength. Tungsten, beryllium and chromium are the least conductive materials in the list. Thus, from the curves shown in figure 5.1, one can vaguely state that the steepness of the lifetime variation with distance is closely related to the conductivity of the metal. Clearly, the higher the conductivity of the metal, the longer the distance range where it effects the fluorescence. However, aluminum acts as an exception to this trend. This is due to its exceptionally high imaginary part of refractive index.

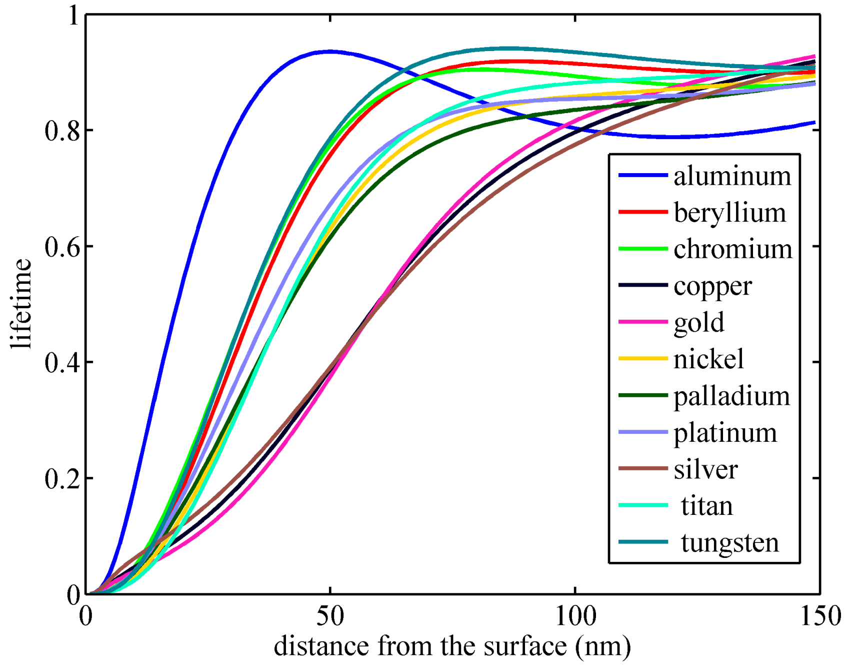

Figure 5.1: Calculated relative lifetime values as a function of distance from the surface of various metals.

Most of the fluorescent dyes exhibit an excited state lifetime τ_f in the range of 1-5 ns. The precision of estimating lifetime values depends on the number of photons collected.

Assuming pure Poisson statistics, the error of lifetime estimation is given by:

$$\Delta\tau \geqslant \frac{\tau_f}{\sqrt{N}} \tag{5.2}$$

where N is the total number of photons. The equality occurs only if the statistics is ideal and there is no background, in the presence of which the error increases. This means that if one has approximately 1000 photons, the relative error within which the lifetime values can be estimated cannot be less than 0.03. Using the MIET curves, this error can be translated into axial errors. For a single molecule, immobilized in a polymer over glass substrate, one collects approximately 10^4 photons before bleaching it. However, due to the quenching of fluorescence in the presence of the metal film, one collects less photons from the same single molecule. This means that the axial localization error of a molecule close to the metal surface is higher. The axial error is also high if the variation of the lifetime curve with height is low. This is shown in figure 5.2. We calculated the number of photons one collects from a single molecule before it bleaches based on the relative intensity that one observes for dipoles above these metal layers, which gives us the relative error of lifetime estimation at each height. Thereafter, this lifetime error was converted into axial localization error by taking the derivative of height with respect to lifetime. In this way, we get an estimate of axial localization error that one would likely measure as a function of the molecule's position on top of the metal surface. We performed the same calculations for air as a medium on top of the metal films shown in figure 5.1. Note that these calculations were performed assuming quantum yield as unity and for a metal thickness of 10 nm. The lifetime curves will show different behavior for a different quantum yield and film thickness, which would result in a different axial error.

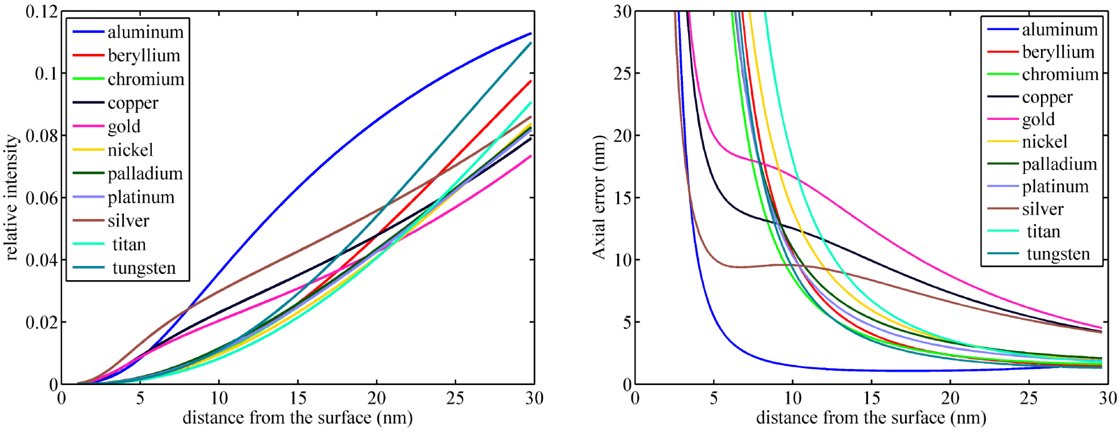

Figure 5.2: Left figure shows the plots of relative intensity of a single molecule that one observes through a 10 nm of metal layer on top of glass with a 1.49 N.A. objective, as a function of distance. The values are normalized to a dipole in water ($n = 1.33$) without any metal film. The right figure shows the plot of axial localization errors as a function of distance above the metal films.

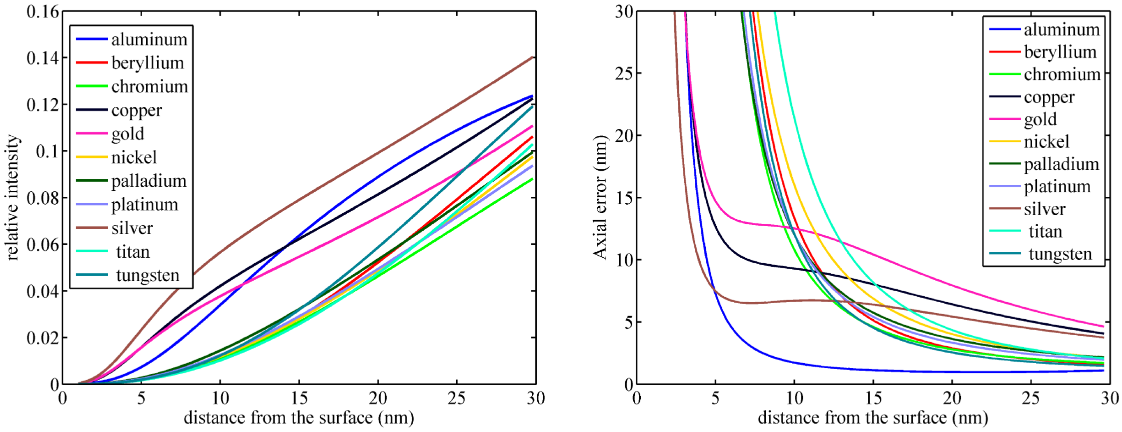

Figure 5.3: The same as figure 5.2, but for air on top of the metal films.

From these simple calculations, we see that gold shows the highest axial error within the range of 10 to 30 nm. The error calculated is extremely high below 5 nm for both, water and air environments. For this reason, while measuring axial positions of dye molecules or labeled biological structures, one usually evaporates a thin layer (at least 10 nm) of transparent SiO_2 as a spacer on top of a gold/copper thin film. However, the advantage of a gold/copper thin film in a MIET experiment is that the lifetime values increase monotonically up to a height of 150 nm as in contrast to most other metals considered here. Morevover, the variation of lifetimes with height is maximal in the range between 40 and 70 nm, which translates to an axial localization precision of less than 5 nm in water and 2 nm in air (see figures above). This makes them useful for live cell nanoscopy [161] where one would like to investigate the structure of biological entities of a cell on top of a surface. For such experiments, an error of 5 nm is tolerable. Aluminum, on the other hand can be used to measure smaller distances, upto 1 nm, between a range of 10 to 30 nm. As can be seen in the figures, the relative intensity in water that one measures through this metal is much higher in comparison to the case of a gold film. The steep variation of the lifetime values with distance from aluminum surface can be useful for achieving a higher resolution in height variation, making it a potential candidate for single-molecule measurements in these conditions. The precaution one must take while working with silver thin films is that they easily form a thin layer of the silver oxide while reacting with oxygen present in the ambient air or dissolved in water over time. This affects the transparency and the overall fluorescence lifetime behavior over the surface. Therefore, one usually evaporates a thin layer (10-20 nm) of transparent SiO_2 additionally on top of an evaporated silver thin film in order to prevent such a layer. This oxidation process is however not a problem in the case of aluminum, in which case the layer of alumina formed is transparent in the visible wavelengths. In any case, the axial error as we calculated for the figures above can be used as a way to characterize the performance of thin metal films for the experimental parameters. The axial error of gold, for example, for a thickness of 20 nm is much lower as compared to the curve shown in figure 5.2 for the same wavelength and quantum yield of the dye.

5.2 smMIET for Structural Biology

With the help of simple experiments, we achieved a nanometer axial localization precision from a thin gold film at single molecule level. Therefore, if the dye molecules are rotating freely in space and are separated spatially or show stochastic blinking, similar to what is typically required for a localization based super-resolution technique such as STORM, PALM or PAINT, then by using the fluorescence lifetime information, one can now localize each emitter with a nanometer axial precision, within the near-field range from a thin metal film (~ 100 nm). This would allow one to study for example, the processes involved in a focal adhesions such as a cell's adhesion to its extra cellular matrix, force transmission, cytoskeletal regulation and signaling [162–164], close to a surface, at single molecule level.

If, on the other hand, the molecules are restricted in their rotation and are somehow fixed with a random orientation, then as we saw in section 4.3.3 one introduces significant lateral localization inaccuracy, as high as ~ 15 nm (see figure 4.33), even when the molecules are present in the focal plane of a high N.A. objective. Although one can achieve a nanometer precision in localization, the point localization based super-resolution methods suffer from these huge inaccuracies which act as major limitations [34, 35]. In this case, it is desirable to utilize the method of defocused imaging where the advantage when combined with smMIET is two-fold. First, it allows one to determine the orientation of the dye molecule with respect to the metal surface, which is necessary for estimating its accurate height from the surface 2.4.3. Second, as was emphasized and shown in discussion of the same chapter, fitting the defocused intensity patterns with a log-likelihood algorithm gives a high lateral localization precision. Since one takes into account the asymmetry in the angular distribution of radiation from an oriented dipole, the lateral position estimated in such a way must be close to its true location, within error limits. One has to explore the applicability of defocused imaging in combination with smMIET.

Even though the thin metal film absorbs and reflects a part of the emission from a fluorophore, preliminary experiments show the possibility of acquiring defocused patterns with such a metal thin film substrate. Figure 5.4 shows a few captured defocused patterns of Atto 655 molecules on top of an SiO_2 spacer of 30 nm. Thus, all that is required is to combine a FLIM microscope together with defocused imaging. Extending a laser-scanning confocal FLIM system by adding a detection channel with a defocused EMCCD camera is one of the many options. The idea is much similar to the experimen-

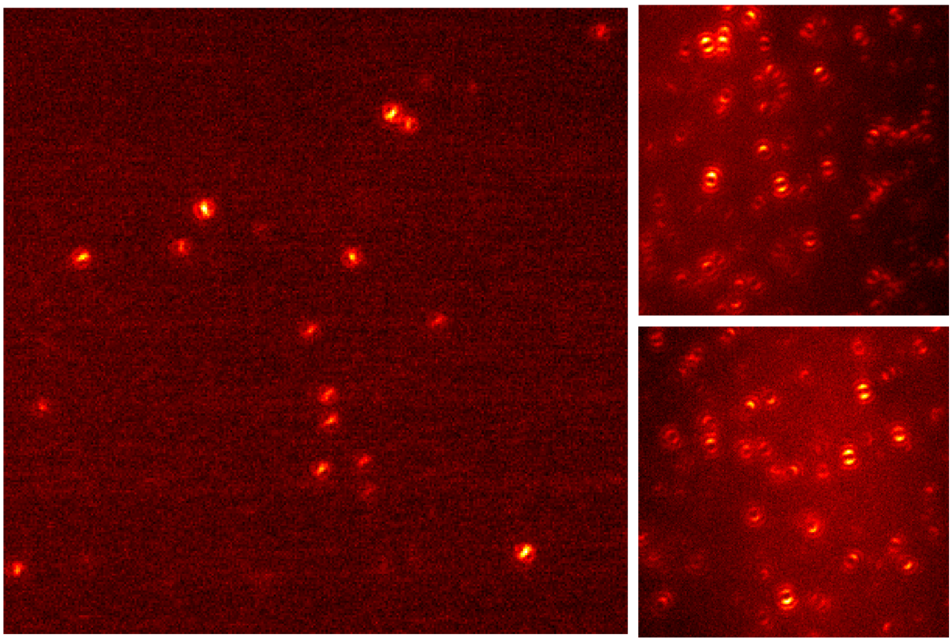

Figure 5.4: Defocused images of Atto 655 molecules, spin-coated on top of a 10 nm gold film with a 30 nm SiO_2 spacer in between, at various defocusing values. The left figure was taken with a defocusing of 0.5 µm whereas the two figures on the right were taken with a defocusing value of 1.2 µm. The setup details can be found in section 3.1.2.

tal method shown in the work for the determination of excitation and emission dipole orientations (section 4.4), using a linearly polarized laser for scanning. A pre-scan is performed first to locate the position of the molecules on top of the substrate using a custom written search-and-seek LabVIEW program, and thereafter, a series of defocused images is acquired for each emitter by parking the scanner at its position. Further, in order to obtain a reliable estimate of the fluorescence lifetimes, a part of the photons are focused onto a Single-Photon Avalanche Diode (τ-SPAD, PicoQuant) during the point measurements. A good compromise between the number of photons required for a good signal-to-noise ratio in the defocused image for orientation and lateral position estimation, and the number of photons for fluorescence lifetime estimation, can be obtained by dividing the total emission in a ratio of 7:3 using a 70 R : 30 T beamsplitter (Thorlabs). The whole setup description can be summarized into a figure, as shown below (figure 5.5).

Now consider an experiment where one would like to determine the distance between two labeled sites on a biomolecular complex or protein. This is a classical problem where one uses FRET to determine such intramolecular distances. However, as we pointed out in chapter 3, one needs *a priori* information regarding the mutual orientation of the acceptor and donor molecule with respect to each other in order to quantify the distance between them, which acts as a major limitation of the method. A possible solution to this problem using smMIET would be to determine the heights of the two

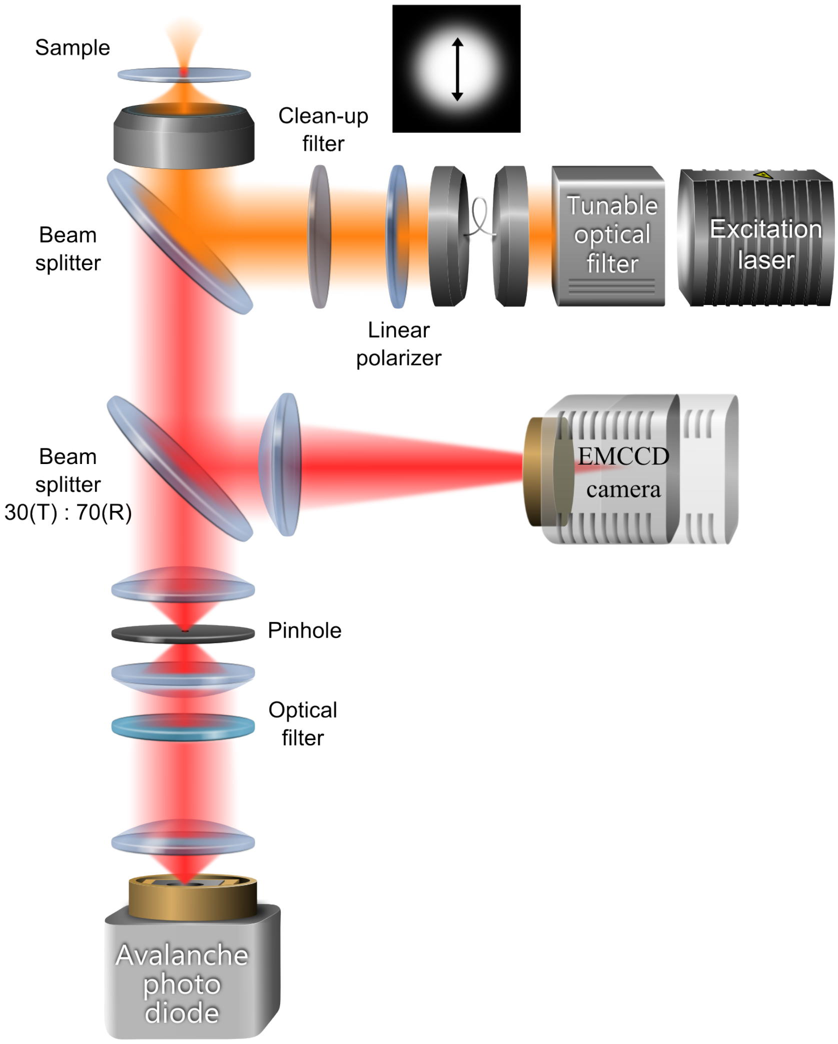

Figure 5.5: Optical setup design for performing smMIET measurements together with defocused imaging. The collected photons are split into two pathways using a beamsplitter (BS). A part of the fluorescence photons are led to a camera that is displaced from the focal plane in image space. The remaining photons are focused onto a SPAD after having passed through a pinhole (PH).

probes in two separate wavelength channels, thereby obtaining a distribution of height differences between both, allowing one to estimate the exact distance between both the sites using rudimentary statistics. This approach was already introduced in figure 3.10. Although this approach suits the nature of the problem, the situation gets complicated if one has multiple labeled sites on a globular protein or biomolecular complex. Of course, one could proceed in a customary way by labeling two sites at a time, resolving the distances between each pair, and subsequently obtaining all distances to determine the complete geometry. Here we propose an alternative solution.

Let us consider a simpler situation where, again, we would like to determine the distance between two labeled sites, as shown in figure 5.6. Further, instead of labeling two chromatically separated dyes, let us assume that the two dyes are identical. This reduces the required knowledge of precise free space parameters such as free space lifetime τ_0 and quantum yield Φ for the two dye species, which are vital for determining the axial distances. Several scenarios and possibilities now exist. If the dye molecules are STORM-able (blinking stochastically) then one can acquire a video of blinking defocused images, together with TTTR scheme based photon recording, using the setup described above. This opens the possibility to measure average photon arrival time together with capturing defocused images of each individual emitter during its *on* time. One can later sort the frames based on the average lifetime measured and add them individually in order to separate the defocused intensity patterns, as summarized in figure 5.6. Fitting the defocused images yields the x, y-position and vertical orientation that is useful for determining the z-distance together with fluorescence lifetime. In this way, all three coordinates of the two dye molecules can be determined. By repeating such measurements on a number of such labeled biomolecules of complexes yields improved statistics for determining the correct distance between the two sites. It is worthy to

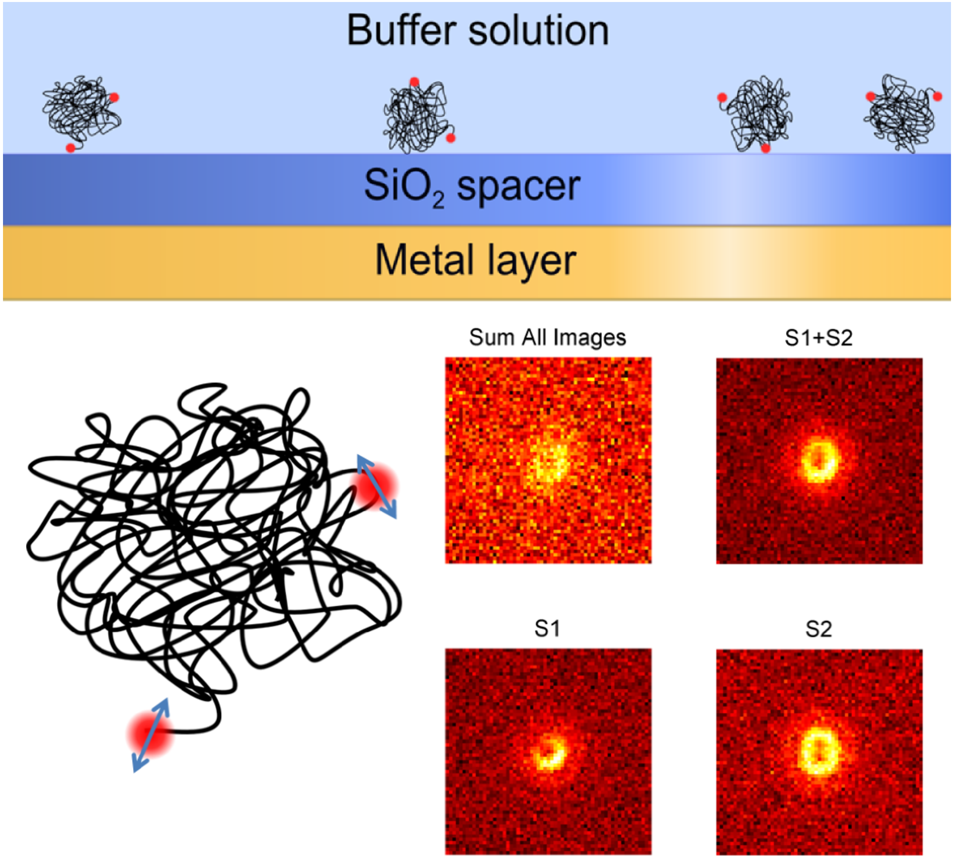

Figure 5.6: The schematic on top shows the geometry of the experiment. The globular protein with two labels is deposited on the spacer. If a buffer is required to stabilize the structure, then one binds these proteins to the surface. The orientation of the structure can be random. A transparent SiO_2 spacer is required to avoid total quenching of emission from the dye molecules. In the right bottom the four subfigures are: Top left, Summation of all the simulated defocused intensity images; top right, the summation of frames where at least one dye molecule is on; bottom two, summation of frames that are sorted out based on the observed fluorescence lifetime for each dye molecule.

note here that if the dye molecules are fixed, one observes defocused intensity patterns, whereas if the molecules are free to rotate around their positions with a negligible height fluctuation, we still obtain a defocused image of an isotropic emitter that can be localized. The heights of such freely rotating dyes can be directly calculated from their fluorescence lifetimes with the MIET calibration curve for an isotropic emitter, as all vertical orientations are averaged out.

Since blinking plays an important role, one can easily combine this technique with the recently developed DNA-PAINT (point accumulation for imaging in nanoscale topography) technique used for super-resolution imaging [32]. In this method one binds each target site of a biomolecule with a docking single strand DNA (docking strand). Later, a solution containing its complementary strand together with a fluorescent label (imaging strand) is added with a predetermined concentration, using the binding and dissociation kinetics, in such a way that one observes stochastic binding events at each target site, separated in time. This introduces blinking at the target sites which is similar, yet more controlled, to the conventional STORM imaging. The added advantage of such a method is that one can collect fluorescence from each target site indefinitely and there is no limitation due to photobleaching. In this way a sub-10-nm lateral resolution can be achieved. Together with the powerful smMIET technique, one can achieve resolutions down to a few nanometers in all three dimensions.

One last case may be considered in the experimental design proposed above. If the dyes are not STORM-able, i.e. they do not blink, such as Atto 655 [165], then due to the exponential photobleaching probability one of the two dye molecules is likely to bleach before the other. One can use the time trace from the SPAD signal to identify such a single step bleaching event which later can be used to calculate the average photon arrival times of the two labels individually. Consequently, one uses the defocused pattern of the last remaining dye molecule to identify its position and later use the information to substract from the image containing the sum of both molecules' intensity patterns. Such subtractive techniques are commonly used as single-molecule localization based super-resolution methods such as Single molecule High-Resolution Imaging with Photobleaching (SHRImP) [166–168]. All the discussion above can be extended beyond just two labeled sites as well, within, however, the experimental limits.

5.3 Dynamics using MIET - dynaMIET

So far we discussed the possibility and options to apply smMIET in combination with a few existing imaging techniques for structural biology. Similar to FRET, one can also apply smMIET for the study of dynamics. The distance dependent energy transfer quenches the fluorescence of a molecule and therefore modifies the total energy radiated much like FRET. Figure 5.7 below shows the variation of intensity as a function of distance. The intensity is roughly proportional to the lifetime curve and increases monotonically with the distance from the surface. Therefore, any variation of the height of a fluorescence molecule reflects in its intensity time trace.

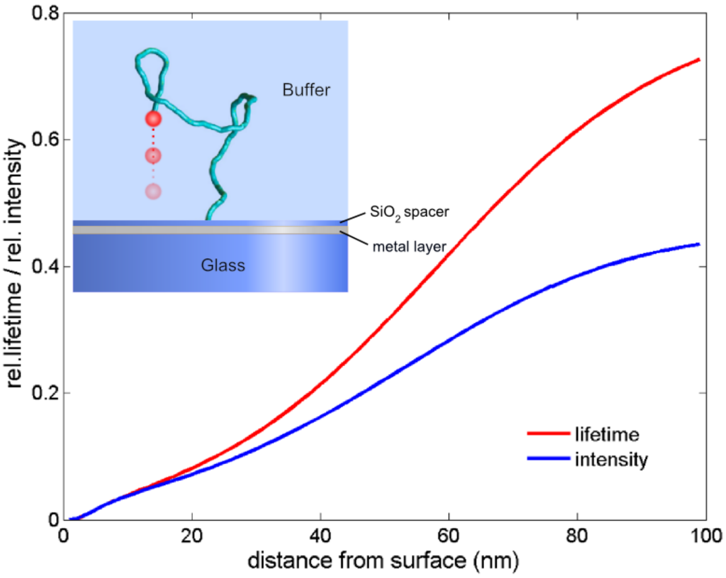

Figure 5.7: The variation of fluorescence lifetime and intensity of an isotropic emitter with the distance above a thin gold film for a dye with unit quantum yield emitting at wavelength $\lambda_{\mathrm{em}} = 690\,\mathrm{nm}$. The values are normailzed to a free dipole in water. The inset on the top left shows a schematic of an Intrinsically Disordered Protein (IDP) bound to surface on one end and a dye molecule attached to the lose end.

Recently, there has been a dramatic interest in the study of the conformational dynamics of Intrinsically Disordered Proteins (IDP) such as the well-known FG repeats which are found in the nuclear pore complex [14]. Various studies on conformational dynamics of large proteins have been performed using spFRET [169–172] and Photo-induced Electron Transfer (PET) [173–175]. If one binds such an IDP on top of passivated SiO$_2$ spacer with a thin metal film beneath, with a dye attached to its free end as shown in figure 5.7 then intensity fluctuations due to the movement of the dye with respect to the surface in time, can be correlated to probe the conformational dynamics of the protein. If $G(z_f, z_i, t)$ is the Green's function for the probability to find the free end at a height z_f at a time t if it was at a height z_i at time $t = 0$, then the correlation function for the intensity fluctuations can be written as:

$$g(t) = g_\infty + \int \mathrm{d}z_i \int \mathrm{d}z_f U(z_i) G(z_f, z_i, t) U(z_f) \tag{5.3}$$

where g_∞ is the correlation at long lag times, which resembles the square of average intensity, $U(z_i)$ and $U(z_f)$ are the Molecular Detection Functions (MDF) at the heights z_i, z_f, respectively, which show the probability to detect a photon from the dye molecule. In principle, the MDF is proportional to the product of the probability to excite a molecule at a given position in the focus and the probability to collect the emitted photons from the same position. If we assume that the conformational dynamics of a protein is in the order of a few nanometers to tens of nanometers, then MDF is directly proportional to the intensity at the respective heights, since the collection efficiency remains a constant on these length scales. Therefore, one can probe and analyze the parameters and properties of the protein chain based on a model for the Green's function. We call this approach for studying conformational dynamics using smMIET as *dynaMIET*. Of course this method can be used for probing polymer chain dynamics under various flow conditions, diffusion and convection in confined environments, etc.

The choice of metal and wavelength of the dye plays an important role while performing such experiments. The quantum yield of a dye, refractive index of the buffer, all play a role in determining the intensity and lifetime variation with the distance from the metal surface as was described earlier in section 5.1. In particular, the influence of refractive index of a metal surface on the lifetime-distance dependence across the entire visible range is not so pronounced, and this dependency is much steeper for shorter wavelengths (since then, the amount of quenching is based on the optical path length). This is shown in figure 5.8. The distance dependent intensity curves are shown here for three different emission wavelengths on top of a 10 nm gold film. As one can see, the distance dependency of intensity at an emission wavelength of 525 nm is much steeper than in red wavelengths. This directly translated to the fact that the fluctuations of intensity that one would observe for a rapidly oscillating dye molecule is high for blue wavelengths. The right graph in the figure above shows the intensity variation $\delta I(z)$ for a height of 10 nm at various heights from the metal surface at the three wavelengths. The correlation amplitude that one would observe is directly proportional to $(\delta I(z))^2$,

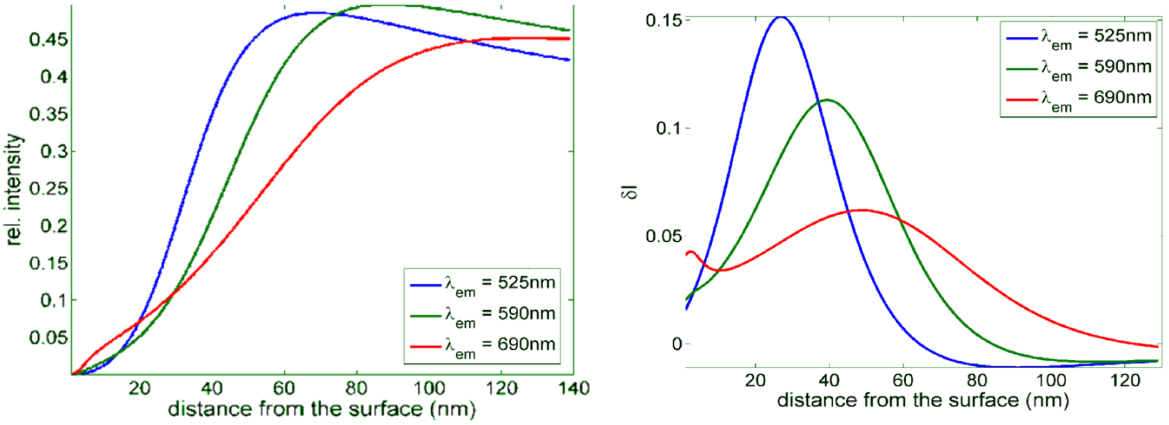

Figure 5.8: Left panel shows the calculated relative intensity values at various distances from a gold thin film for three wavelengths as shown in the legend with water as a medium on top. The right panel show the derivative of the intensity curves for a height variation of 10 nm.

which means that for small height oscillations of the free end of a protein chain, on the order of few nanometers, it is desirable to perform the experiments with a fluorophore emitting at $\sim \lambda_{\mathrm{em}} = 525\,\mathrm{nm}$ in order to observe higher correlation amplitudes for resolving its temporal dynamics. However, gold is known to have a high photoluminescence when a wavelength of $\lambda = 488\,\mathrm{nm}$ is incident on it. Therefore, silver acts as a convenient choice in blue wavelengths, which shows similar quenching effects.

Apart from all the above mentioned applications, one can combine the intensity fluctuations due to diffusion or convection with fluorescence lifetime information using advanced analysis methods such as Fluorescence Lifetime Correlation Spectroscopy (FLCS) [176, 177] or 2D-FLCS [178, 179]. This will allow one to resolve such transport phenomenon in a height dependent manner within the range of MIET that will have huge potential in flow profiling in micro/nano-fluidics and diffusion measurements in lipid bilayers in a leaflet-dependent manner. Such experiments would involve the measurement of fluorescence lifetimes from the molecules traveling through the excitation volume at different heights simultaneously. This poses a requirement of a huge number of photons in order to be able to resolve numerous exponential decays. The number of photons required to obtain the the heights of two molecules emitting simultaneously will depend on the difference of their excited state lifetimes. This is in contrast to the single-molecule Metal-Induced Energy Transfer (smMIET) experiments where we achieved a localization accuracy of around 2.5 nm for Atto 655 molecules at various heights with approximately 10^3 photons, that were recorded separately in different experiments (Chapter 3). This means that in order to resolve distances in the order of about 5 nm on top of a thin gold film using a standard fluorescent molecule that emits in the red wavelengths ($\lambda_{\mathrm{em}} = 690\,\mathrm{nm}$) and decays with a half-time of ~3 ns in free space, one needs to distinguish two lifetime values with a difference in the order of 0.2-0.3 ns, which is experimentally challenging. The small differences between the two lifetimes is due the gradual variation in the energy transfer rate over the first 150 nm from the metal surface in the red emission wavelengths.

There are two possible ways to overcome such a limitation: 1) By using blue wavelength emission fluorophores, 2) by selecting a different metal/metal-oxide thin film that has a lower absorption coefficient in the emission wavelength. Both these options can be explained by referring back to the MIET-theory section 2.4.3, in particular, by looking at equation (2.155). The choice of a shorter emission wavelength is based on the fact that the exponential factor $-2iw_1|z_0|$ decays faster ($w_1 \propto 1/\lambda_1$), whereas the refractive index plays a role in determining the dependence of the effective reflection coefficient $R_{p,s}$ as a function of the angle of the emitted plane wave (taken into account by the variable $u = q/k_1$).

Recently, a group published the application of an Indium Tin Oxide (ITO) for MIET

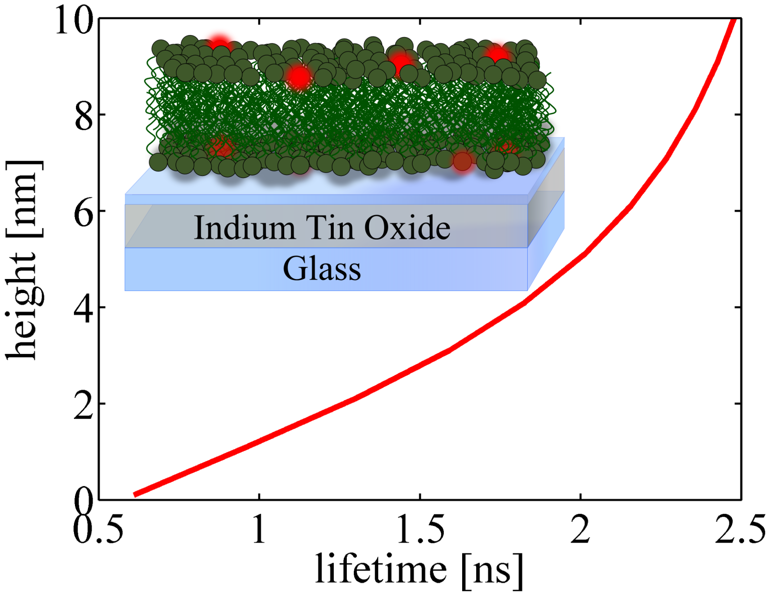

Figure 5.9: The MIET calibration curve for a dye with free space lifetime $\tau_0 = 3.0\,\text{ns}$ and quantum yield $\Phi = 0.45$ on top of ITO layer (thickness 300 nm) with a SiO_2 spacer of 4 nm is shown here. A randomly labeled supported lipid bilayer is shown on top of the spacer. The bilayer is 4-5 nm thick, which corresponds to a difference of at least 1 ns between the lifetime values of the dye in the top and the bottom leaflet.

applications [180] which allows for a steeper distance-fluorescence lifetime variation than the metal films we considered in section 5.1. Such a metal oxide film can be used to distinguish the dyes labeling a the top and bottom leaflets of a lipid bilayer which is approximately 4 nm to 5 nm in thickness. ITO has been applied before to study the binding of small unilamellar vesicles (SUVs) to supported bilayers by using MIET in combination with FLCS by Benda *et al.* [176]. However the main aim of their work was to distinguish between the two-dimensional diffusion of bilayers on the ITO support from the three dimensional vesicle diffusion in solution. Performing long diffusion experiments with focused illumination on labeled lipid molecules or proteins in supported lipid bilayers on ITO substrate would make it possible to distinguish the diffusion in the top and bottom leaflets and resolve the flip-flop dynamics of these molecules across both the leaflets [177] (see for example figure 5.9). Such experiments will open new perspectives in supported lipid bilayer research, especially in estimating the effect of substrate on the lipid diffusion and parameters such as interleaflet coupling in asymmetric bilayers.

In short, there exist a multitude of exciting options and applications of smMIET in future. One needs to explore further possibilities to combine this powerful method with the existing techniques in order to fully utilize its potential.

6 Conclusions

In this thesis, we introduced the concept of metal-induced energy transfer (MIET) giving a complete overview of the theory behind starting from fundamentals. In principle, the theory developed here is not just limited to electric dipole emitters but can be extended to model the emission properties of other exotic emitters such as magnetic dipoles, electric quadrapoles, and semiconductor nanocrystals (quantum dots) which have a two dimensional degenerate emission transition dipole. Further, the study of emission properties of these emitters in peculiar environments such as nanocavities of various geometries can be modeled by extending this theory on similar lines (see for example references [53, 115]).

With the help of simple experiments, as presented in chapter 3, we demonstrated the capability to determine the distances of dye molecules from a metal surface with nanometer accuracy at single molecule level (smMIET). Combining this method with localization based super-resolution techniques such as STORM, PALM or PAINT might achieve an isotropic *three-dimensional* nanometer localization precision within the near-field range of around $\sim 100\,\mathrm{nm}$. Further, using a suitable transparent metal-oxide conductor thin film as a substrate, together with defocused imaging for orientation measurements, opens the possibility to resolve intramolecular distances in biomacromolecules, similar to the conventionally used FRET technique, with angstrom resolution. Unlike in a FRET measurement, where an *a priori* information of the orientation of the acceptor and donor dye molecules with respect to each other is necessary to quantify the exact distances, one would need the orientations of the dyes with respect to the metal surface only. This would allow measuring such intramolecular distances reliably and conveniently.

Towards the end of this thesis, we introduced a second method with which we simultaneously determine the *three-dimensional* orientation and structure of excitation *and* emission transition dipoles of single emitters. The presented measurements with two commercial dye systems show that there is a significant re-organization of molecular structure in their excited states due to which there exists a considerable angle γ between their excitation and emission transition dipole moments. Using this method, where one uses a radially polarized excitation laser for scanning and subsequently acquires defocused images for each individual emitter, the geometry of the transition dipoles of exotic emitters as mentioned above can be studied as well.

7 Other Contributions

Apart from the work presented in this thesis, I have contributed in several other pieces of work during my doctoral studies. The work has been published as the following peer-reviewed journal contributions:

1. Isbaner, S.[†]; **Karedla, N.**[†]; Ruhlandt, D.; Stein, C.S.; Chizhik, A.I.; Gregor, I.; Enderlein, J. *"Dead-time Correction of Fluorescence Lifetime Measurements"* Optics Express **(accepted)**
2. **Karedla, N.**; Gregor, I.; Enderlein, J. *"Analytical approximations of the diffusive dispersion in fluid flows"* European Physics Letters **108** 40007 (2014)
3. **Karedla, N.**; Enderlein, J.; Gregor, I.; Chizhik, A.I. *"Absolute Photoluminescence Quantum Yield Measurement in a Complex Nanoscopic System with Multiple Overlapping States"* The Journal of Physical Chemistry Letters **5** 1198 (2014)
4. **Karedla, N.**; Ruhlandt, D.; Chizhik, A.M.; Enderlein, J.; Chizhik, A.M. *"Metal-Induced Energy Transfer"* in: Advanced time-correlated single photon counting techniques Eds: Kapusta, P.; Wahl, M.; Erdmann, R. Springer International Publishing pp. 265-281 (2015)

[†] *equally contributing authors*

7.1 Dead-Time Correction of Fluorescence Lifetime Measurements

In this work, we present the correction of the dead-time related effects in modern Time-Correlated Single Photon Counting (TCSPC) systems which use independent clock-based Time-to-Digital Converter (TDC) for timing the laser sync and detector pulses in routine fluorescence lifetime measurements. Due to the dead-time of the TDC electronics and the detectors themselves, one loses photons and even worse, introduces severe artifacts which show up as distorted TCSPC curves when measuring at high photon hit rates (number of photons per time hitting the detector). Due to this reason, one usually measures at low photon hit rates, limiting the data acquisition speed in a TCSPC experiment. This is a major drawback for rapid Fluorescence Lifetime Imaging Microscopy (FLIM) applications.

We developed a correction algorithm which takes into account the detector and electronics dead-times and the photon hit rate in order to correct for these artifacts. We tested this algorithm on measurements taken at various photon hit rates as high as an average of 2.5 photons in a laser pulse period (50 ns) on Atto 655 dye solution, where we are able to correctly determine the true fluorescence lifetime value of ~ 1.9 ns within an error of 0.02 ns. Further, we applied this algorithm to correct the lifetime measurements on a cell with labeled actin filaments and reconstructed the lifetime *and* corrected intensity values for each pixel. The brightest pixels in these FLIM measurements corresponded to photon hit rates as high as 0.5 which is more than an order of magnitude higher than a dead-time distortion-free acquisition rate. We also present an elegant way to determine the dead-time values and the absolute photon hit rates that are necessary for the correction algorithm, using Inter-photon Time Distribution (IPTD) and autocorrelation analysis.

It is important to emphasize here that the algorithm does not depend, in any way, on the nature of the TCSPC curve, and can be applied to multi-exponential decay curves as well. More than that, it is applicable to any single-event counting or timing measurements with electronics and/or detector dead-times and is not restricted to just TCSPC measurements. In principle, one can extend the correction algorithm to a reverse start-stop TCSPC system as well on similar lines. This work will enable rapid FLIM measurements with no restriction on photon hit rates and also improve single photon counting based lidar and time-resolved fluorescence anisotropy applications.

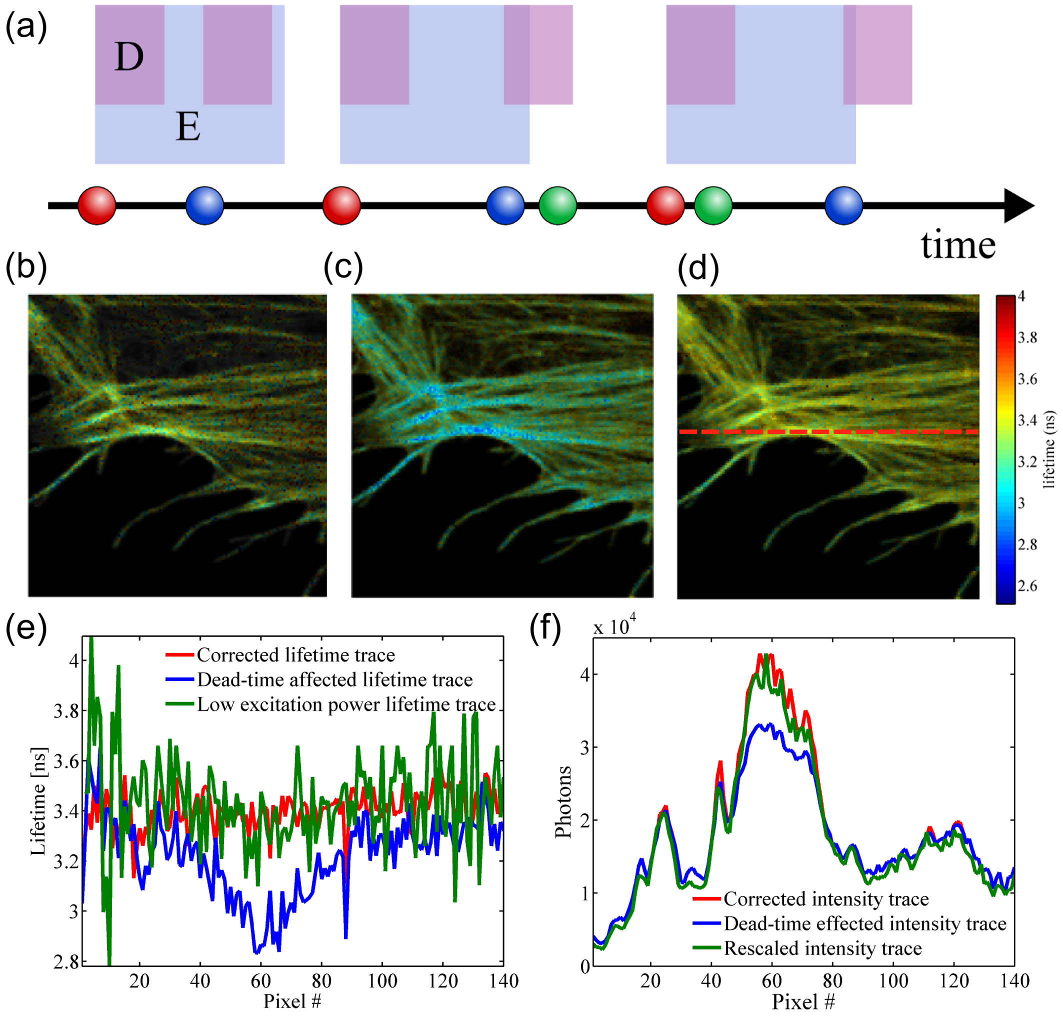

Figure 7.1: (a) A scheme showing all possible effects of electronics (E) and detector (D) dead-times on the photon detection/recording events. The red balls represent the photons that are detected, *i.e.* both the detector and the electronics are in their active states; the blue balls represent the photons that are successfully detected but not recorded, whereas the green balls represent the worst case scenario when the photon is not even detected since it falls within the dead-time of the detector itself. (b) Intensity-weighted fluorescence lifetime image of a Human mesenchymal stem cells with actin filaments labeled with Atto 647N measured at low excitation intensity. (c) Intensity-weighted lifetime image of the same cell area measured at high excitation intensity. The severe impact of the dead-times on the resulting lifetime values of pixels is clearly visible here. In the regions corresponding to high intensity, the lifetimes values are underestimated as compared to the same regions in (a). (d) Intensity-weighted lifetime image after the dead-time correction. (e) Lifetimes of pixels in the line corresponding to the brightest pixel in the image (marked by a red dotted line in (d)) taken from (b), (c), and (d). Two important observations must be pointed out here. First the lifetime values from the low excitation intensity scan are noisier than the corrected lifetime line plot. Second, the dead-time correction faithfully gives back true lifetime values as shown by the red curve. (f) The estimated intensity trace from the dead-time correction perfectly overlaps with the intensity measured at low excitation intensity (rescaled according to the brightest pixel in the corrected intensity image). The blue curve shows the dead-time affected intensity trace which shows the loss of photons.

7.2 Analytical Approximations of the Diffusive Dispersion in Fluid Flows

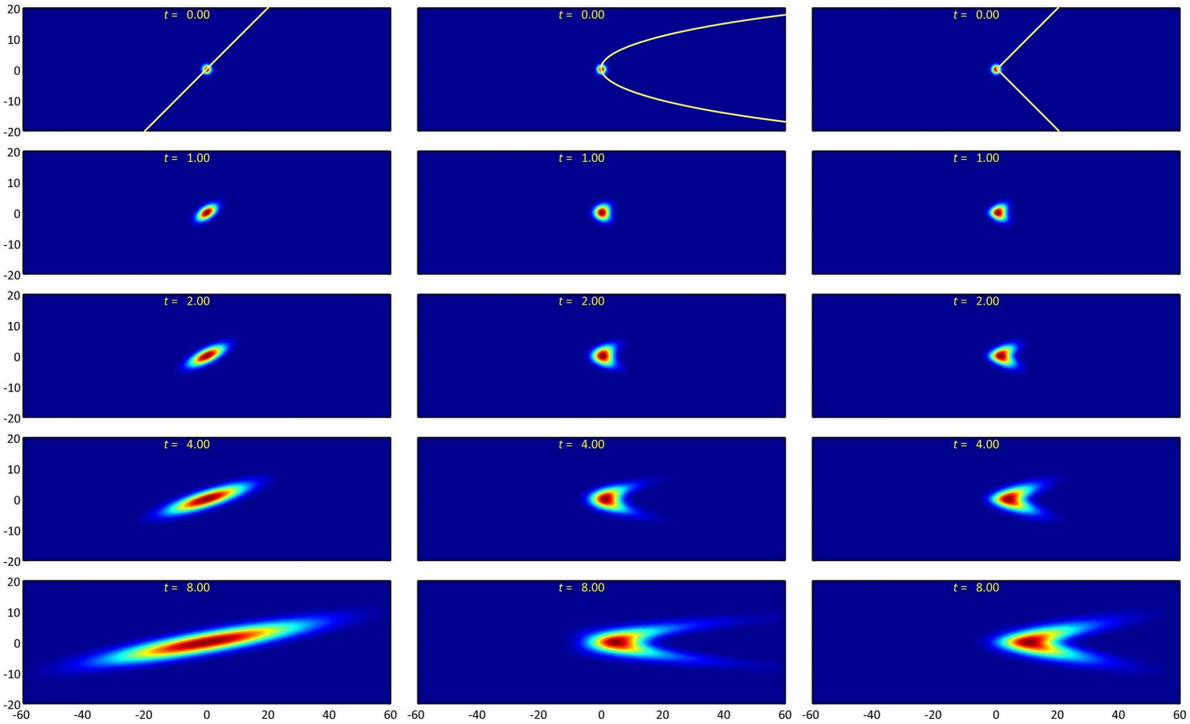

Figure 7.2: Temporal evolution of Gaussian concentration profile in three different flow profiles: linear shear flow $v(z) = z$ (left column), parabolic flow profile $v(z) = 0.2z^2$ (middle column), and linear kink profile $v(z) = |z|$ (right column). Value of diffusion coefficient was set to one.

In this work we, present a path-integral approach for finding solutions of the convection-diffusion equation with inhomogeneous fluid flow, which is notoriously difficult to solve. The equation for diffusion with an advective shear flow profile over an interface can be written in the form

$$\frac{\partial c(\mathbf{r},t)}{\partial t} = D\Delta c(\mathbf{r},t) - v(z)\partial_x c(\mathbf{r},t)$$

where $c(\mathbf{r},t)$ is the local concentration of the transported and diffusing quantity at position $\mathbf{r}$ and time t, D is the diffusion coefficient, and $v(z)$ is the z-dependent flow profile of a flow along the x-direction. We derived a general approximate analytical solution of the convection-diffusion equation which is applicable to arbitrary flow profiles along the z-direction. The approximate solution we found in this work is very similar to the famous Taylor-Aris approximation for the convection-diffusion induced broadening of plug flow in capillaries, where the concentration profile along the flow direction is approximated by a Gaussian distribution whose peak position and width are functions of time [181–183].

As examples, we applied this approximation to the diffusion in a linear shear flow and in a parabolic flow in infinite space and to the diffusion in a linear shear flow over an impenetrable interface. These cases are particularly important when dealing with the diffusion of molecules or particles close to the surface of microfluidic and nanofluidic devices [184, 185], or wetting and spreading phenomena [186]. We compared the analytical approximation with numerical solutions which are obtained from a conventional finite-element time-difference method. The obtained solutions work well as long as the diffusive transport perpendicular to the flow direction dominates over the convective transport over long time-scales, similar to Taylor-Aris dispersion.

The found new path integral representation of the solution in this work can be used for finding exact solutions of convection-diffusion problems occurring in many physical and chemical problems that describe the transport of heat, matter, or other physical quantities, or for devising efficient numerical integration schemes.

7.3 Absolute Photoluminescence Quantum Yield Measurement in a Complex Nanoscopic System with Multiple Overlapping States

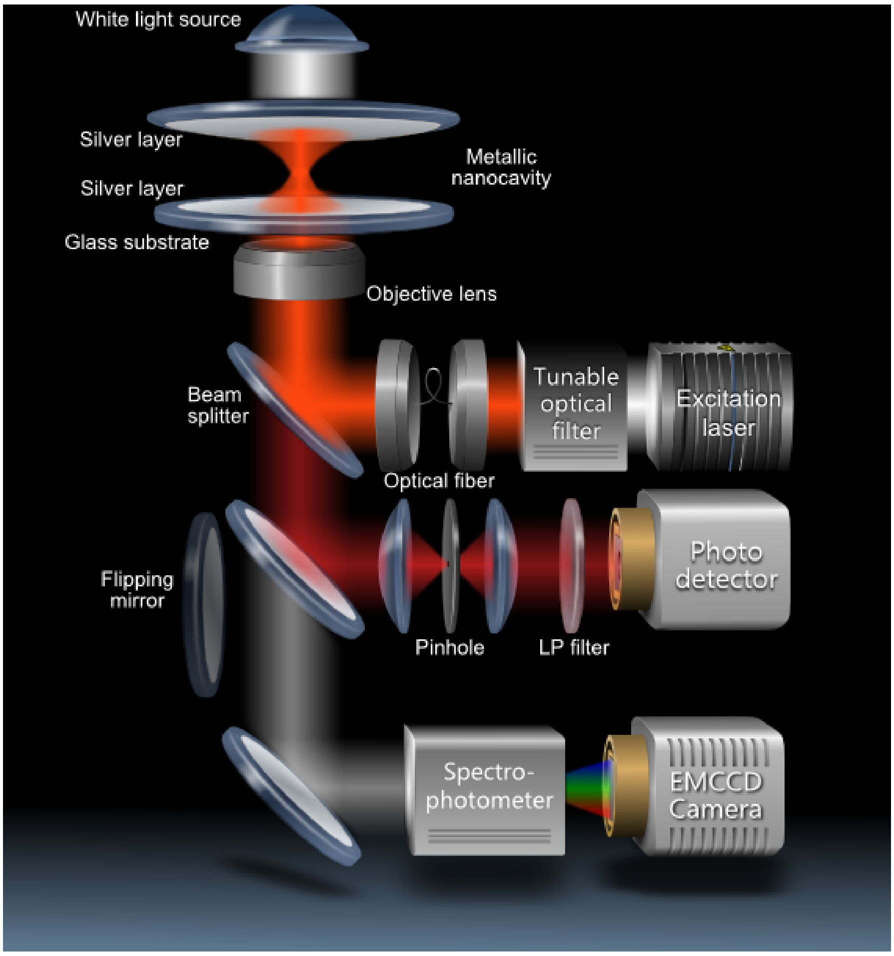

Figure 7.3: Experimental setup for quantum yield measurements. A pulsed white light laser with a tunable acousto-optical filter served as the excitation source. The excitation beam was reflected on a beamsplitter and focused into the sample sandwiched in a metallic nanocavity. The nanocavity consists of two silver layers evaporated on top of glass surfaces. The bottom glass substrate is a flat coverslip of thickness 0.17µm (standard coverslip) whereas the top silver layer is deposited on a plano-convex ens. Within the dimensions of the focal spot, the curvature of the lens can be neglected, and the cavity can be considered as a plane-parallel resonator. Therefore, focusing at various positions along the horizontal plane is equivalent to tuning the cavity length. The collected photons were focused through a pinhole and thereafter focused onto the active area of a photodetector. Any back scattered laser passing through the pinhole was blocked with the help of a long pass (LP) filter. For each cavity length, apart from measuring the excited state decay times, we measured the white light transmission spectrum of the cavity using a white light source. The transmitted light is directed into a spectrophotometer with the help of a flipping mirror.

The quantum yield of a luminescent emitter is defined as the ratio of the radiative decay rate to the sum of the radiative and non-radiative decay rates (see equation (2.11)). Of all the photophysical properties such as absorption cross section, excited state lifetime, excitation and emission spectra etc., the quantum yield is difficult to access. We developed a new approach for determining absolute values of quantum yield based on the modification of the radiative transition rate of an emitter within a metallic nanocavity [53, 187]. The core idea behind this method is to measure the excited state decay lifetime of the emitter inside an optical resonator with subwavelength spacing as a function of the cavity length. As was described in chapter 2, the presence of a metal surface modifies the Local Density of States (LDOS) and the emission properties, which can be modeled exactly based on the experimental parameters such as cavity length, metal refractive indices and thicknesses, and the emission wavelength of the emitter with its quantum yield as a fit parameter (see [53] for a complete description of the theory behind). In this way, one can measure the quantum yield of a single molecule without the need of any calibration.

In this work, we show that measurements can be performed in attoliter volumes, both in liquid and solid phases, for a mixture of photoluminescent emitters if their decay rates at each cavity length are separable. The idea is based on the fact that the modification of the excited state lifetime of each emitter with any quantum yield can be modeled individually taking into account its free space emission spectrum for each cavity length. In order to demonstrate this, we measured an aqueous mixture of Rhodamine 6G and Atto 495, whose emission spectra overlap significantly, in one nanocavity; and a thin polymer film doped with Alexa 647 and CdSe/ZnS quantum dots, both exhibiting an emission maximum around 660 nm, in a second nanocavity. By measuring the excited state decay times for the two mixtures at different cavity lengths and fitting these decay curves separating a short and a long decay component which correspond to individual species, we determined their individual quantum yields by fitting against the theoretical model. Further, we compared the obtained values to the quantum yields determined individually for each emitter measured using a separate nanocavity under identical conditions. The results show a good agreement between the values obtained by measuring individually and in the mixtures.

In conclusion we demonstrated that the nanocavity based approach to measure quantum yields can be used for a large variety of systems showing intrinsically multi-exponential photoluminescence decay for separating individual de-excitation processes, as long as their decay lifetimes can be separated. Since the nanocavity-based method can be applied to any quantum emitter of interest, such as dye molecules, semiconductor NCs, carbon nanotubes, and so on, the possibility to measure quantum yield values of chromophores incorporated into complex photophysical systems opens up new perspectives for studying the photophysics of complex nanometric systems. The method works equally good for solution measurements, as well as measurements for solid phases for samples even at submicromolar concentrations.

List of Figures

Bibliography

[1] W. E. Moerner and L. Kador. "Optical detection and spectroscopy of single molecules in a solid". *Physical Review Letters* 62.21 (1989), p. 2535.

[2] M. Orrit and J. Bernard. "Single pentacene molecules detected by fluorescence excitation in a p-terphenyl crystal". *Physical Review Letters* 65.21 (1990), p. 2716.

[3] M. Wahl, H.-J. Rahn, I. Gregor, R. Erdmann and J. Enderlein. "Dead-time optimized time-correlated photon counting instrument with synchronized, independent timing channels". *Review of Scientific Instruments* 78.3 (2007), p. 033106.

[4] M. Wahl, T. Röhlicke, H.-J. Rahn, R. Erdmann, G. Kell, A. Ahlrichs, M. Kernbach, A. W. Schell and O. Benson. "Integrated multichannel photon timing instrument with very short dead time and high throughput". *Review of Scientific Instruments* 84.4 (2013), p. 043102.

[5] M. Wahl, H.-J. Rahn, T. Röhlicke, G. Kell, D. Nettels, F. Hillger, B. Schuler and R. Erdmann. "Scalable time correlated photon counting system with multiple independent input channels". *Review of Scientific Instruments* 79.12 (2008), p. 123113.

[6] F. Zappa, A. L. Lacaita, S. D. Cova and P. Lovati. "Solid-state single-photon detectors". *Optical Engineering* 35.4 (1996), pp. 938–945.

[7] W. Becker. *Advanced time-correlated single photon counting techniques.* Vol. 81. Springer Science & Business Media, 2005.

[8] E. L. Elson and D. Magde. "Fluorescence correlation spectroscopy. I. Conceptual basis and theory". *Biopolymers* 13.1 (1974), p. 1.

[9] J. Enderlein, I. Gregor, D. Patra, T. Dertinger and U. B. Kaupp. "Performance of fluorescence correlation spectroscopy for measuring diffusion and concentration". *ChemPhysChem* 6.11 (2005), p. 2324.

[10] M. Böhmer, M. Wahl, H.-J. Rahn, R. Erdmann and J. Enderlein. "Time-resolved fluorescence correlation spectroscopy". *Chemical Physics Letters* 353.5 (2002), pp. 439–445.

[11] P. Kapusta, M. Wahl, A. Benda, M. Hof and J. Enderlein. "Fluorescence lifetime correlation spectroscopy". *Journal of Fluorescence* 17.1 (2007), p. 43.

[12] T. Ha, T. Enderle, D. Ogletree, D. Chemla, P. Selvin and S Weiss. "Probing the interaction between two single molecules: fluorescence resonance energy transfer between a single donor and a single acceptor". *Proceedings of the National Academy of Sciences* 93.13 (1996), p. 6264.

[13] A. A. Deniz, M. Dahan, J. R. Grunwell, T. Ha, A. E. Faulhaber, D. S. Chemla, S. Weiss and P. G. Schultz. "Single-pair fluorescence resonance energy transfer on freely diffusing molecules: observation of Förster distance dependence and subpopulations". *Proceedings of the National Academy of Sciences* 96.7 (1999), p. 3670.

[14] X. Michalet, S. Weiss and M. Jäger. “Single-molecule fluorescence studies of protein folding and conformational dynamics”. *Chemical Reviews* 106.5 (2006), p. 1785.

[15] A. N. Kapanidis, N. K. Lee, T. A. Laurence, S. Doose, E. Margeat and S. Weiss. “Fluorescence-aided molecule sorting: analysis of structure and interactions by alternating-laser excitation of single molecules”. *Proceedings of the National Academy of Sciences* 101.24 (2004), p. 8936.

[16] T. A. Laurence, A. N. Kapanidis, X. Kong, D. S. Chemla and S. Weiss. “Photon arrival-time interval distribution (PAID): a novel tool for analyzing molecular interactions”. *The Journal of Physical Chemistry B* 108.9 (2004), p. 3051.

[17] K. Palo, L. Brand, C. Eggeling, S. Jäger, P. Kask and K. Gall. “Fluorescence intensity and lifetime distribution analysis: toward higher accuracy in fluorescence fluctuation spectroscopy”. *Biophysical Journal* 83.2 (2002), p. 605.

[18] S. Weiss. “Fluorescence spectroscopy of single biomolecules”. *Science* 283.5408 (1999), p. 1676.

[19] T. Plakhotnik, E. A. Donley and U. P. Wild. “Single-molecule spectroscopy”. *Annual Review of Physical Chemistry* 48.1 (1997), p. 181.

[20] W. Moerner. “A dozen years of single-molecule spectroscopy in physics, chemistry, and biophysics”. *The Journal of Physical Chemistry B* 106.5 (2002), p. 910.

[21] X. Zou and L Mandel. “Photon-antibunching and sub-Poissonian photon statistics”. *Physical Review A* 41.1 (1990), p. 475.

[22] T. Basché, W. Moerner, M Orrit and H Talon. “Photon antibunching in the fluorescence of a single dye molecule trapped in a solid”. *Physical Review Letters* 69.10 (1992), p. 1516.

[23] V. Zwiller, H. Blom, P. Jonsson, N. Panev, S. Jeppesen, T. Tsegaye, E. Goobar, M.-E. Pistol, L. Samuelson and G. Björk. “Single quantum dots emit single photons at a time: Antibunching experiments”. *Applied Physics Letters* 78.17 (2001), p. 2476.

[24] H. Kimble, M Dagenais and L Mandel. “Photon antibunching in resonance fluorescence”. *Physical Review Letters* 39.11 (1977), p. 691.

[25] D. Brinks, R. Hildner, E. M. van Dijk, F. D. Stefani, J. B. Nieder, J. Hernando and N. F. van Hulst. “Ultrafast dynamics of single molecules”. *Chemical Society Reviews* 43.8 (2014), pp. 2476–2491.

[26] J. Xu and J. R. Knutson. “Ultrafast fluorescence spectroscopy via upconversion: Applications to biophysics”. *Methods in Enzymology* 450 (2008), pp. 159–183.

[27] E. Betzig, G. H. Patterson, R. Sougrat, O. W. Lindwasser, S. Olenych, J. S. Bonifacino, M. W. Davidson, J. Lippincott-Schwartz and H. F. Hess. “Imaging intracellular fluorescent proteins at nanometer resolution”. *Science* 313.5793 (2006), p. 1642.

[28] M. J. Rust, M. Bates and X. Zhuang. “Sub-diffraction-limit imaging by stochastic optical reconstruction microscopy (STORM)”. *Nature Methods* 3.10 (2006), p. 793.

[29] M. Heilemann, S. van de Linde, M. Schüttpelz, R. Kasper, B. Seefeldt, A. Mukherjee, P. Tinnefeld and M. Sauer. “Subdiffraction-resolution fluorescence imaging with conventional fluorescent probes”. *Angewandte Chemie International Edition* 47.33 (2008), p. 6172.

[30] R. Jungmann, M. S. Avendaño, M. Dai, J. B. Woehrstein, S. S. Agasti, Z. Feiger, A. Rodal and P. Yin. “Quantitative super-resolution imaging with qPAINT”. *Nature methods* (2016).

[31] K. I. Mortensen, L. S. Churchman, J. A. Spudich and H. Flyvbjerg. “Optimized localization analysis for single-molecule tracking and super-resolution microscopy”. *Nature Methods* 7.5 (2010), p. 377.

[32] R. Jungmann, M. S. Avendaño, J. B. Woehrstein, M. Dai, W. M. Shih and P. Yin. “Multiplexed 3D cellular super-resolution imaging with DNA-PAINT and Exchange-PAINT”. *Nature Methods* 11.3 (2014), p. 313.

[33] K. Xu, G. Zhong and X. Zhuang. “Actin, spectrin, and associated proteins form a periodic cytoskeletal structure in axons”. *Science* 339.6118 (2013), p. 452.

[34] J. Enderlein, E. Toprak and P. R. Selvin. “Polarization effect on position accuracy of fluorophore localization”. *Optics Express* 14.18 (2006), p. 8111.

[35] J. Engelhardt, J. Keller, P. Hoyer, M. Reuss, T. Staudt and S. W. Hell. “Molecular orientation affects localization accuracy in superresolution far-field fluorescence microscopy”. *Nano Letters* 11.1 (2010), pp. 209–213.

[36] X. F. Wang and B. Herman. “Fluorescence imaging spectroscopy and microscopy”. *Chemical Analysis* ().

[37] T. Förster. “Zwischenmolekulare energiewanderung und fluoreszenz”. *Annalen der Physik* 437.1 (1948), p. 55.

[38] J. Zheng. “FRET and Its Biological Application as a Molecular Ruler”. English. Handbook of Modern Biophysics 3 (2010). Ed. by T. Jue, p. 119.

[39] T. Ha, T. Enderle, D. Ogletree, D. Chemla, P. Selvin and S Weiss. “Probing the interaction between two single molecules: fluorescence resonance energy transfer between a single donor and a single acceptor”. *Proceedings of the National Academy of Sciences* 93.13 (1996), p. 6264.

[40] B. Schuler and W. A. Eaton. “Protein folding studied by single-molecule FRET”. *Current Opinion in Structural Biology* 18.1 (2008), p. 16.

[41] R. Roy, S. Hohng and T. Ha. “A practical guide to single-molecule FRET”. *Nature Methods* 5.6 (2008), p. 507.

[42] N. K. Lee, A. N. Kapanidis, Y. Wang, X. Michalet, J. Mukhopadhyay, R. H. Ebright and S. Weiss. “Accurate FRET measurements within single diffusing biomolecules using alternating-laser excitation”. *Biophysical Journal* 88.4 (2005), p. 2939.

[43] E. Nir, X. Michalet, K. M. Hamadani, T. A. Laurence, D. Neuhauser, Y. Kovchegov and S. Weiss. “Shot-noise limited single-molecule FRET histograms: comparison between theory and experiments”. *The Journal of Physical Chemistry B* 110.44 (2006), p. 22103.

[44] A. K. Woźniak, G. F. Schröder, H. Grubmüller, C. A. Seidel and F. Oesterhelt. “Single-molecule FRET measures bends and kinks in DNA”. *Proceedings of the National Academy of Sciences* 105.47 (2008), p. 18337.

[45] E. Sisamakis, A. Valeri, S. Kalinin, P. J. Rothwell and C. A. Seidel. “Accurate single molecule FRET studies using multiparameter fluorescence detection”. *Methods in Enzymology* 475 (2010), p. 455.

[46] S. Kalinin, E. Sisamakis, S. W. Magennis, S. Felekyan and C. A. Seidel. “On the origin of broadening of single-molecule FRET efficiency distributions beyond shot noise limits”. *The Journal of Physical Chemistry B* 114.18 (2010), p. 6197.

[47] Y. Gambin and A. A. Deniz. “Multicolor single-molecule FRET to explore protein folding and binding”. *Molecular BioSystems* 6.9 (2010), p. 1540.

[48] C. A. Seidel, S. Kalinin, S. Felekyan, A. Valeri and S. Sindbert. “Single Molecule FRET Measures Structure and Fast Dynamics of DNA and RNA Four-Way Junctions”. *Biophysical Journal* 98.3, Supplement 1 (2010), p. 266.

[49] A. Muschielok, J. Andrecka, A. Jawhari, F. Brückner, P. Cramer and J. Michaelis. “A nanopositioning system for macromolecular structural analysis”. *Nature Methods* 5.11 (2008), p. 965.

[50] F. Stefani, K Vasilev, N Bocchio, N Stoyanova and M. Kreiter. “Surface-plasmon-mediated single-molecule fluorescence through a thin metallic film”. *Physical Review Letters* 94.2 (2005), p. 023005.

[51] M. Berndt, M. Lorenz, J. Enderlein and S. Diez. “Axial nanometer distances measured by fluorescence lifetime imaging microscopy”. *Nano Letters* 10.4 (2010), p. 1497.

[52] A. I. Chizhik, I. Gregor, F. Schleifenbaum, C. B. Müller, C. Röling, A. J. Meixner and J. Enderlein. “Electrodynamic coupling of electric dipole emitters to a fluctuating mode density within a nanocavity”. *Physical Review Letters* 108.16 (2012), p. 163002.

[53] A. I. Chizhik, I. Gregor, B. Ernst and J. Enderlein. “Nanocavity-Based Determination of Absolute Values of Photoluminescence Quantum Yields”. *ChemPhysChem* 14.3 (2013), pp. 505–513.

[54] T. Ha, A. Y. Ting, J. Liang, W. B. Caldwell, A. A. Deniz, D. S. Chemla, P. G. Schultz and S. Weiss. “Single-molecule fluorescence spectroscopy of enzyme conformational dynamics and cleavage mechanism”. *Proceedings of the National Academy of Sciences* 96.3 (1999), pp. 893–898.

[55] T. Ha, T. A. Laurence, D. S. Chemla and S. Weiss. “Polarization spectroscopy of single fluorescent molecules”. *The Journal of Physical Chemistry B* 103.33 (1999), p. 6839.

[56] A. P. Bartko and R. M. Dickson. “Imaging three-dimensional single molecule orientations”. *The Journal of Physical Chemistry B* 103.51 (1999), pp. 11237–11241.

[57] R. M. Dickson, D. Norris and W. Moerner. “Simultaneous imaging of individual molecules aligned both parallel and perpendicular to the optic axis”. *Physical Review Letters* 81.24 (1998), p. 5322.

[58] J. N. Forkey, M. E. Quinlan and Y. E. Goldman. “Measurement of single macromolecule orientation by total internal reflection fluorescence polarization microscopy”. *Biophysical Journal* 89.2 (2005), pp. 1261–1271.

[59] M. Böhmer and J. Enderlein. “Orientation imaging of single molecules by wide-field epifluorescence microscopy”. *Journal of the Optical Society of America B* 20.3 (2003), p. 554.

[60] J. Jasny and J. Sepioł. “Single molecules observed by immersion mirror objective. A novel method of finding the orientation of a radiating dipole”. *Chemical Physics Letters* 273.5 (1997), pp. 439–443.

[61] M. A. Lieb, J. M. Zavislan and L. Novotny. “Single-molecule orientations determined by direct emission pattern imaging”. *Journal of the Optical Society of America B* 21.6 (2004), pp. 1210–1215.

[62] J. Hohlbein and C. G. Hübner. “Simple scheme for rapid three-dimensional orientation determination of the emission dipole of single molecules”. *Applied Physics Letters* 86.12 (2005), p. 121104.

[63] C.-Y. Lu and B. D. Vanden. “Analysis of orientational dynamics of single fluorophore trajectories from three-angle polarization experiments.” *The Journal of Chemical Physics* 128.24 (2008), pp. 244501–244501.

[64] S. Stallinga and B. Rieger. “Position and orientation estimation of fixed dipole emitters using an effective Hermite point spread function model”. *Optics Express* 20.6 (2012), pp. 5896–5921.

[65] Z. Sikorski and L. M. Davis. “Engineering the collected field for single-molecule orientation determination”. *Optics Express* 16.6 (2008), pp. 3660–3673.

[66] A. S. Backer, M. P. Backlund, A. R. von Diezmann, S. J. Sahl and W. Moerner. “A bisected pupil for studying single-molecule orientational dynamics and its application to three-dimensional super-resolution microscopy”. *Applied Physics Letters* 104.19 (2014), p. 193701.

[67] M. R. Foreman, C. M. Romero and P. Török. “Determination of the three-dimensional orientation of single molecules”. *Optics Letters* 33.9 (2008), pp. 1020–1022.

[68] M. Prummer, B. Sick, B. Hecht and U. P. Wild. “Three-dimensional optical polarization tomography of single molecules”. *The Journal of Chemical Physics* 118.21 (2003), pp. 9824–9829.

[69] E. Betzig and R. J. Chichester. “Single Molecules Observed by Near-Field Scanning Optical Microscopy”. *Science* 262.5138 (1993), pp. 1422–1425.

[70] L. Novotny, M. R. Beversluis, K. S. Youngworth and T. G. Brown. “Longitudinal Field Modes Probed by Single Molecules”. *Physical Review Letters* 86 (23 2001), pp. 5251–5254.

[71] B. Sick, B. Hecht, U. Wild and L. Novotny. “Probing confined fields with single molecules and vice versa”. *Journal of Microscopy* 202.2 (2001), pp. 365–373.

[72] A. Débarre, R. Jaffiol, C. Julien, D. Nutarelli, A. Richard, P. Tchénio, F. Chaput and J.-P. Boilot. “Quantitative determination of the 3D dipole orientation of single molecules”. *The European Physical Journal D-Atomic, Molecular, Optical and Plasma Physics* 28.1 (2004), pp. 67–77.

[73] M. P. Backlund, M. D. Lew, A. S. Backer, S. J. Sahl, G. Grover, A. Agrawal, R. Piestun and W. Moerner. “Simultaneous, accurate measurement of the 3D position and orientation of single molecules”. *Proceedings of the National Academy of Sciences* 109.47 (2012), pp. 19087–19092.

[74] A. I. Chizhik, A. M. Chizhik, A. Huss, R. Jäger and A. J. Meixner. “Nanoscale Probing of Dielectric Interfaces with Single-Molecule Excitation Patterns and Radially Polarized Illumination”. *The Journal of Physical Chemistry Letters* 2.17 (2011), pp. 2152–2157.

[75] A. M. Chizhik, R. Jäger, A. I. Chizhik, S. Bär, H.-G. Mack, M. Sackrow, C. Stanciu, A. Lyubimtsev, M. Hanack and A. J. Meixner. “Optical imaging of excited-state tautomerization in single molecules”. *Physical Chemistry Chemical Physics* 13.5 (2011), p. 1722.

[76] A. I. Chizhik, A. M. Chizhik, D. Khoptyar, S. Bär and A. J. Meixner. “Excitation isotropy of single CdSe/ZnS nanocrystals”. *Nano Letters* 11.3 (2011), p. 1131.

[77] T. H. Taminiau, F. D. Stefani and N. F. van Hulst. “Enhanced directional excitation and emission of single emitters by a nano-optical Yagi-Uda antenna”. *Optics Express* 16.14 (2008), pp. 10858–10866.

[78] S. Empedocles, R Neuhauser and M. Bawendi. “Three-dimensional orientation measurements of symmetric single chromophores using polarization microscopy”. *Nature* 399.6732 (1999), pp. 126–130.

[79] X. Brokmann, L. Coolen, J.-P. Hermier and M. Dahan. “Emission properties of single CdSe/ZnS quantum dots close to a dielectric interface”. *Chemical Physics* 318.1 (2005), pp. 91–98.

[80] K. Early, K. McCarthy, M. Odoi, P. Sudeep, T Emrick and M. Barnes. “Linear dipole behavior in single CdSe-oligo (phenylene vinylene) nanostructures”. *ACS Nano* 3.2 (2009), pp. 453–461.

[81] A. G. Curto, G. Volpe, T. H. Taminiau, M. P. Kreuzer, R. Quidant and N. F. van Hulst. “Unidirectional emission of a quantum dot coupled to a nanoantenna”. *Science* 329.5994 (2010), pp. 930–933.

[82] D. Patra, I. Gregor, J. Enderlein and M. Sauer. “Defocused imaging of quantum-dot angular distribution of radiation”. *Applied Physics Letters* 87.10 (2005), p. 101103.

[83] J. R. Lakowicz. *Principles of fluorescence spectroscopy.* Springer Science & Business Media, 2013.

[84] S. Kühn, U. Håkanson, L. Rogobete and V. Sandoghdar. “Enhancement of Single-Molecule Fluorescence Using a Gold Nanoparticle as an Optical Nanoantenna”. *Physical Review Letters* 97 (1 2006), p. 017402.

[85] I. N. Levine and P. Learning. *Quantum chemistry.* Vol. 6. Pearson Prentice Hall Upper Saddle River, NJ, 2009.

[86] P. W. Atkins and R. S. Friedman. *Molecular quantum mechanics.* Oxford university press, 2011.

[87] N. Obi-Egbedi and I. Obot. “Adsorption behavior and corrosion inhibitive potential of xanthene on mild steel/sulphuric acid interface”. *Arabian Journal of Chemistry* 5.1 (2012), p. 121.

[88] A. Penzkofer and J Wiedmann. “Orientation of transition dipole moments of rhodamine 6G determined by excited state absorption”. *Optics Communications* 35.1 (1980), p. 81.

[89] L. Cavallo, M. H. Moore, J. E. Corrie and F. Fraternali. “Quantum mechanics calculations on rhodamine dyes require inclusion of solvent water for accurate representation of the structure”. *The Journal of Physical Chemistry A* 108.38 (2004), p. 7744.

[90] M. Kasha. “Paths of molecular excitation”. *Radiation Research Supplement* (1960), p. 243.

[91] E. Clementi and M. Kasha. “Spin-orbital interaction in N-heterocyclic molecules general results in a cylindrical potential approximation”. *Journal of Molecular Spectroscopy* 2.1 (1958), p. 297.

[92] A. Boguta and D. Wróbel. “Fluorescein and phenolphthalein—correlation of fluorescence and photoelectric properties”. *Journal of Fluorescence* 11.2 (2001), p. 129.

[93] R. Englman and J. Jortner. “The energy gap law for radiationless transitions in large molecules”. *Molecular Physics* 18.2 (1970), p. 145.

[94] M. Bixon and J. Jortner. “Intramolecular radiationless transitions”. *The Journal of Chemical Physics* 48.2 (1968), p. 715.

[95] M. Bixon and J. Jortner. “Long radiative lifetimes of small molecules”. *The Journal of Chemical Physics* 50.8 (1969), p. 3284.

[96] E. M. Purcell. “Spontaneous emission probabilities at radio frequencies”. *Physical Review* 69 (1946), p. 681.

[97] P. A. Dirac. “The quantum theory of the emission and absorption of radiation”. In: *Proceedings of the Royal Society of London A: Mathematical, Physical and Engineering Sciences.* Vol. 114. 767. The Royal Society. 1927, p. 243.

[98] R. Ladenbarg. “Die quantentheoretische Deutung der Zahl der Dispersionselektronen”. *Zeitschrift für Physik A* 4.4 (1921), p. 451.

[99] W. L. Barnes, R. Laming, E. J. Tarbox, P. Morkel et al. “Absorption and emission cross section of Er 3+ doped silica fibers”. *IEEE Journal of Quantum Electronics* 27.4 (1991), p. 1004.

[100] R. C. Tolman. “Duration of molecules in upper quantum states”. *Physical Review* 23.6 (1924), p. 693.

[101] S. Strickler and R. A. Berg. “Relationship between absorption intensity and fluorescence lifetime of molecules”. *The Journal of Chemical Physics* 37.4 (1962), p. 814.

[102] J. M. Dixon, M. Taniguchi and J. S. Lindsey. “PhotochemCAD 2: a refined program with accompanying spectral databases for photochemical calculations”. *Photochemistry and Photobiology* 81.1 (2005), pp. 212–213.

[103] N. Karedla, J. Enderlein, I. Gregor and A. I. Chizhik. “Absolute photoluminescence quantum yield measurement in a complex nanoscopic system with multiple overlapping states”. *The Journal of Physical Chemistry Letters* 5.7 (2014), pp. 1198–1202.

[104] S. Lin, S. Lee, Y. Yoon and H Eyring. “Medium-induced radiationless transitions and effect of solvent on radiationless transitions”. *Proceedings of the National Academy of Sciences* 73.8 (1976), p. 2533.

[105] K. Joulain, R. Carminati, J.-P. Mulet and J.-J. Greffet. “Definition and measurement of the local density of electromagnetic states close to an interface”. *Physical Review B* 68.24 (2003), p. 245405.

[106] P. Anger, P. Bharadwaj and L. Novotny. “Enhancement and quenching of single-molecule fluorescence”. *Physical Review Letters* 96.11 (2006), p. 113002.

[107] R. Chance, A Prock and R Silbey. “Molecular fluorescence and energy transfer near interfaces”. *Adv. Chem. Phys* 37.1 (1978), p. 65.

[108] M. Born and E. Wolf. *Principles of optics: electromagnetic theory of propagation, interference and diffraction of light.* CUP Archive, 2000.

[109] L. V. Ahlfors. *Complex analysis: an introduction to the theory of analytic functions of one complex variable.* 1979.

[110] D. J. Griffiths and R. College. *Introduction to electrodynamics.* Vol. 3. Prentice Hall Upper Saddle River, NJ, 1999.

[111] K. H. Drexhage. “IV Inveraction of Light with Monomolecular Dye Lasers”. *Progress in Optics* 12 (1974), p. 163.

[112] R. Amos and W. Barnes. “Modification of the spontaneous emission rate of Eu III ions close to a thin metal mirror”. *Physical Review B* 55.11 (1997), p. 7249.

[113] H. Kuhn. “Classical aspects of energy transfer in molecular systems”. *The Journal of Chemical Physics* 53.1 (1970), p. 101.

[114] J. Enderlein. “A theoretical investigation of single-molecule fluorescence detection on thin metallic layers”. *Biophysical Journal* 78.4 (2000), pp. 2151–2158.

[115] J. Enderlein. “Single-molecule fluorescence near a metal layer”. *Chemical Physics* 247.1 (1999), pp. 1–9.

[116] J. R. Lakowicz. “Radiative decay engineering 5: metal-enhanced fluorescence and plasmon emission”. *Analytical biochemistry* 337.2 (2005), pp. 171–194.

[117] J. R. Lakowicz. “Radiative decay engineering 3. Surface plasmon-coupled directional emission”. *Analytical biochemistry* 324.2 (2004), pp. 153–169.

[118] G. W. Ford and W. H. Weber. “Electromagnetic interactions of molecules with metal surfaces”. *Physics Reports* 113.4 (1984), pp. 195–287.

[119] O. Schulz, Z. Zhao, A. Ward, M. Koenig, F. Koberling, Y. Liu, J. Enderlein, H. Yan and R. Ros. “Tip induced fluorescence quenching for nanometer optical and topographical resolution”. *Optical Nanoscopy* 2.1 (2013), p. 1.

[120] D. Patra, I. Gregor and J. Enderlein. “Image analysis of defocused single-molecule images for three-dimensional molecule orientation studies”. *The Journal of Physical Chemistry A* 108.33 (2004), p. 6836.

[121] N. Karedla, A. I. Chizhik, I. Gregor, A. M. Chizhik, O. Schulz and J. Enderlein. “Single-Molecule Metal-Induced Energy Transfer (smMIET): Resolving Nanometer Distances at the Single-Molecule Level”. *ChemPhysChem* 15.4 (2014), pp. 705–711.

[122] M. R. Beversluis, A. Bouhelier and L. Novotny. “Continuum generation from single gold nanostructures through near-field mediated intraband transitions”. *Physical Review B* 68.11 (2003), p. 115433.

[123] A. D. Rakić, A. B. Djurišić, J. M. Elazar and M. L. Majewski. “Optical properties of metallic films for vertical-cavity optoelectronic devices”. *Applied Optics* 37.22 (1998), p. 5271.

[124] X. S. Xie and R. C. Dunn. “Probing single molecule dynamics”. *Science* (1994), p. 361.

[125] J. Vogelsang, R. Kasper, C. Steinhauer, B. Person, M. Heilemann, M. Sauer and P. Tinnefeld. “A reducing and oxidizing system minimizes photobleaching and blinking of fluorescent dyes”. *Angewandte Chemie International Edition* 47.29 (2008), p. 5465.

[126] M. Böhmer and J. Enderlein. “Orientation imaging of single molecules by wide-field epifluorescence microscopy”. *Journal of the Optical Society of America B* 20.3 (2003), p. 554.

[127] J. Hohlbein and C. G. Hübner. “Three-dimensional orientation determination of the emission dipoles of single molecules: the shot-noise limit”. *The Journal of Chemical Physics* 129.9 (2008), p. 094703.

[128] R. Dorn, S Quabis and G Leuchs. “Sharper focus for a radially polarized light beam”. *Physical Review Letters* 91.23 (2003), p. 233901.

[129] M. Stalder and M. Schadt. “Linearly polarized light with axial symmetry generated by liquid-crystal polarization converters”. *Optics Letters* 21.23 (1996), p. 1948.

[130] P. Török, P. Varga, Z. Laczik and G. Booker. “Electromagnetic diffraction of light focused through a planar interface between materials of mismatched refractive indices: an integral representation”. *Journal of the Optical Society of America A* 12.2 (1995), p. 325.

[131] B. Richards and E. Wolf. “Electromagnetic diffraction in optical systems. II. Structure of the image field in an aplanatic system”. In: *Proceedings of the Royal Society of London A: Mathematical, Physical and Engineering Sciences.* Vol. 253. 1274. The Royal Society. 1959, p. 358.

[132] K. Youngworth and T. Brown. “Focusing of high numerical aperture cylindrical-vector beams”. *Optics Express* 7.2 (2000), p. 77.

[133] K. A. Walther, B. Papke, M. B. Sinn, K. Michel and A. Kinkhabwala. “Precise measurement of protein interacting fractions with fluorescence lifetime imaging microscopy”. *Molecular Biosystems* 7.2 (2011), p. 322.

[134] K. D. Weston, P. J. Carson, H. Metiu and S. K. Buratto. “Room-temperature fluorescence characteristics of single dye molecules adsorbed on a glass surface”. *The Journal of Chemical Physics* 109.17 (1998), p. 7474.

[135] P. Tinnefeld, D.-P. Herten and M. Sauer. “Photophysical dynamics of single molecules studied by spectrally-resolved fluorescence lifetime imaging microscopy (SFLIM)”. *The Journal of Physical Chemistry A* 105.34 (2001), p. 7989.

[136] F. Schleifenbaum, C. Blum, V. Subramaniam and A. J. Meixner. “Single-molecule spectral dynamics at room temperature”. *Molecular Physics* 107.18 (2009), p. 1923.

[137] C. Eggeling, J Widengren, R Rigler and C. Seidel. “Photobleaching of fluorescent dyes under conditions used for single-molecule detection: Evidence of two-step photolysis”. *Analytical Chemistry* 70.13 (1998), p. 2651.

[138] H. Piwoński, A. Sokołowski and J. Waluk. “In Search for the Best Environment for Single Molecule Studies: Photostability of Single Terrylenediimide Molecules in Various Polymer Matrices”. *The Journal of Physical Chemistry Letters* 6.13 (2015), p. 2477.

[139] R. Liu, T. Bernal-Lara, A Hiltner and E Baer. “Polymer interphase materials by forced assembly”. *Macromolecules* 38.11 (2005), p. 4819.

[140] P. R. Dolan, X. Li, J. Storteboom and M. Gu. “Complete determination of the orientation of NV centers with radially polarized beams”. *Optics Express* 22.4 (2014), p. 4379.

[141] M. K. Cheezum, W. F. Walker and W. H. Guilford. “Quantitative comparison of algorithms for tracking single fluorescent particles”. *Biophysical Journal* 81.4 (2001), p. 2378.

[142] S. Stallinga and B. Rieger. “Accuracy of the Gaussian point spread function model in 2D localization microscopy”. *Optics Express* 18.24 (2010), p. 24461.

[143] K. I. Mortensen, L. S. Churchman, J. A. Spudich and H. Flyvbjerg. “Optimized localization analysis for single-molecule tracking and super-resolution microscopy”. *Nature Methods* 7.5 (2010), p. 377.

[144] J. Hu, L.-s. Li, W. Yang, L. Manna, L.-w. Wang and A. P. Alivisatos. “Linearly polarized emission from colloidal semiconductor quantum rods”. *Science* 292.5524 (2001), p. 2060.

[145] A. L. Efros. “Luminescence polarization of CdSe microcrystals”. *Physical Review B* 46.12 (1992), p. 7448.

[146] D. Patra, I. Gregor, J. Enderlein and M. Sauer. “Defocused imaging of quantum-dot angular distribution of radiation”. *Applied Physics Letters* 87.10 (2005), p. 101103.

[147] I. Vragović, E. M. Calzado and M. A. D. García. “The structure and energetics of TPD ground and excited states”. *Chemical Physics* 332.1 (2007), p. 48.

[148] J.-L. Brédas, D. Beljonne, V. Coropceanu and J. Cornil. “Charge-transfer and energy-transfer processes in π-conjugated oligomers and polymers: a molecular picture”. *Chemical Reviews* 104.11 (2004), p. 4971.

[149] R. Scholz and M. Schreiber. “Linear optical properties of perylene-based chromophores”. *Chemical Physics* 325.1 (2006), p. 9.

[150] M. Iwamura, S. Takeuchi and T. Tahara. “Ultrafast excited-state dynamics of copper i complexes”. *Accounts of Chemical Research* 48.3 (2015), p. 782.

[151] N. Karedla, S. C. Stein, D. Hähnel, I. Gregor, A. Chizhik and J. Enderlein. “Simultaneous Measurement of the Three-Dimensional Orientation of Excitation and Emission Dipoles”. *Physical Review Letters* 115.17 (2015), p. 173002.

[152] S. V. Aradhya, M. Frei, M. S. Hybertsen and L Venkataraman. “Van der Waals interactions at metal/organic interfaces at the single-molecule level”. *Nature Materials* 11.10 (2012), p. 872.

[153] M. Bottini and T. Mustelin. “Carbon materials: Nanosynthesis by candlelight”. *Nature Nanotechnology* 2.10 (2007), p. 599.

[154] A. P. Demchenko and M. O. Dekaliuk. “Novel fluorescent carbonic nanomaterials for sensing and imaging”. *Methods and Applications in Fluorescence* 1.4 (2013), p. 042001.

[155] C. Liu, P. Zhang, F. Tian, W. Li, F. Li and W. Liu. “One step synthesis of surface passivated carbon nanodots by microwave assisted pyrolysis for enhanced multicolor photoluminescence and bioimaging”. *J. Mater. Chem.* 21.35 (2011), p. 13163.

[156] A. M. Chizhik, A. I. Chizhik, R. Gutbrod, A. J. Meixner, T. Schmidt, J. Sommerfeld and F. Huisken. “Imaging and Spectroscopy of Defect Luminescence and Electron- Phonon Coupling in Single SiO2 Nanoparticles”. *Nano Letters* 9.9 (2009), p. 3239.

[157] T. Schmidt, A. I. Chizhik, A. M. Chizhik, K. Potrick, A. J. Meixner and F. Huisken. “Radiative exciton recombination and defect luminescence observed in single silicon nanocrystals”. *Physical Review B* 86.12 (2012), p. 125302.

[158] L. Brus, P. Szajowski, W. Wilson, T. Harris, S. Schuppler and P. Citrin. “Electronic spectroscopy and photophysics of Si nanocrystals: relationship to bulk c-Si and porous Si”. *Journal of the American Chemical Society* 117.10 (1995), p. 2915.

[159] S. Empedocles, R. Neuhauser and M. Bawendi. “Three-dimensional orientation measurements of symmetric single chromophores using polarization microscopy”. *Nature* 399.6732 (1999), p. 126.

[160] S. Ghosh, A. M. Chizhik, N. Karedla, M. O. Dekaliuk, I. Gregor, H. Schuhmann, M. Seibt, K. Bodensiek, I. A. Schaap, O. Schulz et al. “Photoluminescence of Carbon Nanodots: Dipole Emission Centers and Electron Phonon Coupling”. *Nano Letters* 14.10 (2014), p. 5656.

[161] A. I. Chizhik, J. Rother, I. Gregor, A. Janshoff and J. Enderlein. “Metal-induced energy transfer for live cell nanoscopy”. *Nature Photonics* 8.2 (2014), p. 124.

[162] K. Burridge and M. Chrzanowska-Wodnicka. “Focal adhesions, contractility, and signaling”. *Annual Review of Cell and Developmental Biology* 12.1 (1996), pp. 463–519.

[163] A. D. Bershadsky, N. Q. Balaban and B. Geiger. “Adhesion-dependent cell mechanosensitivity”. *Annual Review of Cell and Developmental Biology* 19.1 (2003), pp. 677–695.

[164] B. Geiger, A. Bershadsky, R. Pankov and K. M. Yamada. “Transmembrane crosstalk between the extracellular matrix and the cytoskeleton”. *Nature Reviews Molecular Cell Biology* 2.11 (2001), pp. 793–805.

[165] J. Sỳkora, K. Kaiser, I. Gregor, W. Bönigk, G. Schmalzing and J. Enderlein. “Exploring fluorescence antibunching in solution to determine the stoichiometry of molecular complexes”. *Analytical Chemistry* 79.11 (2007), p. 4040.

[166] M. P. Gordon, T. Ha and P. R. Selvin. “Single-molecule high-resolution imaging with photobleaching”. *Proceedings of the National Academy of Sciences* 101.17 (2004), pp. 6462–6465.

[167] P. D. Simonson, E. Rothenberg and P. R. Selvin. “Single-molecule-based super-resolution images in the presence of multiple fluorophores”. *Nano Letters* 11.11 (2011), pp. 5090–5096.

[168] D. T. Burnette, P. Sengupta, Y. Dai, J. Lippincott-Schwartz and B. Kachar. “Bleaching/blinking assisted localization microscopy for superresolution imaging using standard fluorescent molecules”. *Proceedings of the National Academy of Sciences* 108.52 (2011), p. 21081.

[169] E. A. Lipman, B. Schuler, O. Bakajin and W. A. Eaton. “Single-molecule measurement of protein folding kinetics”. *Science* 301.5637 (2003), p. 1233.

[170] D. Nettels, A. Hoffmann and B. Schuler. “Peptide Dynamics Investigated with Single-Molecule FRET and Correlation Spectroscopy from Picoseconds to Seconds”. *Journal of Physical Chemistry B* 112.19 (2008), p. 6137.

[171] D. Nettels, I. V. Gopich, A. Hoffmann and B. Schuler. “Ultrafast dynamics of protein collapse from single-molecule photon statistics”. *Proceedings of the National Academy of Sciences* 104.8 (2007), p. 2655.

[172] B. Schuler and W. A. Eaton. “Protein folding studied by single-molecule FRET”. *Current Opinion in Structural Biology* 18.1 (2008), pp. 16–26.

[173] H. Neuweiler, C. M. Johnson and A. R. Fersht. “Direct observation of ultrafast folding and denatured state dynamics in single protein molecules”. *Proceedings of the National Academy of Sciences* 106.44 (2009), pp. 18569–18574.

[174] H. Neuweiler, A. Schulz, M. Böhmer, J. Enderlein and M. Sauer. “Measurement of submicrosecond intramolecular contact formation in peptides at the single-molecule level”. *Journal of the American Chemical Society* 125.18 (2003), pp. 5324–5330.

[175] S. Doose, H. Neuweiler and M. Sauer. “Fluorescence quenching by photoinduced electron transfer: a reporter for conformational dynamics of macromolecules”. *ChemPhysChem* 10.9-10 (2009), pp. 1389–1398.

[176] A. Benda, V. Fagul’ová, A. Deyneka, J. Enderlein and M. Hof. “Fluorescence lifetime correlation spectroscopy combined with lifetime tuning: New perspectives in supported phospholipid bilayer research”. *Langmuir* 22.23 (2006), pp. 9580–9585.

[177] A. Kułakowska, P. Jurkiewicz, J. Sỳkora, A. Benda, Y. Mely and M. Hof. “Fluorescence lifetime tuning—a novel approach to study flip-flop kinetics in supported phospholipid bilayers”. *Journal of Fluorescence* 20.2 (2010), pp. 563–569.

[178] K. Ishii and T. Tahara. “Two-dimensional fluorescence lifetime correlation spectroscopy. 1. Principle”. *The Journal of Physical Chemistry B* 117.39 (2013), pp. 11414–11422.

[179] K. Ishii and T. Tahara. “Two-dimensional fluorescence lifetime correlation spectroscopy. 2. Application”. *The Journal of Physical Chemistry B* 117.39 (2013), pp. 11423–11432.

[180] R. J. Moerland and J. P. Hoogenboom. “Subnanometer-accuracy optical distance ruler based on fluorescence quenching by transparent conductors”. *Optica* 3.2 (2016), p. 112.

[181] G. Taylor. “Dispersion of soluble matter in solvent flowing slowly through a tube”. In: *Proceedings of the Royal Society of London A: Mathematical, Physical and Engineering Sciences.* Vol. 219. 1137. The Royal Society. 1953, pp. 186–203.

[182] G. Taylor. “The dispersion of matter in turbulent flow through a pipe”. In: *Proceedings of the Royal Society of London A: Mathematical, Physical and Engineering Sciences.* Vol. 223. 1155. The Royal Society. 1954, pp. 446–468.

[183] R. Aris. “On the dispersion of a solute in a fluid flowing through a tube”. In: *Proceedings of the Royal Society of London A: Mathematical, Physical and Engineering Sciences.* Vol. 235. 1200. The Royal Society. 1956, pp. 67–77.

[184] T. M. Squires and S. R. Quake. “Microfluidics: Fluid physics at the nanoliter scale”. *Reviews of Modern Physics* 77.3 (2005), p. 977.

[185] R. B. Schoch, J. Han and P. Renaud. “Transport phenomena in nanofluidics”. *Reviews of Modern Physics* 80.3 (2008), p. 839.

[186] D. Bonn, J. Eggers, J. Indekeu, J. Meunier and E. Rolley. “Wetting and spreading”. *Reviews of Modern Physics* 81.2 (2009), p. 739.

[187] A. I. Chizhik, A. M. Chizhik, D. Khoptyar, S. Bär, A. J. Meixner and J. Enderlein. “Probing the radiative transition of single molecules with a tunable microresonator”. *Nano Letters* 11.4 (2011), pp. 1700–1703.

Acknowledgments

This thesis would not have been possible without the tremendous support and motivation in all possible ways from **Jörg Enderlein**. I thank him for supervising my doctoral thesis, for exposing me to a multitude of projects and providing me with the freedom to follow them, and for sharing all his crazy yet realizable ideas, both experimental and theoretical.

I thank the members of my thesis committee, **Prof. Andreas Janshoff** and **Prof. Sarah Köster** for their input and support whenever I required, and taking their precious time out to regularly monitor and discuss the progress of my work.

I would like to thank **Dr. Ingo Gregor** for constantly providing me with his invaluable experience and all the confidence I needed for building and modifying the setups for all the experiments presented in this thesis. Many thanks to all my colleagues, former and present, for all the fruitful discussions, technical support and suggestions in work, especially **Sid**, **Jan** and **Olaf** for pulling me out of the lab from time to time, listening to all my complains and stories of what I achieved so far. I am extremely grateful to **Sebastian**, **Laura**, **Daja** and **Meenu** for their patience and time going through this thesis line by line. I am grateful to all the secretaries for managing and handling the tons of paperwork for each and every conference and trip.

Many thanks to the complete GGNB team for their tireless guidance through all the formalities, and their arduous effort in organizing fantastic retreats and excursions. Being a part of the PBCS board as a student representative and organizing the 2$^{\text{nd}}$ Third Infinity Conference together with the team members has been a great experience.

I acknowledge the financial support from the Niedersächsisches Ministerium für Wissenschaft und Kultur for providing the excellence stipend, and also the SFB 860 (DFG).

I thank all my friends including **Laura**, **Mara** and **Sebastian**, not only for making my stay in Göttingen memorable and fun, but they, more than anything, were the main reason for my sanity, especially in my writing days. Lastly, I am grateful to my parents for all their love and moral support all along the way, who are the main reason for my existence today.

Glossary

CCD	Charge Coupled Device
STORM	Stochastic Optical Reconstruction Microscopy
PALM	Photoactivated Localization Microscopy
PAINT	Points Accumulation for Imaging in Nanoscale Topography (microscopy)
FLIM	Fluorescence Lifetime Imaging Microscopy
FCS	Fluorescence Correlation Spectroscopy
FLCS	Fluorescence Lifetime Correlation Spectroscopy
MIET	Metal-Induced Energy Transfer
smMIET	single-molecule Metal-Induced Energy Transfer
PSF	Point Spread Function
TTTR	Time-Tagged Time-Resolved
TCSPC	Time-Correlated Single Photon Counting
FRET	Förster Resonance Energy Transfer
spFRET	single-pair Förster Resonance Energy Transfer
NSOM	Near-field Scanning Optical Microscope
DNA	Deoxyribonucleic Acid
PAID	Photon-Arrival-Time Intensity Distribution
FILDA	Fluorescence Intensity and Lifetime Distribution Analysis
CND	Carbon Nanodot
N.A.	Numerical Aperture
NV	Nitrogen-Vacancy
HOMO	Highest Occupied Molecular Orbital
LUMO	Lowest Unoccupied Molecular Orbital
EM	Electromagnetic
DOS	Density of States
LDOS	Local Density of States
TE	Transversal Electric
TM	Transversal Magnetic

TIR	Total Internal Reflection
SPCM	Single Photon Counting Module
TTL	Transistor-Transistor Logic
TEM	Transversal Electromagnetic
MPD	Micro Photon Devices
SPAD	Single-Photon Avalanche Diode
NIM	Nuclear Instrumentation Module
SFLIM	Spectrally-Resolved Fluorescence Lifetime Imaging Microscopy
PVA	Poly(vinyl alcohol)
PMMA	Poly(methyl methacrylate)
CPS	Chance, Prock and Silbey (Theory)
EMCCD	Electron Multiplying Charge Coupled Device
TDM	Transition Dipole Moment
PL	Photoluminescence
IDP	Intrinsically Disordered Protein
PET	Photoinduced Electron Transfer
MFD	Molecular Detection Function
ITO	Indium Tin Oxide
TDC	Time-to-Digital Converter
IPTD	Inter-Photon Time Distribution
SHRImP	Single Molecule High-Resolution Imaging with Photobleaching
IRF	Instrument Response Function
AOTF	Acousto-optical Tunable Filter
MLE	Maximum Likelihood Estimation

Curriculum Vitae

Karedla Venkata Satya Narain

Graduated Chemist (Integrated Master of Science in Chemistry)
born, April 3rd 1989 in Hyderabad, India

Academical Background

08.2012 - present	Doctoral Dissertation Georg - August University, Göttingen, Germany Third Institute of Physics - Biophysics Prof. Dr. Jörg Enderlein
07.2007 - 04.2012	Integrated Master of Science Chemistry Indian Institute of Technology, Roorkee, India
05.2011 – 07.2011	Research Internship National University of Singapore, Singapore Center of BioImaging Sciences (CBIS) Prof. Dr. Thorsten Wohland
05.2010 – 07.2010	Research Internship Ruprecht – Karls University, Heidelberg, Germany Bioquant Dr. Dirk-Peter Herten
06.2009 – 07.2009	Research Internship Indian Institute of Technology, Bombay, India

Department of Chemisty
Prof. G. Naresh Patwari

Talks

11.2016 Superresolution Microscopy Symposium
350 ans Acadèmy des sciences
Institut de France, Paris
"Advanced fluorescence microscopy:
Metal-Induced Energy Transfer (MIET)"

09.2016 22nd International Workshop on "Single Molecule Spectroscopy and Super-resolution Microscopy in the Life Sciences", Berlin Germany
"Measurement of thicknesses and leaflet-dependent diffusion of lipids
in lipid bilayers using MIET and 2f-FLCS"

04.2016 International Discussion Meeting - FRET 2, Göttingen, Germany
"Single-molecule Metal-Induced Energy Transfer (smMIET):
Resolving nanometer distances at single molecule level"

11.2015 Novel Probes for Fluorescence Microscopy, Göttingen, Germany
"Simultaneous measurement of the three-dimensional orientation
of excitation and emission dipoles"

04.2015 Focus On Microscopy (FOM)-2015, Göttingen, Germany
"Three-dimensional orientation imaging of single fluorescent emitter transition dipoles"

03.2015 79th Annual Meeting of the DPG and DPG Spring Meeting
Berlin, Germany
"Three-dimensional orientation imaging of single fluorescent emitter transition dipoles"

09.2014 20th International Workshop on
'Single Molecule Spectroscopy and Ultrasensitive Analysis in Life Sciences'
Berlin, Germany
"Single-Molecule Metal-Induced Energy Transfer (smMIET):

	Measuring axial distances and dynamics at single molecule level”
02.2014	SPIE Photonics West - 2014 Single Molecule Spectroscopy and Superresolution Imaging VIII San Francisco, California, USA *“Metal-Induced Energy Transfer:* *Measuring Quantum Yields and Molecular Distances”*
08.2013	Max Planck Institute - Dynamics and Self-Organization, Göttingen, Germany Seminar Dynamics of Complex Fluids *“Flow measurements using Fluorescence Correlation Spectroscopy (FCS):* *Recent advances and related studies ”*

Fellowships, Awards and Achievements

02.2014	PicoQuant Young Investigator Award (SPIE - 2014)
08.2012 - 07.2015	Ministerium für Wissenschaft und Kultur (MWK) excellence stipend Lower Saxony, Germany
05.2010 - 07.2010	DAAD - WISE stipend

Other Professional Activities

09.2014 - 03.2016	Student representative and board member of the IMPRS-PBCS graduate school, Göttingen
2015	2nd Third Infinity conference organizer
2009	Events Manager, Cognizance 2009, Indian Institute of Technology, Roorkee, India

Publications

Isbaner, S.*; **Karedla, N.***; Ruhlandt, D.; Stein, C.S.; Chizhik, A.I.; Gregor, I.; Enderlein, J. *“Dead-time Correction of Fluorescence Lifetime Measurements and fluorescence lifetime imaging.”* Optics Express **24** 9429-9445 (2016)
*(*equally contributing authors*)

Karedla, N.; Stein, S.; Hähnel, D.; Gregor, I.; Chizhik,A.I.; Enderlein, J.
"Simultaneous Measurement of the Three-Dimensional Orientation of Excitation and Emission Dipoles" Physical Review Letters **115** 173002 (2015)

Karedla, N.; Ruhlandt, D.; Chizhik, A.M.; Enderlein, J.; Chizhik, A.M.
"Metal-Induced Energy Transfer"
In: Advanced time-correlated single photon counting techniques
Eds: Kapusta, P.; Wahl, M.; Erdmann, R.
Springer International Publishing pp. 265-281 (2015)

Valley, C.C.; Arndt-Jovin, D.J.; **Karedla, N.**, Steinkamp, M.P.; Chizhik, A.I.; Hlavacek, W.S.; Wilson, B.S.; Lidke, K.A.; Lidke, D.S. *"Enhanced Dimerization Drives Ligand-Independent Activity of Mutant Epidermal Growth Factor Receptor in Lung Cancer"* Molecular Biology of the Cell **26** 4087 (2015)

Karedla, N.; Gregor, I.; Enderlein, J. *"Analytical Approximations of the Diffusive Dispersion in Fluid Flows"* European Physics Letters **108** 4007 (2014)

Karedla, N.; Enderlein, J.; Gregor, I.; Chizhik, A.I.
"Absolute Photoluminescence Quantum Yield Measurement in a Complex Nanoscopic System with Multiple Overlapping States" The Journal of Physical Chemistry Letters **5** 1198 (2014)

Ghosh, S.; Chizhik, A.M.; **Karedla, N.**; Debaliuk, M.O.; Gregor,I.; Schuhmann, H.; Seibt, M.; Bodensiek, K.; Schaap, I.A.T.; Schulz, O.; Demchenko, A.P.; Enderlein, J.; Chizhik, A.I. *"Photoluminescence of Carbon Nanodots: Dipole Emission Centers and Electron-Photon Coupling"* Nano Letters **14** 5656-5661 (2014)

Karedla, N.; Chizhik, A.I.; Gregor, I.; Chizhik, A.M.; Schulz, O.; Enderlein, J.
"Single-Molecule Metal Induced Energy Transfer (smMIET): Resolving Nanometer Distances at Single Molecule Level" ChemPhysChem **15** 705-11 (2014)